

UNIVERSITY OF TWENTE.

Faculty of Engineering Technology,
Research Chair of Production Technology

Exploratory research of friction stir extrusion additive manufacturing using AA6060 T6



R.C.G. Ariës
M.Sc. Thesis
April 2021

Supervisor:
dr. ir. T.C. Bor

Faculty of Engineering Technology,
Research Chair of Production Technology
University of Twente
P.O. Box 217
7500 AE Enschede
The Netherlands

Acknowledgement

I would like to take this opportunity to thank many people that supported me during the writing of my thesis.

First of all I would like to thank Ton Bor for the supervision during my research. I want to thank him for his enthusiasm and valuable feedback. Although he was busy, he still managed to find time to discuss a number of points.

I also would like to thank the staff members of the workshop in the Horst, especially Norbert and Henk for teaching me how to use the mill and the lathe. Besides that it was possible to use small pieces of material to modify the experimental setup.

The analysis of the specimen would not have been possible without the help of Nick and Bert who guided me through how to use the equipment in the lab. Special thanks for Nick to perform several analysis during the Covid-19.

Thanks to Henk-Jan, the predecessor of this project, who passed knowledge and information about the experimental setup. I also would like to thank my fellow students during my study.

I want to thank the people assisting me during my graduation project of the University of Twente and would like the members of the exam committee for their invested time and effort.

Finally, I would like my family and friends supporting me during my study and graduation project.

Summary

Additive Manufacturing (AM) is an upcoming advanced production process, also known as 3D printing, made possible by the transition of analog to digital processes. During the past years the University of Twente studied different printing techniques by the group of production technology. Techniques studied are friction surfacing, friction surface cladding, friction stir extrusion, and Friction Stir Extrusion Additive Manufacturing (FSEAM) that will be studied in this thesis. The advantage over fusion based techniques is that the material processed stays below the melting temperature (solid-state) that minimizes the chance of solidification cracks to occur, especially useful for the processing of high strength aluminiums. Besides the advantage of preventing solidification cracking, vaporization of alloying elements is prevented as well remaining the chemical composition.

The principle of Friction Stir Extrusion Additive Manufacturing (FSEAM) is that a rod is pressed against a tool leading to internal friction and plastic deformation, heating up the processed material and dispersing the oxide layer. The material is then transported by the tool through a nozzle and extrusion takes place above the substrate. The final step is to move the table to AM several layer upon each other. The build up pressure by the tool in combination with shearing the extruded material upon the substrate/previous layer ensures removal of oxides and enables metal on metal contact. During the experiments, the velocity of the table was varied without changing the volumetric flow, rotational rate, and nozzle. As a result, increasing the table velocity resulted in a decrease in extrusion force and nozzle temperature. In addition, a fluctuating behavior was seen in the extrusion force and nozzle temperature depending on the direction of the table movement due to stiffness of the FSEAM setup. In terms of strength, the best results are obtained when a degree of overfeeding of 1.14–1.26 is used, resulting in widening of the deposited layers. Besides, Scanning Electron Microscope (SEM) images showing strong plastic deformation and dimples formation indicating proper bonds are formed. Also, smaller equiaxed grains are formed that increases the strength of the additive manufactured material. However, the strength does not increase due to the growth/dissolution of precipitates. Decreasing the material supply further, increases signs of starvation resulting in poorer bonds and thus poorer mechanical properties.

Additionally, an isotherm mechanical 3D model was constructed to simulate trends observed in the experimental part with respect to the extrusion force. The model uses a power-law to describe the material as a shear thinning behaviour. This model is capable of reproducing the same trend as was seen in the experimental section that increasing the table velocity decreases the extrusion force (pressure). However, the pressure was overestimated most likely due to full stick conditions.

List of acronyms

FSE	Friction Stir Extrusion
FSEAM	Friction Stir Extrusion Additive Manufacturing
FSC	Friction Surface Cladding
NS	Navier-Stokes
DAQ	Data Acquisition device
SSAM	Solid State Additive Manufacturing
AM	Additive Manufacturing
EDX	Energy Dispersive X-Ray
FS	Friction Surfacing
AFS	Additive Friction Stir
SS	Solid State
SSAM	Solid State Additive Manufacturing
UT	University of Twente
MD-AM	Mechanical Deformation based Additive Manufacturing
UAM	Ultrasonic Additive Manufacturing
AFSD	Additive Friction Stir Deposition
CSAM	Cold Spray Additive Manufacturing
DED	Direct Energy Deposition
PBF	Powder Bed Fusion
HYB	Hybrid Metal and Extrusion bonding
NI	National Instruments
EBSD	Electron Backscatter Diffraction
SEM	Scanning Electron Microscope
TEM	Transmission Electron Microscopy
HAB	High Angle Grain Boundary

Nomenclature

Ω	Rotational rate
σ_0	Material constant (Hall-Petch Eq.)
θ	Tilt angle
d	Grain size diameter (Hall-Petch Eq.)
k_y	Material constant (Hall-Petch Eq.)
p_{cyl}	Cylinder pressure
T_m	Melt temperature
T_{gg}	Critical grain growth temperature
v_t	Translational speed
v_{cyl}	Cylinder input speed

Contents

Acknowledgement	iii
Summary	v
List of acronyms	vii
1 Introduction	1
1.1 Motivation and theoretical background	1
1.2 Goals of the assignment/Research objectives	6
2 Literature review	7
2.1 Precipitation hardening	7
2.2 Dimple formation	9
2.3 Continuous dynamic recrystallization	10
2.4 Comparable techniques to FSEAM	11
2.5 Building directions	15
3 Friction Stir Extrusion Additive Manufacturing experiments	17
3.1 Introduction	17
3.2 Experimental procedure	17
3.2.1 Experimental setup	17
3.2.2 Experiments	20
3.2.3 Materials	23
3.2.4 Analysis methods	24
3.3 Results and discussion	27
3.3.1 AM-1	27
3.3.2 AM-2	30
3.3.3 AM-3 to AM-6	34
3.3.4 Tensile tests	38
3.3.5 Fracture surface analysis tensile test specimen	41
3.3.6 AM-7	45
3.4 Conclusion	47
4 Modeling the material flow and pressure generation during FSEAM	49
4.1 Introduction	49
4.2 General assumptions	49

4.3	Boundary conditions	50
4.4	Previous models	50
4.5	Power-law	51
4.6	Axisymmetric model	52
4.6.1	Velocities and pressure profiles of a parallel section	53
4.6.2	Velocities and pressure profiles of the axisymmetric model	57
4.7	3D models geometry and boundary conditions	58
4.8	Comparison axisymmetric model to the 3D extrusion model	62
4.9	3D additive manufacturing model compared to experimental results	65
4.10	Modeling conclusions	68
5	Discussion	71
6	Conclusions and recommendations	81
6.1	Conclusions	81
6.2	Recommendations	82
	References	85
	Appendices	
A	Alloy AA2024 and AA6060 data sheets	89
B	Data of FSE experiments	93
B.1	Adjustments of the setup	93
B.2	Experimental data FSE-2	96
B.3	Experimental data FSE-3	105
C	Tensile test dimensions	113
D	Data of FSEAM experiments	115
D.1	Reference material	117
D.2	FSEAM-1	121
D.3	FSEAM-2	133
D.4	FSEAM-3	149
D.5	FSEAM-4	153
D.6	FSEAM-5	164
D.7	FSEAM-6	169
D.8	FSEAM-7	179
E	Angular velocity derivation using the Navier-Stokes (NS) equations	191

Introduction

Section 1 of this chapter describes several metal Additive Manufacturing (AM) processes. In addition, techniques studied by the University of Twente (UT) are described. Section 2 describes the goal of this thesis.

1.1 Motivation and theoretical background

An upcoming advanced production process is AM, also known as 3D printing, made possible from the transition of analog to digital processes [1]. During AM actuators are computer controlled to move a printhead that is able to deposit material along a designated path. Or, the actuators control an energy distributor (for example a laser) to print material. Once a part has been modeled in computed-aided-design (CAD) software, the data is used for the path. In most cases, the part is sliced into several layers throughout the height. The AM process deposits material layerwise to build the part. In this way, complex geometrical shapes can be produced. Furthermore, depositing materials only where necessary results in a reduction of excess material, unlike subtractive methods. Examples of subtractive methods are milling and turning where material is removed from a solid part to obtain the correct geometry. The removed material can be seen as waste during these methods. The AM process can also be seen as a rapid prototyping technique as different geometric shapes can be easily manufactured. A drawback of AM is that it is not able to produce large quantities, yet. The most common types of materials used for AM are plastics and metals [2]. This study focuses on aluminium (metal) processed in the solid-state regime. An overview of metal AM processes can be seen in figure 1.1.

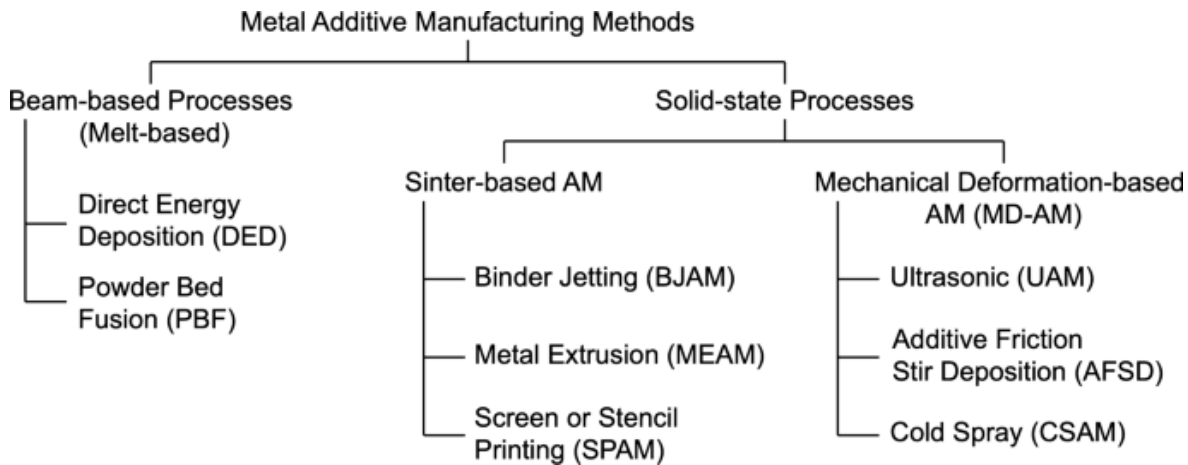


Figure 1.1: An overview of metal AM methods, taken from [3].

The most commonly used AM techniques in the industry are fusion-based approaches, namely Powder Bed Fusion (PBF) and Direct Energy Deposition (DED) [4]. Fusion-based approaches use the melting of material to bond layers together. PBF is a technique that deposits a thin layer of powder (metal or polymeric) in the build chamber using a roller as can be seen in figure 1.2a. Once a layer of powder has been deposited an energy source in the form of a laser or electron beam is used to fuse/sinter the powder to create a solid part. After completion of the solidification process, the next layer of powder is deposited over the existing layers. This process repeats itself until the part has been completed. Some disadvantages that have been encountered using this technique are the anisotropy of the part, powder entrapment in small channels, and cost-effectiveness [4]. Furthermore, the size of the part is limited to the size of the build chamber.

Next, DED is a technique that adds energy and material at the same time to form bonds, unlike PBF. Energy is added to the feed material in the form of a laser, electron beam, or plasma arc as can be seen in 1.2b. The feed material is added in the form of powder or a wire. During DED, the part is printed on top of a build platform instead of using a build chamber, like PBF. Less complex geometric can be manufactured using this technique. Comparing DED to PBF the material porosity is decreased and the maximum build rate is increased from $0.2kg/h$ to $5.5kg/h$. A disadvantage of this technique is that the post-processing has to be performed to a greater extent compared to PBF in order to obtain the desired tolerance [4].

The above described techniques use a melting pool to bond layers together to manufacture good and well-usable products. However, some defects may occur as a result of melting the feed material, such as vaporization of alloying elements, solidification cracking, void formation, and anisotropic behavior of the part [5], [6].

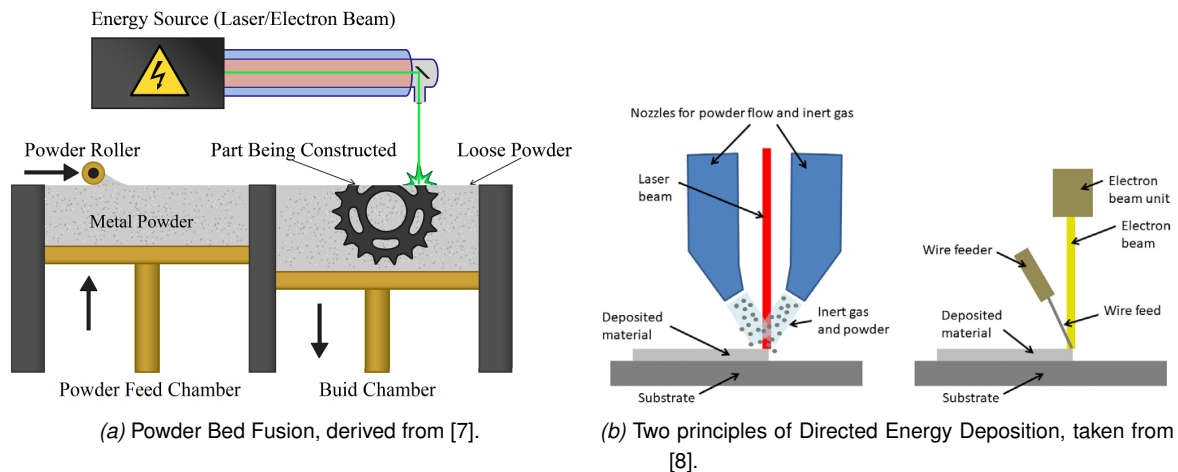


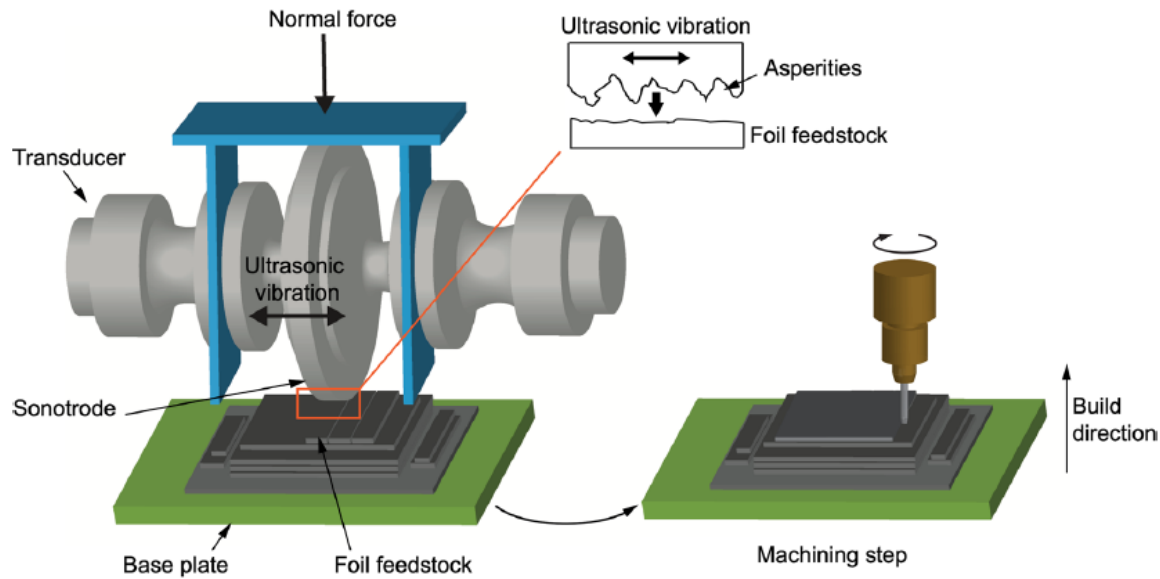
Figure 1.2: Schematic overviews of fusion based Additive Manufacturing techniques.

The solidification cracking and vaporization of the alloying elements can be counteracted by the use of Solid State Additive Manufacturing (SSAM) processes. During these processes, the temperature of the material remains below the melting point resulting in that no vaporization of alloying elements [9]. Besides, the occurrence of solidification cracking is prevented by remaining the temperature below the melting point. In other words, the degree to which the material has to shrink decreases and keeps the material intact [10]. Figure 1.1 shows two groups of Solid State (SS) processes, namely Sinter-based and Mechanical Deformation-based AM techniques. In this thesis, a brief description of the Mechanical Deformation based Additive Manufacturing (MD-AM) processes will be given since they are closely related to the work performed by the UT.

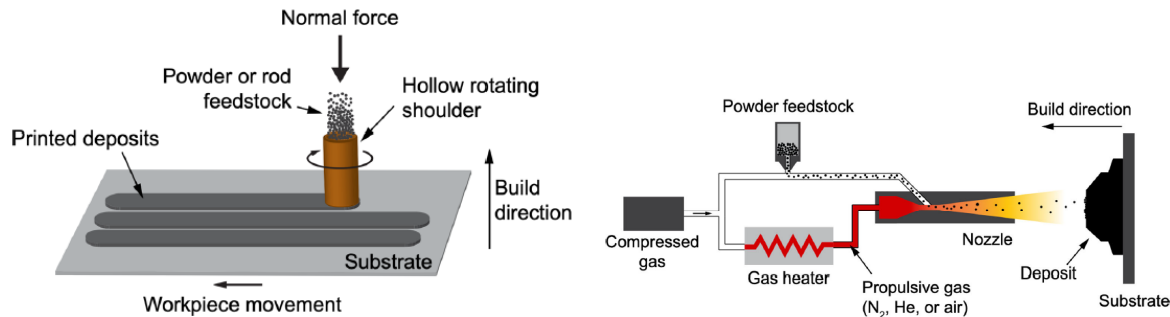
Ultrasonic Additive Manufacturing (UAM) is a technique that uses ultrasonic vibration in combination with a normal force applied to a thin metallic sheet to bond it to the previous layer. This combination introduces severe plastic deformation in combination with smoothing the unevenness of the surface to bond layers of (dis)similar metals. Furthermore, the scrubbing motion ensures that the oxide layers are removed. The ultrasonic frequency is typically around the $20kHz$ [3]. After additive manufacturing of several layers, conventional tooling is required to obtain the final form of the part as can be seen in figure 1.3a.

Next, Additive Friction Stir Deposition (AFSD) uses feedstock material in the form of rods or powder that are forced through a cylindrical tool as shown in figure 1.3b. The conjunction of the rotating tool and normal force ensures sufficient heating between the feedstock and the substrate interface due to friction. The generated heat softens the material enabling it to plastically deform and removes in combination with the exerted normal force the oxide layer. As a result, metal on metal contact is achieved, making bonding between layers possible [3], [11].

The final technique that will be discussed is Cold Spray Additive Manufacturing (CSAM). This technique transports metal powder using a gas (nitrogen, helium, or air) with a temperature that ranges between $25^{\circ}C$ - $1000^{\circ}C$. The velocity of the particles exceeds the speed of sound on impact. This kinematic energy is mostly transformed in plastic deformation and breakage of the oxide layer. As a result, metal on metal contact is achieved, enable bonding between the particles and substrate [3], [12]. The principle of CSAM is shown in figure 1.3c.



(a) Schematic overview of UAM. On the left the AM principle and on the right the machining step, taken from [3].



(b) Schematic overview of AFSD, taken from [3].

(c) Schematic overview of CSAM, taken from [3].

Figure 1.3: Schematic overviews of MD-AM techniques except for AFSD.

The UT studied several cladding techniques using the SS principle, namely Friction Surfacing (FS) and Friction Surface Cladding (FSC). In addition, an extrusion method was studied, called Friction Stir Extrusion (FSE), before starting with the research towards AM that is based on the same extrusion principle, called FSEAM. These techniques will briefly be described and a more detailed explanation regarding FSEAM will be given in chapter 3. A schematic overview of these techniques can be seen in figure 1.4.

FS uses a consumable rod as tool and cladding/printing material, called the mechtrode, and can be seen in figure 1.4a [13]. The process starts with rotating the mechtrode and bringing it in contact with the substrate under an axial load generating heat due to friction. As a result, severe plastic deformation will occur that will disperse the oxide layer of the tool. The high pressure and the relative motion between the tool and the substrate also results in shearing the oxide layer of the substrate. Once the oxide layers are removed, bonding is achieved by the high pressure that ensures the proper spacing between the atoms to form a bond. Unfortunately, this process has three main drawbacks. The first drawback is that the process consumes the mechtrode which needs to be replaced repeatedly, preventing continuous deposition. The second drawback is the formation

of flash. Flash is formed while consuming the mechtrode and is an accumulation of material that occurs around the mechtrode which moves axially towards the tool clamps. The final drawback is that it is hard to control the dimensions of the deposited layers

The undesired flash formation and uncontrollable layer dimensions are solved using a non-consumable tool in the FSC technique as can be seen in figure 1.4b. The feed material is forced through the center of the rotating tool. The non-consumable tool ensures that no flash formation can occur and that additional heat is generated. Using this technique, process parameters such as layer height and width can be controlled well. The FSC technique is similar to AFSD as depicted in figure 1.3b. Several drawbacks of the FSC technique are that it is not convenient to integrate a continuous feeding system, has insufficient temperature control, and the shape of the deposited layers is hard to control, especially the width. Since the minimum width of the layer is determined by the minimum diameter of the feed rod that has to withstand a certain axial force.

As a result of these drawbacks, a new setup was built that made the use of a continuous feed system possible, called FSE. In addition, the system can be cooled using a coolant to gain more control over the temperature and different types of nozzles can be easily exchanged influencing the shape of the extruded profile. The setup used for FSE (shown in figure 1.4c) is similar to the setup for additive manufacturing, called FSEAM as can be seen in figure 1.4d. Before explaining the similarities between these setups, properties of the material that will be used for the experiments must be stated. The material that will be used during the experiments is aluminium. This material will reacts with the oxides in the earth's atmosphere. As a result, a thin layer of aluminium oxide arises that is undesired for creating metallurgic bonds. The principle will be explained using figure 1.4c and 1.4d showing a schematic overview of the setup used for the experiments, respectively FSE and FSEAM. In figure 1.4c aluminium is pressed against a threaded rotary tool resulting in heat generation due to internal friction and severe plastic deformations causing the aluminium to warm up. In addition, the aluminium oxide layer will be dispersed and pressure is build up by the tool's thread forcing the processed material downwards through the nozzle for extrusion. Extrusion completes the FSE process, so far as the similarities between FSE and FSEAM. The biggest difference between the processes is the nozzle used during the experiments and a build platform is added for FSEAM for printing. The build up pressure and the rotary motion of the aluminium introduced by the tool are used to break the aluminium oxide layer of the substrate/previously deposited layer that has the same speed as the build platform. Eventually, the pressure ensures proper spacing between atoms and elevated temperatures increase the diffusion rate to create proper bonds. The final step of AM process is to translate the build platform in a certain direction. The detailed setup is shown in section 3.

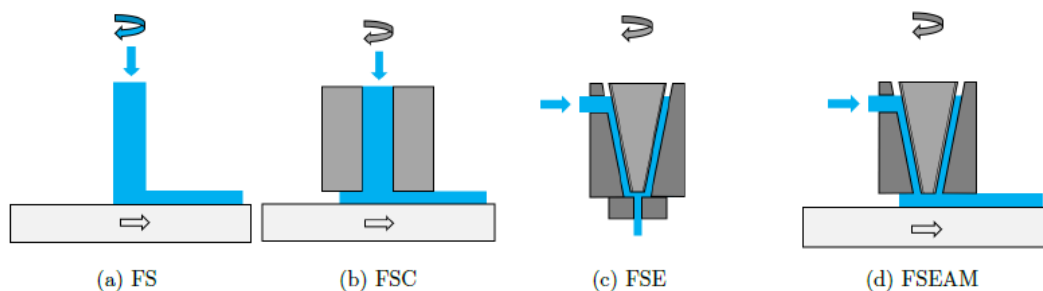


Figure 1.4: Overview of SS techniques studied by the UT.

The main changes from FS to FSEAM focused on the improvements of drawbacks such as flash formation, the possibility of a continuous feeding system, temperature control of the processed material, and the layer dimensions (width and height). Besides these improvements, the bond between the clad layer and substrate has already been studied by L. Shaojie [14] for FSC. In addition, several process parameters of FSE have been studied by J.B. Lind and H.J. Smit with respect to the volumetric flow rate and rotational rate [15], [16]. As a result of the improvements and the performed experimental parametric studies, SSAM has been made possible. Besides the important parameters as the rotation rate of the tool, supply rate of the feed material, and the tool gap (vertical distance between the tool and the nozzle), FSEAM introduces several new parameters. These parameters are the translation speed of the build platform, layer dimensions, and additional building directions. These parameters have not been extensively studied, yet.

1.2 Goals of the assignment/Research objectives

As was mentioned in the previous section, the FSEAM process is relatively new to the UT and introduces new parameters such as the translation speed of the build platform (table velocity), layer dimensions, and additional building directions compared to FSE. The first step is to get an impression of the ratio between the feed material and the table velocity to print solid well-bonded layers. Therefore, the table velocity will be varied while remaining the other parameters constant. Since FSEAM is a poorly understood process, a well-known extrudable aluminium will be used, AA6060 T6. During this research, two building directions are considered, one in horizontal direction and in vertical direction. The main research question to be answered is:

How can the process parameter (table velocity) be related to the microstructure and mechanical properties of Friction Stir Extrusion Additive Manufactured aluminium AA6060 T6?

The main research question considers many important aspects for additive manufacturing. In order to answer this question, sub-questions have been drawn up, which can be categorized in an experimental and modeling part.

Experimental:

- *Is it possible to deposit layers of AA6060 T6 using FSEAM? If so, what is the quality of the bond and is the process reproducible?*
- *How does the parameter 'table velocity' influence the behaviour of the nozzle temperature and extrusion force during the experiments at a constant rotation rate of the tool and a constant volumetric flow rate?*
- *What is the effect of the nozzle temperature and extrusion force on the microstructure and mechanical properties of an AA6060 T6 additive manufactured part?*

Modeling:

- *Can trends observed in the experimental part regarding extrusion force be validated by an isotherm-mechanical model?*

Literature review

The thermo-mechanical nature of the FSEAM process affects the microstructure of the aluminium alloys used. In section 2.1 the heat treatment, called precipitation hardening, will be explained in more detail. Section 2.2 describes what dimple formation entails and section 2.3 describes a mechanism that is observed during FS experiments with respect to the grains. Section 2.4, briefly describes comparable techniques to FSEAM researched by other parties. The final section, explains more about the weakest building directions of additive manufacturing.

2.1 Precipitation hardening

The strength and hardness of metal alloys can be enhanced by precipitation hardening. It uses the formation of extremely small, uniformly dispersed particles of a second phase within the original matrix phase [17]. These particles are called precipitates and can be formed by two heat treatments, namely solution and precipitation heat treatment. The precipitates act like obstacles to dislocation motion in order to increase strength and toughness. Assuming a metal alloy consist of two elements for simplicity, the first step is to dissolve element B completely in element A at an elevated temperature, T_0 , as can be seen in figure 2.1a. The elevated temperature is used to increase the solubility of element B. The amount of element B that can be solved in element A is indicated by the solvus line drawn from point N to M in figure 2.1a. Once element B is completely dissolved, the metal alloy is cooled down rapidly (quenched) in order to create an α -phase (element A) solid solution supersaturated with elements of B at T_1 .

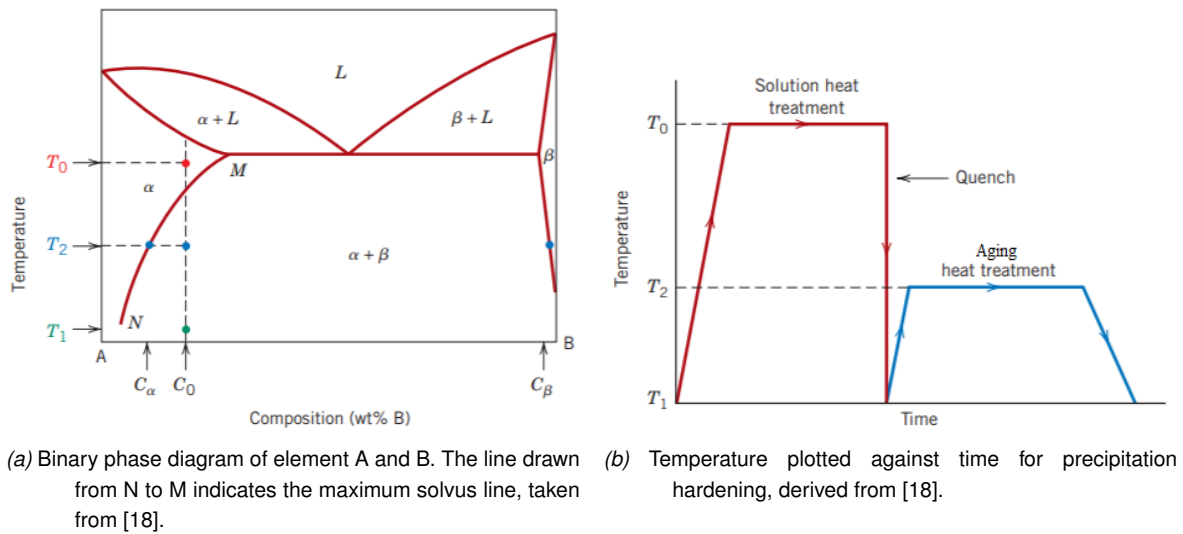


Figure 2.1: Schematic overview of precipitation hardening.

After the solution heat treatment has finished, the metal alloy is relatively soft and weak. Diffusion rates at the temperature T_1 are extremely slow such that the α -phase is retained at this temperature for relatively long periods [17]. To enhance the strength and hardness the metal alloy's temperature is elevated in the $\alpha + \beta$ -regime for a certain period of time, T_2 . During this period, the diffusion rate is increased significantly and β precipitates start to grow. Besides, the number of β precipitates starts to decrease and the spacing between the precipitates starts to grow. The higher the temperature the higher the diffusion rate, so shorter period of time is required to grow the precipitates as can be seen in figure 2.2. An optimum can be found between the precipitate size and the strength/hardness of the metal alloy. If the precipitates increase in size beyond the optimum, the strength and hardness decrease again. This behavior is called overaging and can be seen in figure 2.3.

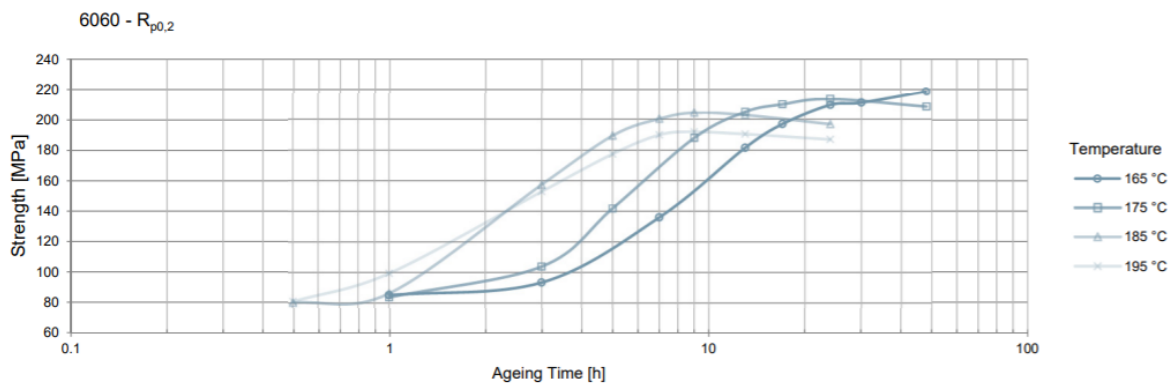


Figure 2.2: The precipitation hardening characteristics of a 6060 aluminium alloy, taken from [19].

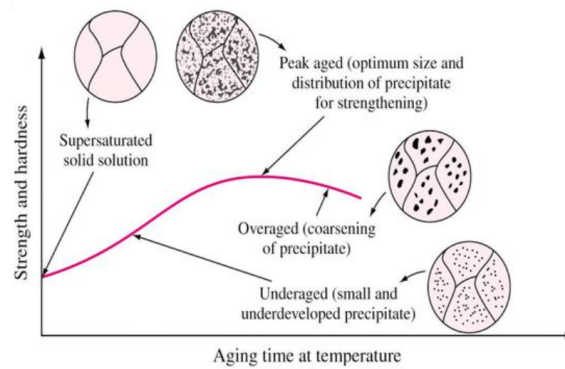


Figure 2.3: Aging process of precipitates ,taken from [18].

2.2 Dimple formation

The precipitates, as a result of the precipitation heat treatment, are usually extremely strong and more brittle than the matrix material (figure 2.4a). Upon plastic deformation, the matrix material deformation rate is higher than that of the stronger, more brittle precipitates. As a result, voids are nucleated near the precipitates to compensate for the incompatibility as can be seen in figure 2.4b. The nucleation may result in fracture of the precipitates or the separation of the matrix-precipitate interface bond. Finally, the material fractures due to reaching its maximum strength. Observing the fracture surface, those nucleation of voids can be seen and are called dimples (figure 2.4c) [20]. Figure 2.5 shows an example of a finely dimpled surface of AA6060 of approximately $5 - 10\mu m$ [21]. The formation of dimples on a fracture surface indicate a high resistance to failure.

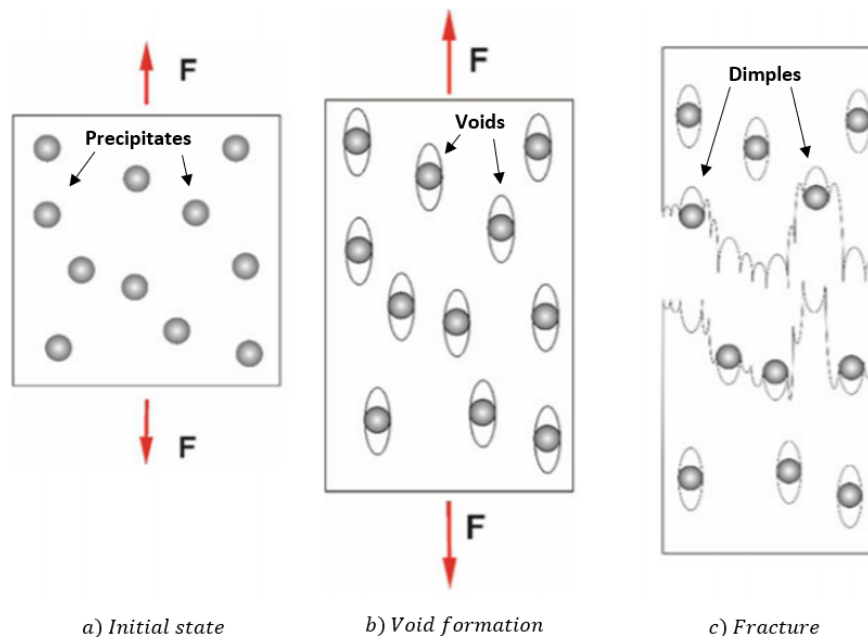


Figure 2.4: The formation of dimples schematically represented, derived from [22].

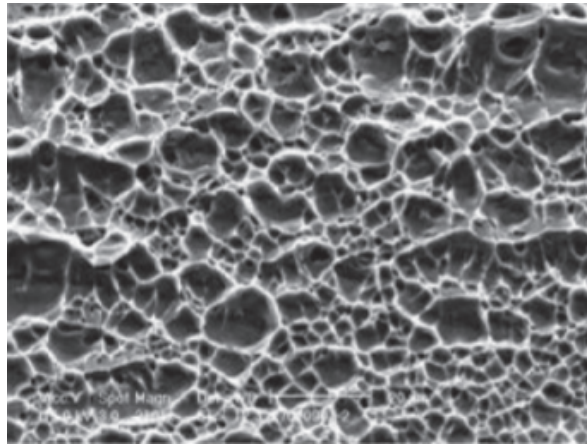


Figure 2.5: Dimple formation in aluminium AA6060 specimen, derived from [21].

2.3 Continuous dynamic recrystallization

Strain hardening is the phenomenon whereby a ductile materials becomes harder and stronger as it is plastically deformed as a result of increasing the dislocation density (figure 2.6a) [17]. These dislocations hold a certain strain energy. During a process called continuous dynamic recrystallization (CDRX), the strain energy is released by the formation of equiaxed subgrains, with a low energy state (figure 2.6b) [23]. In addition, those subgrains have a small misorientation, called low-angle boundaries. Continuing the plastic deformation, the low-angle boundaries can grow into high-angle boundaries as can be seen in figure 2.6c and 2.6d. It is possible for low-angle boundaries co-exist in high-angle boundary grains. Increasing the number of grains leads to smaller grains that eventually will lead to improvement of strength and toughness. The yield stress (σ_y) as a function of the average grain diameter (d) can be calculated using the Hall-Petch equation as can be seen in equation 2.1 [18]. The formation of these equiaxed grains has been seen in processes like FS and FSC.

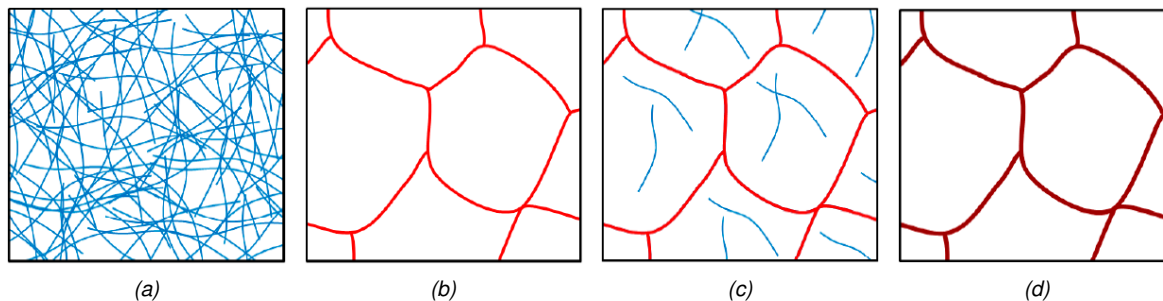


Figure 2.6: In (a) the dislocation density is increased, (b) formation of subgrains with low-angle boundaries, (c) increasing dislocation density inside subgrains, and (d) formation of high-angle boundaries. Derived from [23].

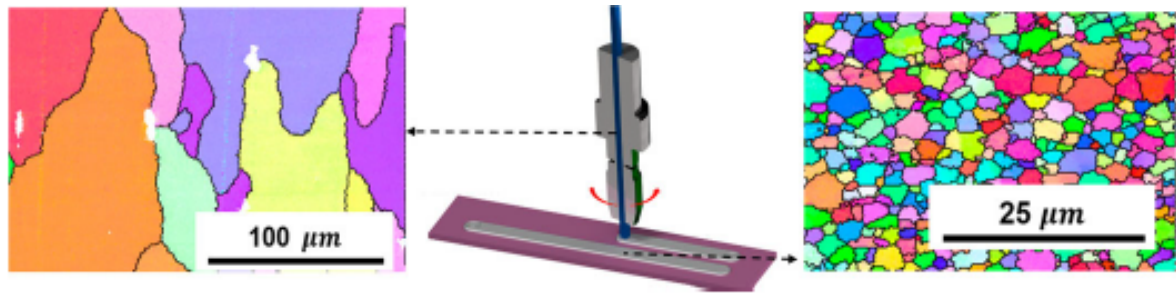


Figure 2.7: Continuous dynamic recrystallization process during AFSD comparable to FSC, taken from [11].

$$\sigma_y = \sigma_0 + k_y d^{-1/2} \quad (2.1)$$

where σ_0 and k_y are material constants.

Grains can grow in size if the metal remains above a critical temperature. This phenomenon is called grain growth and decreases the hardness and strength of the material according to equation 2.1. As a rule of thumb, the critical grain growth temperature (T_{gg}) is half the melting temperature in Kelvin ($\frac{T_m[K]}{2}$). Besides that the temperature has to remain above the critical temperature, the grain growth rate increases by an increase in the temperature [18].

2.4 Comparable techniques to FSEAM

Comparable techniques to FSEAM studied abroad are MELD (previously known as Additive Friction Stir (AFS)) and Hybrid Metal and Extrusion bonding (HYB). These techniques will briefly be discussed, starting with MELD. The MELD technology can be described using figure 2.8a. As feed material, powder is used that will be transported using a screw. During the transportation heat is generated and pressure is built up. As a result, the powder particles will bond and the dispersion of the oxide layers take place. Once the extruded material makes contact with the substrate it is approximately at 50-90% of the melting temperature of the matrix material. The outer part of the extruder also rotates to create additional heat and relative motion between the substrate and the feed material to enable bonding.

MELD has a second setup that is similar to the FSC setup of the UT and is shown in figure 2.8b. This setup is able to process many composites shown in table 2.1. MELD is able to process materials with a particle loading volume up to 30% [24]. A disadvantage of those composites might be that the particles introduce additional wear on the tool, but this is an area that has to be investigated in more detail, yet. Deposition rates that can be achieved using MELD for different materials are $1020 \text{ cm}^3/\text{hr}$ for aluminium, $622 \text{ cm}^3/\text{hr}$ for steel, $553 \text{ cm}^3/\text{hr}$ for titanium, and $81.8 \text{ cm}^3/\text{hr}$ for inconel 6xx/7xx serie [25].

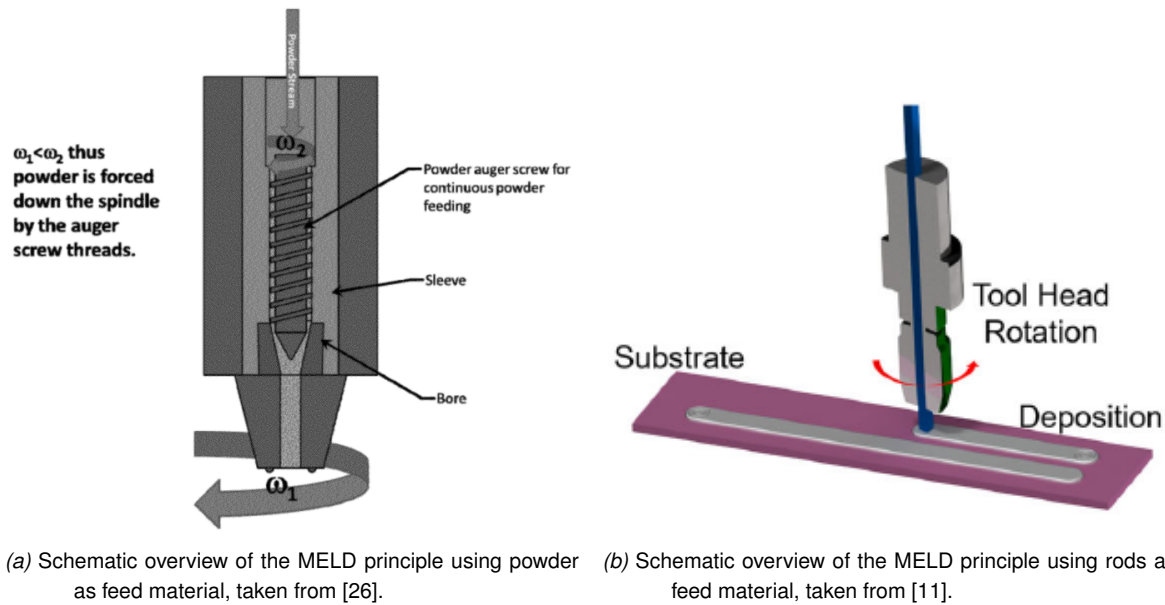


Figure 2.8: Schematic overview of the principles of MELD.

Table 2.1: Materials processed using the setup shown in figure 2.8b [25].

Material	Specific alloy
Steel	HY 80, Stainless 316L, ODS 14YWT-F82H, 300M-4140, Aermet 100-4140
Aluminum	Al-SiC, Al-Fe, Al-W, Al-Mo, Al-steel, 1xxx-, 2xxx-, 5xxx-, 6xxx-, 7xxx-series
Magnesium	AZ31, WE43, E675, AMX602, E21
Titanium	Ti64
Nickel	In625-HY80, In600-SS304, Cu-Ni200-Mo
Copper	Cu-Tungsten, Cu-Tantalum, Cu-Ta, Cu-Nb, Cu-Mo

One research of MELD focuses on the deposition of aluminium AA2219 T851 on top of an aluminium AA2219 T851 substrate and examines the microstructure and mechanical properties of the processed material [27]. A total of six layers on top of each other were printed with a layer thickness of 1mm and a length of 100mm . In addition, the deposition rate at which the experiment was conducted was $1000\text{cm}^3/\text{h}$. After printing, the Electron Backscatter Diffraction (EBSD) images were taken to examine the grain size and Transmission Electron Microscopy (TEM) images were taken to examine the precipitation growth. Besides, compression test and tensile test were conducted to examine mechanical properties. The yield strength of AA2219 T851 is 340MPa and the ultimate tensile strength is 460MPa [28]. A reduction in strength was seen after printing the material as can be seen in table 2.2. The reduction in strength is the result of elimination of the nano-precipitates during MELD, overaging the material [27].

Table 2.2: Comparison of as-deposited AA2219 YS, TS, and ϵ_f based on location and strain rate. Values in parenthesis are the standard deviations, taken from [27].

Location	Top		Middle		Bottom		
	Strain Rate	0.001/s	2500/s	0.001/s	2500/s	0.001/s	2500/s
YS (MPa)		159 (0.7)	275 (0.6)	140 (1.0)	242 (4.2)	125 (3.5)	225 (4.2)
TS (MPa)		390 (2.1)	283 (1.4)	364 (5.2)	245 (1.4)	335 (7.1)	236 (8.5)
ϵ_f (%)		25 (0.7)	37 (0.7)	27 (2.1)	41 (0.7)	28 (1.4)	42 (2.1)

Another research of MELD also studies the grain refinement of aluminium and copper. In addition, the research tries to link the grain size to the process window [29]. The process window is defined by the rotational rate of the tool (Ω) and the travel velocity of the tool (V). The ratio between the feed rate and the travel velocity was kept 1:3, respectively. The aluminium used for this experiment was AA6061 T6 and an indication of grain refinement is given in figure 2.9. The percentage of High Angle Grain Boundary (HAB) is given in this figure as well, indicating the degree of continuous dynamic recrystallization. Observed in [29] is that increasing the strain rate which seem related to Ω/V should result in smaller grains. However, at higher temperatures precipitates dissolve, negatively influencing the grain refinement as is shown in figure 2.9.

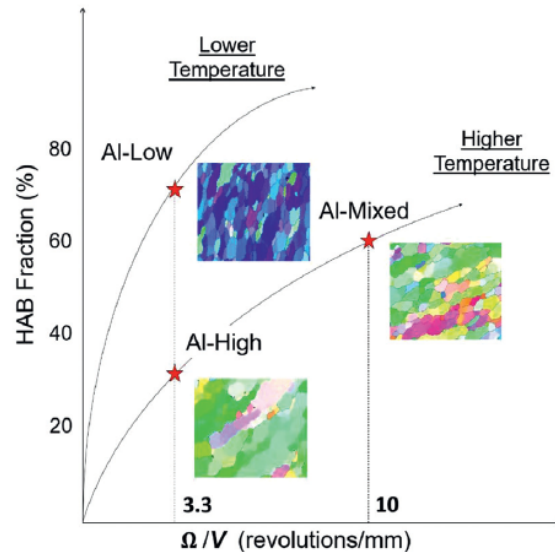


Figure 2.9: An indication of the grain refinement and the content measured of HAB as a function of the process conditions (Ω/V).

Next, the principle of HYB will be described using figure 2.10. HYB uses a different approach compared to FSEAM and MELD regarding the breakage/dispersion of the oxide layer. This process is based on a continuous extrusion method, called conform extrusion. The material being processed is forced by a coining wheel into a slot of the extruder wheel. The material is carried away until it hits an abutment resulting in plastic deformation and dispersion of the oxide layer. This can also be seen as compression of the material in order to fill the entire cross-section of the die. In addition, heat is generated by physical shear and pressure builds up. The material flows towards the substrate/previous layer due to the pressure. In order to remove the oxide layer of the substrate/previous layer, a scraper is used to achieve metal on metal contact enabling bonding. A disadvantage of this method might be that the scraper that has to scrape off material in order to remove the oxide layer. Therefore, the substrate should have a certain flatness otherwise too much material is removed [30]–[32].

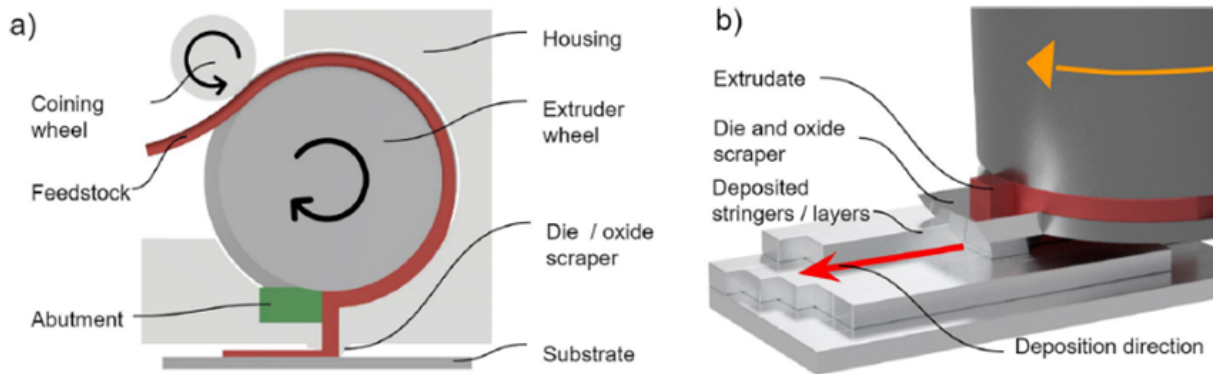
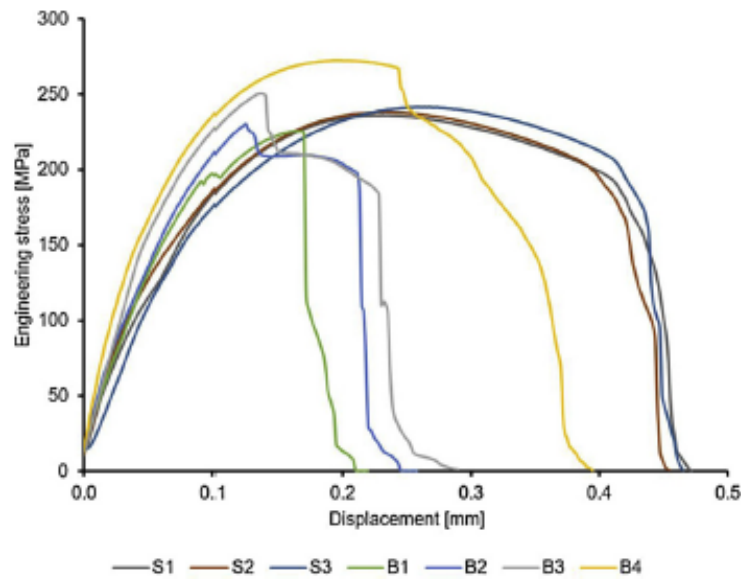
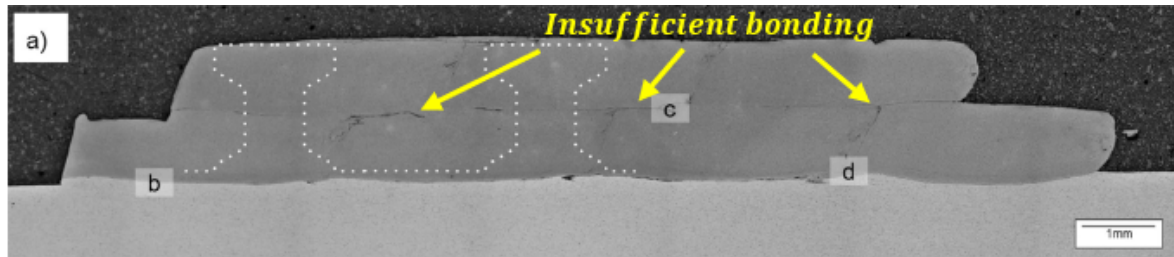


Figure 2.10: Principle of HYB production method, taken from [31].

HYB printed layers of AA6082-T4 with a deposition rate of $185\text{mm}/\text{min}$ and a deposition temperature of 500°C on top of a substrate consisting of the same alloy. After deposition, the printed layers of aluminium were quenched [32] resulting in similar strengths to the substrate, however lower elongations were observed as can be seen in figure 2.11a. The fracture surface of the tensile test specimen showed dimples formation [32], indicating metallurgic bonds were achieved. Nevertheless, HYB experiences problems with respects to insufficient bonding between layers as can be seen in figure 2.11b.



(a) Engineering stress vs. displacement curves for different tensile specimens. Included in the figure are four specimens, B1-B4, crossing two bonded layers, and three specimens representing the substrate material, S1-S3, taken from [32].



(b) Optical micrographs of (a) Section of a deposited structure along with the superimposed contours of the tensile specimens, derived from [32].

Figure 2.11: Mechanical properties and microstructure of HYB.

2.5 Building directions

Additive manufacturing processes build parts on a layer by layer basis. Most of the time a layer is printed in the horizontal plane which includes two different directions, namely x and y . An additional direction in the height is required to complete a part, also called the building direction. An example of how layers are stacked on top of each other can be found in figure 2.12 including a coordinate system. In AM processes it is known that the weakest direction is in the build direction (height) of the part [3], [33]. This building direction has also been tested by HYB [32].

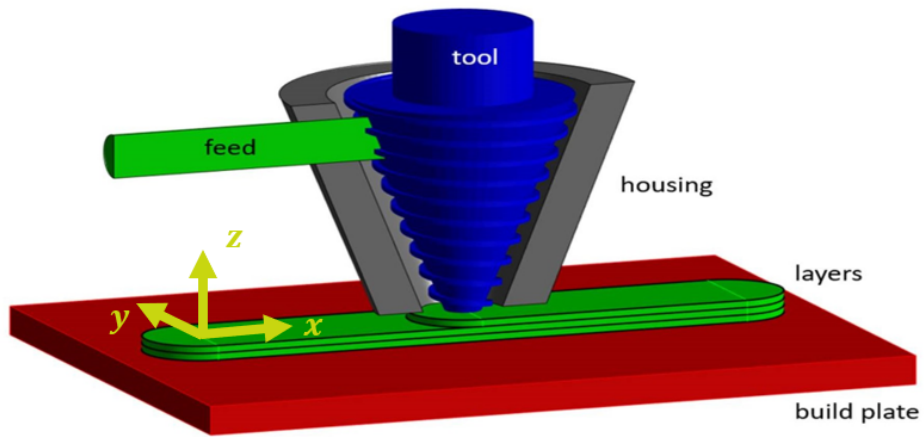


Figure 2.12: Build directions and layers stacked on top of each other using FSEAM.

Friction Stir Extrusion Additive Manufacturing experiments

3.1 Introduction

Different cladding/extrusion techniques (FS, FSC, and FSE) were and still are examined by the UT as mentioned in chapter 1. The FSE technique is closely related to FSEAM as the name implies. After the FSE experiments, that were partly done during this thesis and studied by H.J. Smit [15], the process window of this technique has been mapped as can be seen in section 3.2.2. The process window can be used to determine parameters necessary for FSEAM, for example the rotation rate of the tool. Known from other printing techniques parameters such as the layer height, layer width, and table velocity play an important role. Since the FSEAM is a new technique these parameters are not examined by the UT, yet. The influence of these parameters is unknown and leads to the experimental sub questions stated in section 1.2. In short, how does the table velocity influence the microstructure and mechanical properties of an AM part while remaining the other process parameters constant? These parameters are the rotational rate of the tool, the volumetric flow rate, the tool gap, and the layer geometries.

3.2 Experimental procedure

3.2.1 Experimental setup

Section 1.1 described the principle of FSEAM using a simplified schematic overview (figure 1.4d). In practice, the FSEAM setup consist of an old planer machine with an electric motor that has an in-house developed extrusion head attached to it. The planer machine is capable of translating in three separate direction, two in the horizontal direction (x and y) and one in vertical direction (z). Furthermore, the electric motor could be tilted by an angle (θ). During the FSEAM experiments the tilt angle will be set to zero and the movement in the y-direction will not be used. These movements can be seen in figure 3.1. The electric motor has a power of $13kW$, a rotation rate range of 212 up to 1500 rounds per minute, and is limited to a torque of $100Nm$. Furthermore, a hydraulic cylinder is attached to the in-house developed extrusion head that is able to operate up to a pressure of $190bar$.

The planer machine and hydraulic cylinder specifications can be found in table 3.1.

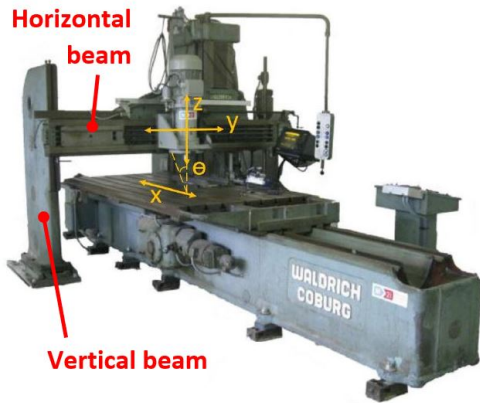


Table 3.1: Planer, cylinder and extruder specifications.

Parameter	Symbol	Range	Unit
Rotational speed	Ω	212-1500	$[\frac{1}{min}]$
translational speed	v_t	0-500	$[\frac{mm}{min}]$
Tilt angle	θ	(-10)-10	$[^\circ]$
Cylinder input speed	v_{cyl}	0-130	$[\frac{mm}{min}]$
Cylinder pressure	p_{cyl}	0-190	$[\frac{N}{mm^2}]$

Figure 3.1: Planer movement directions, derived from [15], [16].

The extrusion head (on the right) in combination with the hydraulic cylinder (on the left side) can be seen in figure 3.2. The hydraulic cylinder is equipped with two sensors, one for measuring the force ($K-13\ 50kN$) and one for monitoring the cylinder position using a displacement sensor. The force sensor (F_{cyl}) is used to avoid the occurrence of high forces that could lead to buckling of the pushpin, damaging the feeding channel, jamming of the feed material, or stalling of the tool. Furthermore, the sum of three strain based force sensors ($HBM\ KMR\ 100kN$) is used to measure the extrusion force (F_{extr}). An additional displacement sensor is attached to the planer table that can not be seen on the figures to measure the displacement of the table.

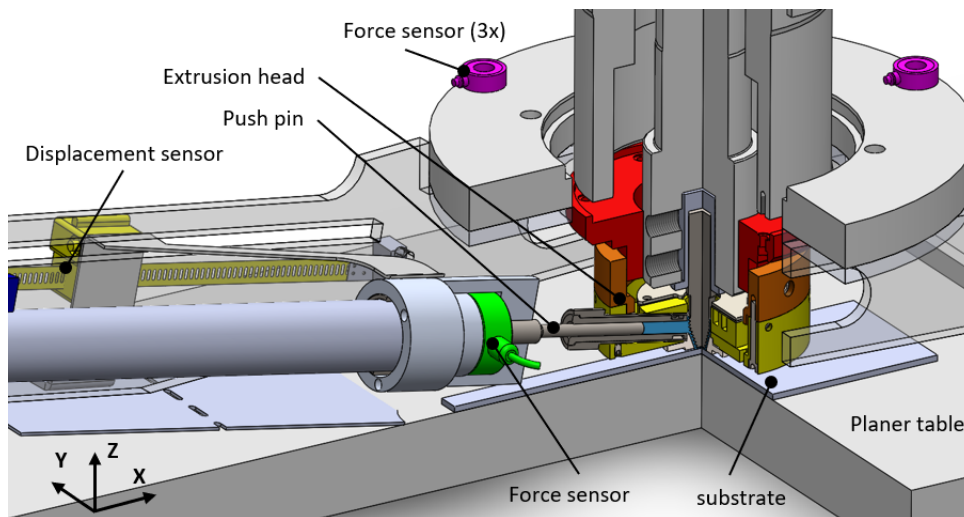


Figure 3.2: Final FSEAM setup.

Feed material, in the form of rods with a diameter $8mm$ and length of approximately $45mm$, is forced through the feeding channel using a push pin that is actuated by the hydraulic cylinder as

can be seen in figure 3.3. Before the rods are pressed against the threaded tool, the tool should rotate at its desired rotational rate. Heat is generated by internal friction when contact between the rod and rotating tool is made. Once the feed material has softened and heated up sufficiently downward pressure builds up by the rotation of the threaded tool. The pressure forces the material to move in downwards direction through the nozzle outlet. The final step is to move the planer table with the substrate relative to the extrusion head. The nozzle temperature is measured by a manually made type-K thermocouple that is placed between the nozzle and the lower mounting bracket (indicated by yellow) shown in figure 3.3. Optionally, thermocouples can be placed in the side of the substrate directly underneath the deposited layers. The distance between two adjacent thermocouples is $40mm$.

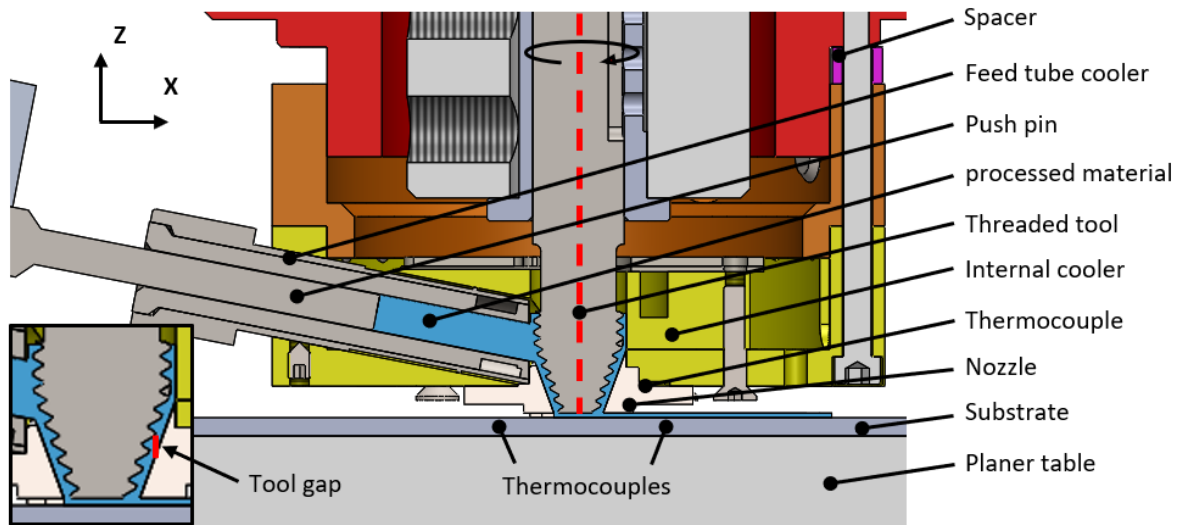


Figure 3.3: Close up of the FSEAM extrusion head.

The feed tube cooler and internal cooler are water cooled to prevent the supplied rods from overheating which may lead to jamming of the feed material or damage to the components. Both cooling circuits use the same container of approximately $200l$ of water. For each cooler an aquarium pump (*Tetra WP600*) is placed in the container. The pump is connected to a plastic hose that is connected to one of the water coolers using a threaded-to-tube fitting. Once the coolant exchanged heat in the cooler it enters another tube using a threaded-to-tube fitting and returns to the water container.

One parameter that has not been mentioned yet is the tool gap (t_{tool}). The tool gap is the vertical distance between the conical part of the threaded tool and nozzle as can be seen at the bottom left corner of figure 3.3. The tool gap can be varied by changing the height (in z-direction) of the spacers, see top right part of figure 3.3. Increasing the height of the spacers results in a larger tool gap.

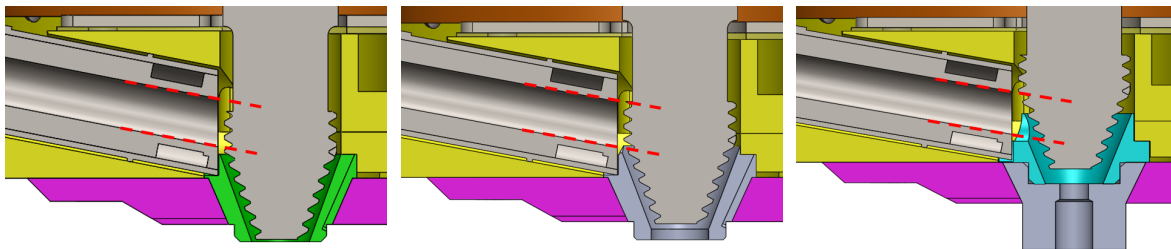
Experimental data was monitored and recorded using a Data Acquisition device (DAQ) during the experiments. The DAQ contains three National Instruments (NI) modules. The NI-9213 is used for the thermocouple(s), NI-9237 for the force sensors, and NI-9215 for the displacement sensor. The DAQ was hooked up to a laptop that is exclusively used for experiments regarding FS, FSC, FSE, and FSEAM. The program used for reading the data is an UT made interface using LabVIEW.

3.2.2 Experiments

A total number of ten experiments has been performed during this thesis. Three of the experiments are related to FSE and seven to FSEAM. The FSE setup is similar to the FSEAM setup and is described in detail in [15]. The main difference between the extrusion and the AM setup is the nozzle. In addition, the FSEAM setup extrudes on top of a substrate rather than in air, like FSE. The FSE experiments were used for determining the process window for the FSEAM experiments. Before the process window could be determined, the setup should be able to run continuously as it was not the case at the time. The reason for this uncertainty is that the setup was changed after the work of J.B. Lind [16] and that it was still not working properly despite several modifications made by H.J. Smit [15]. The final recommendation of H.J. Smit was to change to the threaded tool used during the experiments of J.B. Lind. As a result, the setup is able to run continuously again. The most important parameters for the FSE experiments are listed below.

- i Totalational rate of the tool (Ω)
- ii Tool gap (t_{tool})
- iii Volumetric flow rate (V_f)

The parameters rotational rate and volumetric flow rate were mainly changed during the FSE experiments. As a result, the rotational rate has a range of from 300 up to 600rpm and the volumetric flow rate has a range from 11 up to 115mm³/s. Besides determining the process window, the effect of the cylindrical force was examined for different positions (in height) of the feed tube relative to the threaded tool, see figure 3.4. For the first FSE experiment the material was fed partially against the vertical part of the threaded tool and a vertical part without thread (figure 3.4a) that resulted in relatively high cylindrical forces compared to the work done by J.B. Lind [16]. During this test a tool gap of 2.5mm was used. The second position that has been tried is to press the feed material fully against the vertical part of the threaded tool (figure 3.4b) and a tool gap of 3.2mm was used that resulted in lower cylindrical forces. The final position was that the feed material was pressed against the conical part of the threaded tool (figure 3.4c) using a tool gap of 2.5mm that led to the lowest cylindrical force, but still higher than the cylindrical forces measured by J.B Lind. The collected data of the FSE experiments are not studied since the study of the FSE process is not in scope of this thesis, however the measured data can be found in appendix B.



(a) Partially on vertical threaded part.

(b) Fully on vertical threaded part.

(c) Partially on vertical and tapered threaded part.

Figure 3.4: Feed positions of the feed material.

Additional important parameters that are introduced by the FSEAM experiments and are listed below.

- iv Table velocity (v_t)
- v Layer height (h_l)
- vi Layer width (w_l)

For the first FSEAM experiment the rotational rate was set at $400rpm$, because this rotational rate was also used as a starting value for the extrusion experiments. Furthermore, the volumetric flow rate was set at the lowest value of $11mm^3/s$ in order to make the process slow, because it had to be operated manually and the process was unfamiliar. The layer height and width were chosen to be constant, respectively, $1mm$ and $10.5mm$. The same goes for the tool gap that was set to $3.2mm$. The remaining parameter is the table velocity that was adjusted between $20 - 60mm/min$ during the first experiments. Slow table velocities were chosen to ensure that the substrate would heat up sufficiently, enough pressure was generated to create metallurgical/atomic bonds, and that enough material was supplied at the layer-substrate interface per unit time to create a layer with the required dimensions. The parameters described above remain constant, except for the table velocity and the Volumetric flow rate of the last FSEAM experiment, AM-7. An overview of the constants can be found in table 3.2.

Table 3.2: Parameters kept constant during the FSEAM experiments.

Parameter	Symbol	Value	Unit
Tool gap	t_{tool}	3.2	[mm]
Rotational rate	Ω	400	[1/min]
Layer height	h_l	1	[mm]
Layer width	w_l	10.5	[mm]

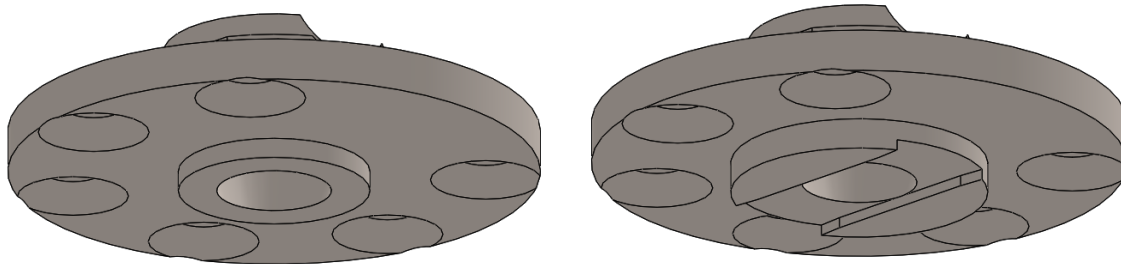
Regarding the supply of material, two terms are introduced, namely overfeeding and starvation. These terms can be explained using volume equilibrium which means that the material that is going in a system should also go out of a system. The theoretical table velocity (v_t) can be calculated using equation 3.1.

$$v_t = \frac{V_f}{h_l * w_l} \quad (3.1)$$

where V_f is volumetric flow rate of the feed material, h_l the layer height, and w_l the width of the layer. Using the constants in table 3.2, a volumetric flow of $11mm^3/s$, and substituting them into equation 3.1 results in a theoretical table velocity of approximately $63mm/min$. This table velocity ensures a volumetric equilibrium of material going in and out. Overfeeding is the term when more material is supplied than necessary. In other words, the table velocity is below the theoretical table velocity. The opposite of overfeeding is starvation. In this case the material supplied is less than required. The phenomena of overfeeding and starvation will be seen later on.

As mentioned earlier, feeding the material at the conical part of the threaded tool is most beneficial for the cylindrical force, see figure 3.4c. However, this results in a threaded tool that is somewhat withdrawn in the lower mounting bracket as can also be seen in figure 3.4c. In order to ensure the

removal of the oxide layer of the substrate/previous layer a relative rotating motion of the deposited aluminium with respect to the substrate/previous layer is desired. The rotating motion of the deposited aluminium is introduced by the rotating threaded tool. For that reason it was chosen to feed the material partially on the vertical and the conical part of the thread. In addition, a slimmer nozzle design was developed to have a better view on the deposited layer which meant that the nozzle was integrated in the nozzle holder (respectively the green and purple component in figure 3.4a). The nozzle integrated in the nozzle holder used for the first experiment can be seen in figure 3.5a.



(a) Nozzle integrated in the nozzle holder used for AM-1, type I. (b) Modified version of the nozzle used for the remaining AM-experiments, type II.

Figure 3.5: Nozzles used for the FSEAM experiments.

After the first AM experiment, a redesign of the nozzle was made as a waviness pattern appeared on the surface. An attempt was made to reduce the waviness pattern by adding flanges to the nozzle to stop material from moving in lateral direction. The new design of the nozzle is shown in figure 3.5b. This nozzle was used for FSEAM experiments AM-2 up to AM-7. In the second FSEAM experiment, AM-2, the phenomena overfeeding and starvation were examined in more detail by setting a range of table velocities different from the theoretical table velocity. The table velocity varied between 40 and $75\text{mm}/\text{min}$ and for each table velocity four layers were stacked on top of each other. Four table velocities were examined more extensively due to promising results, namely experiments AM-3, AM-4, AM-5, AM-6 (respectively, at a table velocity of 50, 55, 60, and $65\text{mm}/\text{min}$) with the other parameters remaining constant as described in table 3.2. The final experiment, AM-7, was performed to examine the capabilities of the AM technique. During this experiment, the volumetric flow rate and the table velocity were varied to study the influence of the deposition speed on the process. The table velocity varied between 55 and $410\text{mm}/\text{min}$. An overview of the performed FSE and FSEAM experiments is shown in table 3.3.

Table 3.3: Parameters used during FSEAM experiments.

Experiment [<i>type</i> – #]	Rotational rate [<i>rpm</i>]	Volume flow [<i>mm</i> ³ / <i>s</i>]	Table speed(s) [<i>mm/min</i>]	Nozzle type [–]	Number of layers [–]
AM-1	400	11	20-30-40-50-60	<i>I</i>	6
AM-2	400	11	40-50-55-60-65-70-75	<i>II</i>	28
AM-3	400	11	50	<i>II</i>	51
AM-4	400	11	55	<i>II</i>	52
AM-5	400	11	60	<i>II</i>	50
AM-6	400	11	65	<i>II</i>	47
AM-7	400	11-108	55-120-220-320-410	<i>II</i>	24

3.2.3 Materials

During the experiments, two aluminium alloys were used, namely aluminium AA2024 and AA6060 T6. The aluminium AA2024 is used as substrate material and its principle alloying element is copper. This aluminium is a high strength, high performance aluminium. The strength of this aluminium is excellent over a wide range of temperatures. The chemical composition of AA2024 can be found in table 3.4. The substrate is a rectangular plate with a length, width, and thickness, respectively, of 300mm, 70mm, and 4mm.

The aluminium alloy AA6060 T6 is used as feed material in the form of rods. The rods used for these experiments had a diameter of 8mm and a length of approximately 45mm. In most cases two rods were inserted at the same time. The AA6xxx series principle alloying elements are magnesium and silicon. This aluminium is dominantly used in the extrusion industry and is used for many structural components. The chemical composition of AA6060 can be found in table 3.4. Furthermore, the AA6060 T6 was acquired as precipitation heat treated exhibiting the highest tensile strength. Using a T6 heat treatment the aluminium alloy is at its peak strength of approximately 190MPa. Corresponding precipitation size is mainly between the 0.6 – 3.0µm [34]. Aluminium AA6060 T6 melt temperature is approximately 650°C [35] estimating the critical grain growth temperature at approximately 189°C using the rule of thumb mentioned in section 2.3.

Table 3.4: Chemical composition of AA2024 and AA6060 expressed in weight percentage [%], derived from [36], [37].

Material	Si	Fe	Cu	Mn	Mg	Cr	Zn	Ti	Other
AA2024	0.5	0.5	3.8-4.9	0.3-0.9	1.2-1.8	0.1	0.25	0.15	0.05
AA6060	0.3-0.6	0.1-0.3	0.1	0.1	0.35-0.6	0.05	0.15	0.1	0.15

Increasing the temperature of an aluminium alloy decreases the mechanical properties, such as the yield strength ($\sigma_{y0.2\%}$) and the ultimate tensile strength (σ_{UTS}). The strength as a function of temperature for aluminium 6060 T66 (comparable to AA6060 T6) can be seen in table 3.5 [38]. Additional information about AA2024 and AA6060 can be found in appendix A.

Table 3.5: Strength as function of temperature for AA 6060 T66, derived from [38].

Temperature [°C]	$\sigma_{y0.2\%}$ [N/mm ²]	σ_{UTS} [N/mm ²]
20	187	210
173	147	149
269	72	76
302	55	56
401	18	18

3.2.4 Analysis methods

In total six different analysis methods have been used, namely light microscopy, Energy Dispersive X-Ray (EDX), hardness test, tensile test, SEM, and EBSD.

Preparation of microscopic samples

Before samples of the FSEAM experiments can be polished using the 'Struers Tegramin 30', the samples have to be cut at the desired dimensions and then be embedded in cups of 25 or 50mm. Depending on the analysis process the type of embedding differs. If the sample will be analyzed using the EBSD a conductive epoxy is required. For other analysis methods used during this thesis normal epoxy can be used. In both cases a hardener is added to cure the epoxies. The curing time of a non-conductive epoxy takes approximately a day and for a conductive epoxy five days. Once the epoxy is cured, the samples are ready to be polished. A total of six cups with the same diameter can be polished at the same time. The general program used for polishing includes grinding, polishing, chemical polishing of the surface of the cups as can be seen in table 3.6.

Table 3.6: General program used for polishing.

Step [-]	Surface [-]	Suspension [-]	Lubrication [-]	Time [min]
1	Gekko #500	-	water	1:30
2	Gekko #1000	-	water	1:30
3	Gekko #2000	-	water	2:00
4	Largo	DiaDuo-2 9 μ m	-	5:00
5	Dac	DiaDuo-2 3 μ m	-	2:00
6	Nap	DiaDuo-2 1 μ m	-	2:00
7	Chem	OP-S NonDry	-	6:00
8	Chem	-	Water	0:50

Digital light microscopy

The first examination of the AM products were done using a digital light microscope. The microscopic images are created using the 'Keyence VHX 5000 digital microscope' that was equipped with a lens

that has zoom capabilities of 100 – 1000 times. Using a digital microscope relatively large overview images could be created with the stitching option.

Hardness test

Hardness tests are performed using the '*Leco LM 100 AT*' hardness tester. During the tests a force of 300 *kgf* has been applied in combination with a diamond pyramid indenter. The indentation is used to measure the Vickers microhardness (HV). Furthermore, a dwell time of 15*s* has been used. The hardness value is related to the tensile strength of a material, typically $\sigma_{tensile} = 3HV$.

Tensile test and Aramis system

Tensile test specimens were manufactured using an electrical discharge machine. The benefits of this machine are a low amount of heat is put into the specimen, no mechanical stresses are introduced, and a relatively high accuracy can be obtained. However, the process is relatively expensive and does not have the desired surface roughness according to ASTM E8/E8M [39]. Besides not meeting the roughness requirements, the tensile test specimen dimensions differ from the standard specimen size and have an overall length of 45*mm*, a gauge length of 20*mm*, a width of 5*mm*, and a thickness of 1*mm*. A technical drawing is shown in appendix C. Before the tensile test specimen were tested, a black-white speckle pattern was added to one side of the surface to examine the displacement using an Aramis system.

The actual test consists of two setups, the tensile test setup and Aramis system as shown in figure 3.6. The tensile tests were performed using a '*Zwick Z5.0 mechanical tester 5kN*' with a load cell that is capable of measuring up to 5*kN* and that was attached to a top clamp, the '*Zwick/Roell typ 8306 F_{max} = 10kN*'. The top clamp was able to move in the vertical directions as indicated with the red arrow in figure 3.6. The same type of clamp was used on the bottom side of the tensile test machine and was fixed. Data with respect to the force and displacement was gathered using a computer with the corresponding software. The Aramis system was used to examine the displacement in more detail using a camera of '*Schneider/Kreuznach*' that was hooked up to a separate computer for data acquisition using the software '*GOM-v6.3.0-9*'. This systems used a hand held trigger to start the measurement. Before a test was performed, a tensile test specimen was aligned in the machine manually using markings on the clamps that indicated the middle of the clamp. Once the specimen was aligned correctly, the start button of the tensile test setup and the trigger of the Aramis system had to be pushed at the same time to synchronize the collected data.

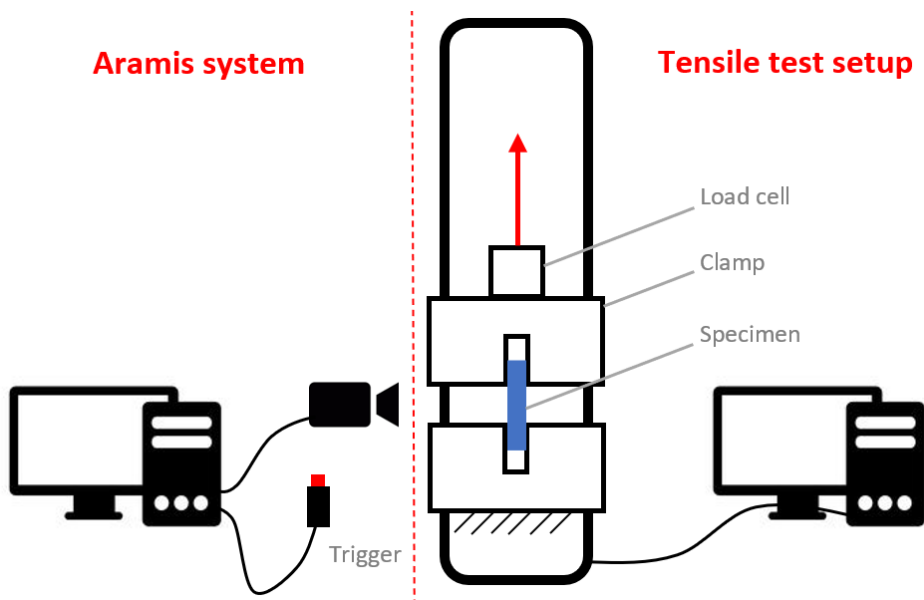


Figure 3.6: The setup of the tensile test machine in combination with the Aramis system.

The procedure for tensile testing was performed in a slightly different order than it should have been done. Fixing the specimen in the clamps typically introduces some force on the specimen shown by the measurement of the load cell. This force should be approached for zero employing the *'approach force zero'* function of the tensile tester software which means that the machine moves the clamp and tries to find the position where the force on the load cell is zero. Unfortunately, the option *'set force zero'* was used which means that non-zero force was plotted as zero. In other words, the force introduced by clamping was still present but shown as zero Newtons. The machine operator thought that these forces were around 30 – 40N. This mistake happened throughout the tensile test consistently.

EDX, SEM, and EBSD

The EDX, SEM, and EBSD analyses could all be performed on the same machine, namely the *'JEOL JSM 7200f'*. During the analyses, the machine was operated by a qualified employee of the UT.

Analysis method per experiment

In table 3.7 an overview is given of what analyses have been performed on a certain experiment. If an analysis has been performed on a sample produced during the experiments it has been indicated by an *'x'*.

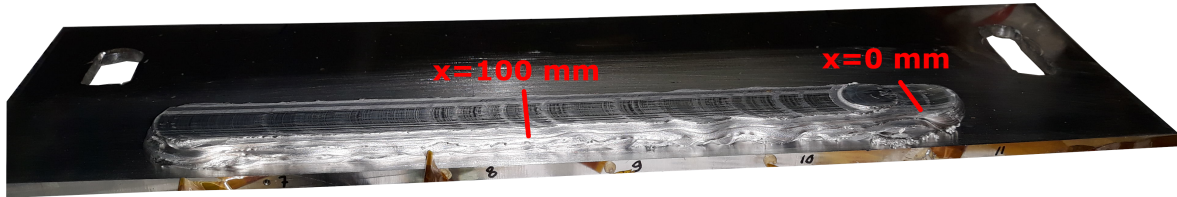
Table 3.7: Performed tests for each FSEAM experiment.

Experiment	Digital microscopy	EDX	Hardness	Tensile	SEM	EBSD
AM-1	X	X				
AM-2	X					
AM-3	X		X	X	X	X
AM-4	X		X	X	X	
AM-5	X		X	X	X	
AM-6	X		X	X	X	
AM-7	X					

3.3 Results and discussion

3.3.1 AM-1

Figure 3.7 shows the result of the first deposited layers of the FSEAM setup, experiment AM-1. The experiment consist of the deposition of six layers with a length of approximately $175mm$ and a width of approximately $18mm$ per layer instead of the designed nozzle outlet of $10.5mm$ (mentioned in table 3.2). The width is much larger as a result of overfeeding. Once the deposited material has left the nozzle with an excessive volumetric flow, the material flows in radial direction and increases the width of the printed wall. Furthermore, a wavy pattern is visible at the sides of AM-1. The reason for the waviness of the surface might be a non-constant material outflow that was noted during the FSE experiments.

**Figure 3.7:** The first AM result using the new setup.

The events that took place during the experiments are described in more detail using figures 3.8 and 3.9. Figure 3.8 shows the nozzle and substrate temperature corresponding to the cylinder and table position as a function of time (at $x = 0mm$ as depicted in figure 3.7). Figure 3.9 shows the cylinder and table force corresponding to the cylinder and table position as a function of time. A note regarding the table position is that the sensor was not set correctly. As a result, the sensor measured the table position from $0 - 100mm$. This range corresponds to the x -positions depicted in figure 3.7.

The process starts by inserting two aluminium rods in the feed chamber and pushing them against the threaded tool using the push pin that is actuated by the hydraulic cylinder. The extrusion head is position far above the substrate to prevent insufficiently heated, extruded aluminium from touching

the substrate. Once the rods make contact on both sides (push pin and tool), at $t \approx 32s$, the cylinder force increases rapidly due to the tool slowly consuming the aluminium rods. After a period of approximately twenty seconds ($t \approx 52s$) the nozzle temperature increases due to internal friction. The time that is required to heat up the setup completely is equal to consuming two aluminium rods and is about 480 seconds (at $t \approx 516s$). At this point, the feed material needs to be refilled and the cylinder is quickly withdrawn to insert two new rods. As a result, no heat is generated and the nozzle temperature decreases. In addition, the cylinder force is zero as well since it does not exert any force. Once the rods are in the feed tube, the cylinder is extended as quickly as possible until it pushes the rods against the thread again at $t \approx 555s$. The speed of the cylinder is set back to the correct speed to obtain the desired volumetric flow rate. As a result of the quick contact, a slight peak in cylinder force can be observed and the nozzle temperature increases again. At this point the setup is sufficiently heated and excessive extruded material is cut off to lower the extrusion head to the required height relative to the substrate. The AM process starts at $t \approx 625s$. Upon reaching the substrate, the extrusion force increases and so does the substrate temperature (at $x = 0mm$). During heating up of the substrate, the extrusion force increases as well since the table is not moving yet. Once the substrate temperature reached the nozzle temperature at $t \approx 710s$, the table starts to move with a table velocity of $30mm/min$. As a result of moving away of the $x = 0mm$ position, the substrate temperature decreases. In addition, the extrusion force decreases as well. Around $t \approx 850s$ the extrusion force seems to be a bit low for the first layer, thus the table velocity is decreased to $20mm/min$ (change in slope of the table position) and the extrusion force increases again. At $t \approx 1015s$ the material in the feed tube is empty again and needs to be refilled. The table movement is set to zero while refilling the feed tube. Once material is coming out of the nozzle again (increase in extrusion force around $t \approx 1080s$), the table starts to move decreasing the extrusion force. At the end of the first layer, the table velocity is set to zero and the extrusion head is positioned $1mm$ higher manually and the table starts moving in opposite direction to deposit the second layer at $t \approx 1220s$. During the second layer, a refill of the feed tube is required at $t \approx 1445s$. At $t \approx 1530s$ the second layer has finished and the height of the extrusion head is set manually $1mm$ higher to deposit the third layer. This process is repeated a couple of times to print the desired height of the wall.

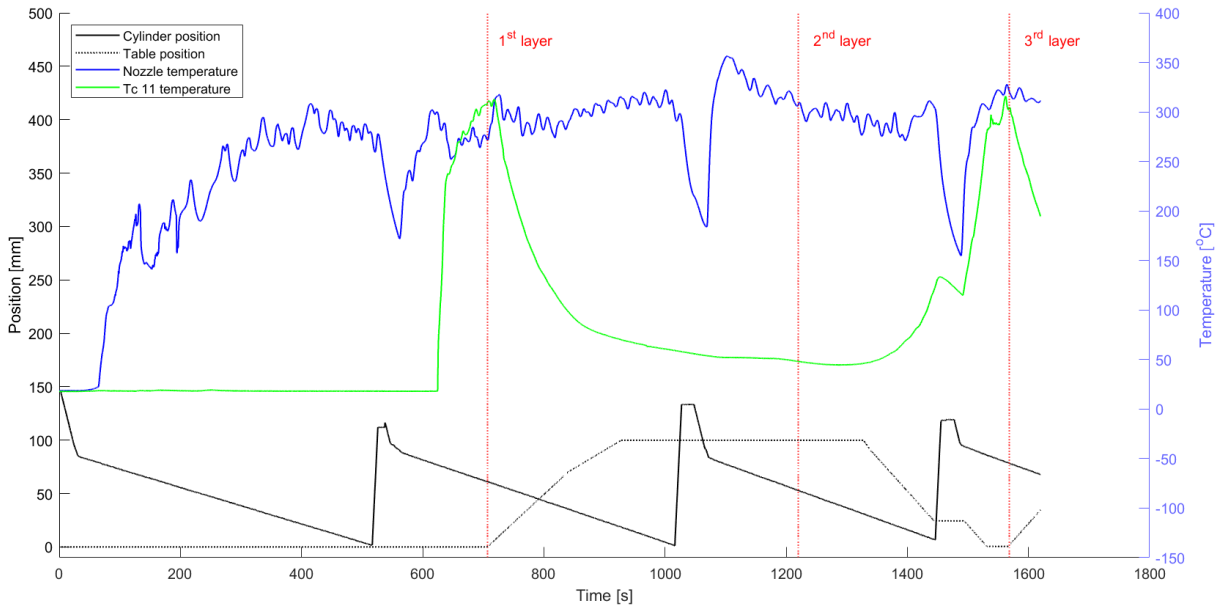


Figure 3.8: The cylinder and table position, nozzle and substrate temperature plotted against time.

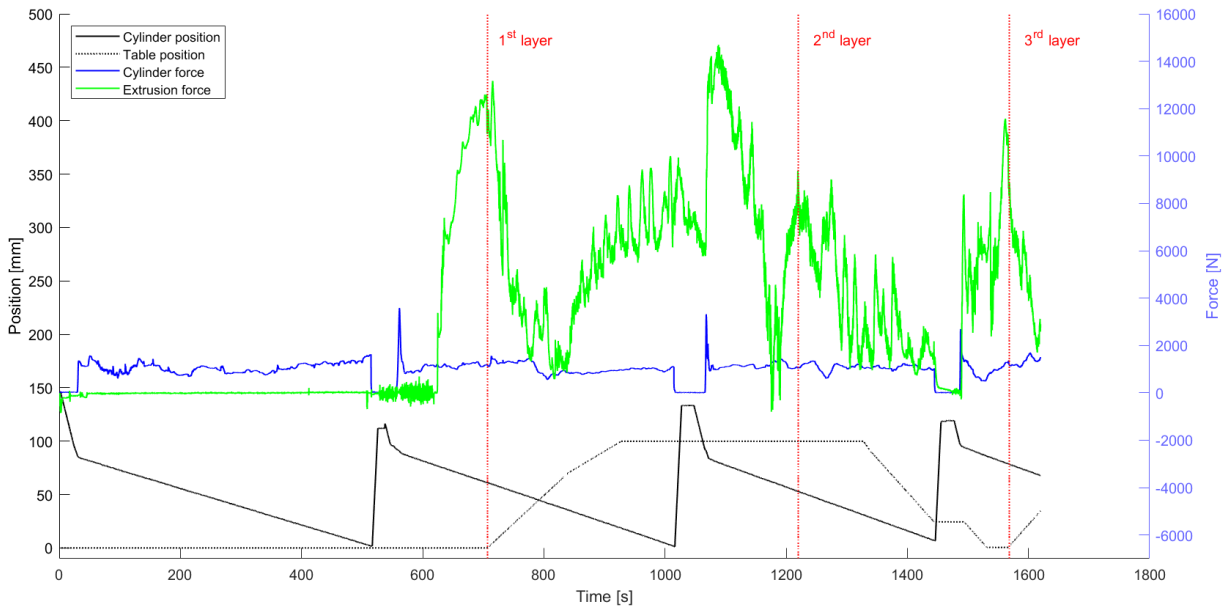


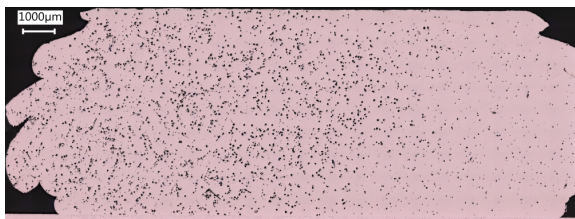
Figure 3.9: The cylinder and table position, cylinder and extrusion force plotted against time.

The microscopic images of experiment AM-1 have been examined to see if the results look promising. Figure 3.10a shows the positions of where microscopic images are taken from and the yellow arrows indicate from what side the microscopic images are taken. Figure 3.10b and 3.10c,

respectively, AM-1A and AM-1C, show clear signs of overfeeding (the bulges on the sides) and the width of the layer is much larger than the outlet diameter of the nozzle. Fortunately, the cross-sections seem to be almost crack free. Comparing AM-1A to AM-1C, AM-1A has black particles present over the full cross-section particular on the left middle side. These particles were examined using the EDX and the particles seem to be mostly carbon with some oxides as can be seen in appendix D.2. Checking the processes that the samples have been gone through, no explanation has been found for these carbon and oxide particles. A suspicion was that those particles were introduced by mixing pieces of the gasket of the internal cooler with the feed material. However, examining the microscopic images the particles would be expected throughout the layer(s). Instead, those particles are present at a few cross-sections assuming something odd happened in the lab. Fortunately, this phenomena was not observed on the samples of the other AM-experiments.



(a) Positions with respect to AM-1 experiment.



(b) position AM-1A



(c) position AM-1C

Figure 3.10: Cross-sections of the first AM experiment.

3.3.2 AM-2

Continuing with the sample of experiment AM-2 that was printed using the type *II* nozzle that has additional flanges (see figure 3.5b) to prevent too large lateral flow. Contour graphs have been made the (nozzle) temperature and extrusion force. Instead of plotting these parameters against time, they are plotted against the table position. So, the nozzle temperature and extrusion force data as a function of time have been converted to a function of the table position. First, the data of the table position are rounded to integers, then the average nozzle temperature and extrusion force are calculated for each integer overlapping a certain time interval. Once the printing in forward direction is finished, the table moves in backward direction to print the next layer knowing the extrusion head

is raised by 1mm . As a result, the nozzle temperature and extrusion force are plotted against the position in x -coordinate (length direction) and z -coordinate (height direction). The orientation of a contour graph with respect to an additive manufactured sample is shown in figure 3.11. Figure 3.12a shows the nozzle temperature and figure 3.12b the extrusion force. These figures show only the additive manufacturing of the aluminium and not the preheating of the system, unlike the plots shown in figures 3.8 and 3.9. However, the refilling of the feed chamber can still be seen as nozzle temperature drops or as peak extrusion forces in the contour graphs. These graphs are used to relate the analysis methods to the position of the AM wall. The tensile test sample locations were selected to avoid disturbances of nozzle temperature and extrusion force as much as possible. The reason for this avoidance is that the aim is to run the FSEAM process continuously, without refilling the feed chamber, therefore the disturbances are not of interest. The green lines/areas depicted in the figures, indicate the positions of the microscopic images.

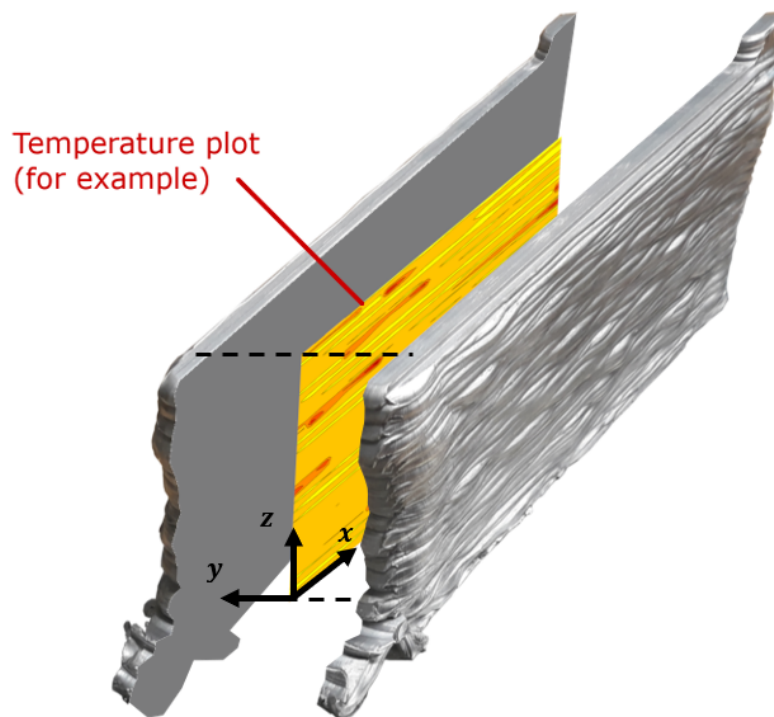
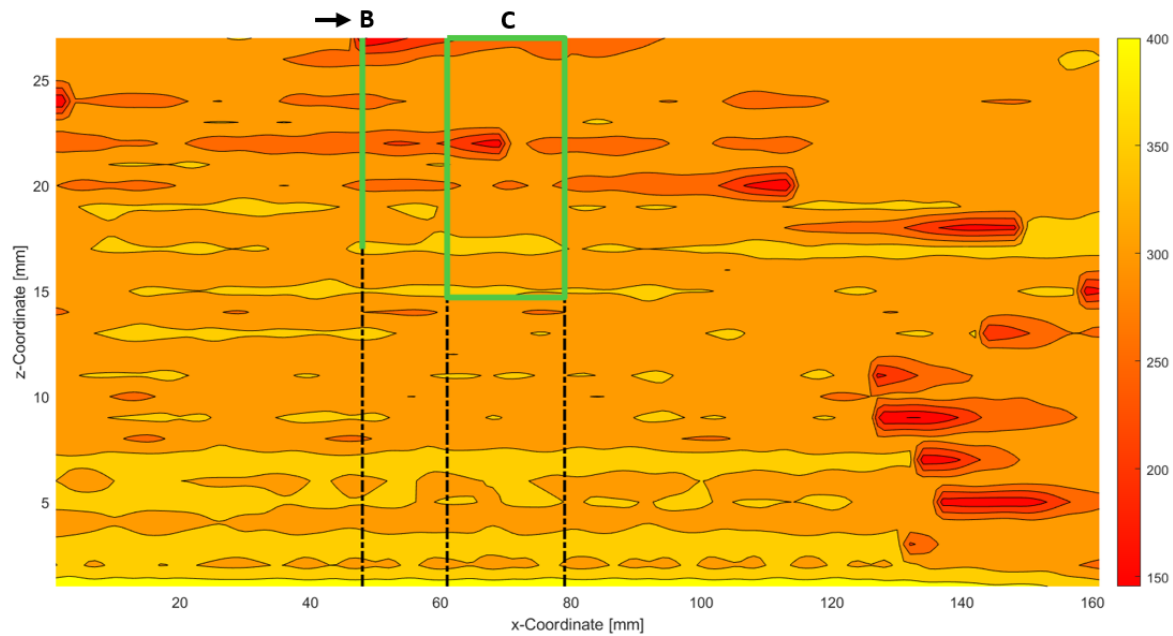
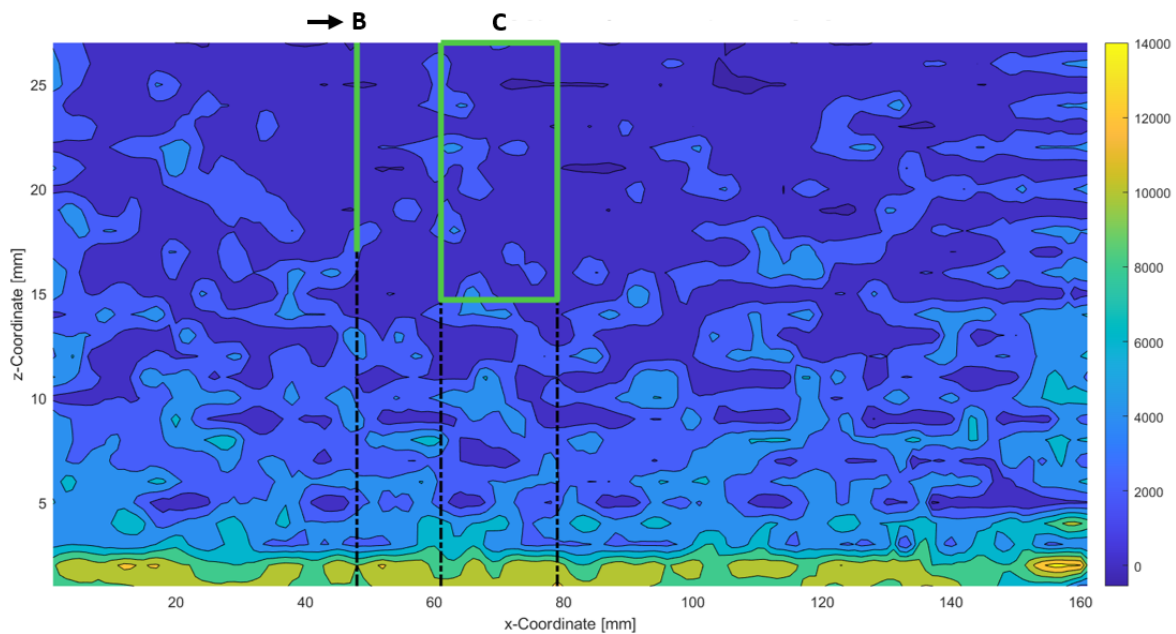


Figure 3.11: The implementation of the nozzle temperature and pressure plots relative to the AM product.



(a) Nozzle temperature plotted against wall position of AM-2.

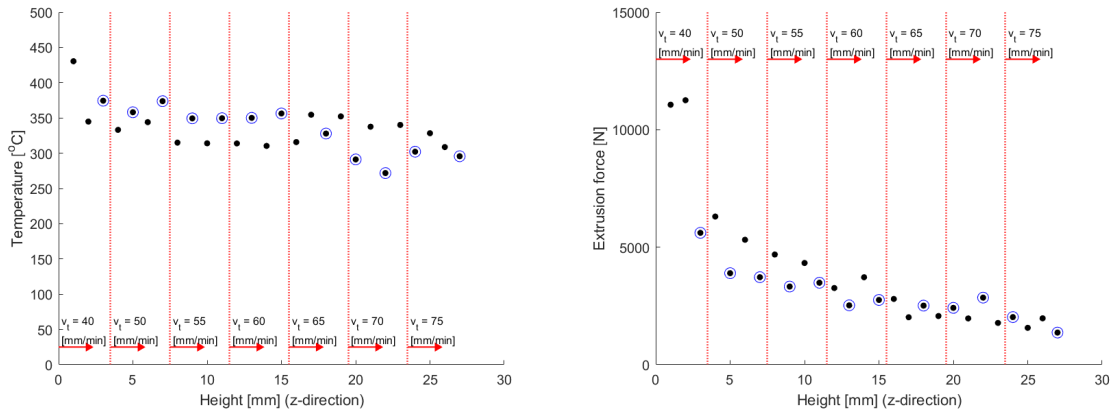


(b) Extrusion force plotted against wall position of AM-2.

Figure 3.12: Contour plots of the (a) nozzle temperature and (b) extrusion force at the time of deposition relative to the position of the AM-2 experiment.

The contour graphs are useful for relating analysis methods to the nozzle temperature and extrusion force at a certain position in the AM wall, but are not convenient to examine possible trends. In addition, the contour graphs provide a clear overview of the development of nozzle temperature and extrusion force over time and can be used to check whether the process has gone according to plan. Figure 3.13a and 3.13b shows the average nozzle temperature and extrusion

force, respectively, of each deposited layer as a function of the table velocity. During AM-2, the table velocity varied between 40 and $75\text{mm}/\text{min}$ as can be seen in these figures. Refilling the feed chamber is indicated by a blue circle around a data point. Only refills between the starting and end points of the table position are considered, so refills while increasing the height of the extrusion head are not. The nozzle temperature seems to remain relatively constant while increasing the table velocity whereas the extrusion force decreases while increasing the table velocity. Furthermore, the nozzle temperature and extrusion force seem to be dependent whether the table is moving in forward or backward direction. A saw-tooth like development seems to appear. However, this development seems to be reversed for the extrusion force. In other words, when the nozzle temperature indicates a relatively higher temperature the extrusion force indicates a relatively lower value and vice versa. This behavior seems to be consistent in the case of the extrusion force, but does not always seem to be true for the nozzle temperature as can be seen in figure 3.13a for a table velocity of 50 and $75\text{mm}/\text{min}$. The saw-tooth like pattern is not fully understood and will be discussed in section 5. The last thing that stands out is the increased nozzle temperature and extrusion force at the start. The increased temperature can possibly be explained by the fact that the substrate has to be heated for a longer time, which causes the average temperature to increase. This may also be an explanation for the first extrusion force with $F_{ext} \approx 11000\text{N}$, that is also relatively high compared to the other values, but it does not explain the second high average value at $F_{ext} \approx 11250\text{N}$. This average value is possibly the result of an incorrect layer height of 0.8mm that was not equal to the required layer height of 1mm , increasing the degree of overfeeding.



(a) Average nozzle temperature for each layer plotted against the layer height including the different table velocities.

(b) Average extrusion force for each layer plotted against the layer height including the different table velocities.

Figure 3.13: Averages of (a) the nozzle temperature and (b) the extrusion force for each layer plotted against the layer height related to table velocities of 40, 50, 55, 60, 65, and $75\text{mm}/\text{min}$ (experiment AM-2).

Clear signs of starvation can be seen at table velocities of $70\text{mm}/\text{min}$ or higher as shown in figure 3.14. During the deposition of layers with higher table velocities with a volumetric flow rate of $11\text{mm}^3/\text{s}$, porosities can be observed. Material is still spread over the width of 10.5mm , but most signs of starvation are seen at the middle, possibly due to the extrusion shape.

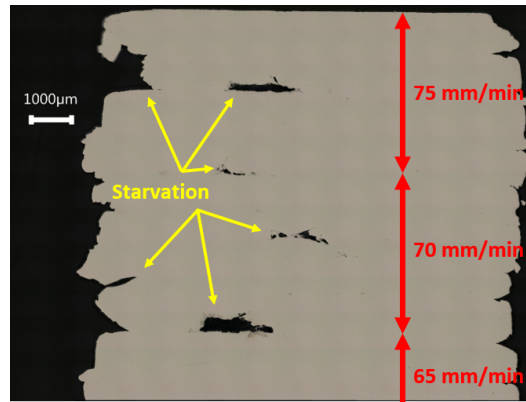
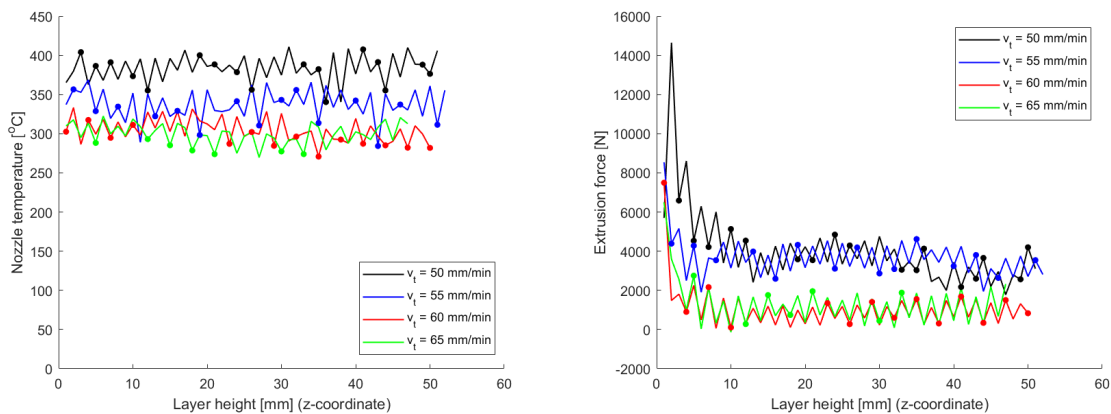


Figure 3.14: Microscopic image of the higher table velocities of AM-3 showing the starvation phenomenon.

3.3.3 AM-3 to AM-6

The average nozzle temperature and extrusion force of experiments AM-3 up to AM-6 are also plotted against the layer height as can be seen in figure 3.15a and 3.15b respectively. The saw-tooth like pattern remains consistent for the extrusion force during these experiments, comparable to the results of experiment AM-2. The circles indicate refilling of the feed chamber. In contrast to the nozzle temperature that appears to vary from the saw-tooth pattern as the table velocity increases. The first sign of the deviating behavior can be seen for a table velocity of $55\text{mm}/\text{min}$ around a layer height of 22mm . This deviating behavior seems to be the worse for a table velocity of $65\text{mm}/\text{min}$. The reason for this behavior is unknown and will be discussed in chapter 5. Remarkable is that the nozzle temperature seems to decrease while the table velocities increases, unlike experiment AM-2. The extrusion force still seems to decrease while increasing the table velocity, however the table velocities of 50 and $55\text{mm}/\text{min}$ seem to have fairly the same extrusion force. The same holds for the table velocities of 60 and $65\text{mm}/\text{min}$. This phenomenon will be discussed in chapter 5.



(a) Average nozzle temperature plotted against the layer height for experiment AM-3 to AM-6.

(b) Average extrusion force plotted against the layer height for experiment AM-3 to AM-6.

Figure 3.15: Averages of each layer plotted against the height for experiment AM-3 to AM-6.

Examining microscopic images of AM-3A, AM-4A, AM-5A, and AM-6A (see appendix D) it is mainly noted that increasing the table velocity decreases the layer width as can be clearly seen in figure 3.16. Figure 3.16a shows an average width of approximately $20mm$ for AM-3A. Followed by a width of approximately $14mm$ for AM-4A (figure 3.16b), a width of approximately $11mm$ for AM-5A (figure 3.16c), and a width of approximately $10mm$ for AM-6A (figure 3.16d). Besides decreasing the width, the material starts to show signs of starvation on the left side of AM-5 as depicted in figure 3.16c. There are no visible pores in the current microscopic image of AM-6A, but they are present in the sample at other locations and even visible to the naked eye in the tensile test specimens as will be shown in section 3.3.4. In general, the microscopic images of these experiments look quite promising, because these images do not show regions of insufficient bonding such as pores or large quantities of starvation.

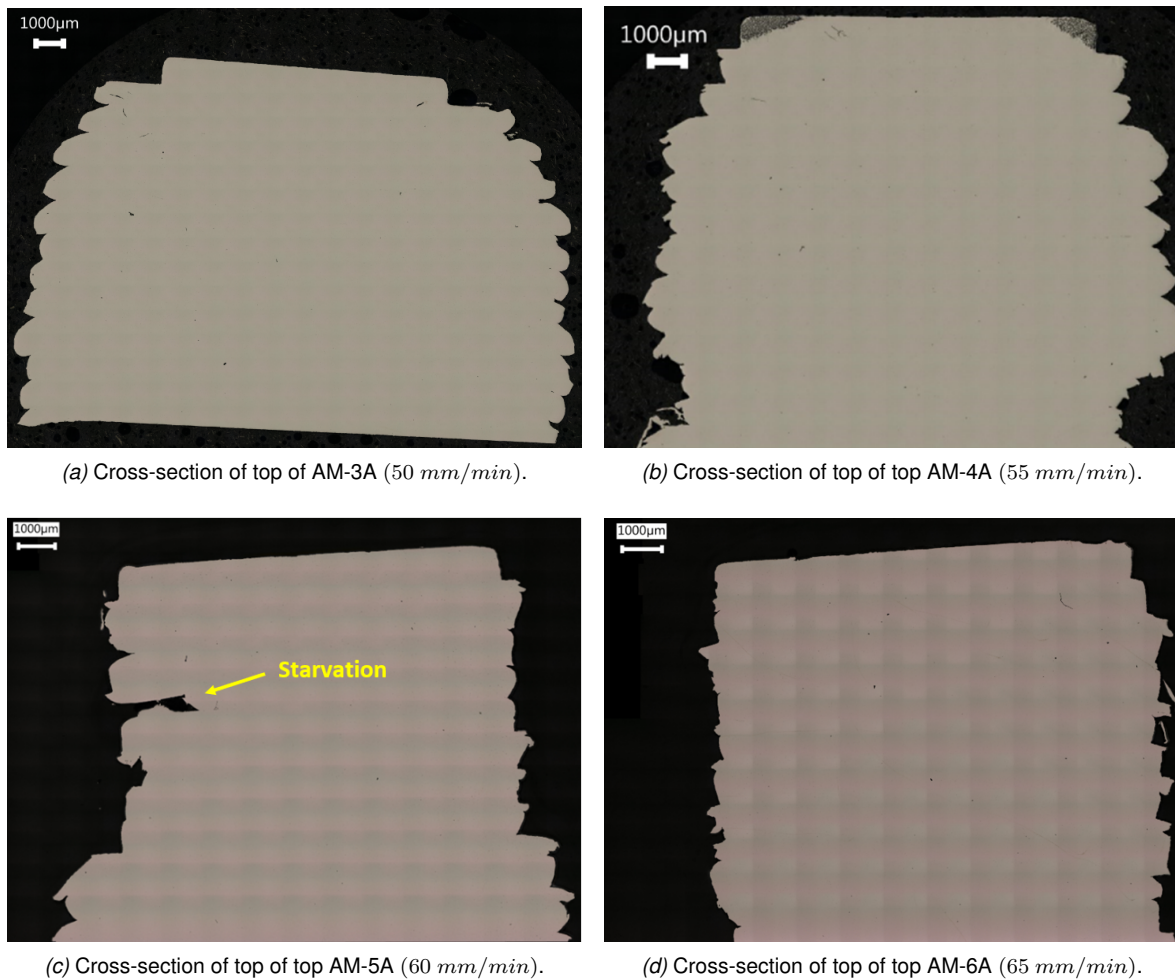
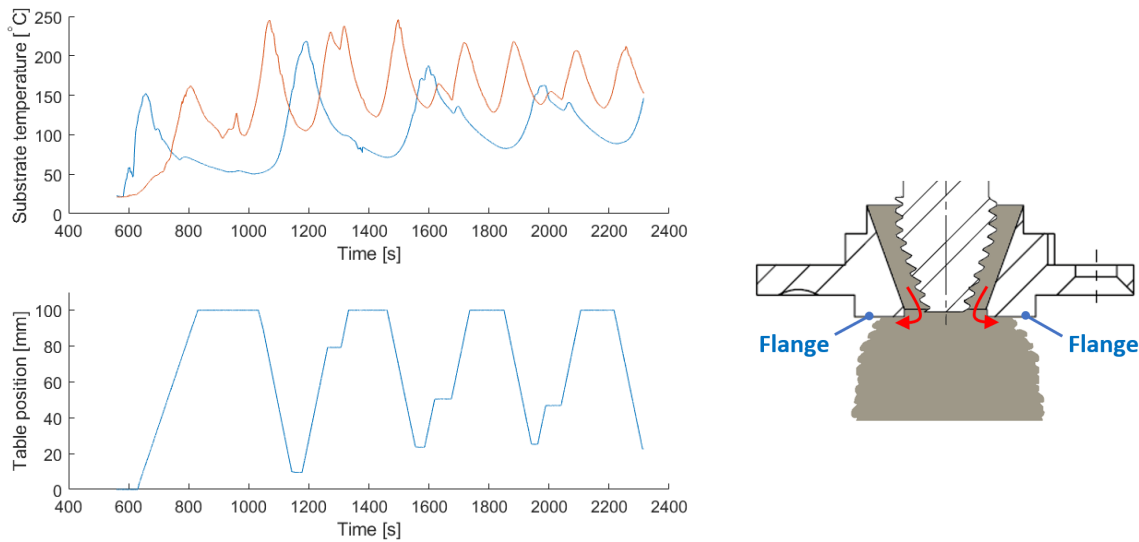


Figure 3.16: Cross-section of AM-3A, AM-4A, AM-5A, and AM-6A.

The top layer of each experiment shows the layer width as it was supposed to be. So, the top layer indicates a width of $10.5mm$ (figures 3.16a, 3.16b, 3.16c, and 3.16d). In case of overfeeding, AM-3 and AM-4, the pressure generated at the outlet of the nozzle is approximately $117MPa$ exerting on the substrate/previous layer. The pressure is calculated by taking the average extrusion force ($\approx 4kN$

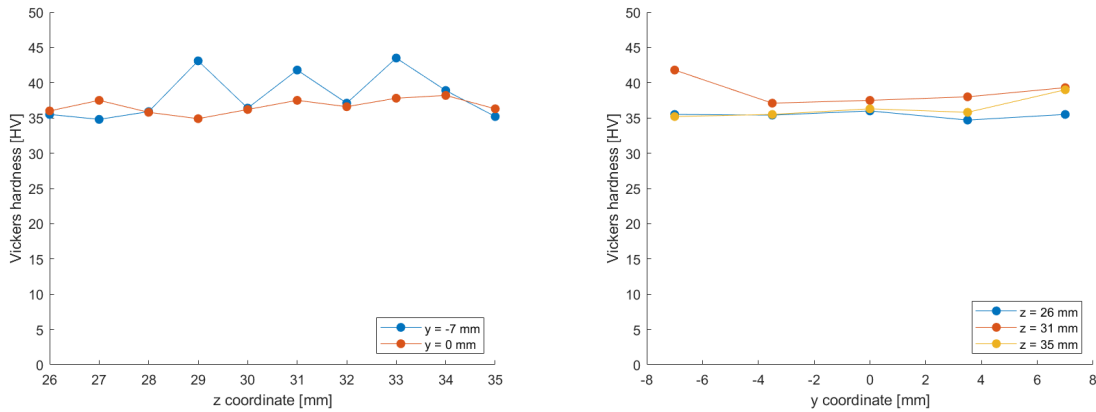
taken from figure 3.15b) and divide it by the ring shaped nozzle outlet area (34.2mm^2). Figure 3.17a shows the substrate temperature as a function of time. In addition, the table position is also shown as a function of time. The peaks in the substrate temperature appears when deposition of aluminium takes place directly above the thermocouple. The temperature of a previous deposited layer is based on the peaks of the substrate temperature and is approximately $200 - 225^\circ\text{C}$ or even higher due to the newly deposited aluminium. As a result of the increased temperature, the yield strength decreases $125 - 106$, respectively, using linear interpolation with the values given in table 3.5. Considering the higher temperature of 225°C the previous layer will plastically deform and material is able to flow underneath the nozzle flanges as is depicted in figure 3.17.



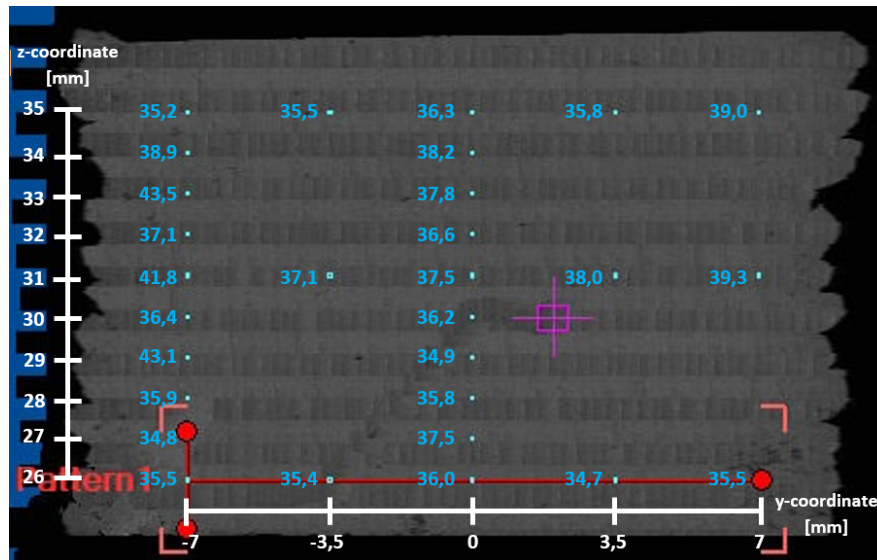
(a) Substrate temperature during the deposition of the first 8 layers of aluminium (b) Material flow underneath the nozzle flanges during experiment AM-3 ($v_t = 50\text{mm}/\text{min}$).

Figure 3.17: Figure (a) showing the substrate temperature of the first layers and (b) showing the material flow underneath the nozzle flanges.

The hardness is measured in transverse (#A) and longitudinal section (#B) of experiments reference material, AM-3, AM-4, AM-5, and AM-6. The hardness of AM-3 in transverse direction can be seen in figure 3.18c. In addition, the hardness is plotted in x - and z -direction to examine if any trend can be observed and seem to be relatively constant throughout the height and width (respectively figures 3.18a and 3.18b).



(a) Hardness throughout the height of AM-3A in transverse direction. (b) Hardness throughout the width of AM-3A in transverse direction.



(c) Hardness throughout the transverse cross-section of AM-3A.

Figure 3.18: Overview of the hardness of AM-3A in transverse direction.

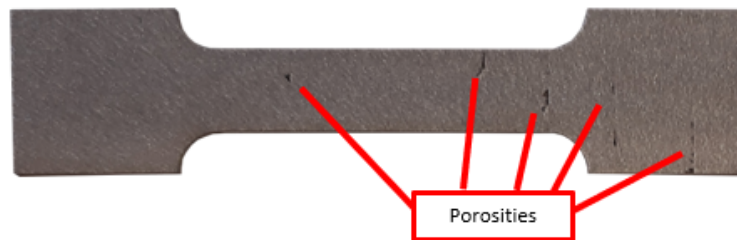
The average micro Vickers hardness and corresponding standard deviation (SD) for AM-2 to AM-6 and the reference material (AA6060 T6) can be found in table 3.8. The hardness remains fairly constant for each experiment. Unknown is if the hardness is measured between the bonding of two layers and it is hard to see in figure 3.18c since the image was taken with a low resolution camera of the hardness measurement setup. All samples show a hardness considerably lower than the reference material, the rods used for the FSEAM experiments. The reduced hardness is possibly the result of overaging or dissolution of the precipitates due to exposure to increased temperature during processing. Or, the temperature increases even further resulting in dissolving the precipitates reducing the hardness of the material. The hardness plotted in figures 3.18a and 3.18b show some kind of saw-tooth like pattern, especially throughout the height, that may also be the result of the forward and backward motion. This behavior will also be discussed in chapter 5.

Table 3.8: Average micro Vickers hardness and corresponding standard deviation.

Experiment [#]	Data points [-]	Average hardness [HV]	SD [HV]
AA6060 T6 transverse (A)	22	76.8	3.0
AA6060 T6 longitudinal (B)	16	83.5	3.0
AM-3A	29	37.2	2.3
AM-3B	35	37.1	0.9
AM-4A	29	41.4	1.7
AM-4B	35	40.7	1.8
AM-5A	30	39.2	1.8
AM-5B	29	40.9	1.7
AM-6A	30	41.2	2.0
AM-6B	29	40.1	2.0

3.3.4 Tensile tests

Tensile test specimens were created using electrical discharge machine as mentioned in section 3.2.4. The rough surface produced by this machine is shown in figure 3.19. In addition, porosities that were not directly visible in the microscopic image of figure 3.16d can clearly be seen in this figure, as indicated. These porosities can be seen in each tensile test specimen of experiment AM-6. The specimens were taken from the center ($y = 0mm$ shown in figure 3.11) of the AM-manufactured in height direction (z-direction) to test the strength of the bond of between the aluminium layers. This direction is known in additive manufacturing processes to be the weakest one as mentioned in section 2.5. Furthermore, the start/stops during the experiments were avoided as much as possible to obtain a tensile test specimen without temperature/extrusion force disturbances. The reason for avoiding start/stop conditions is that the setup will be modified to run continuously getting rid of those conditions.

**Figure 3.19:** Visible porosities in tensile test specimen AM-6.2 (65 mm/min).

The coupling between the Aramis system and data measured by the tensile test machine using specimen AM-3.3 can be found in figure 3.20. Where the force measured is plotted against the displacement. The displacement measured by the tensile tester includes the play of the machine. The Aramis images show the the strain in z -direction whereby the blue color indicates the minimum strain and the red color the maximum strain of that specific frame. So, The color dark blue in point

III has a different value of strain than point *IV*.

At point *I* in figure 3.20 the test starts and the specimen is at rest. Point *II* is approximately at the end of the elastic regime of the tensile test specimen. From that point onwards the tensile test specimen deforms plastically. Results of the plastically deformed specimen can be seen halfway and before necking, respectively points *III* and *IV*. Point *V* shows the start of necking and point *VI* shows the failure of the specimen.

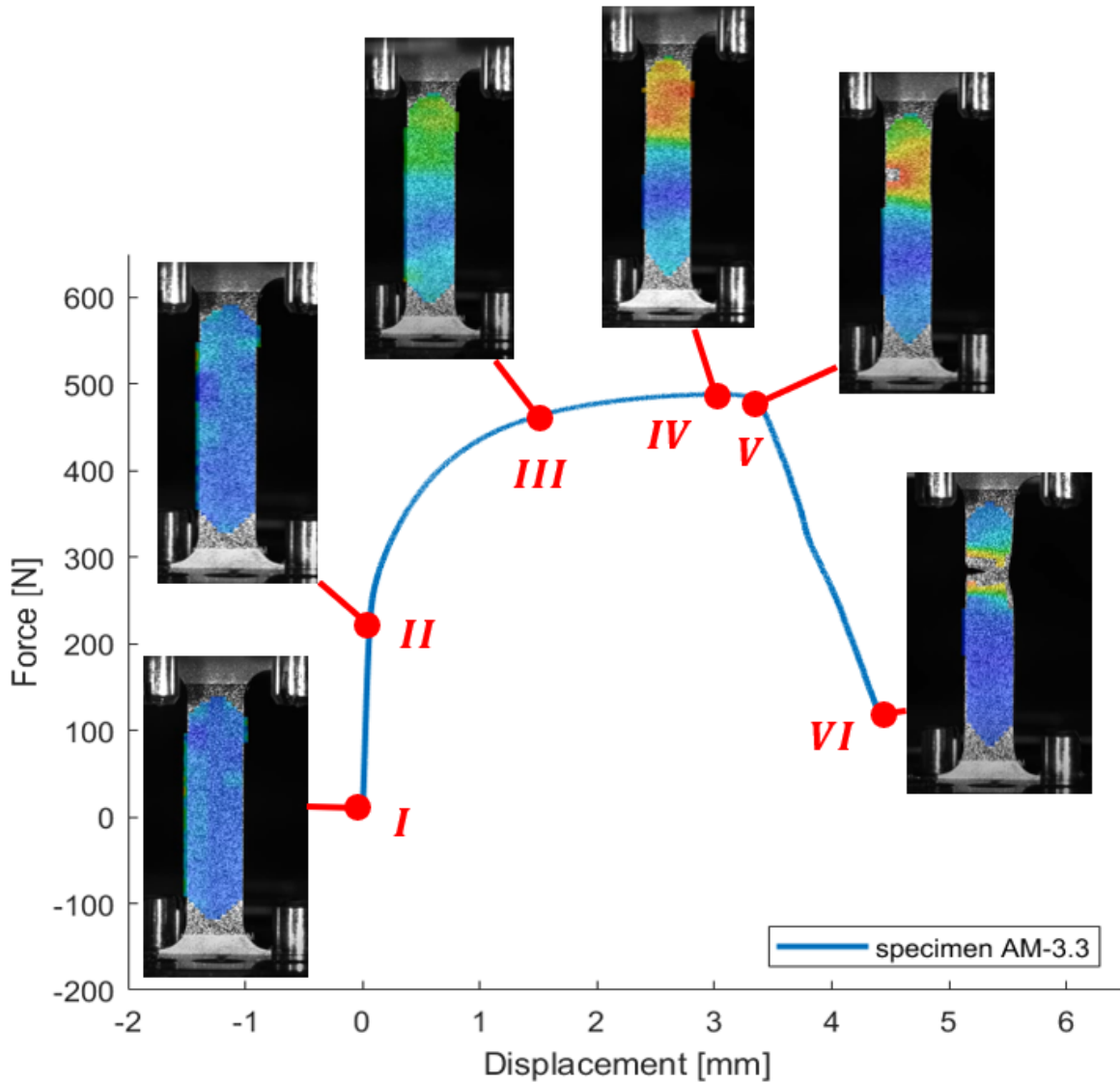
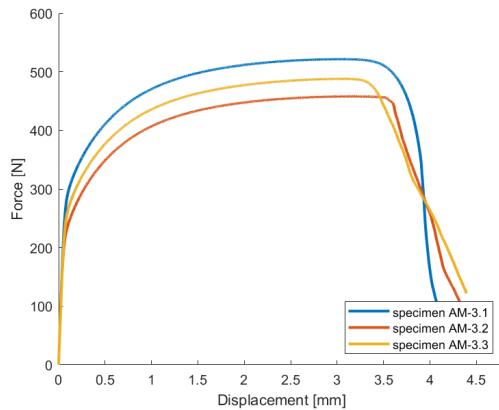


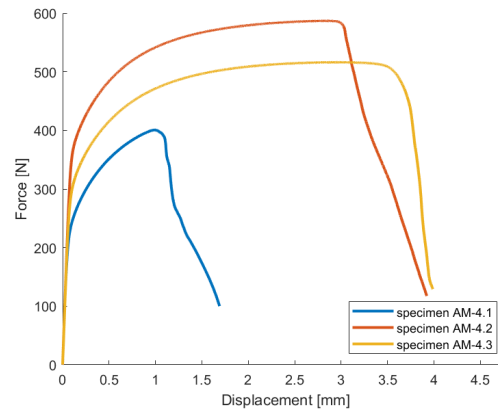
Figure 3.20: Force displacement curve obtained using the tensile test machine of specimen AM-3.3 ($v_t = 50\text{mm}/\text{min}$) corresponding to strain images measured by the Aramis system.

Figure 3.21 shows the tensile test results of the experiments AM-3, AM-4, AM-5, and AM-6, respectively table velocities are 50, 55, 60, and $65\text{mm}/\text{min}$. Three tensile test specimen have been tested for each experiment except for AM-5 due to a malformed specimen. The specimens tested with a relatively large degree of overfeeding (experiments AM-3 and AM-4) show the most promising

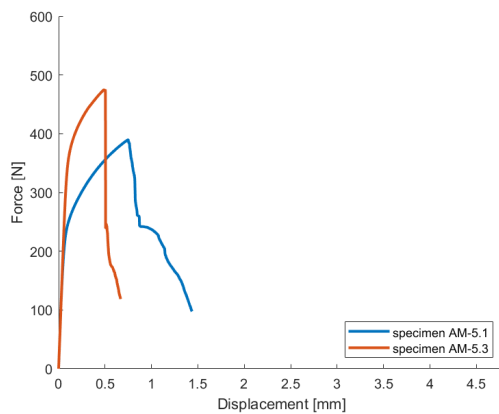
results in terms of mechanical properties except for specimen 4.1 that failed prematurely as can be seen in figure 3.21b. Examining the Aramis system in combination with the contour graphs the cause does not seem to be related with a start/stop condition to refill the feed chamber. However, a drop in extrusion force is present near the fracture location ($z \approx 30mm$) that may have decreased the oxide removal resulting in poor bonding. The cause of the premature failure will be studied in more detail using SEM in section 3.3.5.



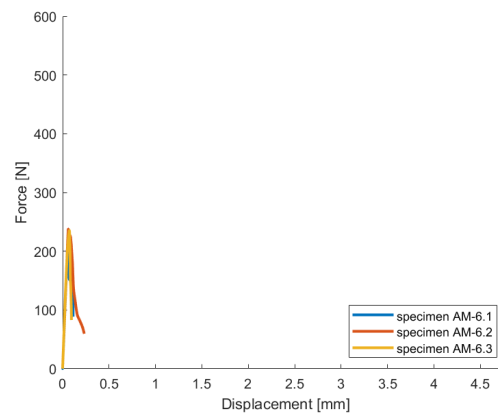
(a) Tensile test results of AM-3 (50 mm/min).



(b) Tensile test results of AM-4 (55 mm/min).



(c) Tensile test results of AM-5 (60 mm/min).

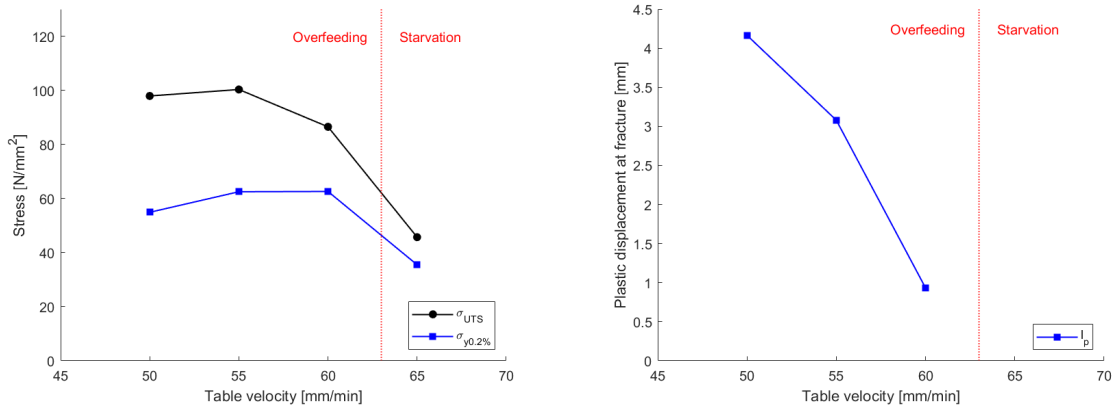


(d) Tensile test results of AM-6 (65 mm/min).

Figure 3.21: Overview of the tensile test results of AM-3, AM-4, AM-5, and AM-6.

Using the data shown in figure 3.21 the average mechanical properties of the specimens have been determined. The mechanical properties that are determined are the yield strength ($\sigma_{y0.2\%}$), the Ultimate Tensile Strength (UTS), and the plastic elongation at fracture (l_p) as can be seen in figure 3.22. In this figure the division between overfeeding and starvation is visible from the red dashed vertical line. The yield strength and tensile strength of aluminium AA6060 T6 are $150 N/mm^2$ and $190 N/mm^2$ respectively. One of the experiments showed a yield strength of approximately $63 N/mm^2$ and an ultimate tensile strength of approximately $100 N/mm^2$ that is about half (or less) of the original values. The reason for the decrease in strength is probably that precipitates are overaged or dissolved. This state is possibly reached due to the exposure of the feed material to elevated temperatures in the

region between the threaded tool and the nozzle (see figure 3.3), called the chamber. The duration of feed material entering the chamber and exiting through the nozzle for deposition is approximately 7 : 30min, which is equal to the time required for filling this chamber. Assuming the chamber temperature is the same or even higher than the nozzle temperature diffusion takes place in large quantities, resulting in growth of precipitates and overaging the precipitates. The material temperature will be discussed in chapter 5 in more detail. At even higher temperatures the precipitates may dissolve and the precipitation hardening start from the beginning, starting with small precipitates that do not strengthen/harden the material as was mentioned in section 2.1. As a result, the strength decreases. Approaching the division between overfeeding and starvation, the mechanical properties decrease drastically as a result of poor bond quality, probably due to the increase of porosities as mentioned in section 3.3.3.



(a) Average yield and ultimate tensile strength plotted against table velocity. (b) Average elastic and plastic elongation plotted against table velocity.

Figure 3.22: Average mechanical properties plotted against the table velocity.

3.3.5 Fracture surface analysis tensile test specimen

After the tensile tests, SEM images of the fracture surfaces are made to improve the understanding of bond quality and to study the fracture process. In order to understand the strong plastic deformation occurring on a SEM image a schematic side view of a tensile test specimen is shown in figure 3.23. If a tensile test is not properly bonded, the cross-section has a rectangular shape (figure 3.23a). However, this is not the case for a specimen that shows strong plastic deformation (figure 3.23b). At the start of the deformation, the left and right surface are stretched towards the middle, decreasing the area that holds the specimen together, also called necking. Eventually, the voids are nucleated near the precipitates to compensate for the incompatibility resulting in dimples after fracture as was mentioned in section 2.2. The dimple formation indicates high resistance to failure.

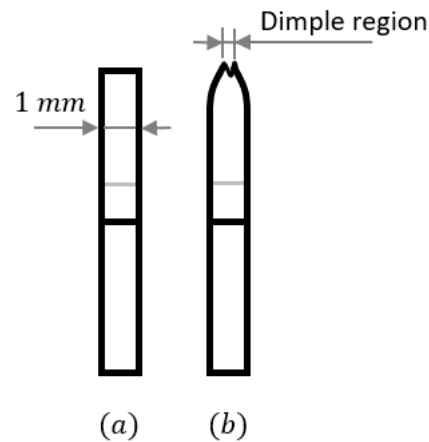
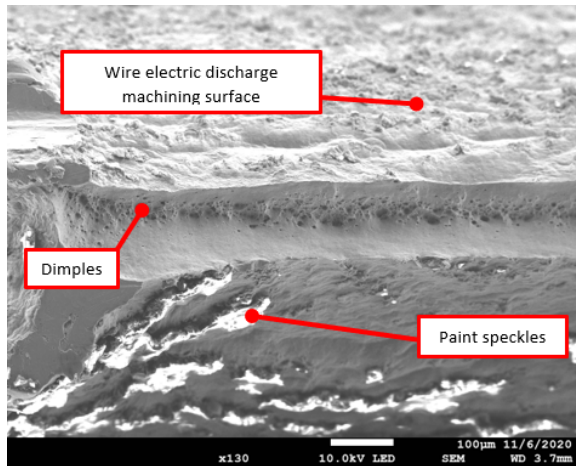


Figure 3.23: Schematic side view of a tensile test specimen with (a) poor bonding behaviour (b) a fracture after strong plastic deformation.

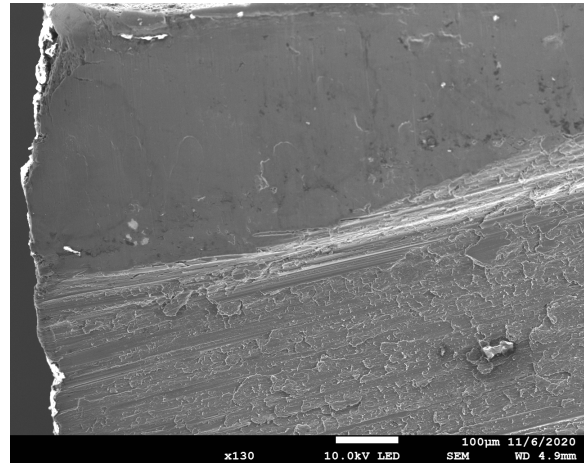
the result of two extremes of fracture surfaces with respect to deformation is shown, namely a tensile test specimen that shows strong plastic deformation (AM-2.1) and a specimen that shows no plastic deformation (AM-6.2). In addition, a closer look will be given at a prematurely failed specimen (AM-4.1) and a specimen that shows a needle like structure (AM-7.1).

Starting with the fracture surface of AM-2.1, figure 3.24a. The rough surface at the top is the result of the manufacturing of the tensile test specimen with the wire electric discharge machine and the speckle pattern present at the bottom surface is paint that was used for measuring with the Aramis system. These surfaces are only visible if the specimen has plastically deformed as is depicted in figure 3.23b. In addition dimples can be seen at the center of figure 3.24a indicating high resistance to failure. The dimple region has a width of $\approx 0.1mm$ instead of the original width of $1mm$. These surfaces and dimple formation can not be seen in specimen AM-7.1 (figure 3.24b) indicating no plastic deformation has occurred. Figure 3.24a and 3.24b are shown on the same scale for comparison, showing clearly the deformation behavior depicted in figure 3.23.

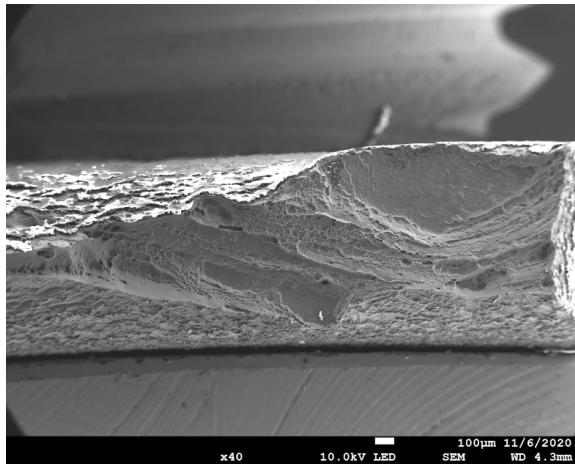
Next, the side of the prematurely failed specimen (AM-4.1) is shown in figure 3.24c and on the top right corner it can be seen that the fracture surface remains fairly a rectangular shape indicating that the material was not properly bonded and could not tolerate plastic deformation. Finally, the specimen AM-6.1 shows a needle like structure at the location depicted in figure 3.24d and how the needles look can be found in figure 3.24e. This structure possibly consists of precipitates and have clearly be seen in fracture surfaces of tensile test specimen of AM-6 (appendix D) whereby the fracture is expected to be in the interface between deposited layers. However, it is unknown if the needle structure is present at the fracture surfaces of the other experiments since they were not seen on the SEM images.



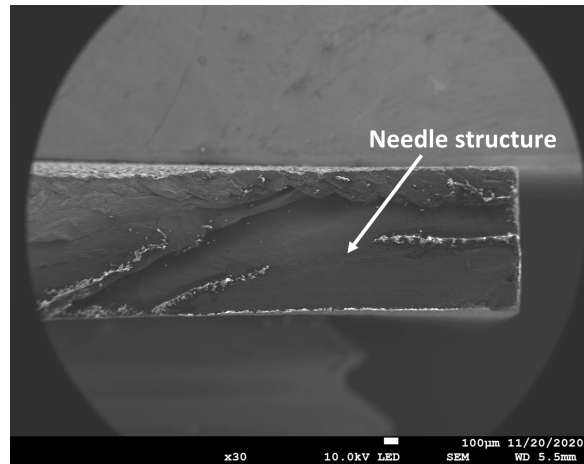
(a) Fracture surface of tensile test specimen AM-2.1 ($v_t = 50\text{mm}/\text{min}$).



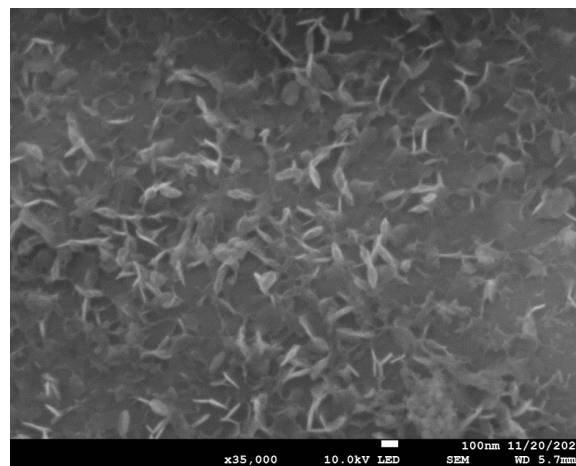
(b) Fracture surface of tensile test specimen AM-6.2 ($v_t = 60\text{mm}/\text{min}$).



(c) Fracture surface of tensile test specimen AM-4.1 ($v_t = 55\text{mm}/\text{min}$).



(d) Fracture surface of tensile test specimen AM-6.1 ($v_t = 60\text{mm}/\text{min}$).



(e) Zoomed in view of needle structure indicated in figure 3.24d (AM-6.1, $v_t = 60\text{mm}/\text{min}$)

Figure 3.24: Several fracture surfaces after tensile testing.

The average grain size measured of the feed rod material, AA6060 T6, is approximately 36 and 51 μm shown in figure 3.25a and 3.25b, respectively.

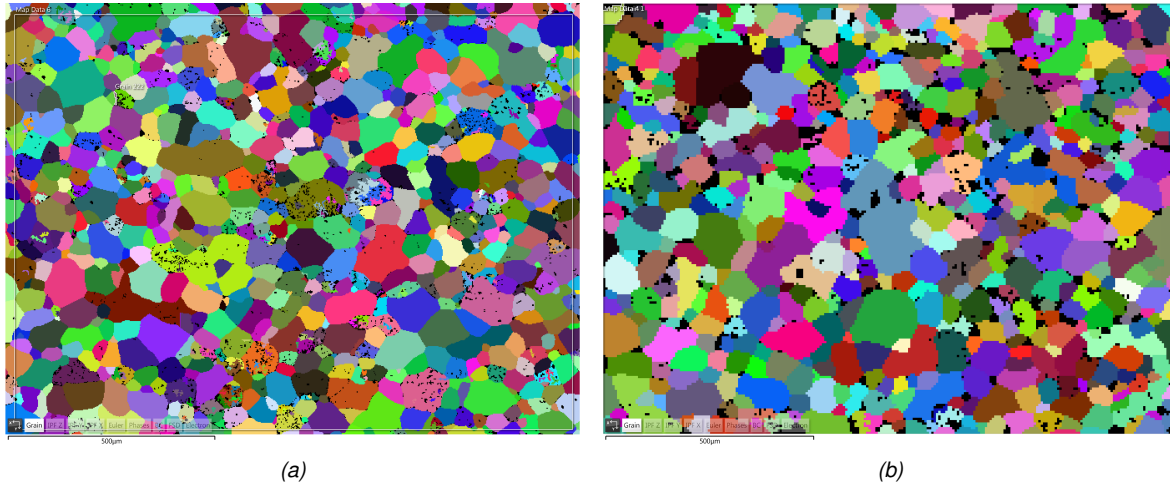


Figure 3.25: Grain size measurement of the feed rod material (AA6060 T6, scale bar equals 500 μm)

Figures 3.26a and 3.26b shows the microstructure formations of equiaxed grains that are most likely formed due to continuous dynamic recrystallization as was mentioned in section 2.3. As a result of the equiaxed grains, the mechanical properties in y - and z - should be of similar magnitude, at least at the measured locations, shown in table 3.9. The average grain size of the six measurements is roughly between 3.5 – 4 μm that is significantly smaller than the average grain size of the feed material. In addition, the average grain size throughout the height does not show an increasing trend, despite that the first deposited layer is significantly longer exposed to higher temperatures than the last deposited layer. However, the grain size increases if the critical grain growth temperature (T_{gg}) is exceeded and is estimated at 189 $^{\circ}C$ (see section 3.2.3) which is lower than the temperature of the previous deposited layer that estimated at 225 $^{\circ}C$ (see section 3.3.3). This temperature is above the critical grain growth temperature that should increase the grain size, however at this temperature is relatively low compared to the critical grain size temperature decreasing the growth rate. Therefore, no significant changing in grain size are observed throughout the height.

The reduction in grain size should increase the yield strength according to the Hall-Petch equation (equation 2.1) mentioned in section 2.3. However, the yield strength of the material did not increase. Therefore, the decrease in strength is the results of the precipitates growth or dissolving the precipitates. Some black particles can be seen on figure 3.26a and have been examined using the EDX. The particle depicted in figure 3.26c appears to be an iron precipitate. Therefore, the black particles are assumed to be precipitates and not pores.

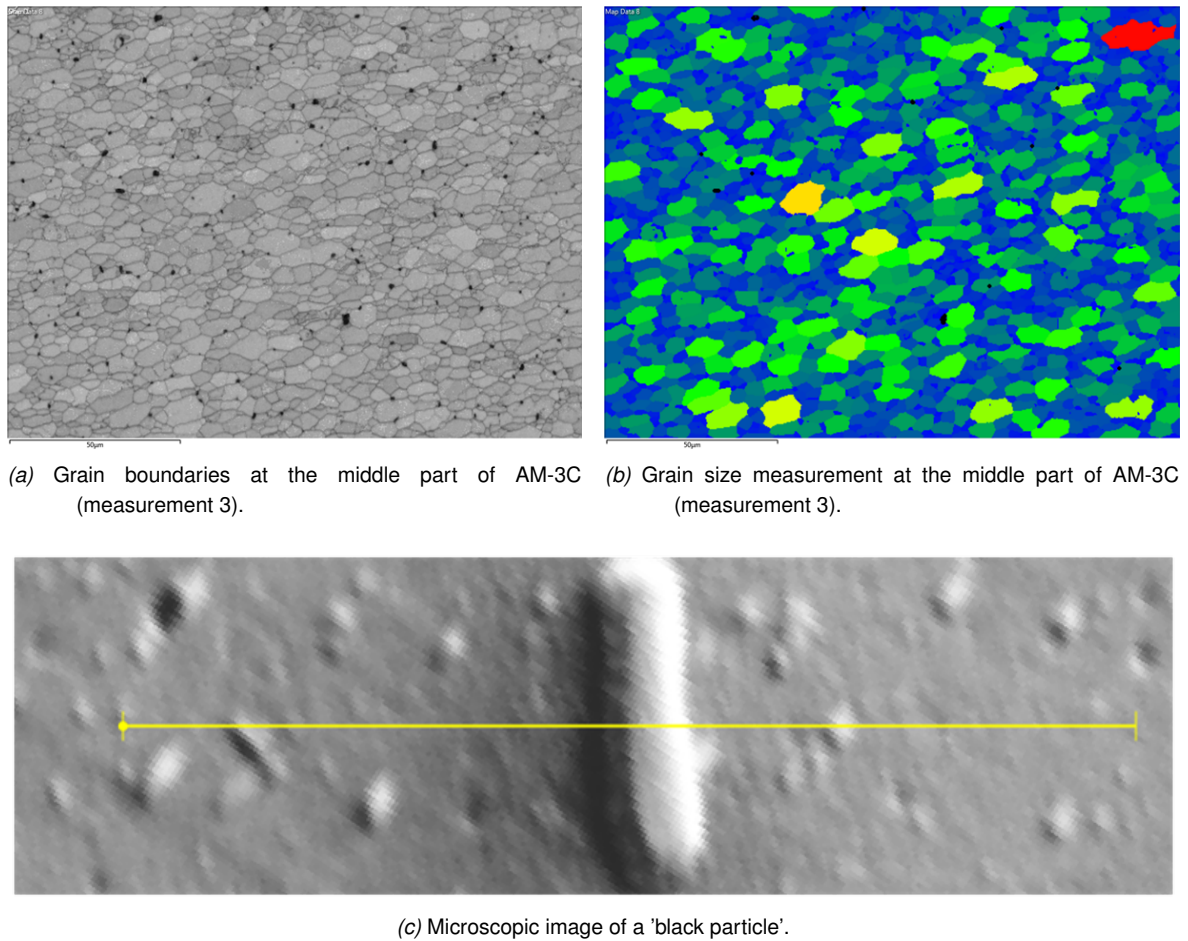


Figure 3.26: Grain boundaries and size measurements of AM-3C middle and microscopic image of a black particle (precipitate).

Table 3.9: Average grain size of AM-3C taken from an area near the interface with the substrate (measurement 1) up to top of the AM layers (measurement 6), $v_t = 50\text{mm}/\text{min}$.

Measurement [#]	AA6060 T6	1	2	3	4	5	6
Coordinates (x,y,z) [mm]	-	(73, 0, 1.8)	(73, 0, 3,4)	(73, 0, 21-30)*	(73, 0, 21-30)*	(73, 0, 44.0)	(73, 0, 47.7)
Average grain size [μm]	36-51	3.83	3.71	3.53	3.67	3.94	3.56

* The exact z -coordinate of measurement 3 and 4 are unknown.

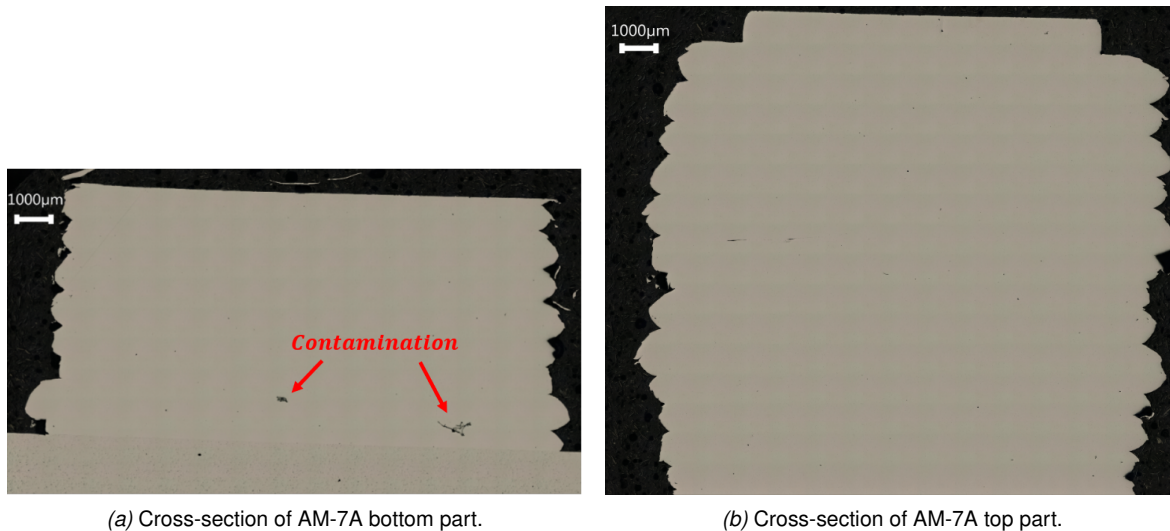
3.3.6 AM-7

As the results above show is that the setup is capable of printing material at relatively low speeds with a promising bond quality. The question that arises is at what speed the FSEAM setup is able to print. This question is partially answered in the final experiment, AM-7, that was able to run with a table velocity of approximately $400\text{mm}/\text{min}$. The maximum speed of the planer machine is $500\text{mm}/\text{min}$, but was not tested because the process became unmanageable due to manual operation of the setup. Besides increasing the table velocity, the volumetric flow rate was also increased to keep an

overfeeding situation to ensure enough material was present. The result of the printed wall can be found in figure 3.27. Comparing the surface of the wall of AM-7 to the other walls (of AM-1 up to AM-6), the surface quality seems to improve since the waviness pattern is hardly visible as can be seen in figure 3.27. The side bulges can be explained by refilling the feeding chamber of the FSEAM setup. before moving the table again, a bulge should be visible to ensure enough material was deposited to continue the additive manufacturing. The microscopic image of AM-7 can be found in figure 3.28. These microscopic images do not show any visible cracks, however, some contamination can be seen on the surface. The table velocities and corresponding volumetric flow rates can be found in tabel 3.10. The results of experiment AM-7 will not further be discussed since it was not really intended to be part of this study.



Figure 3.27: Macroscopic result of AM-7.



(a) Cross-section of AM-7A bottom part.

(b) Cross-section of AM-7A top part.

Figure 3.28: Cross-section of AM-7A.

Table 3.10: Table velocities with corresponding volumetric flow rates of experiment AM-7.

Table velocity	Layers	V_f	Degree of overfeeding
[mm/min]	[#]	[mm ³ /s]	[-]
55	4	11	1.14
122	4	26	1.22
225	10	51	1.30
295 325	5	80	1.41-1.55
412	1	106	1.47

3.4 Conclusion

The sub questions that this chapter tries to answer are listed below.

- i *Is it possible to deposit layers of AA6060 T6 using FSEAM? If so, what is the quality of the bond and is the process reproducible?*
- ii *How does the parameter 'table velocity' influence the behaviour of the nozzle temperature and extrusion force during the experiments at a constant rotation rate of the tool and a constant volumetric flow rate?*
- iii *What is the effect of the nozzle temperature and extrusion force on the microstructure and mechanical properties of AA6060 T6 additive manufactured part?*

(i) Multiple layers of aluminium AA6060 T6 were successfully deposited using the FSEAM setup as described in section 3.2.1 with promising results. In the case of a degree of overfeeding of 1.26 – 1.14 (table velocity of 50 and 55mm/min) the deposited layers were well-bonded. No porosity was visible (figure 3.16a and 3.16b), ductile fracture surface was observed (figure 3.24a), and no fracture at the interface of layers was observed for these experiments. Increasing the table velocity (AM-5 and AM-6), signs of starvation were seen and a decrease in mechanical properties observed. Plastic deformation also occurred in a lesser extent to none. Furthermore, a volumetric flow rate that can be processed is $\approx 382\text{cm}^3/\text{h}$ observed in experiment AM-7. Comparing this volumetric flow rate to the volumetric flow rate of MELD for aluminium that is $622\text{cm}^3/\text{h}$ (mentioned in section 2.4) shows promising results since the maximum capabilities of the FSEAM setup has not been tested, yet.

(ii) During experiment AM-2 a clear trend was observed between table velocity and extrusion force. Increasing the table velocity at constant volumetric flow rate resulted in a decrease in extrusion force at a relative constant temperature (figure 3.13a). This behavior was also seen during the experiments AM-3, AM-4, AM-5, and AM-6 but seemed slightly off this trend and resulted in similar extrusion forces for AM-3 and AM-4 and also for AM-5 and AM-6 (figure 3.15b). Considering that a lower nozzle temperature resulted in a more viscous material, the extrusion force could be higher. An additional reason for the faster table velocities (leading to starvation) is that extrusion force does not increase (force in vertical direction), because the pressure has to fill the entire layer before. This phenomenon will be discussed in more detail in section 5. Next, the nozzle temperature decreases while increasing the table velocity (figure 3.15a). One possible reason is that lower extrusion forces are measured for higher table velocities meaning that material can flow relative easily through the nozzle. As a result, material heats up less by the internal friction and plastic deformation. Or, an increase in table velocity

results in a decreased heat absorption by the substrate/previous layer affecting the measurement of the temperature at the location of the thermocouple as will be discussed in 5. Therefore, it would be interesting to place several thermocouples near the tool to get a better estimation of the material's temperature.

(iii) A higher extrusion force indicates that sufficient material is supplied (overfeeding) to deposit a solid layer. In addition, the nozzle temperature (reducing the yield strength) and in combination with the extrusion force result in material flowing underneath the nozzle flanges and print wider parts (figure 3.17). Lower extrusion forces (experiment AM-5 and AM-6) are the result of insufficient material supply resulting in signs of starvation which was clearly seen in the tensile test specimen of AM-6 (figure 3.19). So, higher extrusion forces ensure proper removal of the oxide layer enabling metal on metal contact for bonding. In the case of experiment AM-3 ($v_t = 50\text{mm}/\text{min}$) the nozzle temperature was higher compared to experiment AM-4 ($v_t = 55\text{mm}/\text{min}$) resulting in a slightly lower strength (figure 3.22a). In addition, the plastic deformation at fracture of experiment AM-3 (figure 3.22b) was higher than experiment AM-4 indicating that the combination of nozzle temperature and continuous dynamic recrystallization smaller grains are formed (section 2.4). Or, precipitates overaged to a lesser extent or did not dissolve, increasing the strength but decreasing the ductility. However, no EBSD images are created of experiment AM-4, yet.

During the experiments the nozzle temperature and extrusion force follow a saw-tooth like pattern that cannot be explained yet. The forward and backward motion of the planer table seem to have influence on the nozzle temperature and extrusion force that will be discussed in more detail in chapter 5.

Modeling the material flow and pressure generation during FSEAM

4.1 Introduction

Chapter 3 examined the bond quality of layers of aluminium AA6060 T6 printed using the FSEAM process. During the experiments, the table velocity varied at a constant volumetric supply rate and the nozzle temperatures and extrusion forces were measured. Using an isothermal-mechanical model (constant temperature) the pressure distribution at the bottom of a layer during deposition can be computed. The pressure distribution can be used to calculate the force applied between the substrate/previous layer and the deposited aluminium underneath the nozzle outlet. This force will be used to compare the extrusion forces generated during the experiments (figures 3.13b and 3.15b) to check if the upcoming model produces similar results. In other words, the goal of this chapter is to examine if the trend with respect to the extrusion force observed in section 3.3.2 and 3.3.3 can be understood. So, does the extrusion force decrease while the table velocity increases at a constant volumetric supply rate?

A derivation was made for an axisymmetric numerical model to understand the flow and pressure behavior of the aluminium between the threaded tool and the nozzle, this model will be called the *axisymmetric model*. Besides this model, an additional model in three dimensional space with the same geometry is considered to calculate these profiles as well, called the *3D extrusion model*. An extension to the *3D extrusion model* has been made to include a printed layer of aluminium, *3D additive manufacturing model*. The software used to solve these partial differential equations are MATLAB and COMSOL.

4.2 General assumptions

In order to model the flow and pressure profile of the processed aluminium several assumptions with respect to the material will be made. A common method to model hot solid-state metal alloy that are strongly deformed is to assume that material flows under ideal plastic conditions [40], [41]. So, the influence of elastic regime was neglected due to strong plastic strain and strain hardening can be neglected due to recovery and recrystallization at elevated temperatures [42]. As a result of

these assumptions, the processed material can be modeled as an incompressible shear thinning high viscous fluid.

The shear thinning behavior will be modeled using the power-law that describes the viscosity as a function of the total strain rate with temperature depended variables. The power-law is described in more detail in section 4.5.

4.3 Boundary conditions

In the *axisymmetric model* and *3D extrusion model* only stick boundary conditions are assumed at the interface between the processed material and the parts (threaded tool and nozzle). A stick boundary condition means that the material velocity relative to the part is zero. The *3D additive manufacturing model* also uses a slip boundary condition meaning that the material velocity in normal direction to the plane with is zero. So, it cannot move through this plane. This boundary condition does not have an effect on the material velocity in parallel direction and can therefore be seen as a restriction of the material flow. A schematic representation of these boundary conditions can be found in figure 4.1.

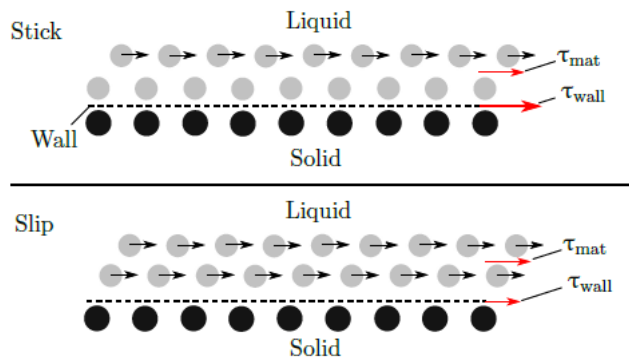


Figure 4.1: Schematic representation of a stick boundary and a slip boundary. In the top part a stick configuration is shown. The first layer of liquid particles (grey circles) stick to the solid wall (black circles). In the bottom part of the image there is a slip configuration. The first layer of liquid particles slip alongside the wall, taken from [43].

4.4 Previous models

Various models of FSC and FSE have been made by the UT in recent years [14]–[16]. The model of S. Liu studies the heat generation during FSC while varying the process parameters and the tool opening diameter of the FSC process. In order to relate the temperature and strain rate to the viscosity the Zener-Holloman constitutive law was used [14]. The model of J.B. Lind studied the pressure and temperature development during FSE also using the Zener-Holloman relation. The final model made by H.J. Smit studied the pressure development in the parallel and conical section as is depicted in figure 4.2. This model will be called the *axisymmetric constant viscosity model* and used a high constant viscosity to model the aluminium as a highly viscous fluid, overestimating

the pressure developed significantly. In order to make a more realistic model the viscosity will be modeled using a power-law that describes a shear thinning behavior of the material. The power-law model will be discussed in more detail in section 4.5. Besides modeling the viscosity differently, the geometry is shifted towards FSEAM. Instead of modeling the parallel and conical section of the nozzle, a new geometry has been modeled. The new geometry consists of the conical section of the nozzle and a deposited aluminium layer. It is assumed that the parallel section does not build up pressure, but only transports the feed material towards the conical part. Therefore, this part is not modeled. This new geometry makes it possible to vary the planer table velocity and examine the corresponding pressure distributions.

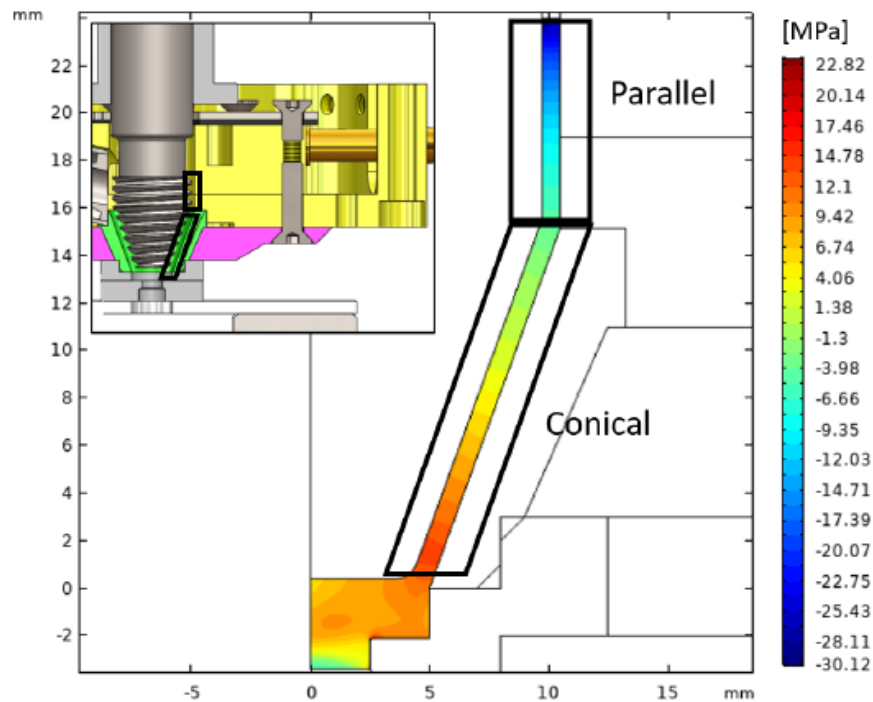


Figure 4.2: Indicative pressure profile of thermo-mechanical model of FSEAM setup during extrusion. Shown for demonstration of assumptions for upcoming models. Black markings indicate the parallel and conical sections for later references, taken from [15].

4.5 Power-law

The viscosity will be modeled using the power-law based constitutive model. The power-law describes a shear thinning behavior if the flow behavior index $n < 1$ meaning that the viscosity of the material decreases under the shear rate. The viscosity (μ) and shear stress (τ) can be related using equation 4.1.

$$\begin{aligned}\mu &= m\dot{\gamma}^{n-1} \\ \tau &= \mu\dot{\gamma} = m\dot{\gamma}^n\end{aligned}\tag{4.1}$$

where m and n are temperature dependent parameters that can be obtained experimentally, and $\dot{\gamma}$ the total strain rate. The required data will be obtained from literature. Experimental data of AA6060 was found up to $350^\circ C$ [44]. However, the range of the average nozzle temperature (at the thermocouples location shown in figure 3.15a) ranged from $\approx 275^\circ C$ up to $\approx 400^\circ C$ and the temperature of the material is expected to be higher. For that reason available, data of a comparable material, AA6063, has been used for a temperature range of $250^\circ C$ up to $550^\circ C$ [45]. In this report the flow stress is given as a function of the shear stress that can be rewritten in terms of the strain rate to determine the indices m and n . The equation for the flow stress (σ_f) can be found in equation 4.2.

$$\sigma_f = \sqrt{3}\tau = \sqrt{3}m\dot{\gamma}^n \quad (4.2)$$

Using the equation above, the parameters m and n can be determined for the aluminium AA6063 for different temperatures. The values for these indices can be found in table 4.1.

Table 4.1: Flow indexes, m and n , as a function of temperature using equation 4.2 [45].

Temperature [$^\circ C$]	m [MPa · s]	n [–]
250	54.9	0.05
300	40.7	0.08
350	33.0	0.11
400	23.2	0.12
450	19.6	0.15
500	13.5	0.16
550	12.8	0.20

4.6 Axisymmetric model

The axisymmetric model is used to calculate the velocities and pressure profiles in the conical part of the threaded tool assuming a non-Newtonian material at a constant temperature. In order to solve the fluid flow behaviour, the equations for the conservation of mass and NS equations will be used, respectively equation 4.3 and 4.4.

$$\nabla \cdot \vec{v} = 0 \quad (4.3)$$

$$\rho \left(\frac{\partial \vec{v}}{\partial t} + \vec{v} \cdot \nabla \vec{v} \right) = -\nabla p + \mu \nabla^2 \vec{v} + \rho g \quad (4.4)$$

Several simplification have been made to solve the problem. The first simplification is that the material's feed directions is assumed to be at the top of the conical part instead of the side which is the feed direction during the experiments as can be seen in figure 4.3. Furthermore, full stick conditions are assumed on the inner and outer wall. In addition, the centrifugal forces are neglected (creeping flow) and an atmospheric outlet pressure has been assumed. The final assumption is that

the total strain rate only depends on the angular velocity since the axial velocity is much smaller, so it is neglected.

A similar procedure that was used by H.J. Smit [15] will be used to calculate the velocities and pressure profiles using the parallel sections. The parallel sections can be found in figure 4.3. Additional assumptions and methods used to calculate these profiles can be found in section 4.6.1.

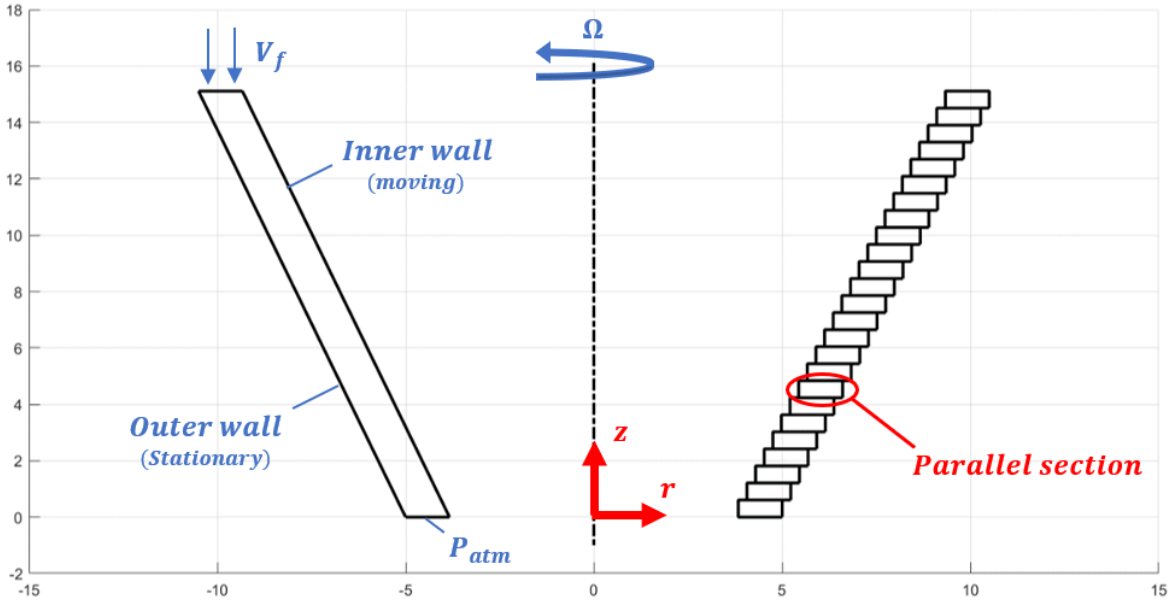


Figure 4.3: Setup of axisymmetric model of the conical part (shown in figure 4.2).

4.6.1 Velocities and pressure profiles of a parallel section

The parallel sections shown in figure 4.3 can be considered as hollow cylinders which makes it valid to assume that the angular and axial velocity is not a function of the height ($\frac{\partial v_r}{\partial z} = \frac{\partial v_\theta}{\partial z} = \frac{\partial v_z}{\partial z} = 0$). Furthermore, the velocities and pressure profiles do not change with respect to the θ -coordinate due to its axisymmetric nature ($\frac{\partial v_r}{\partial \theta} = \frac{\partial v_\theta}{\partial \theta} = \frac{\partial v_z}{\partial \theta} = 0$). In addition, the problem is considered steady state and therefore does not change with respect to time. Also, effects of gravity are neglected for this problem. Substituting the power-law in the NS equations and using the above assumptions, the NS equation can be reduced to equation 4.5.

$$r - \text{component} : \quad \rho \frac{v_\theta^2}{r} - \frac{\partial p}{\partial r} = 0 \quad (\text{neglected}) \quad (4.5a)$$

$$\theta - \text{component} : \quad \frac{\partial}{\partial r} \left(mr^2 \left| \frac{\partial v_\theta}{\partial r} - \frac{v_\theta}{r} \right|^{n-1} \left(\frac{\partial v_\theta}{\partial r} - \frac{v_\theta}{r} \right) \right) = 0 \quad (4.5b)$$

$$z - \text{component} : \quad \frac{\partial p}{\partial z} + \frac{1}{r} \frac{\partial}{\partial r} \left(mr \left| \frac{\partial v_\theta}{\partial r} - \frac{v_\theta}{r} \right|^{n-1} \frac{\partial v_z}{\partial r} \right) = 0 \quad (4.5c)$$

A schematic overview of the setup of a parallel section can be found in figure 4.4. Knowing the volumetric flow rate (V_f), velocities at the inner and outer wall, and the pressure at the outlet, the velocities and pressure profiles can be calculated.

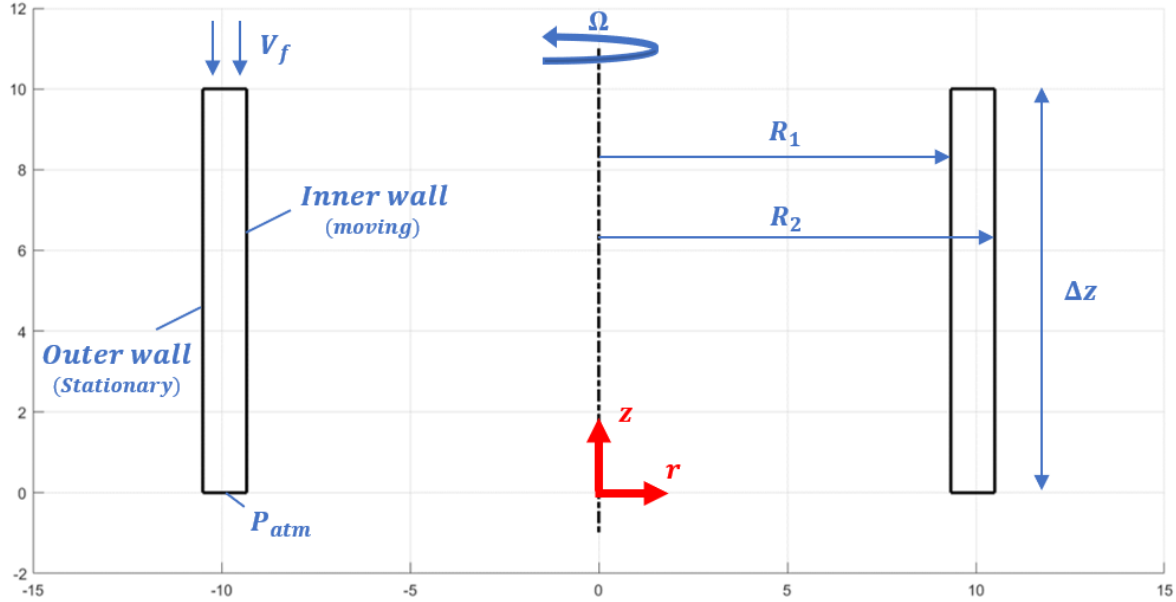


Figure 4.4: Setup of a parallel section of the conical part.

An analytic solution for the the angular velocity (v_θ) can be obtained using the θ -component, equation 4.5b. This solution can be found in equation 4.6 and the derivation can be found in appendix E.

$$v_\theta(r) = -\frac{n}{m^{1/n}} C_1^{1/n} r^{\frac{n-2}{n}} + C_2 r, \quad (4.6)$$

where C_1 and C_2 are unknown constants that can be solved using the boundary conditions shown in equation 4.7.

$$\begin{aligned} v_\theta(R_1) &= v_{\theta,tool} = \frac{2\pi\Omega[1/min]R_1}{60} \\ v_\theta(R_2) &= v_{\theta,wall} = 0 \end{aligned} \quad (4.7)$$

Solving equation E.6 using the boundary conditions mentioned in 4.7 for the θ -component, results in the following equation to describe the angular velocity.

$$v_\theta(r) = \frac{v_{\theta,wall} - \frac{R_2}{R_1} v_{\theta,tool}}{R_2 - R_1^{\frac{2}{n}} R_2^{\frac{n-2}{n}}} \left(r - R_1^{\frac{2}{n}} r^{\frac{n-2}{n}} \right) + \frac{r}{R_1} v_{\theta,tool} \quad (4.8)$$

Next, the velocity in z -direction (v_z) as a function of the radius can be determined using the z -momentum equation of 4.5c. Equation 4.5c can be rewritten using separation of variables to solve the velocity in z -direction and pressure profile as a function of the height (z -coordinate).

$$\frac{1}{r} \frac{\partial}{\partial r} \left(mr \left| \frac{\partial v_\theta}{\partial r} - \frac{v_\theta}{r} \right|^{n-1} \frac{\partial v_z}{\partial r} \right) = -\frac{\partial p}{\partial z} = \lambda \quad (4.9)$$

It is not possible to solve equation 4.9 analytically, because there are more unknown constants than boundary conditions. Therefore, the problem will be approach numerically. The part that can

still be further elaborated is in the square root, namely $(\frac{\partial v_\theta}{\partial r} - \frac{v_\theta}{r})$. The expression for this can be found in equation 4.10.

$$\begin{aligned}\frac{\partial v_\theta}{\partial r} &= \frac{v_{\theta,wall} - \frac{R_2}{R_1} v_{\theta,wall}}{R_2 - R_1^n R_2^{\frac{n-2}{n}}} \left(1 - \frac{n-2}{n} R_1^{\frac{2}{n}} r^{-\frac{2}{n}}\right) + \frac{v_{\theta,tool}}{R_1} \\ \frac{v_\theta}{r} &= \frac{v_{\theta,wall} - \frac{R_2}{R_1} v_{\theta,wall}}{R_2 - R_1^n R_2^{\frac{n-2}{n}}} \left(1 - R_1^{\frac{2}{n}} r^{-\frac{2}{n}}\right) + \frac{v_{\theta,tool}}{R_1} \\ \frac{\partial v_\theta}{\partial r} - \frac{v_\theta}{r} &= \frac{R_1^{\frac{2}{n}} \left(v_{\theta,wall} - \frac{R_2}{R_1} v_{\theta,wall}\right)}{R_2 - R_1^n R_2^{\frac{n-2}{n}}} \left(\frac{2}{n}\right) r^{-\frac{2}{n}}\end{aligned}\quad (4.10)$$

To make the formula clearer, the following constants are introduced and the expression, $\frac{\partial v_\theta}{\partial r} - \frac{v_\theta}{r}$ can be rewritten as follows.

$$\begin{aligned}b &= \frac{2}{n} \\ A &= \frac{R_1^b \left(v_{\theta,wall} - \frac{R_2}{R_1} v_{\theta,wall}\right)}{R_2 - R_1^n R_2^{1-b}}\end{aligned}\quad (4.11)$$

$$\frac{\partial v_\theta}{\partial r} - \frac{v_\theta}{r} = Abr^{-b}$$

Using the known boundary conditions as shown in equation 4.12 the discretization shown in equation 4.13 can be obtained for the unknowns $v_{z,j}$ for $j = 1 \dots N - 1$. A schematic representation of the schematic discretization can be seen in figure 4.5.

$$\begin{aligned}v_{z,0} &= \frac{S * \Omega[1/min]}{60} \quad (z - \text{velocity at inner wall}) \\ v_{z,N} &= 0 \quad (z - \text{velocity at outer wall})\end{aligned}\quad (4.12)$$

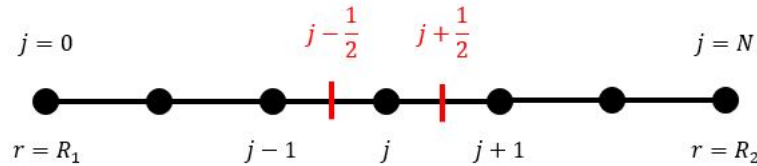


Figure 4.5: Discretization of the z-momentum of equation 4.5c at constant Δr .

$$\frac{m}{\Delta r^2} \left[r_{j+\frac{1}{2}} \left| Abr_{j+\frac{1}{2}}^{-b} \right|^{n-1} (v_{z,j+1} - v_{z,j}) - r_{j-\frac{1}{2}} \left| Abr_{j-\frac{1}{2}}^{-b} \right|^{n-1} (v_{z,j} - v_{z,j-1}) \right] = \lambda r_j \quad (4.13)$$

To obtain a solution for the discretization, an initial guess for the constant λ is required. After solving the non-linear system of equations for the velocity in the z-direction, the volumetric flow rate has to be checked and it should correspond to V_f . If the numerically determined volumetric flow rate differs too much from the practical volumetric flow rate, another value for λ will be estimated and the

script will run again. This loop will repeat itself until the error term is small enough. This way, a λ corresponding to the correct volumetric flow rate will be estimated. Once the pressure gradient, λ , is determined, the inlet pressure can be calculated using equation 4.14.

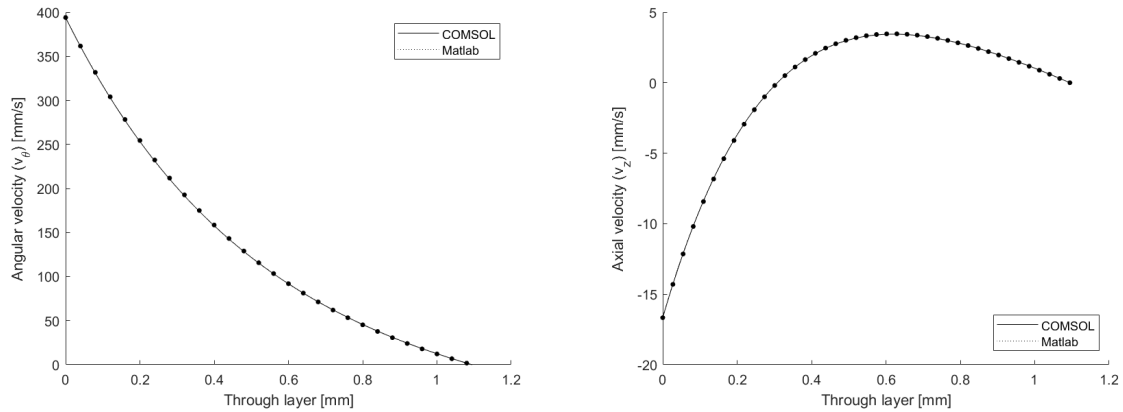
$$P_{in} = P_{out} - \lambda * \Delta z \quad (4.14)$$

where Δz is the height of a block shown in figure 4.4. Equations 4.8, 4.13, and 4.14 are used to calculate the angular velocity, axial velocity, and inlet pressure, respectively. This model has been solved using Matlab and has been checked by a model made in COMSOL with similar boundary conditions. The parameters used are shown in figure 4.4 and are given values that are listed in table 4.2.

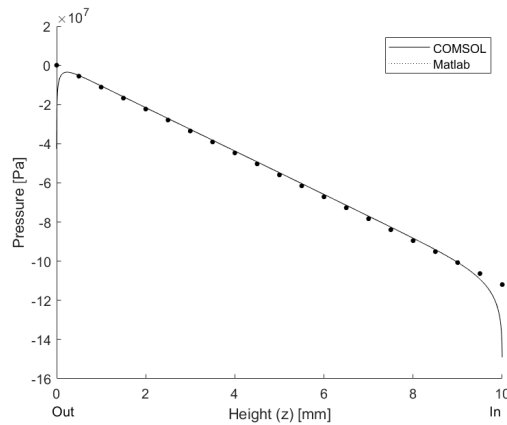
Table 4.2: Parameters values given for the parallel section to verify the model.

Parameter	Symbol	Value	Unit
Volumetric supply rate	V_f	11	mm^3/s
Rotational rate	Ω	400	$1/min$
Pitch	S	2.5	mm
Flow consistency index	m	33.0	$MPa \cdot s$
Flow behavior index	n	0.11	–
Inner radius	R_1	9.4	mm
Outer radius	R_2	10.5	mm
Section height	Δz	10	mm

The angular velocity can be found in figure 4.6a, the axial velocity in figure 4.6b, and the pressure in figure 4.6c. The axisymmetric model of Matlab matches the axisymmetric model of COMSOL perfectly, except near the in- and outlet of the pressure profile. This is expected to be caused by how COMSOL deals with the boundary conditions. At the outlet where the height is zero an increased pressure would be expected. However, the negative pressure at the inlet is required to satisfy the atmospheric pressure boundary condition at the outlet. So, the threaded tool builds up pressure when looked at it from inlet to outlet.



(a) Angular velocity profile for a non-Newtonian fluid behavior for a parallel section. (b) Axial velocity profile for a non-Newtonian fluid behavior for a parallel section.



(c) Pressure profile for a non-Newtonian fluid behavior for a parallel section.

Figure 4.6: Velocities and pressure profile for a non-Newtonian fluid behavior for a parallel section

4.6.2 Velocities and pressure profiles of the axisymmetric model

In order to estimate the velocities and pressure profiles in the conical part (figure 4.2) using the parallel sections as basis, several adjustments/assumptions are required. One assumption is that the volumetric flow rate is constant throughout each parallel section. Furthermore, the inner and outer radius (respectively R_1 and R_2) vary with increasing height as can be seen in figure 4.7. Also, the outlet pressure of a parallel section is the the inlet pressure of a previous section, except for the first section (at $z = 0\text{mm}$) where the outlet is exposed to atmospheric pressure (figure 4.3). In order to improve the estimation of the pressure profile, the layer thickness is defined perpendicular to the threaded tool wall (t_\perp) and the velocity in z -direction is assumed to be the velocity along the threaded tool ($v_{z\perp}$) as can be seen in figure 4.7. These values can be calculated using equation 4.15. After the pressure profile has been determined, the velocity profile along the threaded tool wall is converted to axial velocity profile again, and so is the layer thickness. This conversion is necessary to compare the axial velocity profile of the *axisymmetric model* and of the *3D extrusion*

model as can be seen in section 4.8.

$$\begin{aligned} t_{\perp} &= t_{tool} \sin(\varphi) \\ v_{z\perp} &= v_z \cos(\varphi) \end{aligned} \quad (4.15)$$

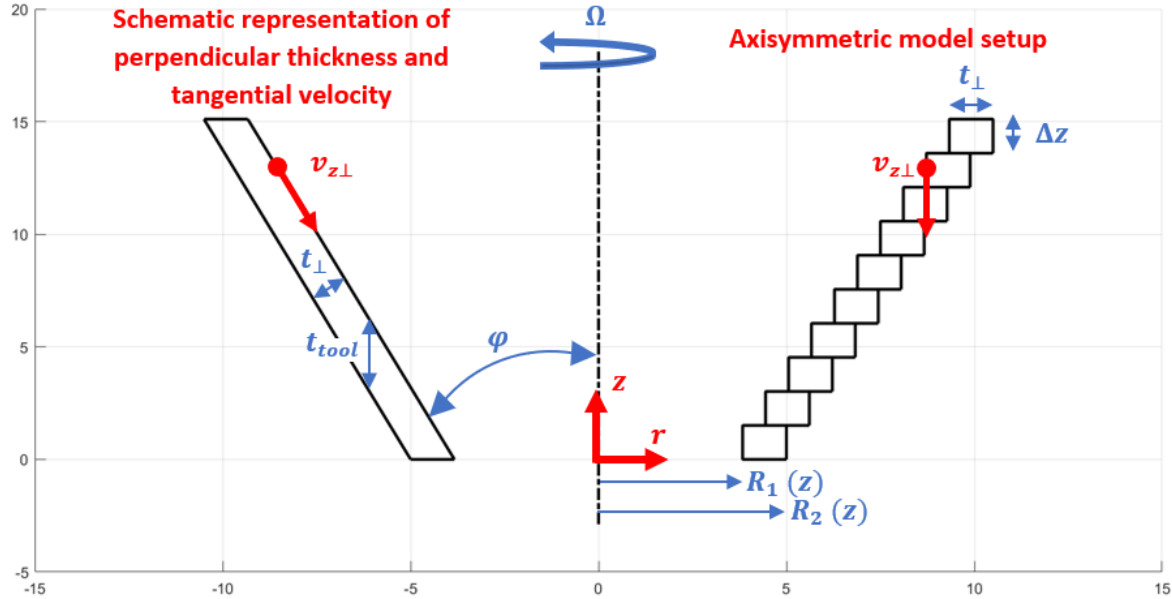


Figure 4.7: Representation of how the thickness is assumed perpendicular to the screw and the velocity tangential to the screw in the axisymmetric model.

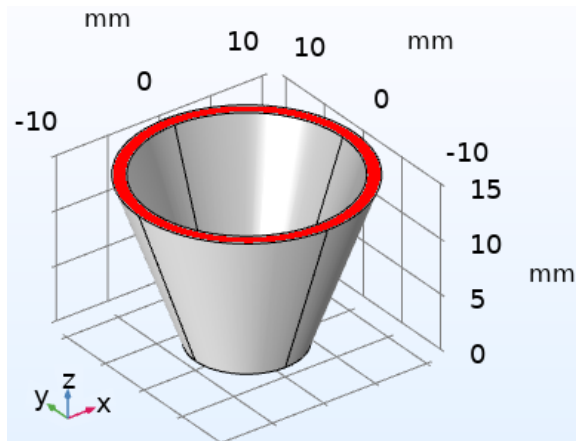
4.7 3D models geometry and boundary conditions

The 3D model is divided into two models closely related to each other. Both models are modeled as a creeping flow using a fluid with power-law viscosity (non-Newtonian). The first 3D model is used to compare the results of the axisymmetric model and vice versa, and check if the conversion of cylindrical coordinates to Cartesian coordinates was done properly, called the *3D extrusion model*. The boundary conditions of this model will be described and afterwards the boundary conditions of the second model which makes an extension to layer deposition, called the *3D additive manufacturing model*.

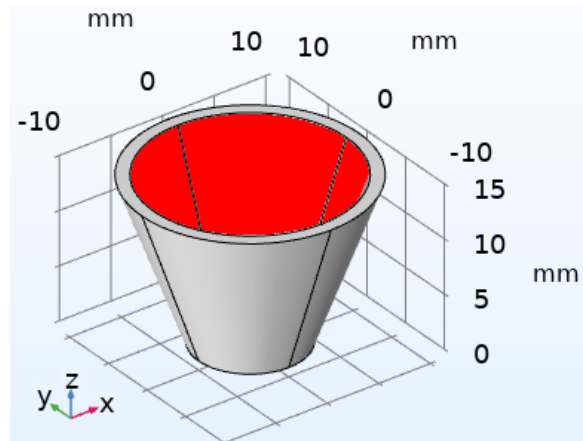
For the *3D extrusion model* at the top surface, as indicated in figure 4.8a, a normal inlet flow (v_f) has been assumed, similar to the *axisymmetric model*. Also, the boundary conditions at the inner and outer wall (respectively, figure 4.8b and 4.8c) are the same. The expressions shown in equation 4.16 are used to convert the boundary conditions from the conical section from x -, y -, and z -coordinates to cylindrical coordinates. The final assumption for the *3D extrusion model* is an

atmospheric pressure at the outlet as can be seen in figure 4.8d.

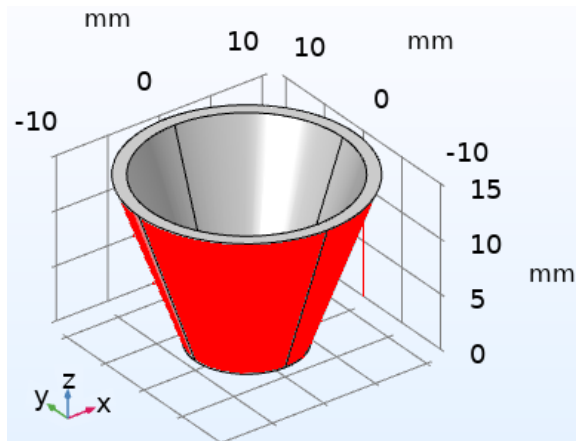
$$\begin{aligned}
 r &= \sqrt{x^2 + y^2} \\
 \theta &= \text{atan}(y/x) \\
 v_x &= -r\Omega \sin(\theta) \\
 v_y &= r\Omega \cos(\theta) \\
 v_z &= \frac{S * \Omega [1/min]}{60} \quad (\text{as defined in equation 4.12})
 \end{aligned}
 \tag{4.16}$$



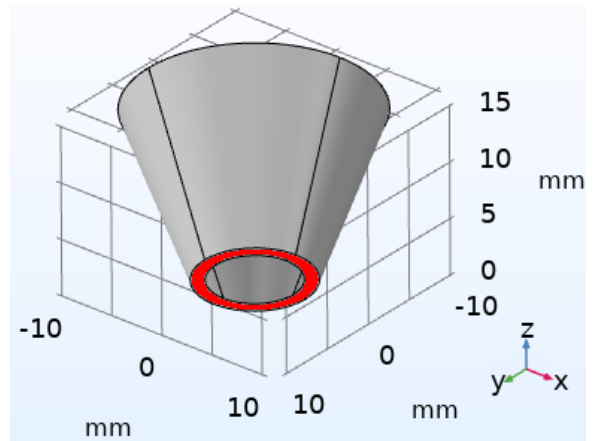
(a) Inflow velocity inwards normal to the red indicated surface $v_f = 0.6 \text{ mm/s}$.



(b) Boundary conditions at the inner wall, such as the angular velocity ($v_\theta = \sqrt{v_x^2 + v_y^2}$) and the axial velocity (v_z) described using equations 4.16.



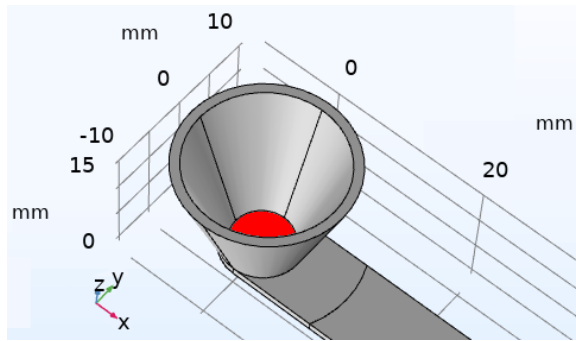
(c) The no slip zero velocity boundary condition ($v_\theta = v_z = 0 \text{ mm/s}$) at the outer wall.



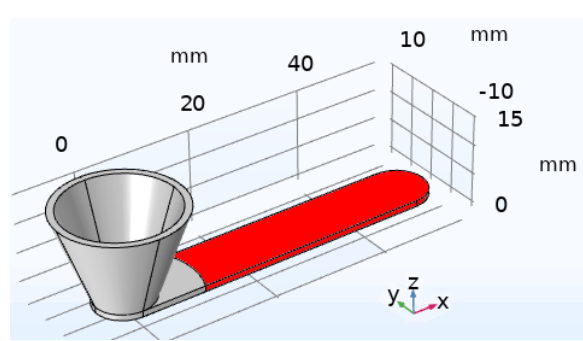
(d) Atmospheric outlet pressure ($p_{atm} \approx 1 \text{ bar}$) indicated by the red part.

Figure 4.8: Boundary conditions of the first 3D model.

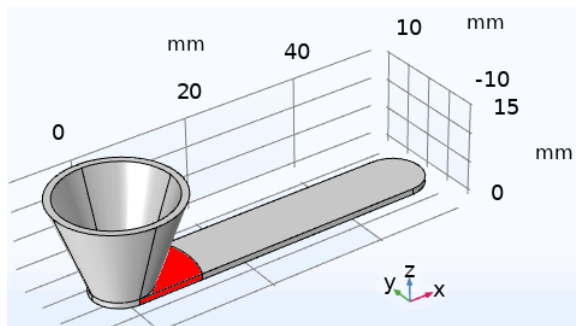
The *3D additive manufacturing model* uses similar boundary conditions to the *3D extrusion model* except for the atmospheric outlet pressure at the bottom since a layer is present at the outlet. The first assumption regarding the deposited layer is that the bottom of the tool has also influence on the material behavior as can be seen in figure 4.9a. The velocities assumed here are similar to the boundary conditions of the inner wall except for the velocity in the z -direction which is assumed to be zero. Furthermore, the atmospheric outlet pressure is defined after the moment when the aluminium material leaves the nozzle at $x \approx 10 - 12mm$ as depicted in figure 4.9b. The second assumption is that there is a slip boundary present at the red indicated parts of figure 4.9c where the top of the nozzle and the flanges of the nozzle move along. This seems to be a valid assumption since no material sticks at these parts of the nozzle after the experiments. The plane indicated in red in figure 4.9d is in contact with the atmosphere, so an atmospheric boundary condition would apply. However, the *3D additive manufacturing model* shows a material flow in the outward direction of this plane that does not correspond with the experiments. Therefore, a slip boundary condition is used. The final boundary condition regarding the *3D additive manufacturing model* is a velocity of the table movement which is in the x -direction and also indicated by the red part in figure 4.9e. The table velocity will vary during the simulation while the other parameters remain unchanged.



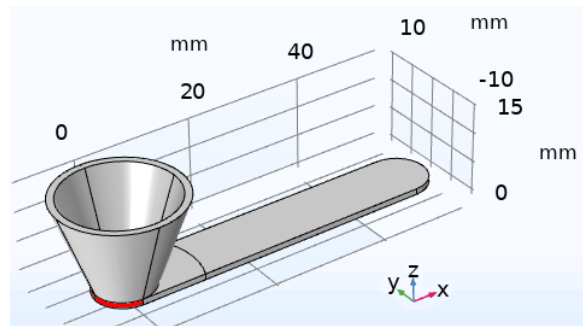
(a) No slip boundary condition at the bottom of the tool assuming only angular velocities ($v_\theta = \sqrt{v_x^2 + v_y^2}$, $v_z = 0 \text{ mm/s}$).



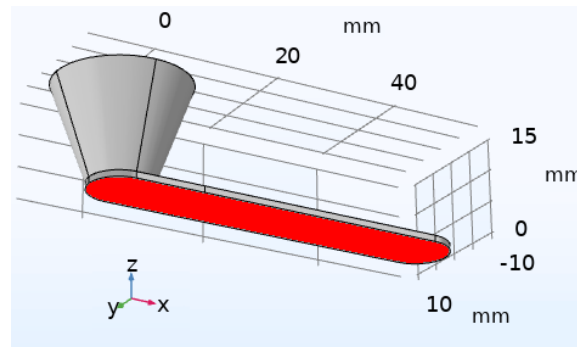
(b) Atmospheric pressure assumed at the outlet of the aluminium deposited layer $p_{atm} = 1 \text{ bar}$.



(c) Slip boundary condition assumed at the flanges of the nozzle.



(d) Slip boundary condition assumed at the front of the printing direction.



(e) Assuming table velocity in x -direction. Varying between ($v_x = 50, 55, 60, \text{ or } 65 \text{ mm/min}$).

Figure 4.9: Boundary conditions of the second model.

4.8 Comparison axisymmetric model to the 3D extrusion model

A comparison will be made between the *axisymmetric model* and the *3D extrusion model*. The relevant parameters are given in table 4.3, where m and n are based on a temperature of 350°C of AA6063.

Table 4.3: Values for the *axisymmetric* and *3D extrusion* model parameters when not stated otherwise.

Parameters	Symbol	Value	Unit
Inflow velocity	v_f	0.6	mm/s
Rotational rate	Ω	400	$1/\text{min}$
Pitch	S	2.5	mm
Flow consistency index	m	33.0	$\text{MPa}\cdot\text{s}$
Flow behavior index	n	0.11	–
Tool gap	t_{tool}	3.2	mm

The most interesting part is how much pressure can be build up using this setup. Before this can be calculated the models should have been verified. This will be done using the angular and axial velocity profile. The position of where the velocities profiles are taken from are 20% and 80% of the total height indicated by the red lines in figure 4.10. Figure 4.10 can also be seen as a cross-section of figure 4.8, where $y = 0\text{mm}$. Therefore, the coordinate system can be seen as Cartesian or cylindrical. In figure 4.11a the angular velocity is shown as a function of the radius for both solutions and in figure 4.11b the axial velocity as a function of the radius for both solutions. The results obtained for the *3D extrusion model* are indicated with the solid lines and the results obtained for the *axisymmetric model* are dashed lines from now on.

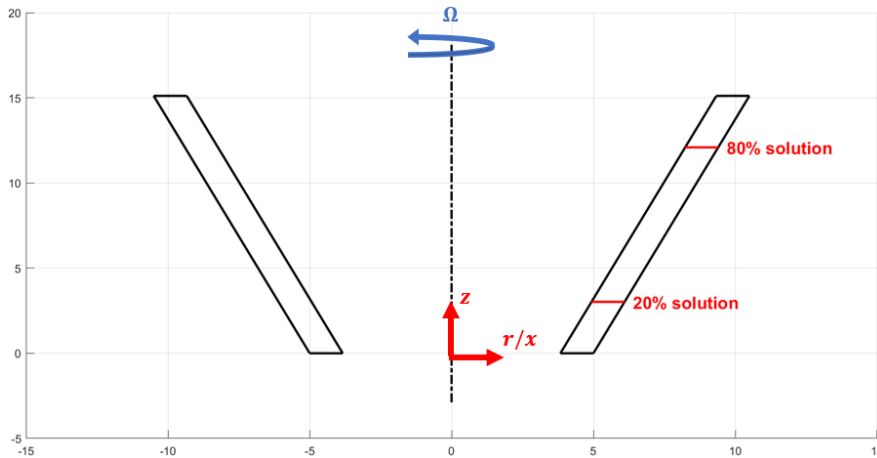
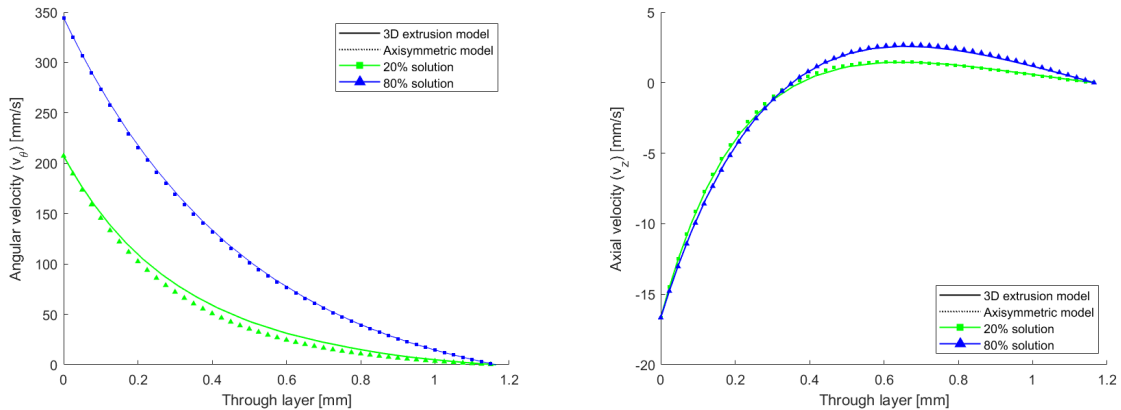


Figure 4.10: Angular and downward velocity taken from the 20%- and 80%-solution line.

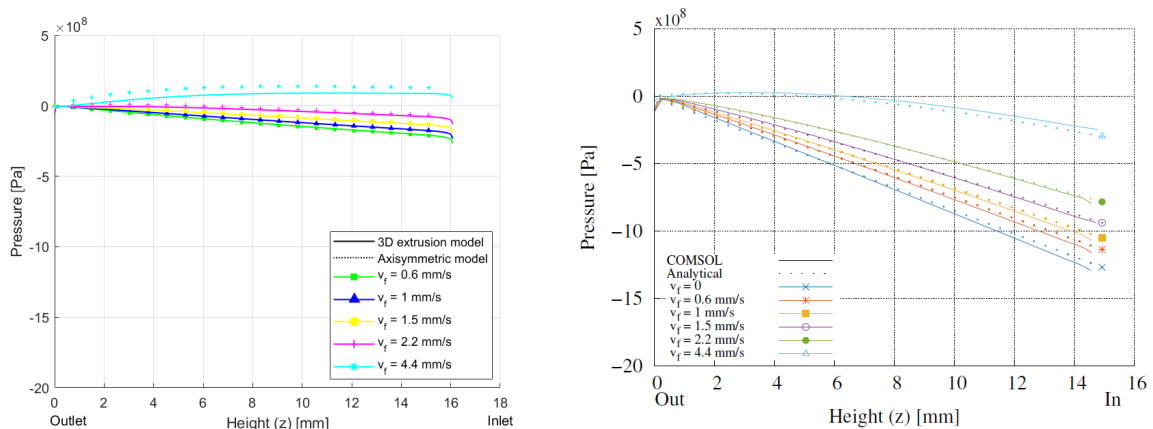


(a) Angular velocity (v_θ) plotted through layer for the 20% and 80% solution as indicated in figure 4.10. (b) Axial velocity (v_z) plotted through layer for the 20% and 80% solution as indicated in figure 4.10.

Figure 4.11: Velocity profiles through layers.

Comparing the velocity profiles (figures 4.11a and 4.11b) of the *axisymmetric model* and the *3D extrusion model*, both models produce similar results. In addition, the calculated pressure profiles shown in figures 4.12a, 4.13a, and 4.14a do also produce relatively similar results with each other. As a result of the agreement, the conversion to a *3D extrusion model* has been verified.

The pressure profile will be studied in more detail while varying the inflow velocity, rotational rate, or pitch to examine if trends can be observed assuming a shear thinning material behaviour (respectively figure 4.12a, 4.13a, and 4.14a). The results are compared to the worked performed by H.J. Smit [15]. The negative pressure at the inlet is required to satisfy the atmospheric pressure boundary condition at the outlet. So, the threaded tool builds up pressure when looked at it from inlet to outlet, similar to a parallel section as described in section 4.6.1.



(a) Non-Newtonian fluid behavior dependent on inlet flow (v_f). (b) Newtonian fluid behavior dependent on inlet flow (v_f), taken from [15].

Figure 4.12: Comparison of a fluid with a constant viscosity and a viscosity described using the power-law while remaining the rotation rate, tool gap, and pitch constant, but varying the inlet flow (v_f).

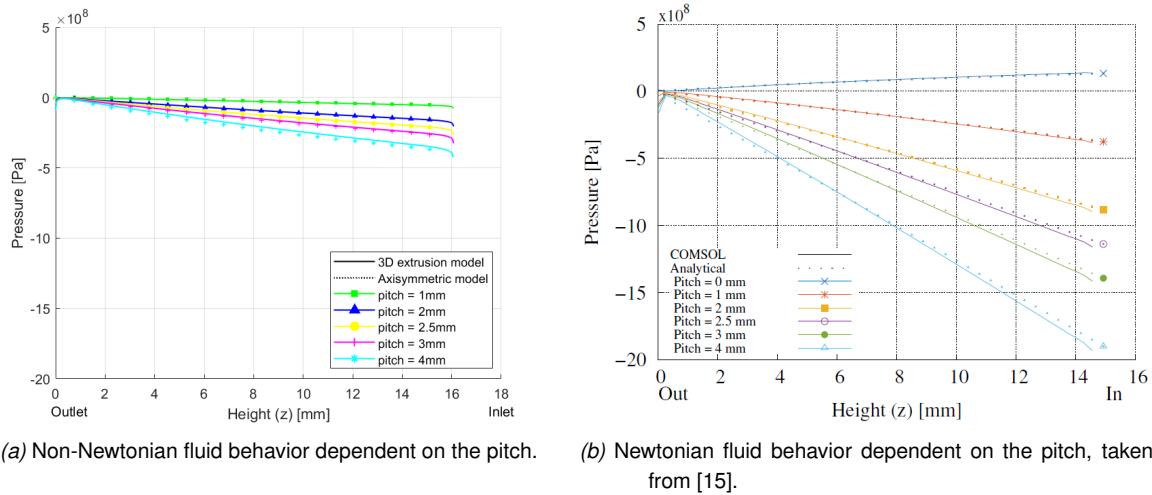


Figure 4.13: Comparison of a fluid with a constant viscosity and a viscosity described using the power-law while remaining the rotational rate, tool gap, and inlet flow constant, but varying the pitch.

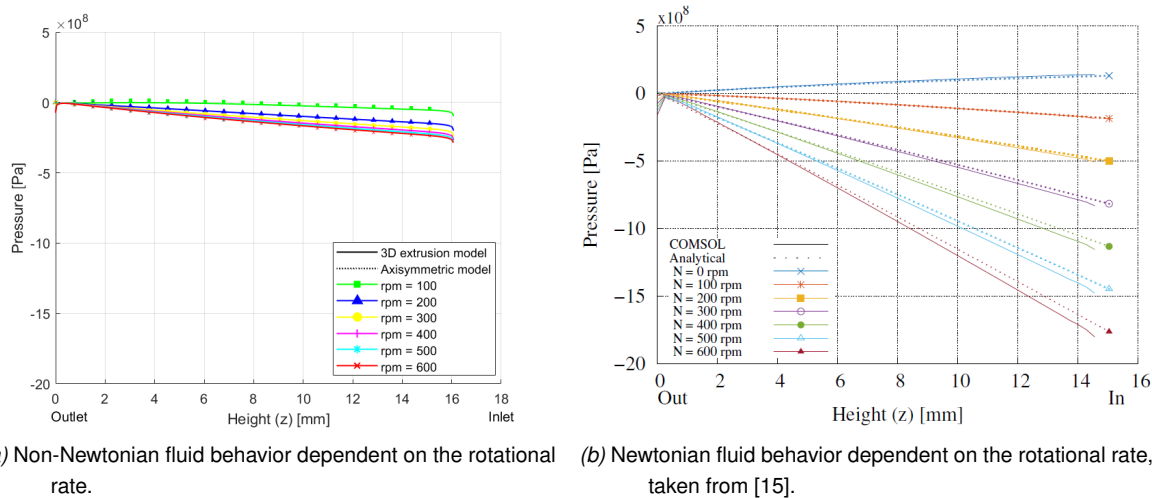


Figure 4.14: Comparison of a fluid with a constant viscosity and a viscosity described using the power-law while remaining the pitch, tool gap, and inlet flow constant, but varying the rotational rate (Ω).

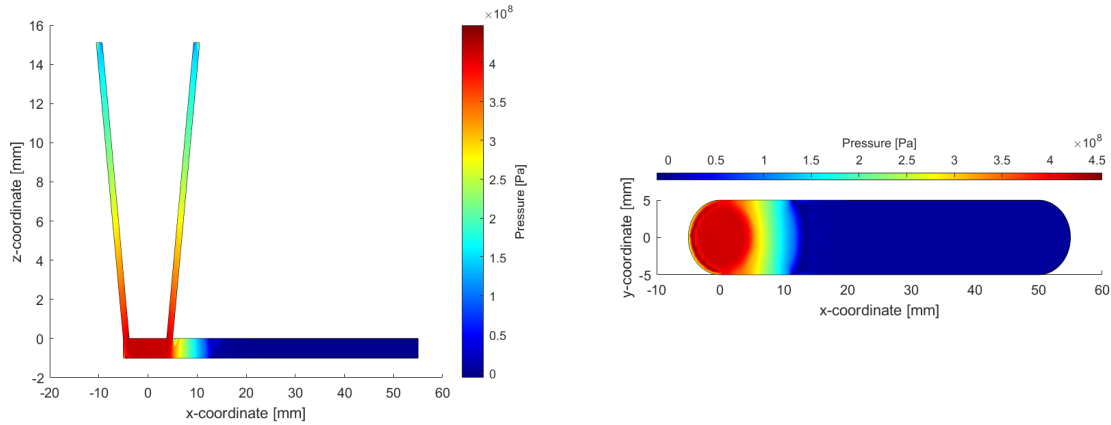
The pressure profiles of the *axisymmetric model* will be compared to the results of the *axisymmetric constant viscosity model* to examine if deviating trends can be observed using a material modeled as a shear thinning behaviour. The first remark is that the pressure profiles decreased significantly using a shear thinning material behaviour as can be seen in figures 4.12, 4.13, and 4.14. Also, consider that the following trends are observed using stick boundary conditions.

Examining the pressure profile with respect to the increase in inlet flow (figure 4.12a), the pressure becomes less negative. In other words, the higher the inlet flow the less pressure is required to be

generated by the threaded tool to obtain an atmospheric pressure at the outlet of the nozzle. This behaviour is in agreement with the *axisymmetric constant viscosity model* as can be seen in figure 4.12b. Next, increasing the pitch results in a higher axial velocity near the threaded tool as can be seen in equation 4.12. Increasing the axial velocity, v_z , results in a stronger pressure gradient, λ , which is relatively constant through height. As a result, the pressure builds up while increasing the pitch as can be seen in figure 4.13a. The final parameter is the rotational rate as can be seen in figure 4.14a. By increasing the rotational rate, the pressure tends to create similar pressure profiles. So, the pressure becomes less dependent on the rotational rate, unlike the *axisymmetric constant viscosity model* (figure 4.14b). This effect is introduced by describing the viscosity as a shear thinning behaviour using the power-law. Thus, increasing the shear rate results in similar viscosity values for higher rotational rates. However, the pressure profile still tends to become less negative as the rotational rate increases and is caused by the fact that the rotational rate increases the axial velocity caused by the pitch of the tool as is described in equation 4.12. The meaning of this behavior in practice is that the pressure build up is not greatly influenced by higher rotational rates. However, the viscosity is not only a function of the strain rate but also of the temperature which has not been considered yet. In other words, a higher rotational rate may increase the temperature that in turn changes the viscosity behavior and may cause in a different pressure gradients. As a result of the stick boundary conditions, the pressure has to overcome the stress to shear the material (τ_{mat}) as depicted in figure 4.1 to move the material downwards. However, the calculated pressure is higher than in the experiments and therefore a slip boundary condition is required to estimate the pressure correctly.

4.9 3D additive manufacturing model compared to experimental results

In the *3D additive manufacturing model* simulation the same table velocities values (50, 55, 60, and 65mm/min) will be used to calculate the pressure exerted below the outlet of the nozzle. In addition, the inlet flow has been changed from $v_f = 0.6mm/s$ to $v_f = 0.15mm/s$ in order to recreate the volumetric flow rate of $V_f = 11mm^3/s$ during the experiments. The other parameters used are listed in table 4.3. Figure 4.15a shows the pressure development in the xz -plane at $y = 0mm$ derived from the geometry shown in figure 4.9. And, figure 4.15b shows the pressure development in xy -plane at $z = -1mm$ (bottom of the layer) from the geometry that is also shown in figure 4.9. Pressure builds up in the conical section and is the highest below the outlet of the nozzle (between $x = -5mm$ and $x = 5mm$). In this case, the planer table moves in positive x -direction (thus printing in negative x -direction) and material leaves the nozzle flanges (as depicted in figure 3.5b) at $x \approx 10 - 12mm$ reducing the pressure to atmospheric conditions as can be seen in figure 4.15a and 4.15a.



(a) Pressure distribution of the xz -plane for a planer table velocity of 50 mm/min . (b) Pressure distribution of the xy -plane at the bottom of the layer for a planer velocity of 50 mm/min .

Figure 4.15: Pressure distribution for a planer table velocity of 50 mm/min . Parameters used are $\Omega = 400 \text{ rpm}$, $v_f = 0.15 \text{ mm/s}$, $S = 2.5 \text{ mm}$, $m = 33 \text{ MPas}$, $n = 0.11$, and $t_{tool} = 3.2 \text{ mm}$.

A trend can clearly be seen by increasing the table velocity. Increasing the table velocity results in a lower pressure at the nozzle outlet area (between $x = -5 \text{ mm}$ and $x = 5 \text{ mm}$) as is depicted in figure 4.16. Remarkable is the behaviour of the pressure with a table velocity of $v_t = 65 \text{ mm/min}$. This table velocity exceeds the theoretical table velocity of 63 mm/min that was calculated using equation 3.2.2. Therefore, this table velocity leads to the starvation phenomenon. In other words, not enough material is deposited to complete a fully dense layer and material that is at the bottom ($z = -1 \text{ mm}$) is pushed in opposite direction (negative pressure) to fulfill the boundary conditions as can be seen in figure 4.16. In practice, material would still flow out of the nozzle, but the pressure that would built up is minimal.

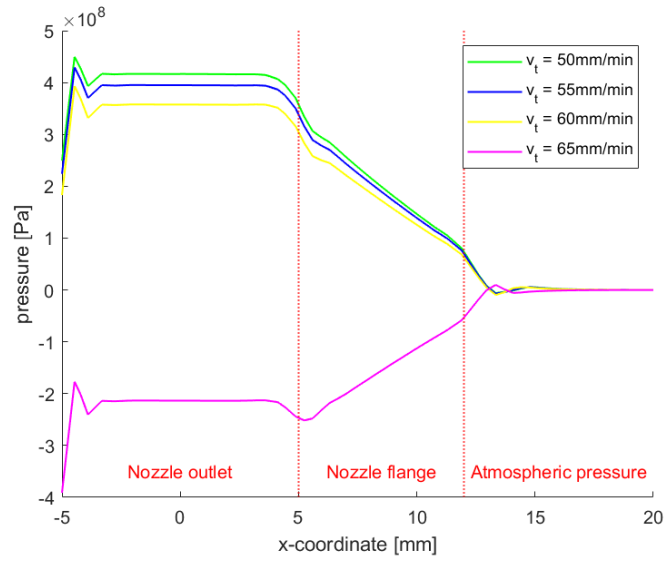


Figure 4.16: Pressure plotted against the x-coordinate at the bottom of the layer for various table velocities. Parameters used are $\Omega = 400rpm$, $v_f = 0.15mm/s$, $S = 2.5mm$, $m = 33MPas$, $n = 0.11$, and $t_{tool} = 3.2mm$.

Next, a comparison between the experimentally measured extrusion forces and the extrusion force that is obtained via the 3D model has been made for a table velocity of $50mm/min$ using equation 4.17.

$$F_{ext}^{model} = r_{nozzle}^2 \pi p_{nozzle} \approx 32.7[kN] \quad (at 350^\circ C) \quad (4.17)$$

where r_{nozzle} is the radius of the nozzle and p_{nozzle} the pressure as indicated in figure 4.16 ($p_{nozzle} \approx 417 * 10^6 Pa \approx 417MPa$). The extrusion force during the experiments AM-3 ($v_t = 50mm/min$) has an average value of approximately $4kN$ (figure 3.15b) which is significantly lower than the extrusion force calculated with equation 4.17.

Differences between the practical and theoretical value might be the assumption of a steady state velocity profile in the model meaning that the flow is fully developed along the threaded tool. If not, the velocity profile changes and so does the pressure built up and is probably less than calculated now. Another explanation might be that the the substrate/previous deposited layer is assumed to have an infinite stiffness which is not the case in practice as was shown in section 3.3.3. The infinite stiffness could lead to an overestimation of the pressure, because no pressure is used to deform the substrate/previous deposited layer. Furthermore, the temperature of the material is assumed to be the temperature measured at the thermocouple (see figure 3.3 for the location) which, in fact, does underestimate the real temperature of the material. The effect of a change in temperature on the pressure will be examined next.

Assuming the material flow is sufficient, so no starvation is present, and the temperature could be controlled well, the influence of the temperature is examined on the pressure. During the experiments the average temperature ranges from $300^\circ C$ up to $400^\circ C$. The temperature is ranged from $250^\circ C$ up to $550^\circ C$ in the 3D model for a table velocity of $50mm/min$ as can be seen in figure 4.17. Increasing the temperature decreases the viscosity of the material. As a result, less pressure is required to push

the material through the nozzle and to deposit the material on top of the substrate. In other words, if the temperature can be controlled easily, for example with the rotational rate, the pressure can be decreased as well. Decreasing the pressure may be beneficial to additive manufacture smaller parts as long as the pressure in combination with the shear rate is high enough to remove the oxide layer of the previous layer. Furthermore, the influence on the pressure of the higher temperature range is smaller than for the lower temperatures as can be seen in figure 4.17. This behaviour is seen because the flow indices used in section 4.5 become similar. the viscosity is more uniform when the aluminum is liquid [46]. Assuming that the temperature of the material was $550^{\circ}C$ that corresponds to a $p_{nozzle} \approx 148 \cdot 10^6 Pa \approx 148 MPa$, resulting in an extrusion force of $F_{ext}^{model} \approx 11.6 kN$ using equation 4.17 still overestimating the actual extrusion force of $4 kN$. In order to move material downwards in the conical part the pressure has to overcome the stress to shear the material (τ_{mat}) as depicted in figure 4.1 to move the material downwards. However, the calculated extrusion force is higher than in the experiments and therefore a slip boundary condition is required to estimate the pressure correctly.

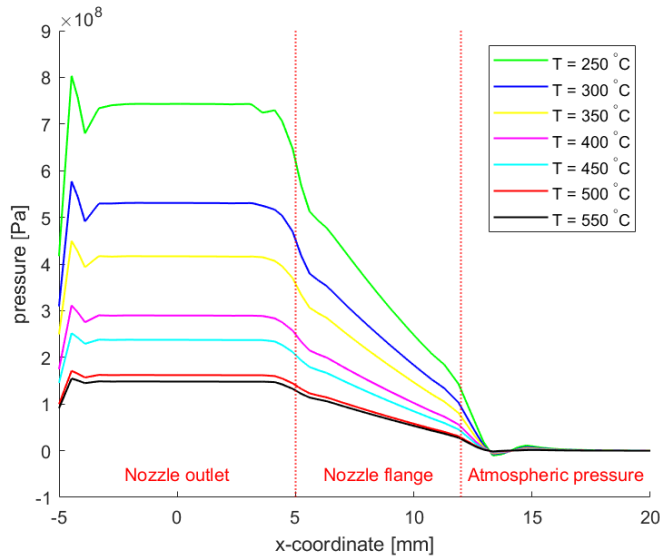


Figure 4.17: Pressure plotted against the x-coordinate for different temperatures (power-law indexes) for a table velocity of $50 mm/min$. Parameters used are $\Omega = 400 rpm$, $v_f = 0.15 mm/s$, $S = 2.5 mm$, and $t_{tool} = 3.2 mm$.

4.10 Modeling conclusions

Before answering if the the *3D additive manufacturing model* can validate if similar trends can be observed regarding the extrusion force, it can be concluded that the *axisymmetric model* produces similar results as the *3D extrusion model*. Thus, the conversion from cylindrical to the Cartesian coordinate system is valid. In addition, the magnitude of the pressure generation compared to the *axisymmetric constant viscosity model* has been decreased, resulting in better approximation of the pressure. An additional trend was observed while varying the rotation rate of the tool. The pressure generation is less depended on the rotational rate due to describing the material as a shear thinning behaviour using the power-law.

In the *3D additive manufacturing model* the trend that increasing the table velocity decreases the extrusion force (pressure) could indeed be seen. However, the extrusion force was significantly overestimated. Reasons for this behaviour might be the plastic deformation of the substrate/previous deposited layer or the underestimated temperature resulting in a higher pressure generation. However, calculating the extrusion force using a material temperature of $550^{\circ}C$ still overestimated the force (section 4.9). The cause must be a result of the stick boundary condition assumption. It is therefore recommended to study the pressure generation assuming stick/slip boundary conditions.

Discussion

The most important aspect of this study is that it is possible to bond layer upon layer using the FSEAM setup. However, several aspects are far from ideal. These aspects will be discussed and are the inconsistent material outflow, deviating behavior in the extrusion force and nozzle temperature, debonding of the first deposited layer, promising bonding conditions, and the shape of the extrusion opening.

Inconsistent material outflow

During the FSE experiments a non-constant outflow of material was observed, unlike the experiments performed by J. B. Lind [16]. The non-constant outflow of material can also be observed at the side surfaces of the printed walls in the form of a waviness pattern as can be seen in figure 3.7 and 3.11. The setup used by J.B. Lind was redesigned by W.A. Lievestro to be able to perform additive manufacturing instead of just extrusion [47]. As a result of the redesign, the hydraulic cylinder was placed under an angle of 79° instead of 79° with respect to the z -axis (as depicted in figure 3.2). In addition, a bearing was removed of the setup of J.B. Lind to be able to remove the extrusion head while the tool is still rotating (simplifying the disassembly after an experiment). These were the main aspects of the redesign of the setup and the previous setup can be seen in figure 5.1. During the experiments of J.B. Lind an extrusion opening of 5mm was used and tool gaps of 3.0 and 3.3mm were used [16]. In this study, the same extrusion opening diameter was used and comparable tool gaps of 2.5 , 3.2 and again 2.5mm were used during the FSE experiments (appendix B). In addition, the same threaded tool was used. Besides these comparable geometries, the feed position relative to the threaded tool was also changed during the FSE experiments as mentioned in section 3.2.2. The feed position was on the vertical part of the thread, conical part of the thread and a combination of vertical and conical part of the threaded tool. Each position with respect to the tool showed a non-constant outflow behavior.

Considering the aspects described above the deviating behavior of the material outflow seems to be related to the angle of the feed position or the removal of the bearing as other aspects remain fairly constant. However, these aspects do not reflect the cause of the discontinues flow yet and is not believed to be the cause.

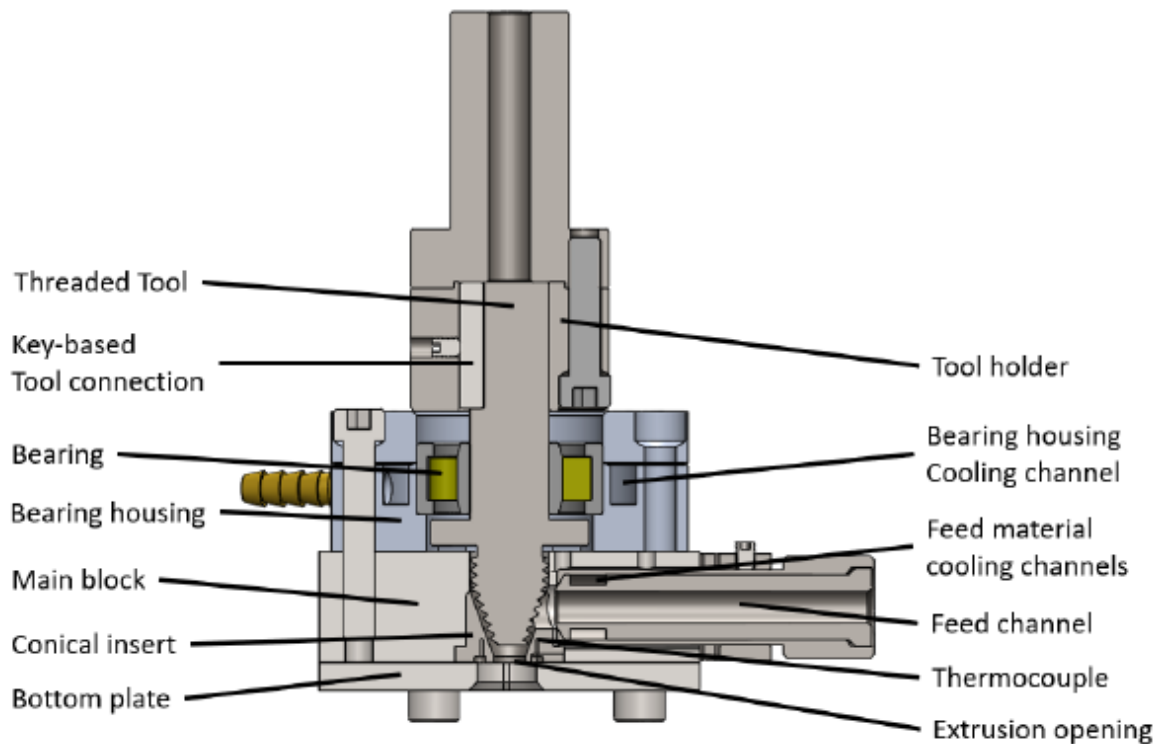


Figure 5.1: Setup used during the experiments of J.B. Lind, taken from [16].

Examining the input speed of the hydraulic cylinder this parameter seems to remain relatively constant as well (derived from the cylinder position as a function of time using figure 3.8 or 3.9). In other words, the volumetric flow rate at the inlet is constant. A possible cause might be the thread in combination with the rotational rate of the threaded tool as was seen in an alternative for the conventional extrusion of profiles, namely screw extrusion of aluminium [48], [49]. This extrusion process operates at much lower rotational rates and uses aluminium granulate of a diameter of 3mm and a length of approximately 8mm as feed material. However, a clear trend has been observed between the amount of feed material that is inserted and the extrusion rate. In addition, the angular screw position seems to have an influence on the extrusion rate. Figure 5.2 shows the extrusion rate as a function of time and each vertical lines indicates a full rotation. During these experiments different feed rates from 20% up to 80% of the maximum capacity have been used [48]. Increasing the feed rate results in an increasing extrusion rate in combination with a larger difference between the minimum and maximum extrusion rate for a given feed rate. In addition, a phase transitioning seems to take place at higher extrusion rates which will be explained later on.

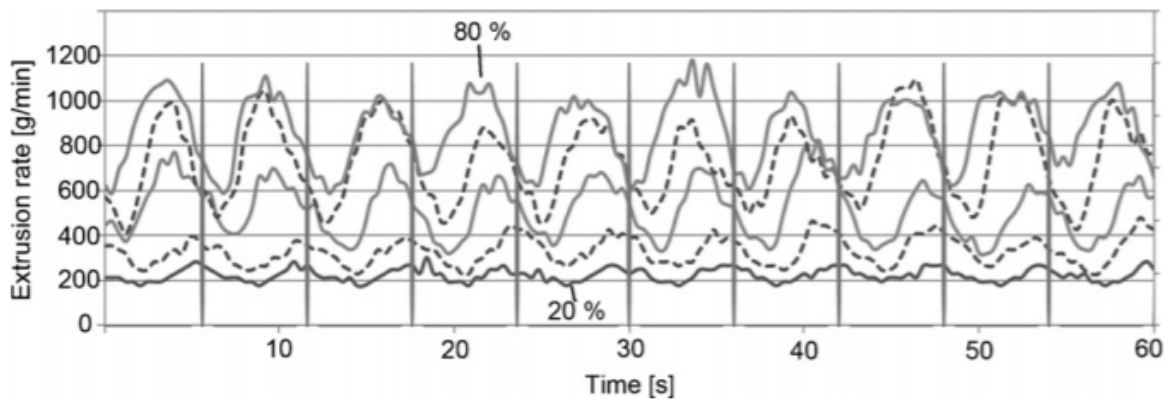


Figure 5.2: Variations of the extrusion velocity for a single flight of a screw extruder for different feed rates, taken from [48].

The difference in extrusion rate throughout a cycle is explained using figure 5.3. In the case of 5.3a the plug is not in contact with the granulate and has not enough material to make contact with the container resulting in a low pressure, thus low extrusion force. Once the plug reaches the granulate the material starts to consolidate and contact is made between the plug/granulate and the container increasing the pressure as can be seen in figure 5.3b. As a result of the increasing pressure the extrusion rate increases. At the position depicted in c the granulate is compacted and kneaded into the plug reaching its maximum pressure and thus maximum force. Excessive granulate that is not consolidated with the plug yet will merge the next cycle, however this results in a lower pressure and decreases the extrusion rate. Figure 5.2 shows a transition from the peak of the extrusion rate at the end of a rotation for a low feed rate (20% of the maximum feed rate) to a peak in the halfway of a rotation at a high feed rate (80% of the maximum feed rate). This phase transition observed in Figure 5.2 is believed to be due to the addition of more granulate at higher feed rates. As a result, the plug makes contact with the granulate in an earlier stage and starting cycle ($a - d$) earlier as well.

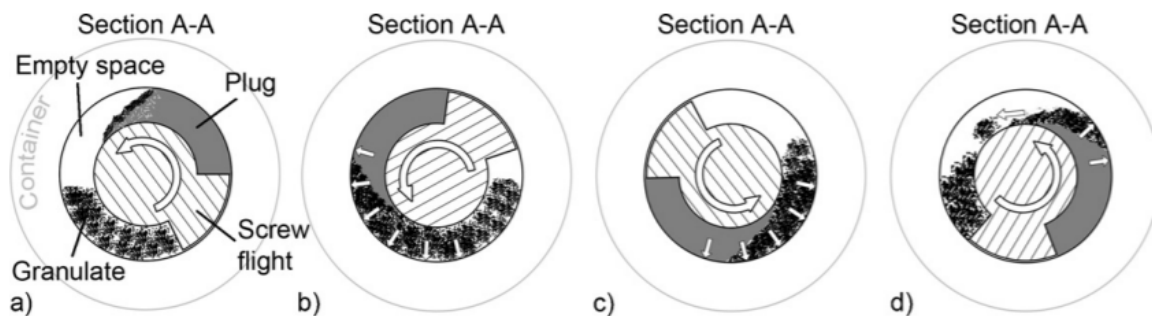


Figure 5.3: (a–d) Illustration showing an explanatory model of interaction between the plug and newly fed material. Viewed in the direction of extrusion, taken from [48].

This setup is horizontally aligned instead of vertically, like the FSEAM setup, and uses granulates instead of rods. Assuming that the conical part is only responsible for the pressure build up and that the cylindrical part is assisting the feed system of delivering material to the conical part, a transition zone can be observed from the cylindrical to the conical part encircled in black in figure

5.4a that needs to be filled completely in order to generate pressure. Occasionally, the cylindrical part is transporting sufficient material to enable the conical part to build up pressure in this part, varying the material outflow, resulting in an inconsistent flow behaviour. If feed material is supplied at a high enough flow and pressure through the feed tube, the cylindrical part is able to deliver sufficient material to the conical part as is depicted in figure 5.4b. As a result, a more consistent material flow may be observed. For example, the feed rate of AM-7 was relatively high and resulted in a smoother side surfaces as can be seen in figure 3.27. This transition zone was not part of the extrusion during the experiments of J.B. Lind as can be seen in figure 5.1 and may have resulted in the consistent material outflow.

Measuring the extrusion rate would be interesting for different locations of the feed tube with respect to the threaded tool to examine the influence of transition zone black encircled in figure 5.4a. Furthermore, measuring the extrusion rate at high feed rates to see if a constant material outflow can be observed. The extrusion velocity could be measured by attaching a trailer wheel to the extrudate.

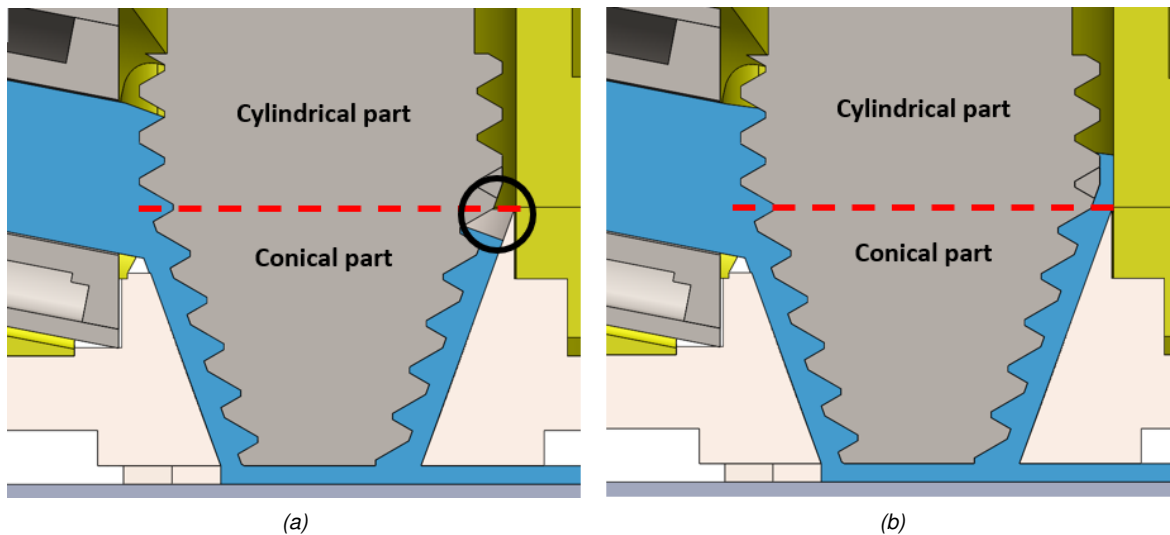


Figure 5.4:

Saw tooth pattern in extrusion force and nozzle temperature

The forward and backward motion of the table seem to have influence on the extrusion force and nozzle temperature as was seen in figures 3.13b, 3.13a, 3.15b, and 3.15a as a saw tooth like pattern. The tilt angle (shown in figure 3.1 indicated by θ) was properly set to zero during the FSEAM experiments and did not result in a fluctuation in the extrusion force. If the tilt angle would not be equal to zero and is tilted in the direction of the printing, the extrusion force would decrease and support the table by moving to the right as can be seen in figure 5.5. Moving in opposite direction the horizontal component of the extrusion force would counteract the table movement. However, the table velocity is set and controlled to remain at a certain speed and as a result the extrusion force increases in a certain direction. This could be a method to control the force exerted in vertical direction to limit/prevent the deformation of the substrate or the previous layer.

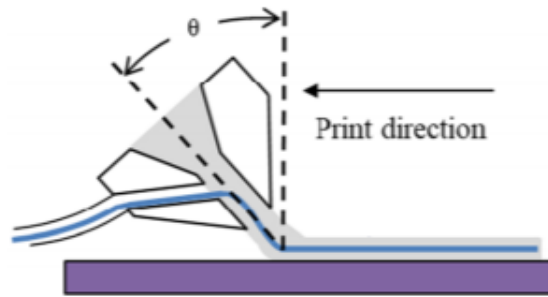


Figure 5.5: Schematic overview of a tilted nozzle, derived from [50].

The saw tooth pattern in the extrusion force can also be a result of the rigidity of the structure used for FSEAM. Figure 5.6 shows schematic images of the right side of the FSEAM setup as depicted in figure 3.1. Figure 5.6a shows a table movement in positive x -direction with a shear force (F_s) acting in the same direction on the extrusion head during aluminum printing and figure 5.6b shows table movement in opposite direction, reversing the direction of shear force. The moment introduced by the shear forces with respect to the horizontal beam deflects the the extrusion head away in the case of a negative table movement. In the case of a positive table movement this moment decreases the deflection and increases the extrusion force.

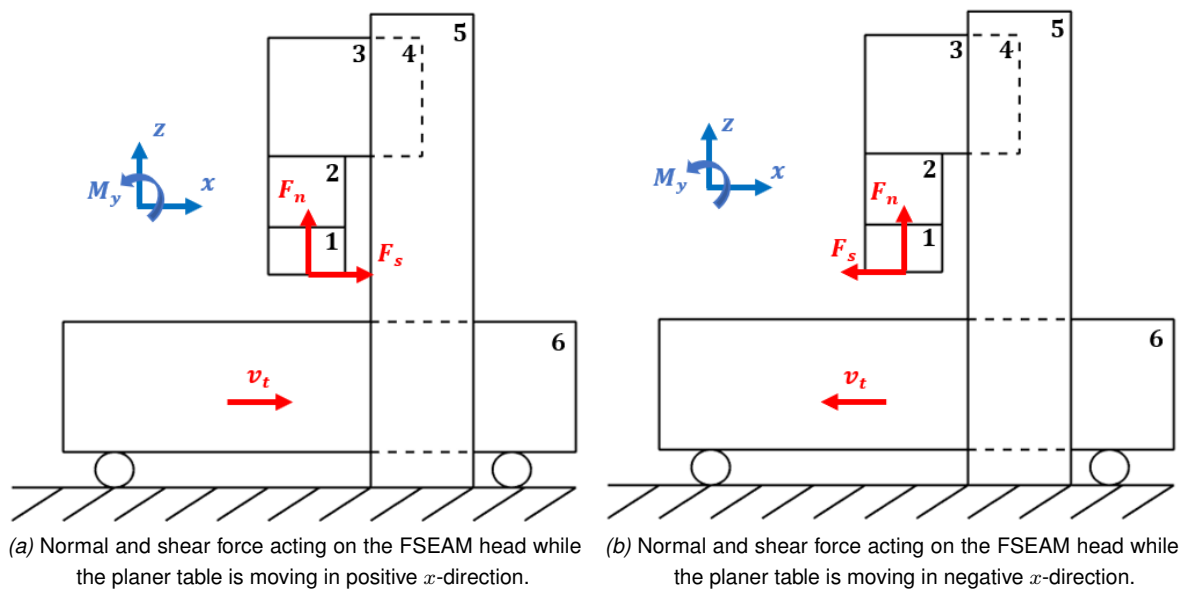


Figure 5.6: Forces acting on the FSEAM head in forward or backward table motion.

Table 5.1: Legend of the schematic images shown in figure 5.6.

Part number	Part name
1	FSEAM head
2	Intermediate part
3	Electrical motor
4	Horizontal beam planer machine
5	Vertical Beam planer machine
6	Planer table

The table movement of AM-3 is in negative direction and the average extrusion force is lower than the second layer as is shown in figure 3.15b. In addition, experiment AM-4, AM-5, and AM-6 started with a higher average extrusion force and the planer table movement was also in positive direction, indicating that the behaviour described above is true.

The saw tooth like pattern in the nozzle temperature is not understood, yet. The position of the thermocouple used for measuring the nozzle temperature can be seen in figure 3.3 at the center of a additive manufactured wall ($y = 0mm$ in figure 3.11). If the planer table is moving in positive x -direction, the thermocouple is above the newly deposited layer and if the planer table is moving in negative x -direction the thermocouple is above previous deposited layer. In addition, the height between the previous layer is $1mm$ higher than the newly deposited layer. These factors influence the thermal gradient in forward and backward motion and may result in the saw tooth like pattern in the nozzle temperature. So, the temperature of the material is not measured but a process temperature at the interface between the housing and the nozzle is measured.

Known is that a less viscous material (higher temperatures) requires less force to be deposited. This behavior is also seen for the average extrusion force and nozzle temperature graphs, respectively figure 3.15b and 3.15a, for almost every time. If the extrusion force may differ as a result of the tilt angle this could also be a possible cause for the fluctuations in temperature.

Debonding of the first deposited layer

During experiment AM-6 the deposited aluminium sheared off from the substrate due to insufficient bonding between the substrate and the first deposited layer as can be seen in figure 5.7. The extrusion force (F_{ext}), substrate temperature at starting position ($T_{substrate}$), nozzle temperature (T_{nozzle}), and table position data for the deposition of the first layer for experiment AM-3, AM-4, and AM-5 as a function of time can be found in figure 5.8. Experiment AM-3 started depositing aluminium with a layer height of $2mm$ with a table velocity of $30mm/min$. The height of the layer was gradually reduced to $1mm$ that was reached at a table position of $50mm$ ($t \approx 125s$). The table velocity remained unchanged. Experiment AM-4 did not start directly above the thermocouple in the substrate and therefore a peak in the substrate temperature was observed at $t \approx 60s$. During this experiments the layer height was kept at $1.1mm$ with a table velocity of $55mm/min$. The data from experiment AM-5 is omitted since the measurement started from the second deposited layer. The final experiment, AM-6, deposited the first layer with a height of $1.5mm$ and started with table velocity of $40mm/min$ that was decreased to a velocity of $35mm/min$ after approximately 10 seconds. During all FSEAM experiments the regulator for volumetric supply rate was put on the same level. However, the volumetric supply rate measured for the deposition of the first layer of

experiment AM-3 was approximately $13\text{mm}^3/s$ and for experiments AM-4 and AM-6 the volumetric supply rate was approximately $9\text{mm}^3/s$. Indicating that it is hard to control the volumetric supply rate accurately with the manual regulator, resulting in inconsistent process parameter.

The cause of the debonding of the first deposited layer is not clear from figure 5.8. The nozzle temperature of experiment AM-6 is lower compared to the other experiments, however the substrate temperature is heated equally to experiment AM-4 and even larger than AM-3. Another possibility might be the layer height of 1.5mm that may have led to a reduction in the rotating motion of the deposited material, insufficiently removing the oxide layer. As a result, the deposited material is not able to fully bond to the substrate. In addition, contamination may be present at the surface of the substrate resulting in poor bonding.

After depositing the first few layers of experiment AM-6, the material was not attached to the substrate anymore. Continuing the deposition of aluminium resulted in a higher AM product, but also introduced a larger moment due to the shear force (depicted in figure 5.6) with respect to the substrate that peeled the deposited material even further from the substrate. Eventually, the deposited aluminium was ruptured from the substrate material. Therefore, it would be interesting to examine the peeling behavior of the deposited layers and the layer substrate deposition.

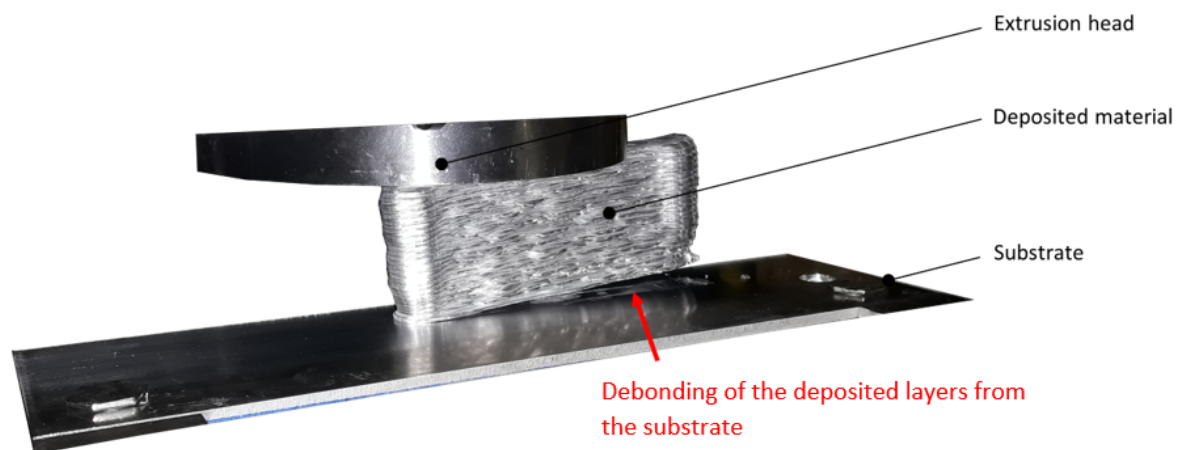


Figure 5.7: Contribution of the shear forces during the deposition of layers (experiment AM-6).

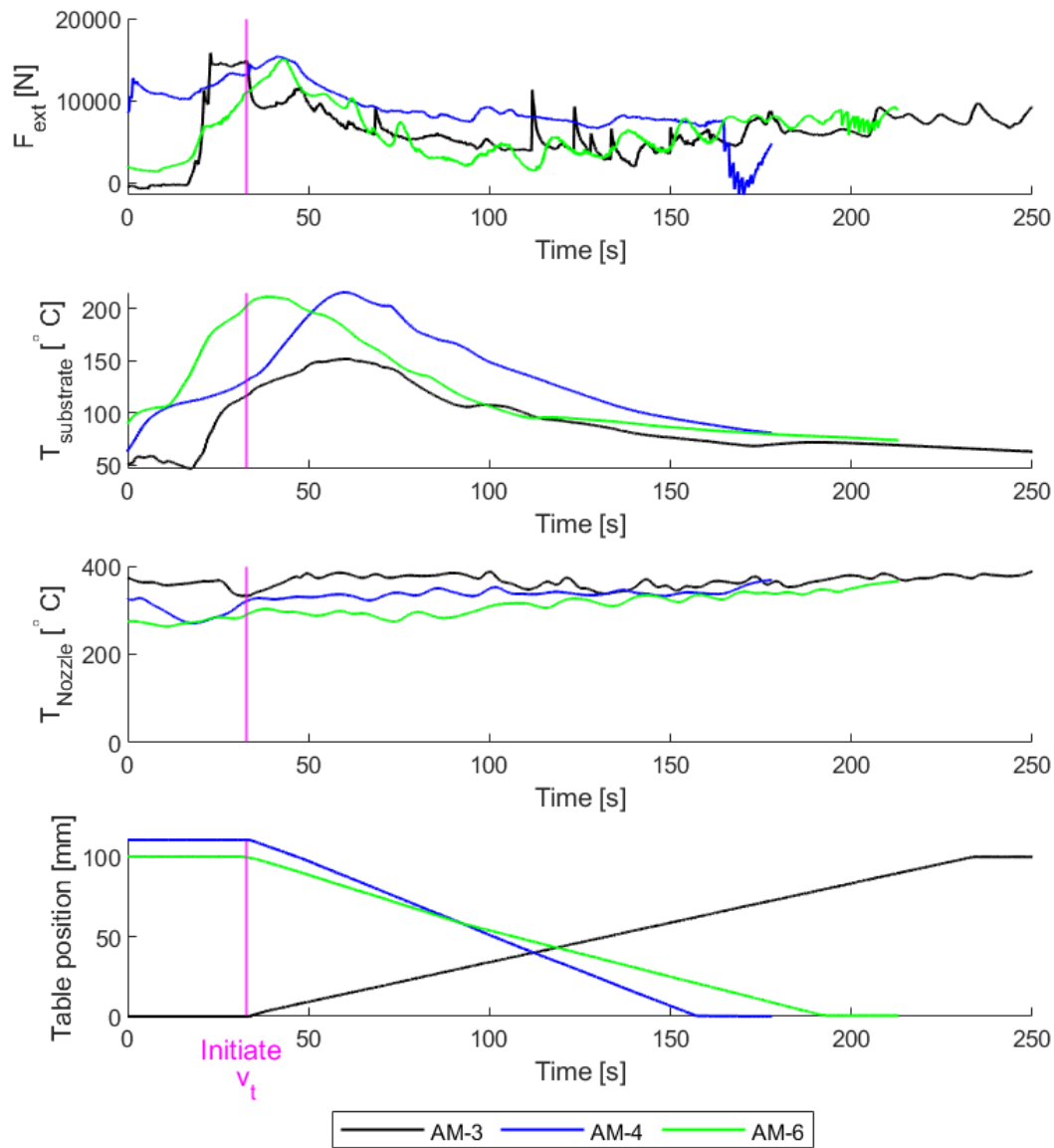


Figure 5.8: Extrusion force (F_{ext}), substrate temperature at starting position ($T_{substrate}$), nozzle temperature (T_{nozzle}), and table position plotted against time for experiment AM-3, AM-4, and AM-5 (respectively a table velocity of 50, 55, and 65 mm/min).

Promising bonding conditions

The best bonding conditions in terms of the microstructure and mechanical properties are obtained from experiment AM-3 and AM-4. In order to enable this bonding a degree of overfeeding of 1.26-1.14 was required (respectively $v_t = 50 \text{ mm/min}$ and $v_t = 55 \text{ mm/min}$). So, important is that sufficient material is supplied to enable bonding. The overfeeding in combination with the nozzle temperature led to an extrusion force of approximately 4 kN (see figure 3.15). The microscopic

images of AM-3 and AM-4 showed no sign of insufficient bonding in the form of porosities see figures 3.16a and 3.16b, unlike the work of HYB (see figure 2.11b).

The strength of the AA6060 T6 material decreased using FSEAM as a result of overaging the precipitates or dissolving the precipitates. Shown by MELD (see section 2.4) was that an increase in strain rate should result in smaller grains if the temperature is not too high. Otherwise, the precipitates dissolve and negatively influencing the grain refinement. In this study the precipitation size is not clear and therefore it would be recommended to examine the size of the precipitates. If the precipitates would have grown overaging would decrease the strength and the precipitates would assist the grain refinement as shown in figure 2.9. However, figure 3.24e and 3.26a does not show signs of oversized precipitates, indicating that the precipitates should have been dissolved. If this is the case, the refinement of the grains would be improved using the threaded tool (FSEAM setup) compared to MELD.

So, the FSEAM setup seem to have better microscopic results than HYB. Examining the setup of MELD (figure 2.8) the outer parts are rotating in contrast to FSEAM, where a threaded tool is rotating in the center (figure 3.3). Because of this, the FSEAM setup can be relative easily modified to add additional cooling elements to get a better control of the process parameters.

Extrusion opening shape

During FSEAM an hollow cylindrical cross-section is extruded upon a substrate/previous layer as can be seen in figure 5.9. The cross-section is divided into stripes with a width of 1.05mm up to the middle and in the table next to it the area of such a section can be found. In addition, the area that is left blank can also be found in this figure. Assuming a constant material outflow from the extrusion opening more material is deposited near the sides of the nozzle than in the center if the table is moving in forward/backward direction. As a result, the theoretical table velocity differs per stripe and may result in different bonding qualities throughout the width of the layer. However, this was not studied in this research because all the samples were taken from the center of the width ($y = 0\text{mm}$ in figure 3.11). This may be interesting for further research to see if the extrusion opening shape has an influence on the bond quality.

Comparing the extrusion force obtained during the experiments with the pressure profile of the *3D additive manufacturing model*, the pressure decreases while the table velocity increases, such as experiment AM-2 (figure 3.13b). This trend was less obvious for experiments AM-3 up to AM-6 while plotting the average extrusion forces as was seen in figure 3.15b. In this figure, the extrusion force dropped significantly comparing the table velocity of $55\text{mm}/\text{min}$ to $60\text{mm}/\text{min}$. The extrusion force seemed to stay relatively constant for a table velocity of $60\text{mm}/\text{min}$ or higher in figure 3.15b. A possible reason for the relative constant extrusion force might be that the generated pressure forces material towards the center of the hollow cylinder as depicted in figure 5.9 instead of creating a force in z -direction, the extrusion force.

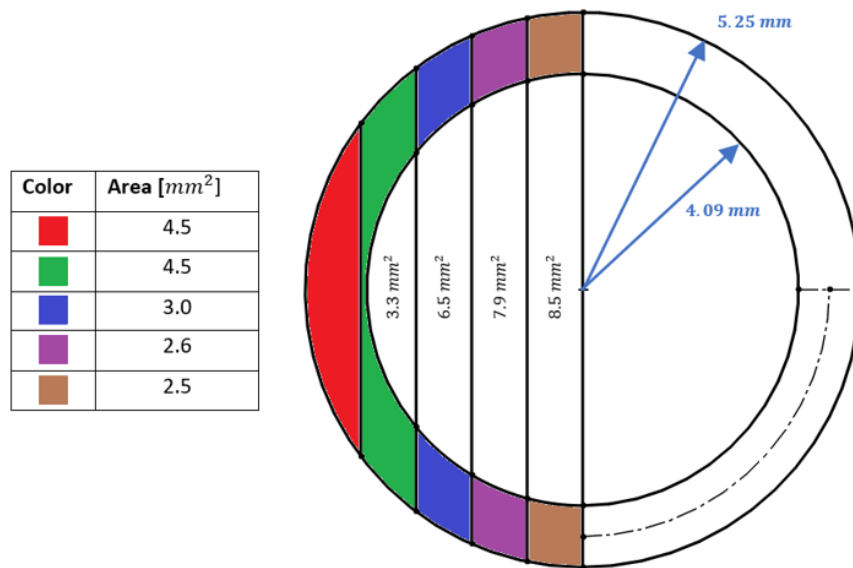


Figure 5.9: Nozzle outlet divided into strips with a width of 1.05mm to determine areas.

Conclusions and recommendations

6.1 Conclusions

During this research, a FSEAM setup was used to print aluminium layers of AA6060 T6 in solid-state on top of each other. In order to do so, aluminium rods were semi-continuous pushed through a feed chamber against a rotating threaded tool which generated heat due to friction and severe plastic deformation. During this process, the aluminium is able to flow towards the nozzle opening by the built up pressure from the threaded tool and is able to extrude the aluminium. In addition, dispersion of the aluminium oxide layer takes place. The extruded material is deposited on top of a substrate/previous deposited layer and removes the aluminium oxide layer by the extrusion force and relative motion between the extruded material and substrate/previous deposited material. The removal of the aluminium oxide layers enables metal on metal bonding. In addition, the extrusion force ensures proper spacing between atoms to bond and the elevated temperatures increase the diffusion rates. The main research question to be answered is:

How can the process parameter (table velocity) be related to the microstructure and mechanical properties of Friction Stir Extrusion Additive Manufactured aluminium AA6060 T6?

In order to be able to produce proper bonds, sufficient material supply is required to deposit solid layers. Experiments conducted with a table velocity of 50 and 55mm/min (respectively AM-3 and AM-4) with a constant rotation rate of the tool, constant tool gap, and a constant volumetric supply rate of feed material showed clear signs of overfeeding by the generated extrusion force ($\approx 4kN$). The overfed specimen did not show any signs of porosities in the microscopic images, only widening of the predefined layer width. The microscopic images of experiment with a table velocity of 60mm/min (AM-5) that suffered almost from starvation and experiment with a table velocity of 65mm/min (AM-6) that suffered from starvation also looked promising. However, cracks were visible on the tensile test specimen of experiment AM-6 by eye (figure 3.19).

The yield strength and ultimate tensile strength of the overfed experiments, AM-3 and AM-4, was approximately 60 and 100MPa, respectively. Half the strength of the original aluminium AA6060 T6. This decrease in strength was not cause by the grain size, because the grains decreased in size after FSEAM that in fact increases the strength. However, precipitates were dissolved or overaged (which has not been determined, yet) decreasing the strength of the material. The yield strength and ultimate

tensile strength of experiment AM-5 was approximately 60 and 85MPa showing a slight decrease in ultimate tensile strength most likely to cracks as a result of near starvation. Experiment AM-6 has relatively low mechanical properties due to the visible cracks by eye. The fracture surfaces of the tensile tests of AM-3 and AM-4 showed strong plastic deformation and dimple formation (indicating high resistance to failure), resulting in a proper formed bond. Experiment AM-5 plastic deformation and dimple formation to a lesser extent and experiment AM-6 showed no sign of plastic deformation at all. So, proper bonding was achieved using a table velocity of 50 and 55mm/min using a degree of overfeeding of 1.26 – 1.14, respectively.

6.2 Recommendations

Based on the experiments and studying of the results, additional recommendations can be made for future work. Also, recommendation with respect to modeling will be given.

The decrease in strength of printed AA6060 T6 is due to precipitation growth or dissolution which is not clear, yet. Therefore, the precipitation size of the performed experiments should be determined to examine the cause. If the precipitates are larger than before, an alternative feed material with smaller precipitates should be chosen, for example AA6060 T4, for an increased strength after deposition. If the precipitates are smaller than before, the precipitates were dissolved. A possible solution might be to decrease the temperature during the process or to select a material that is less dependent on temperature.

During the experimental part, tensile test were conducted in height direction at $y = 0mm$ as depicted in figure 3.11. However, less material is deposited at the center compared to the side of the layer as can be seen in figure 5.9. Therefore, it would be interesting to see if material properties differ at locations where $y \neq 0mm$.

Section 4.9 showed an overestimation of the pressure generation by the *3D additive manufacturing model* compared to the experimental results. Also when assuming a higher material temperature than seen in the experiments. As a result, the pressure generation by the threaded tool is overestimated. Therefore, the slip/stick conditions at the inner and outer wall need to be studied in greater detail to estimate the pressure generation correctly.

During the FSEAM experiments (chapter 3), many actions have to be performed manually, such as refilling the feed chamber, set volumetric flow regulator correctly, increasing the height of the extrusion head, and reverse the printing direction introducing disturbances in the nozzle temperature and extrusion force. These disturbances affect the quality of the bond and are unwanted. Therefore, it is recommended to modify the setup with a continuous feed system and using actuators to computer control the movement in x -, y -, and z -direction.

The FSEAM setup uses a container of approximately 200l as coolant that heats up during the process and cold water needs to be added periodically to prevent cooling water to become too hot. This container could be actively cooled to prevent the coolant from heating up too much. An additional remark for the setup is that a plateau that carries all the components for the hydraulic cylinder stands on the planer table that moves. As a result, the table is not free to move due to the

hoses that are connected to the hydraulic cylinder. A solution might be to attach the plateau to the horizontal beam as depicted in figure 3.1, so it does not have to move in any direction anymore.

The final recommendation is with respect to the performed FSE experiments that were conducted to determine the feed position with respect to the threaded tool (see section 3.2.2). The extruded rods could be further analyzed with the measured data found in appendix B.

Bibliography

- [1] "What is additive manufacturing?" [Online]. Available: <https://www.ge.com/additive/additive-manufacturing#:~:text=Additive%20manufacturing%20uses%20data%20computer,material%20to%20create%20an%20object>.
- [2] "Additive manufacturing materials: Metals, plastics amp; glass," Sep 2020. [Online]. Available: <https://www.spilasers.com/application-additive-manufacturing/additive-manufacturing-materials>
- [3] N. Tuncer and A. Bose, "Solid-state metal additive manufacturing: A review," *JOM*, pp. 1–22, 2020.
- [4] F. Khodabakhshi and A. Gerlich, "Potentials and strategies of solid-state additive friction-stir manufacturing technology: A critical review," *Journal of Manufacturing Processes*, vol. 36, pp. 77–92, 2018.
- [5] B. E. Carroll, T. A. Palmer, and A. M. Beese, "Anisotropic tensile behavior of ti-6al-4v components fabricated with directed energy deposition additive manufacturing," *Acta Materialia*, vol. 87, pp. 309–320, 2015.
- [6] Z. Wang, T. A. Palmer, and A. M. Beese, "Effect of processing parameters on microstructure and tensile properties of austenitic stainless steel 304l made by directed energy deposition additive manufacturing," *Acta Materialia*, vol. 110, pp. 226–235, 2016.
- [7] "Intro to metal 3d printing processes - powder bed fusion (dmls, sls, slm, lmf, dmp, ebm) - 3deo - metal additive manufacturing," Aug 2020. [Online]. Available: <https://www.3deo.co/manufacturing/intro-to-metal-3d-printing-processes-powder-bed-fusion-dmls-sls-slm-lmf-dmp-ebm/>
- [8] S. Sing, C. Tey, J. Tan, S. Huang, and W. Y. Yeong, "3d printing of metals in rapid prototyping of biomaterials: Techniques in additive manufacturing," in *Rapid Prototyping of Biomaterials*. Elsevier, 2020, pp. 17–40.
- [9] M. Holzer, K. Hofmann, V. Mann, F. Hugger, S. Roth, and M. Schmidt, "Change of hot cracking susceptibility in welding of high strength aluminum alloy aa 7075," *Physics Procedia*, vol. 83, pp. 463–471, 2016.
- [10] P. Kah, E. Hiltunen, and J. Martikainen, "Investigation of hot cracking in the welding of aluminium alloys (6005 & 6082)," in *Proceedings of the International Conference on Advances in Welding Science & Technology for Construction, Energy & Transportation*, 2010, pp. 373–380.

- [11] H. Z. Yu and R. S. Mishra, "Additive friction stir deposition: a deformation processing route to metal additive manufacturing," *Materials Research Letters*, vol. 9, no. 2, pp. 71–83, 2021.
- [12] S. Pathak and G. C. Saha, "Development of sustainable cold spray coatings and 3d additive manufacturing components for repair/manufacturing applications: A critical review," *Coatings*, vol. 7, no. 8, p. 122, 2017.
- [13] A. K. Singh, G. M. Reddy, and K. S. Rao, "Pitting corrosion resistance and bond strength of stainless steel overlay by friction surfacing on high strength low alloy steel," *Defence Technology*, vol. 11, no. 3, pp. 299–307, 2015.
- [14] S. Liu, "Friction surface cladding of aa1050 onto aa2024: parameter study and process window development," Ph.D. dissertation, University of Twente, Dec. 2016.
- [15] H.-J. Smit, "Friction screw extrusion: Towards solid state additive manufacturing of high-strength aluminium alloys," University of Twente, Tech. Rep., 2020.
- [16] J. B. Lind, "Towards continuous solid state additive manufacturing of aluminium alloys," 2018.
- [17] W. D. Callister and D. G. Rethwisch, *Materials science and engineering*. John Wiley & sons NY, 2011, vol. 5.
- [18] W. F. Smith, J. Hashemi, and F. Presuel-Moreno, *Foundations of materials science and engineering*. Mcgraw-Hill Publishing, 2006.
- [19] *Technical datasheet - Extruded products Alloy EN AW-6060 [AlMgSi]*, Hydro, 2019. [Online]. Available: <https://www.hydro.com/Document/Index?name=Hydro%20EN%20AW%206060.PDF&id=7822>
- [20] S. M. C. van Bohemen and H. K. D. H. Bhadeshia, "Ductile fracture." [Online]. Available: <http://www.phase-trans.msm.cam.ac.uk/2008/weld/weld.html>
- [21] A. den Bakker, R. Werkhoven, W. Sillekens, and L. Katgerman, *An integrated approach for predictive control of extrusion weld seams: experimental support*. IOS Press, 2010.
- [22] G. Hütter and L. Zybelle, *Recent Trends in Fracture and Damage Mechanics*. Springer, 2016.
- [23] M. Azarbarmas, S. S. Mirjavadi, A. Ghasemi, and A. M. Hamouda, "A combined method to model dynamic recrystallization based on cellular automaton and a phenomenological (cap) approach," *Metals*, vol. 8, no. 11, p. 923, 2018.
- [24] R. J. Griffiths, M. E. Perry, J. M. Sietins, Y. Zhu, N. Hardwick, C. D. Cox, H. A. Rauch, and Z. Y. Hang, "A perspective on solid-state additive manufacturing of aluminum matrix composites using meld," *Journal of Materials Engineering and Performance*, vol. 28, no. 2, pp. 648–656, 2019.
- [25] M. manufacturing. Materials of your choice. [Online]. Available: <http://meldmanufacturing.com/materials-of-your-choice/>
- [26]

- [27] O. Rivera, P. Allison, L. Brewer, O. Rodriguez, J. Jordon, T. Liu, W. Whittington, R. Martens, Z. McClelland, C. Mason *et al.*, "Influence of texture and grain refinement on the mechanical behavior of aa2219 fabricated by high shear solid state material deposition," *Materials Science and Engineering: A*, vol. 724, pp. 547–558, 2018.
- [28] MakeItFrom. 2219-t851 aluminum. [Online]. Available: <https://www.makeitfrom.com/material-properties/2219-T851-Aluminum>
- [29] R. J. Griffiths, D. Garcia, J. Song, V. K. Vasudevan, M. A. Steiner, W. Cai, and Z. Y. Hang, "Solid-state additive manufacturing of aluminum and copper using additive friction stir deposition: Process-microstructure linkages," *Materialia*, vol. 15, p. 100967, 2021.
- [30] J. Blindheim, Ø. Grong, U. R. Aakenes, T. Welo, and M. Steinert, "Hybrid metal extrusion & bonding (hyb)-a new technology for solid-state additive manufacturing of aluminium components," *Procedia Manufacturing*, vol. 26, pp. 782–789, 2018.
- [31] J. Blindheim, T. Welo, and M. Steinert, "First demonstration of a new additive manufacturing process based on metal extrusion and solid-state bonding," *The International Journal of Advanced Manufacturing Technology*, vol. 105, no. 5-6, pp. 2523–2530, 2019.
- [32] J. Blindheim, Ø. Grong, T. Welo, and M. Steinert, "On the mechanical integrity of aa6082 3d structures deposited by hybrid metal extrusion & bonding additive manufacturing," *Journal of Materials Processing Technology*, p. 116684, 2020.
- [33] Y. Kok, X. P. Tan, P. Wang, M. Nai, N. H. Loh, E. Liu, and S. B. Tor, "Anisotropy and heterogeneity of microstructure and mechanical properties in metal additive manufacturing: A critical review," *Materials & Design*, vol. 139, pp. 565–586, 2018.
- [34] B. Adamczyk-Cieślak, J. Mizera, and K. J. Kurzydłowski, "Microstructures in the 6060 aluminium alloy after various severe plastic deformation treatments," *Materials Characterization*, vol. 62, no. 3, pp. 327–332, 2011.
- [35] M. Nahmany, V. Shribman, S. Levi, D. Ashkenazi, and A. Stern, "On additive manufactured alsi10mg to wrought aa6060-t6: Characterisation of optimal-and high-energy magnetic pulse welding conditions," *Metals*, vol. 10, no. 9, p. 1235, 2020.
- [36] Smiths. (2018) 2024 aluminium technical datasheet. [Online]. Available: <https://www.smithmetal.com/pdf/aluminium/2xxx/2024.pdf>
- [37] N. aluminium. (November 2017) Alloy data sheet en-aw 6060[almgsi] (type: General extrusion alloy). [Online]. Available: <https://www.nedal.com/wp-content/uploads/2017/11/Nedal-alloy-Datasheet-EN-AW-6060.pdf>
- [38] J. Maljaars, "Local buckling of slender aluminium sections exposed to fire," Ph.D. dissertation, TU Delft, Delft University of Technology, 2008.
- [39] A. Y. Book, "Tension testing of metallic materials1," *Book of ASTM standards: with related materials*, p. 201, 1967.
- [40] E. D. Schmitter, "Modelling massive forming processes with thermally coupled fluid dynamics," in *Proceedings of the COMSOL Multiphysics User's Conference*, 2005.

- [41] COMSOL. Fluid-structure interaction in aluminum extrusion. [Online]. Available: <https://www.comsol.nl/model/fluid-structure-interaction-in-aluminum-extrusion-4386>
- [42] G. Glover and C. Sellars, "Recovery and recrystallization during high temperature deformation of α -iron," *Metallurgical Transactions*, vol. 4, no. 3, pp. 765–775, 1973.
- [43] R. Kievitsbosch, "Friction surface cladding: Flow field modelling," University of Twente, Tech. Rep., 2019.
- [44] V. Vilamosa, T. Børvik, O. S. Hopperstad, and A. H. Clausen, "Behaviour and modelling of aluminium alloy aa6060 subjected to a wide range of strain rates and temperatures," in *EPJ Web of Conferences*, vol. 94. EDP Sciences, 2015, p. 04018.
- [45] Y. Prasad, K. Rao, and S. Sasidhar, *Hot working guide: a compendium of processing maps*. ASM international, 2015.
- [46] M. J. Assael, K. Kakosimos, R. M. Banish, J. Brillo, I. Egry, R. Brooks, P. N. Quested, K. C. Mills, A. Nagashima, Y. Sato *et al.*, "Reference data for the density and viscosity of liquid aluminum and liquid iron," *Journal of physical and chemical reference data*, vol. 35, no. 1, pp. 285–300, 2006.
- [47] W. A. Lievestro, "Friction screw cladding; een prototype als stap naar het continu-cladden van aluminiumlegeringen." University of Twente, Tech. Rep., 2019.
- [48] F. Widerøe and T. Welø, "Using contrast material techniques to determine metal flow in screw extrusion of aluminium," *Journal of Materials Processing Technology*, vol. 213, no. 7, pp. 1007–1018, 2013.
- [49] —, "An investigation of the material flow in a screw extruder of aluminium using contrast material," in *Key Engineering Materials*, vol. 504. Trans Tech Publ, 2012, pp. 475–480.
- [50] K. Sugiyama, R. Matsuzaki, M. Ueda, A. Todoroki, and Y. Hirano, "3d printing of composite sandwich structures using continuous carbon fiber and fiber tension," *Composites Part A: Applied Science and Manufacturing*, vol. 113, pp. 114–121, 2018.

Alloy AA2024 and AA6060 data sheets

2024 Aluminium

Technical Datasheet



High Strength Aluminium Alloy

Service. Quality. Value.

Applications

- Aircraft fuselage
- Commercial & military aircraft
- Wing tension members
- Critical Aircraft structures

Key features:

- Good fatigue resistance
- Good strength
- Excellent toughness at moderately high strength levels
- Improved fracture toughness

Product Description

Alloy 2024 is one of the more prominent aluminium alloys. Due to the alloys good fatigue resistance, especially in thick plate form, the material is specified for use in the aerospace and military sector in fuselage applications in such areas as structures and wing tension members. With improved fracture toughness and fatigue crack growth, Alloy 2024 continues to maintain strength characteristics. The alloy is available in T3, T4 and T8 tempers and in the annealed state.

Corrosion Resistance

Resistance to atmospheric attack is poor.

Machinability

Good

Availability

Sheet, plate

Chemical Composition (weight %)

Weight (%)	Al	Si	Fe	Cu	Mn	Mg	Cr	Zn	Ti	Other
min.	Bal			3.80	0.30	1.20				
max.	Bal	0.50	0.50	4.90	0.90	1.80	0.10	0.25	0.15	0.05

Mechanical Properties

Temper	Thickness (mm)	Tensile Strength ksi (MPa)	Yield Strength ksi (MPa)	Elongation %
0-Sheet & plate	0.010-0.499 (0.25-12.44)	32.0 (max) (220)	14.0 (max) (96)	12
T3-Flat Sheet	0.008-0.249 (0.203-6.32)	63-64 (434-441)	42 (289)	10-15
T351-Plate*	0.250-4.000 (6.35-101.60)	64-57 (441-393)	42-41 (289-282)	12-4
T4-Coiled Sheet	0.010-0.125 (0.254-3.16)	62 (427)	40 (276)	12-15
T81-Flat Sheet	0.010-0.249 (0.254-6.32)	67 (462)	58 (400)	5
T851-Plate	0.250-1.499 (6.35-38.07)	67-66 (462-455)	58-57 (400-393)	5

* Strength decreases as thickness increases

Technical Assistance

Our knowledgeable staff backed up by our resident team of qualified metallurgists and engineers, will be pleased to assist further on any technical topic.

www.smithmetal.com

sales@smithmetal.com

Biggleswade 01767 604604	Birmingham 0121 7284940	Bristol 0117 9712800	Chelmsford 01245 466664	Gateshead 0191 4695428	Horsham 01403 261981	Leeds 0113 3075167
London 020 72412430	Manchester 0161 7948650	Nottingham 0115 9254801	Norwich 01603 789878	Redruth 01209 315512	Verwood 01202 824347	General 0845 5273331



All information in our data sheet is based on approximate testing and is stated to the best of our knowledge and belief. It is presented apart from contractual obligations and does not constitute any guarantee of properties or of processing or application possibilities in individual cases. Our warranties and liabilities are stated exclusively in our terms of trading. © Smiths Metal Centres 2018

ALLOY DATA SHEET EN-AW 6060[AlMgSi] (Type: General extrusion alloy)

The alloy EN AW-6060 is a widely used extrusion alloy, suitable for applications where no special strength properties are required. Parts can be produced with a very good surface quality, suitable for many coating operations. Typical application fields are furniture, finishing materials, windows and doors, carbody finishing, façade construction, lighting columns and flagpoles, architecture, and food industry.

Chemical composition according to EN573-3 (weight%, remainder Al)

Si	Fe	Cu	Mn	Mg	Cr	Zn	Ti	remarks	others	
									each	total
0.30-0.6	0.10-0.30	max.0.10	max.0.10	0.35-0.6	max.0.05	max.0.15	max.0.10		max.0.05	max.0.15

Mechanical properties according to EN755-2

Temper*	Wallthickness e*** [mm]	Yield stress Rp _{0.2} [MPa]	Tensile strength Rm [MPa]	Elongation		Hardness** HB
				A [%]	A ₅₀ [%]	
T4	≤ 25	60	120	16	14	45
T5	≤ 5	120	160	8	6	55
	5 < e ≤ 25	100	140	8	6	50
T6	≤ 5	150	190	8	6	65
	5 < e ≤ 25	140	170	8	6	60
T66	≤ 5	160	215	8	6	70
	5 < e ≤ 25	150	195	8	6	65

*Temper designation according to EN515: T4-Naturally aged to a stable condition, T5-cooled from an elevated temperature forming operation and artificially aged, T6-Solution heat treated, quenched and artificially aged, T66-cooled from an elevated temperature forming operation and artificially aged to a condition with higher mechanical properties through special control of manufacturing processes. (T6/T66 properties can be achieved by press quenching)

** Hardness values are for indication only

***For different wall thicknesses within one profile, the lowest specified properties shall be considered as valid for the whole profile cross section

Physical properties (approximate values, 20°C)

Density [kg/m ³]	Melting range [°C]	Electrical Conductivity [MS/m]	Thermal Conductivity [W/m.K]	Co-efficient of thermal Expansion 10 ⁻⁶ /K	Modulus of Elasticity [GPa]
2700	585-650	28-34	200-220	23.4	~70

Weldability¹

Gas: 3 TIG: 2 MIG: 2

Typical filler materials (EN ISO18273): SG-AlMg5Cr(A) or AISi5, and AlMg3 when the product has to be anodised. Due to the heat input during welding the mechanical properties will be reduced by approximately 50% (ref. EN1999-1).

Machining characteristics¹

T4 temper: 3

T5 and T6 temper: 2

Coating properties¹

Hard protecting
anodising: 1

Decorative/bright/colour
anodising: 1

Corrosion resistance¹

General: 1 Marine: 2

¹Relative qualification ranging from 1-very good to 6 unsuitable



Data of FSE experiments

B.1 Adjustments of the setup

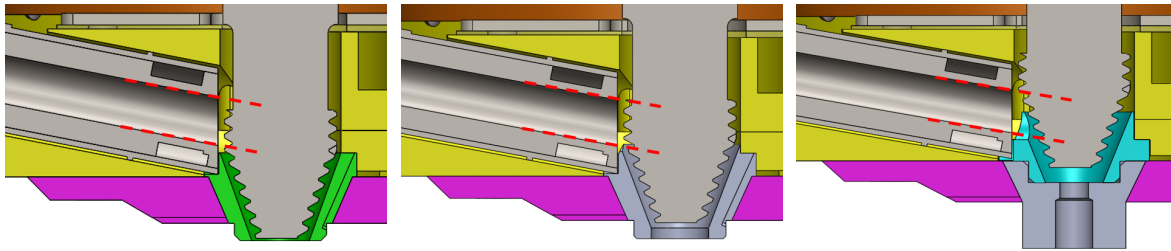
A new setup was introduced by W.A. Lievestro [47] and has been modified by H.J. Smit [15] to create a usable setup. Unfortunately, the setup is still not able to extrude material. The final recommendation by H.J. Smit is to swap the threaded tool with slots with an earlier used tool in the experiments of J.B. Lind [16] without slots as can be seen in figure B.1. As a results, the setup was able to perform continuous extrusion.



Figure B.1: Current tool on the left and the earlier used tool on the right.

A total of three extrusion experiments have been performed mainly to adjust the height of the feed tube with respect to the threaded tool to minimize the cylindrical force used to push the feed rods into the system. The first experiment, FSE-1, the rod was pushed against a vertical part without thread and a vertical part with thread as can be seen in figure B.2a. Unfortunately, the setup jammed due to insufficient cooling of the setup as a result of a kink in the cooling hose. The data has not been implemented in the appendix, however relatively high cylindrical forces were observed. As a result of those high forces, the feed tube was positioned fully on the vertical threaded part as can be seen in figure B.2b reducing the cylindrical force. In the final FSE experiment, FSE-3, the feed tube was positioned on the conical part of the threaded tool (shown in figure B.2c) resulting in the lowest

cylindrical force that was desired. An overview of the used parameters and remark can be found in table B.1.



(a) Partially on vertical threaded part. (b) Fully on vertical threaded part. (c) Partially on vertical and tapered threaded part.

Figure B.2: Feed positions of the clad material.

Table B.1: Parameters used during FSE experiments.

Experiment [type – #]	Rotational rate [rpm]	Volume flow [mm ³ /s]	Remark [–]
FSE-1	400	11-34	Jammed due to a hitch in the water hose
FSE-2	400-500-600-300-220	11-115	Using a rotation rate of 500rpm only up to a key of 6.0 is extruded. Furthermore, at 220rpm the setup jammed due to insufficient generation of heat.
FSE-3	400-500-600-300	11-115	-

To measure the temperature of the material thermocouples were placed near the nozzle as can be seen in figure B.3 indicated by TC_1 and TC_2

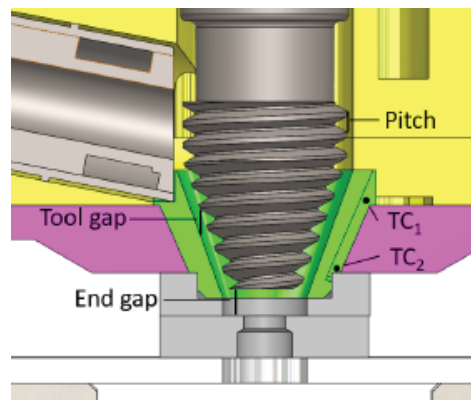


Figure B.3: Positions of the thermocouples with respect to the nozzle (green), taken from [15].

An example of how an extruded specimen looks like can be found in figure B.4. The rings present

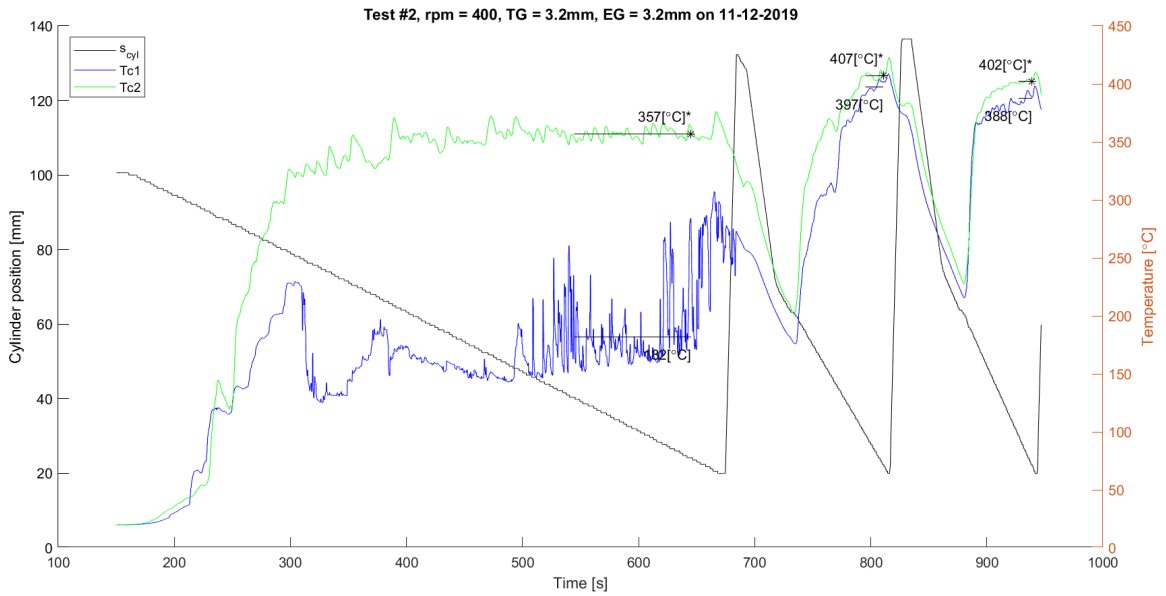
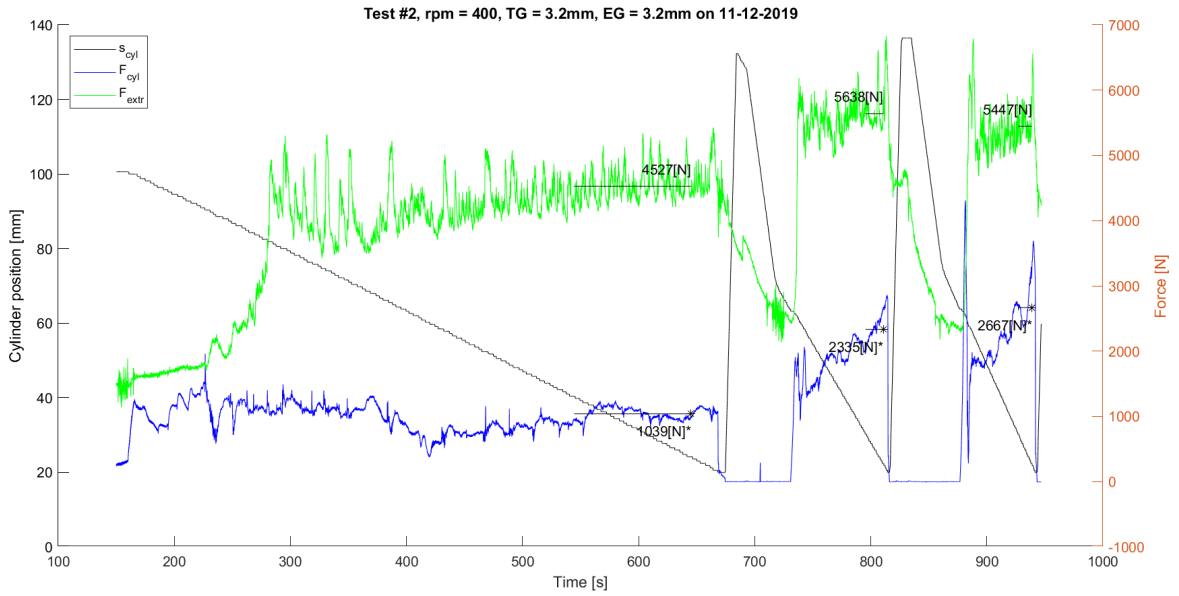
at the surface seem to be in helix form that may be the result of the rotational rate of the threaded tool. These shapes were no further analyzed. Figure B.4 also shows an indent to mark a change in rotational rate of the threaded tool. The final remark about the specimen is that it does not look straight. The curves in the specimen is the result of pulling the extruded part away from the planer table since the extrusion was performed above it.

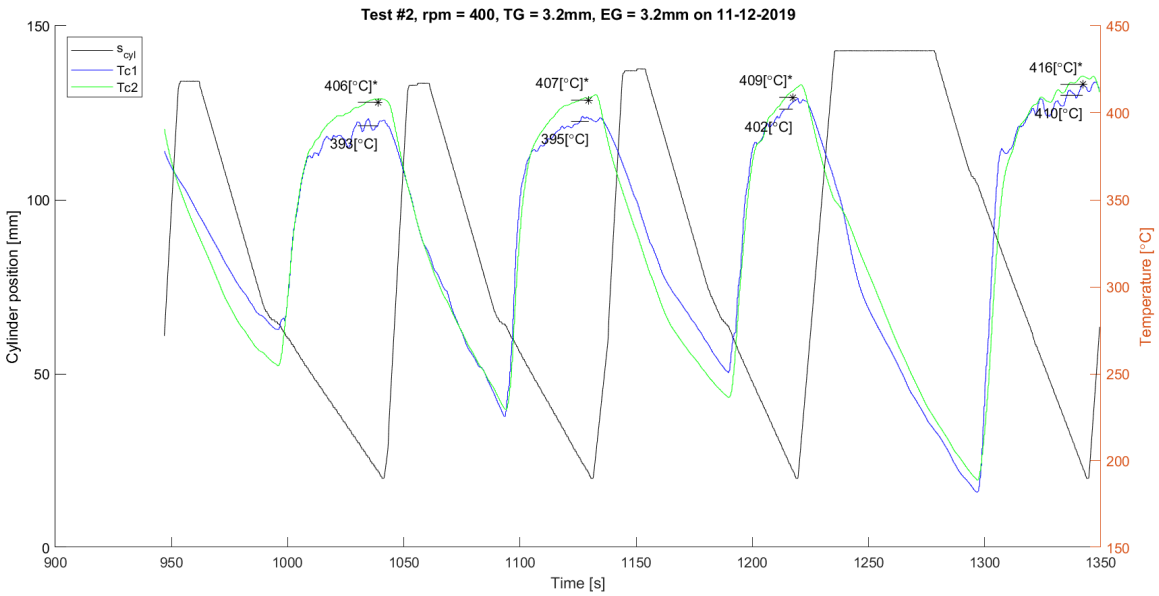
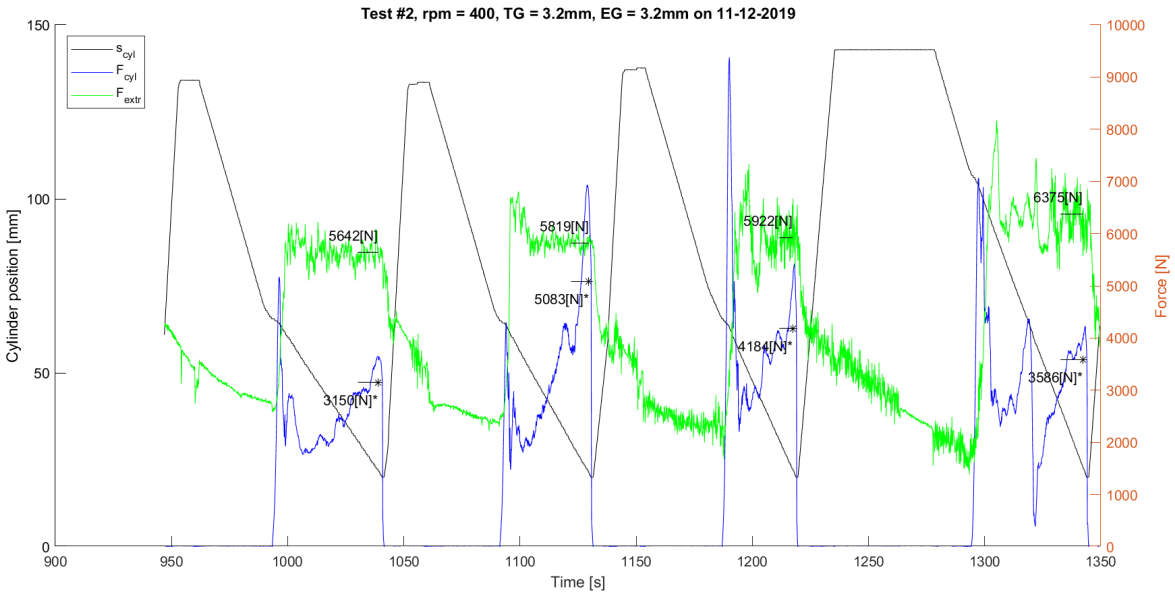


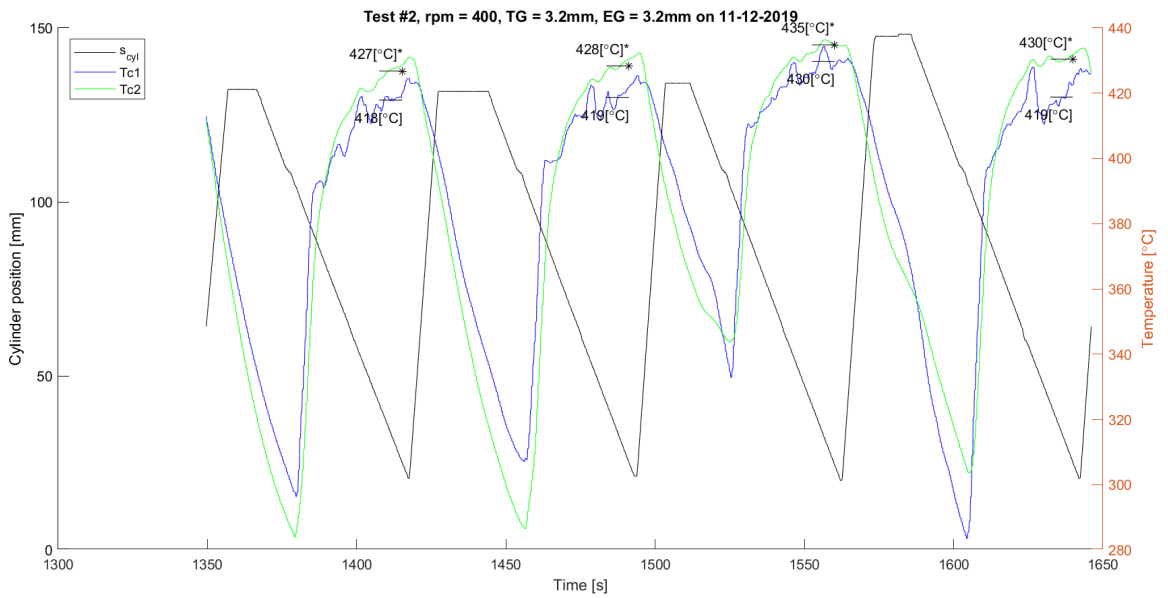
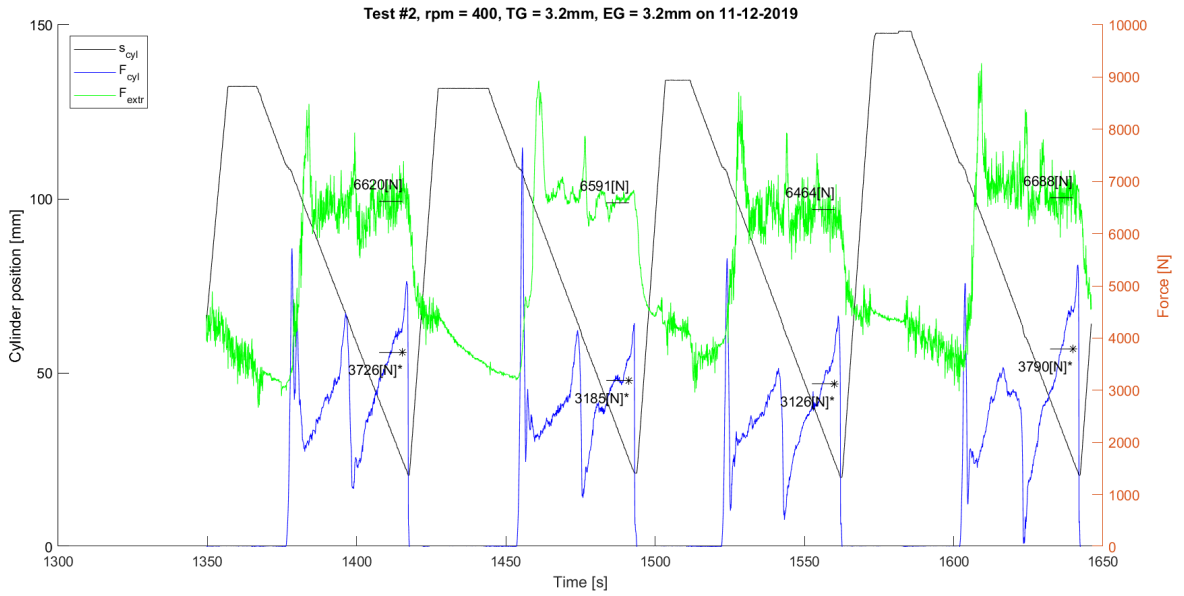
Figure B.4: Example of an extruded specimen.

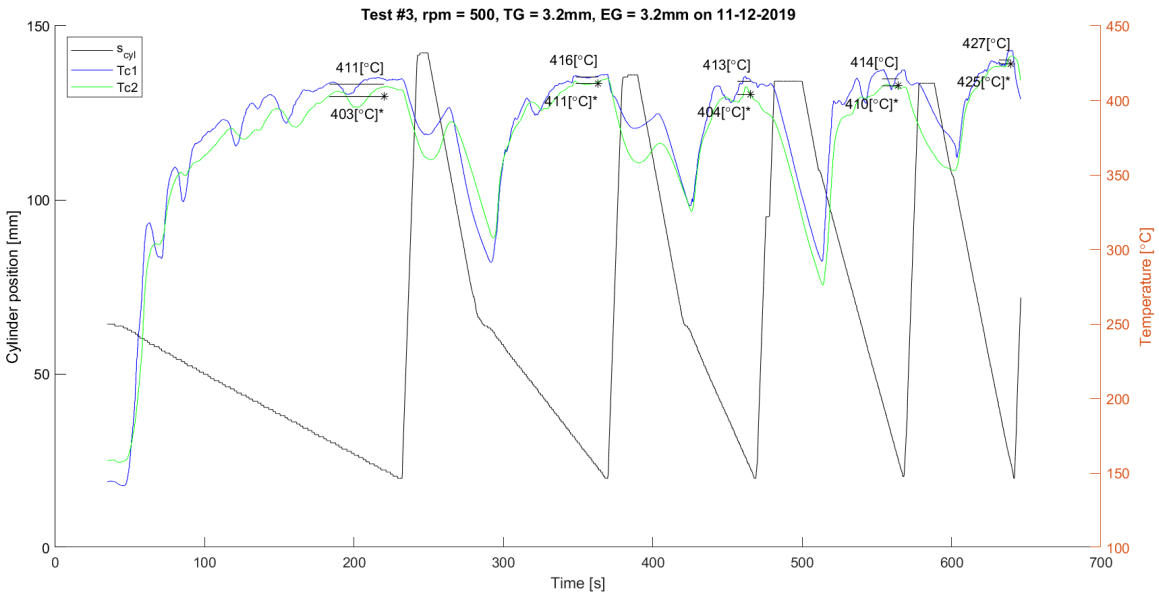
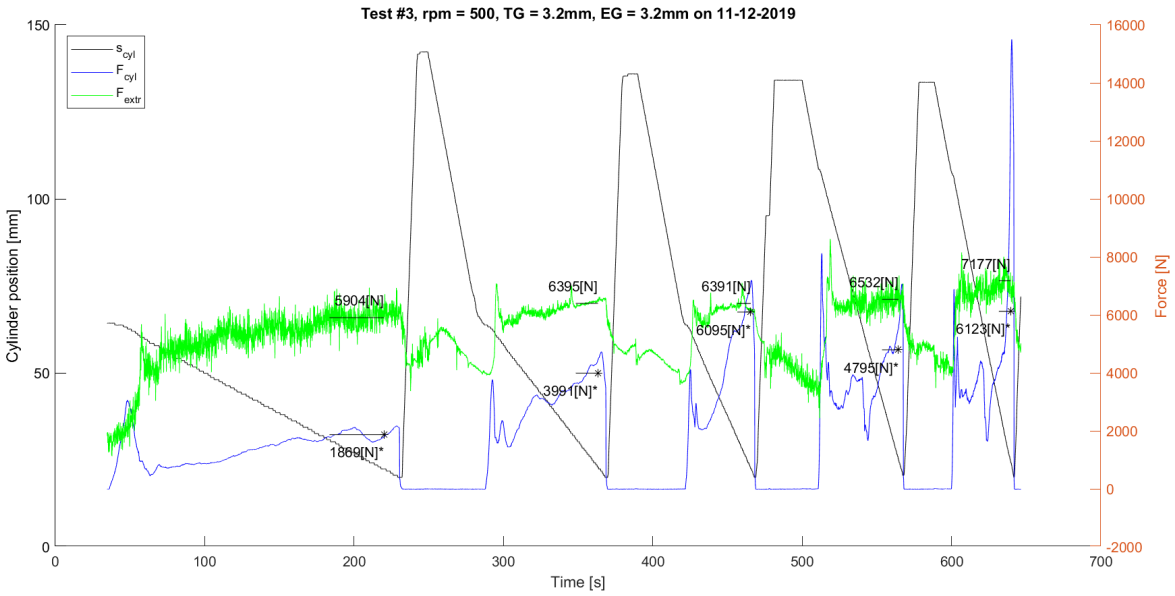
B.2 Experimental data FSE-2

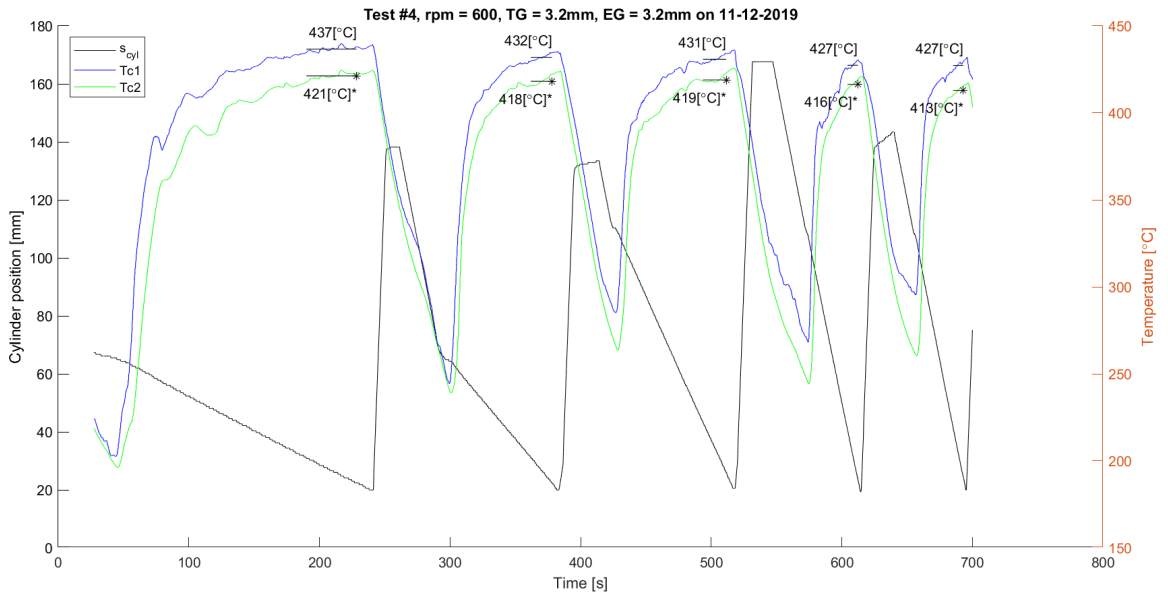
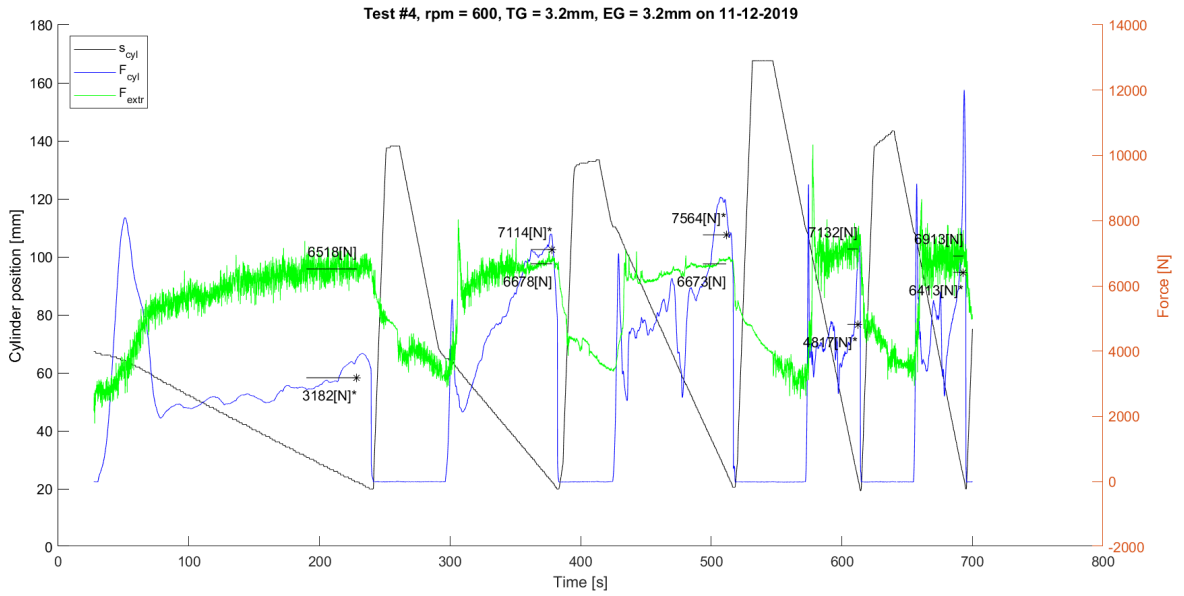
This experiment varies the rounds per minute of the tool in the following order: 400-500-600-300-200 and different volume flows were used between $11 - 115 \text{mm}^3/\text{s}$. Some data of the experiment is divided in multiple graphs to display the data clearly, for example the experiment with a rotational rate of 400rpm . For each rotational rate the table position, cylindrical and extrusion force is plotted as a function of time. In addition, the temperature in the nozzle has been measured at two places and are in combination with the table position also plotted against time for each rotational rate. Between 75 and 95% of table position average values are taken from the forces and temperature and plotted against the extrusion rate as will be seen later on. Starting with a graph of the rotational rate of 400rpm on the next page.

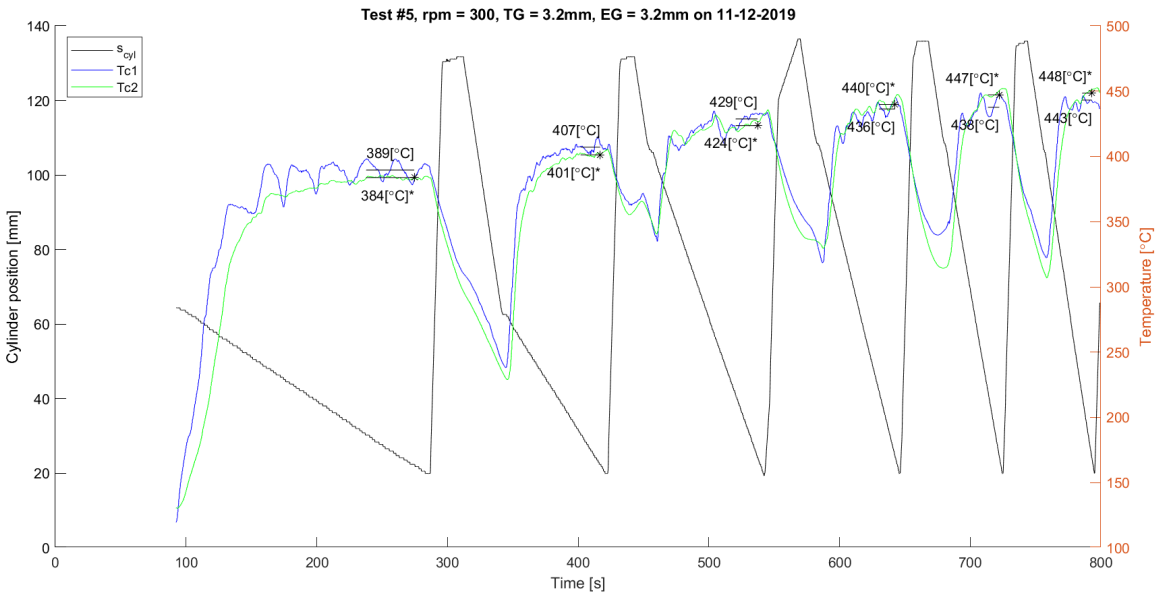
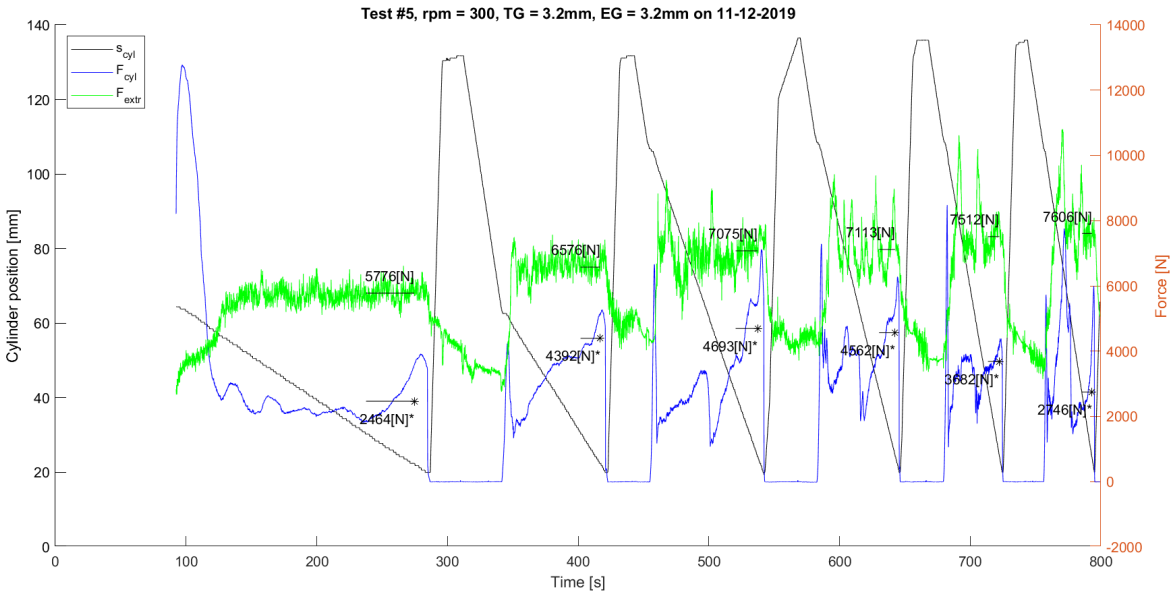


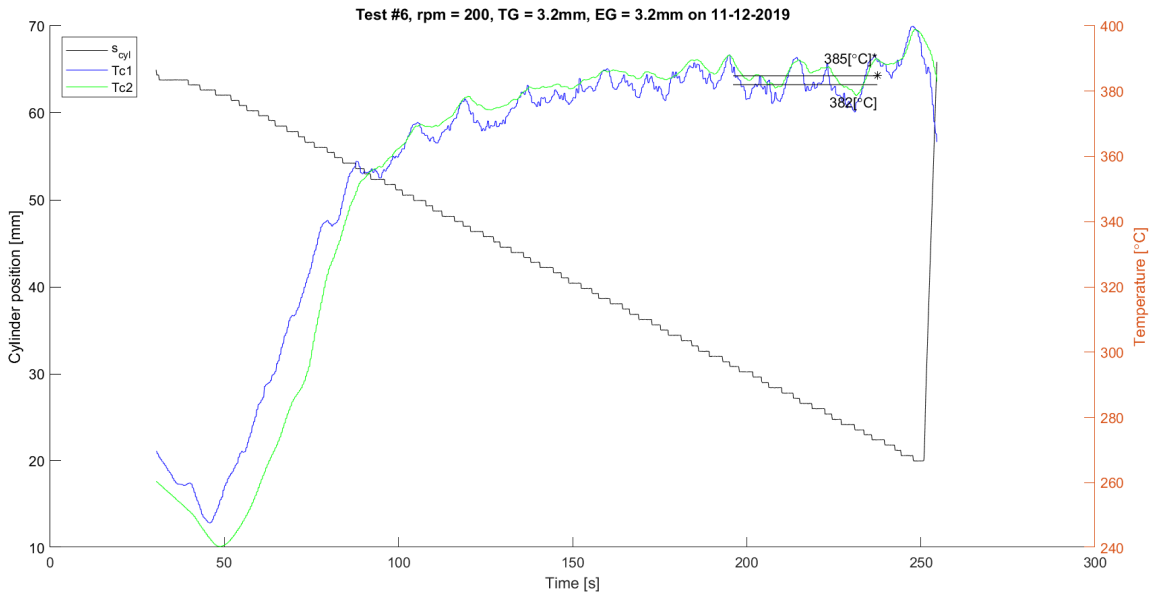
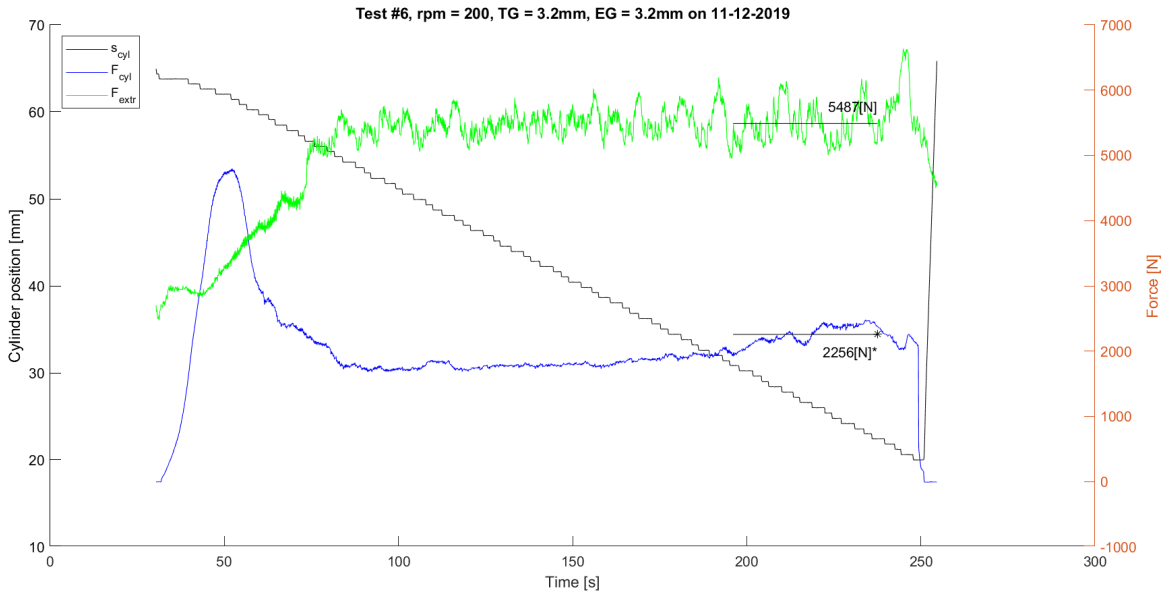




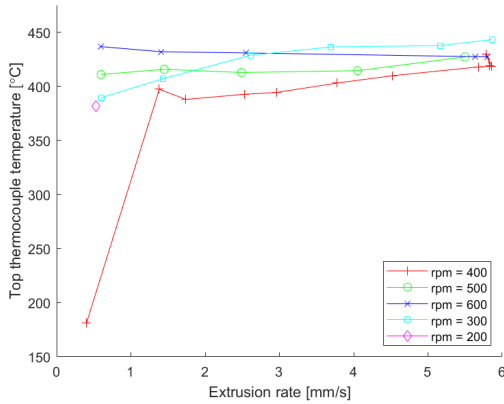




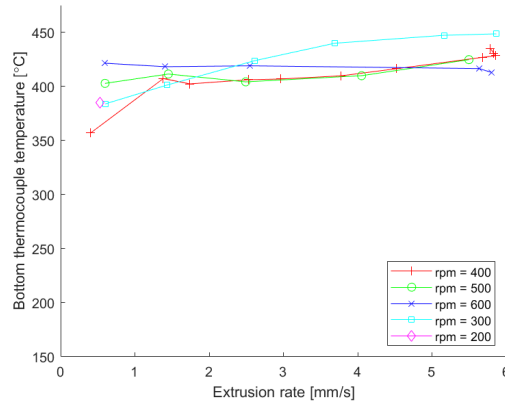




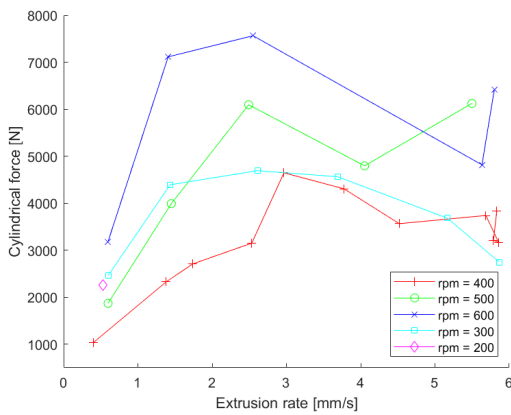
Using the average values of the figure above both the forces and temperatures are plotted against the extrusion rate. The temperature seem to increase with increasing rotational rate. However, this may not seem to be the case of a rotational rate of $300rpm$. This could also be the result of heating the setup in total. Also, increasing the volumetric flow rate (extrusion rate) seem to increase the temperature slightly. Examining the cylindrical force the overall force increases while increasing the rotational rate. In the case of a rotational rate of 300 and $400rpm$ the forces are similar. Also, a certain pattern is seen that the cylindrical force increases at an extrusion rate between $2 - 3mm/s$ then decreasing and starts to increase again. Since the data is not analyzed in detail no explanation if found for this behavior. Finally, the extrusion force increases while increasing the rotational rate, except for $300rpm$ that might also have to do with an overall heating of the setup. However, the warmer the setup (warmer material) the less viscous behavior would be expected, so a reduced extrusion force would be expected that is not the case. Therefore it would be interesting to study this behavior in more detail. Overall, the extrusion force increases while the extrusion rate increases.



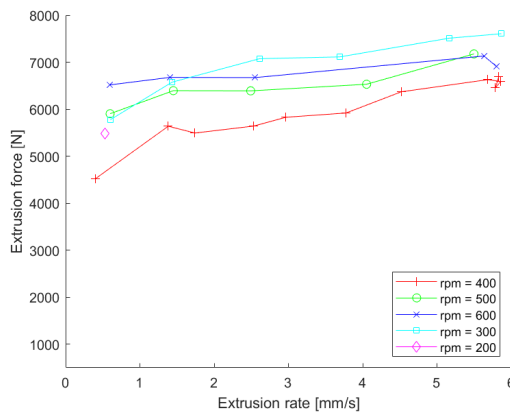
(a) Top nozzle temperature against extrusion rate.



(b) Bottom nozzle temperature against extrusion rate.



(c) Cylindrical force against extrusion rate

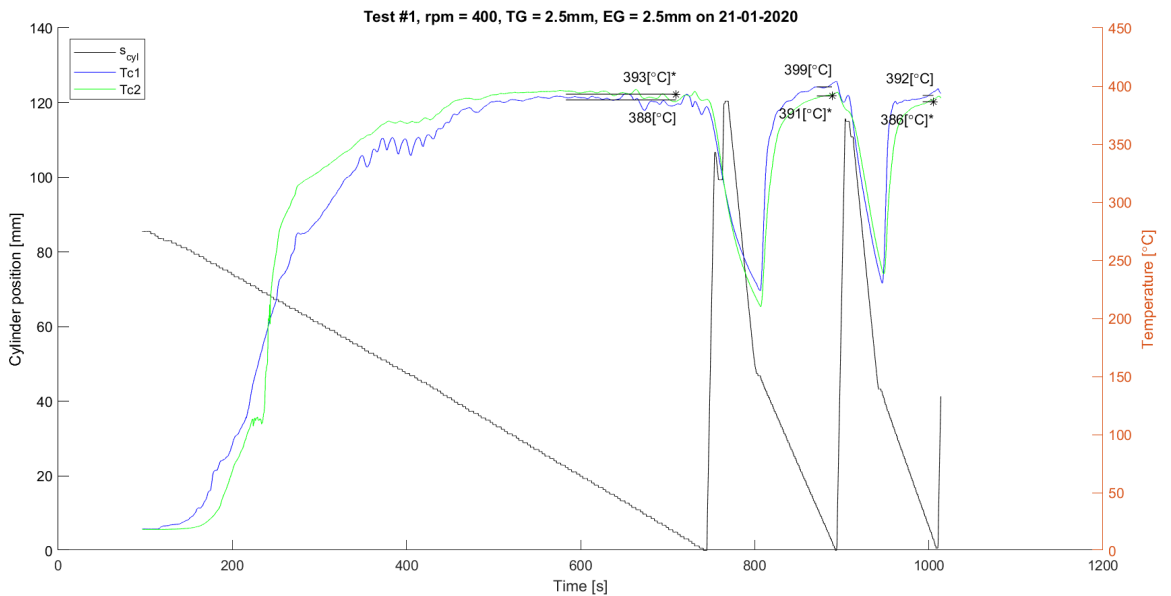
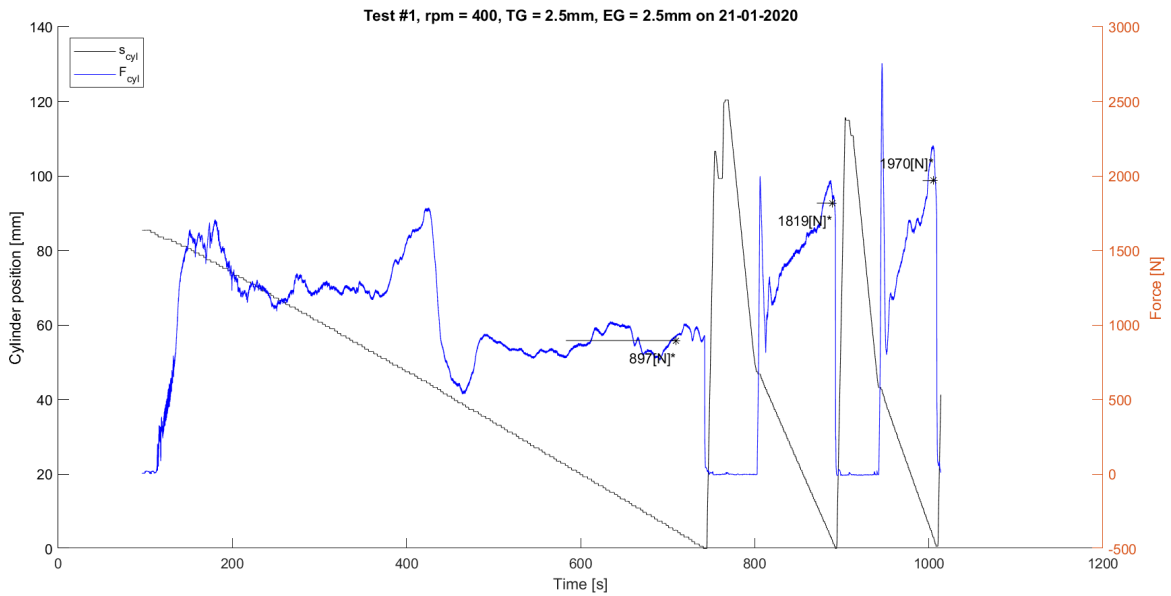


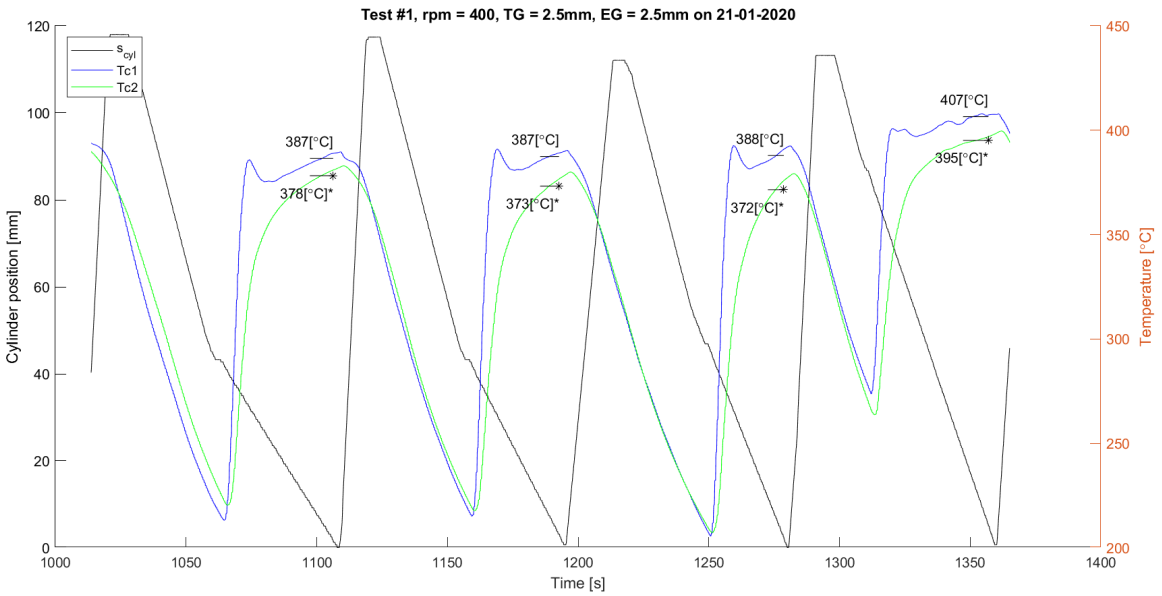
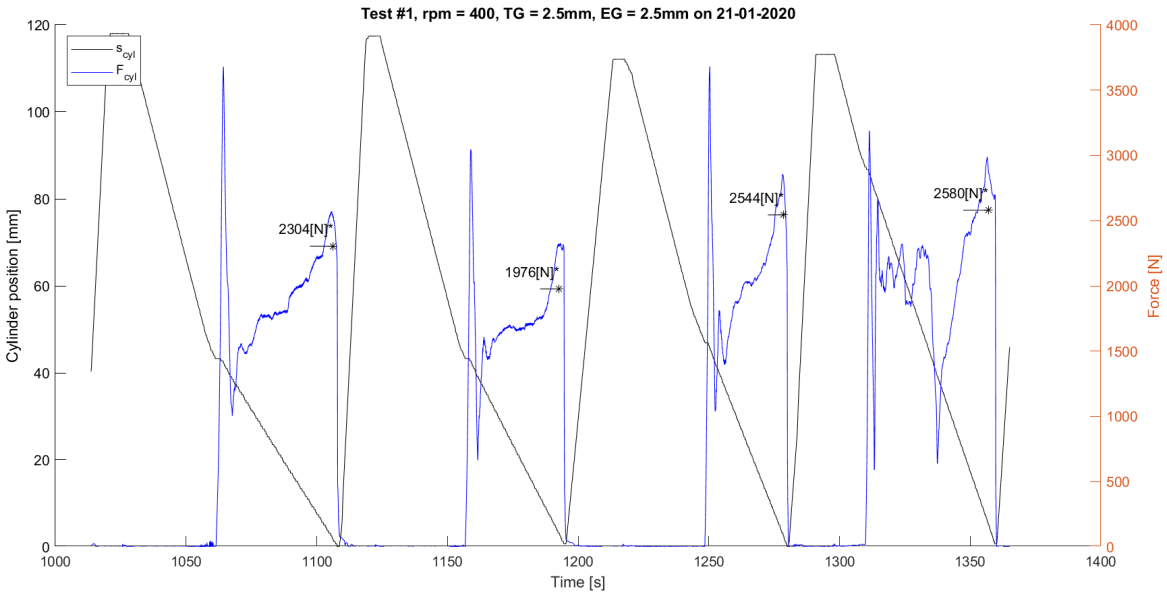
(d) Extrusion force against extrusion rate

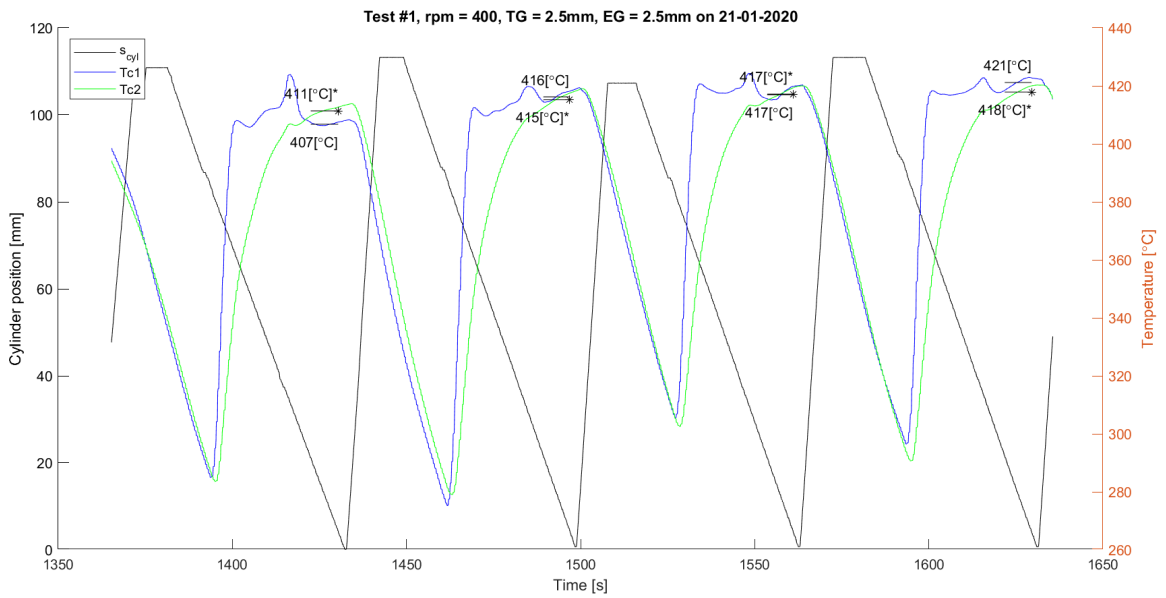
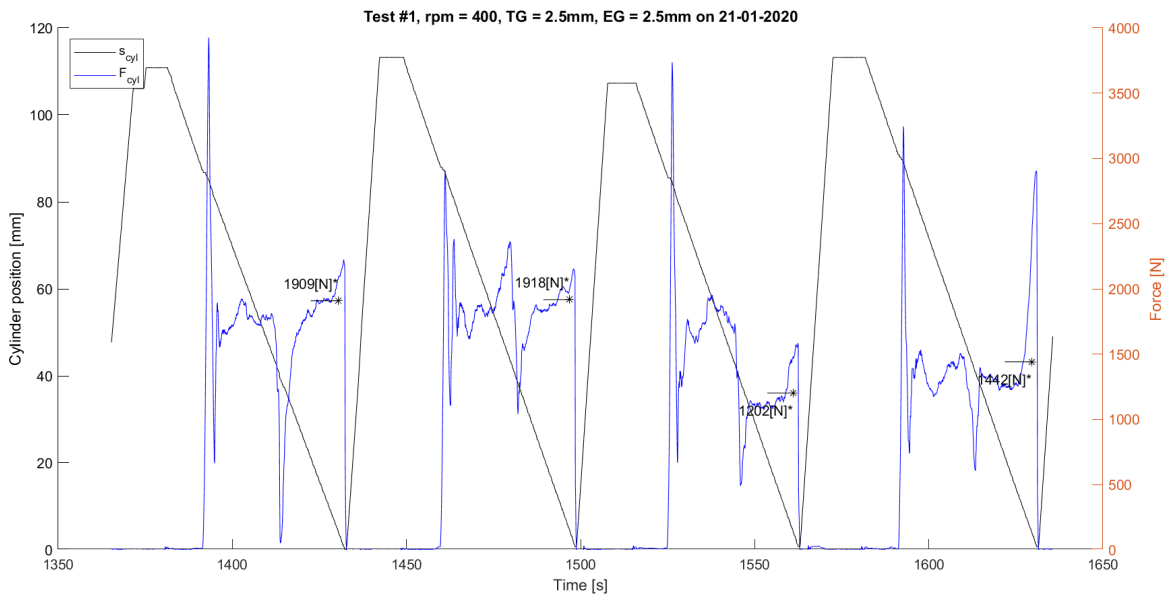
Figure B.5: Average temperature and forces plotted against the extrusion rate of experiment *FSE-2*.

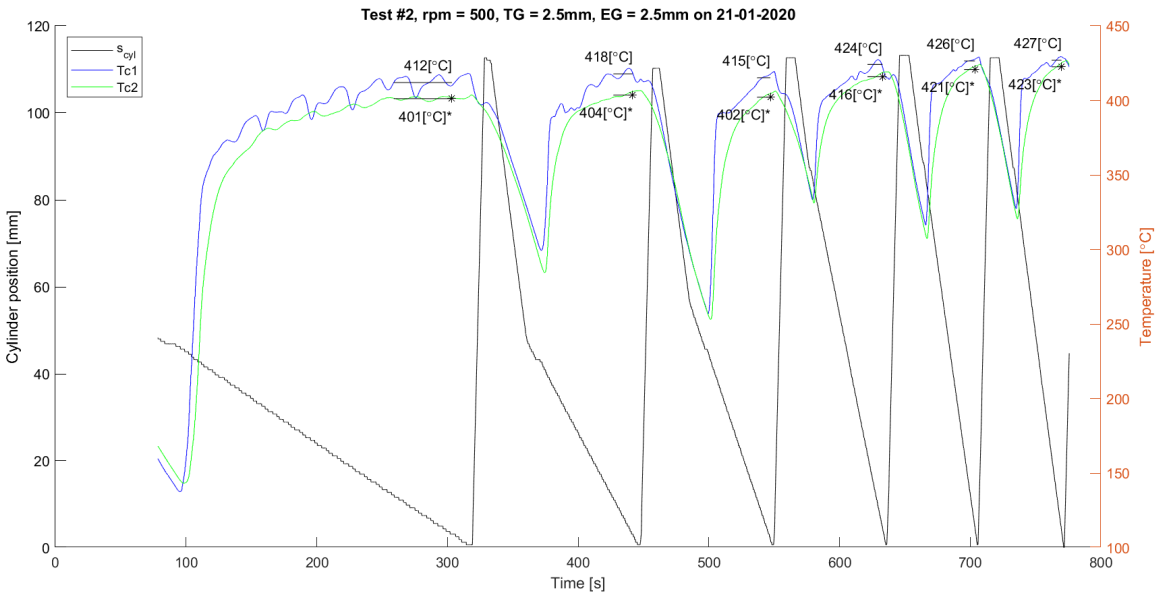
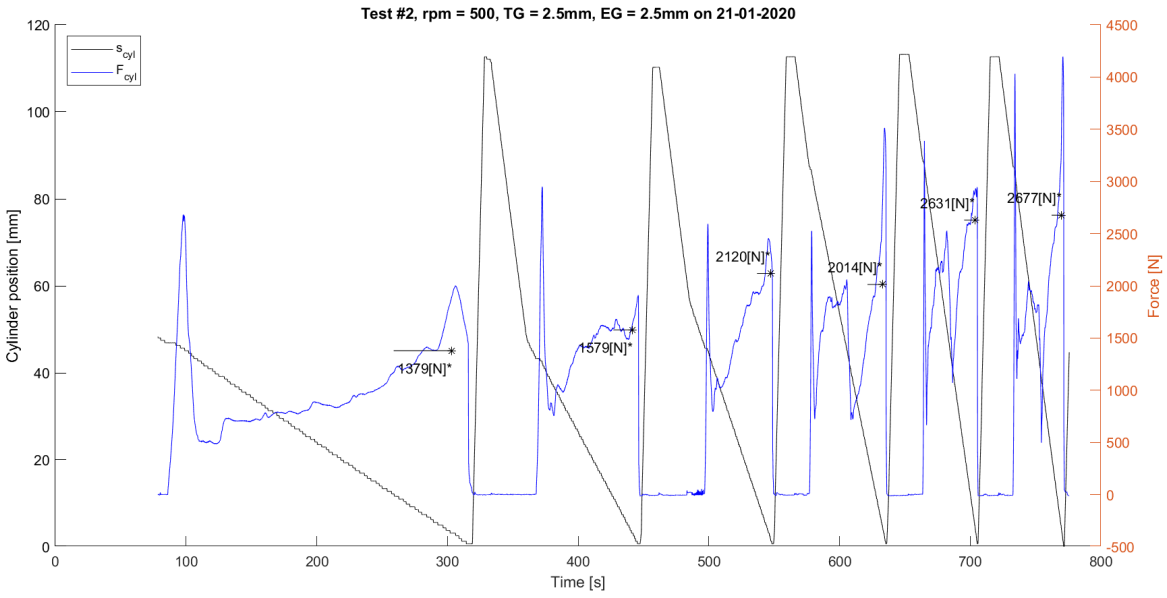
B.3 Experimental data FSE-3

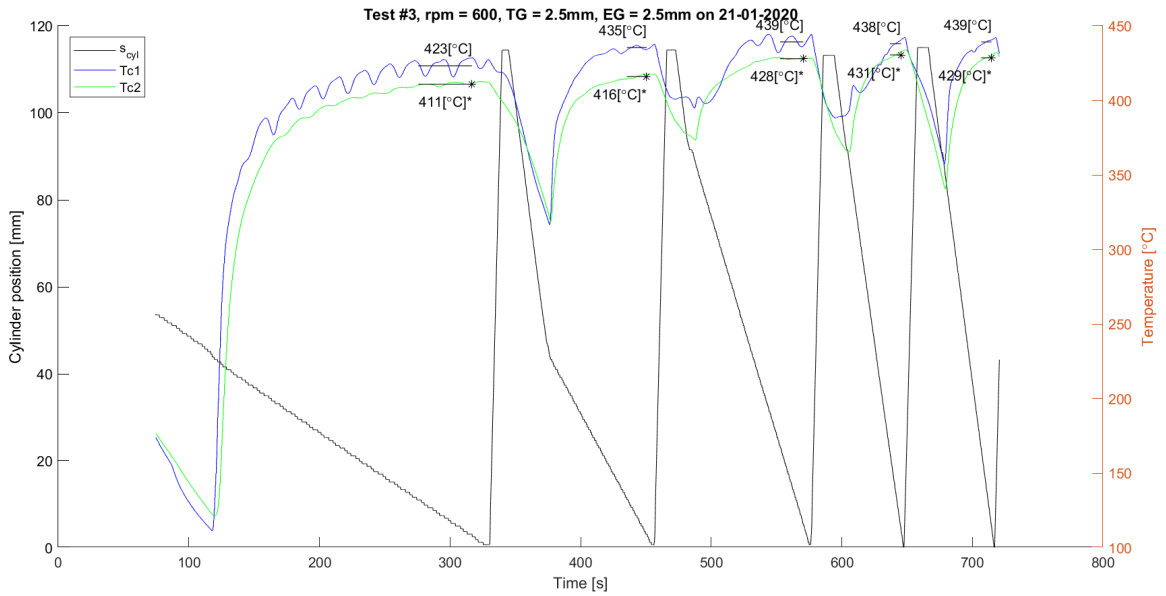
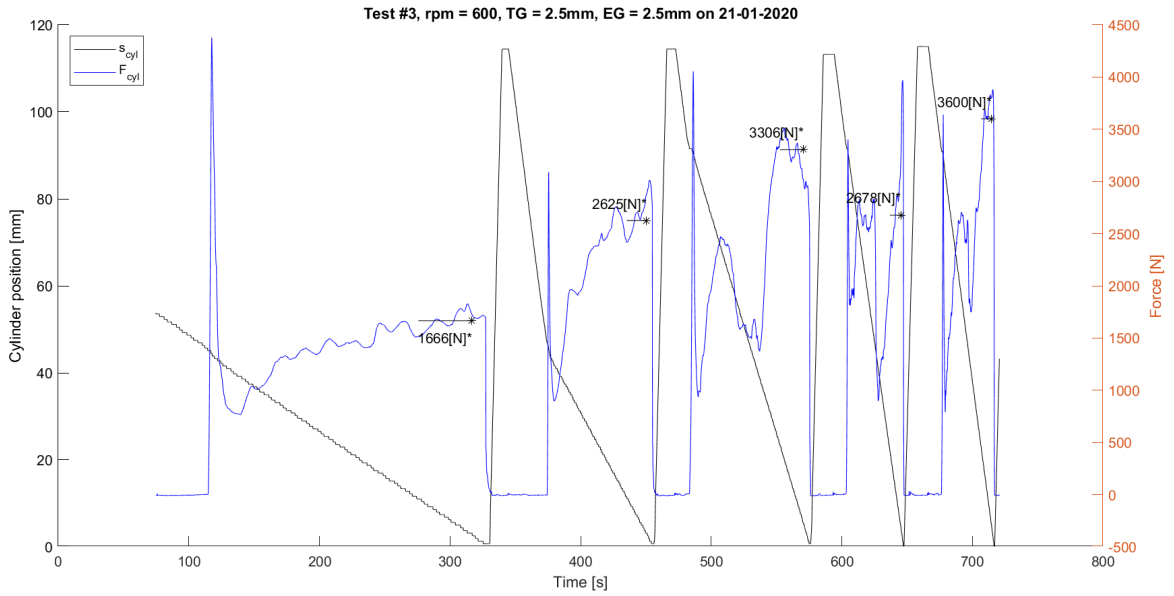
This experiment varies the rotational rate of the tool in the following order: 400-500-600-300 and different volumetric flow rates between $11 - 115\text{mm}^3/\text{s}$ were used. Some data of the experiment is divided in multiple graphs to display the data clearly, for example the experiment with a rpm of 400. A rotational rate of 200rpm was not examined during this experiments because jamming occurred in experiment FSE-2. Besides not using a rotational rate of 200rpm the extrusion force was not measured either. This was the result of a different nozzle setup that was not able to measure the extrusion force.

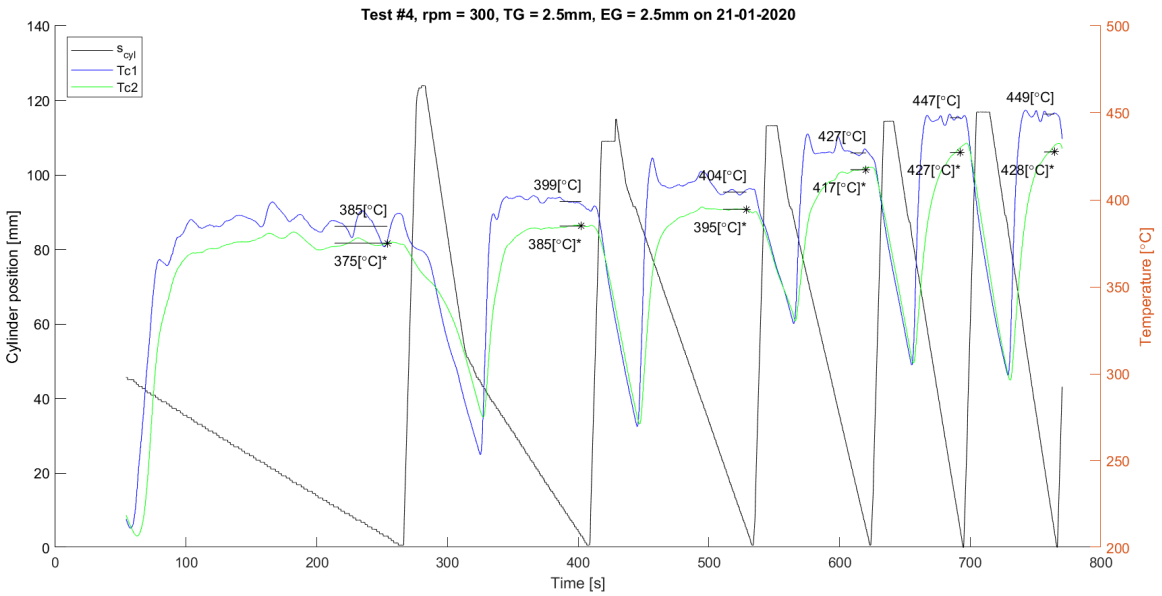
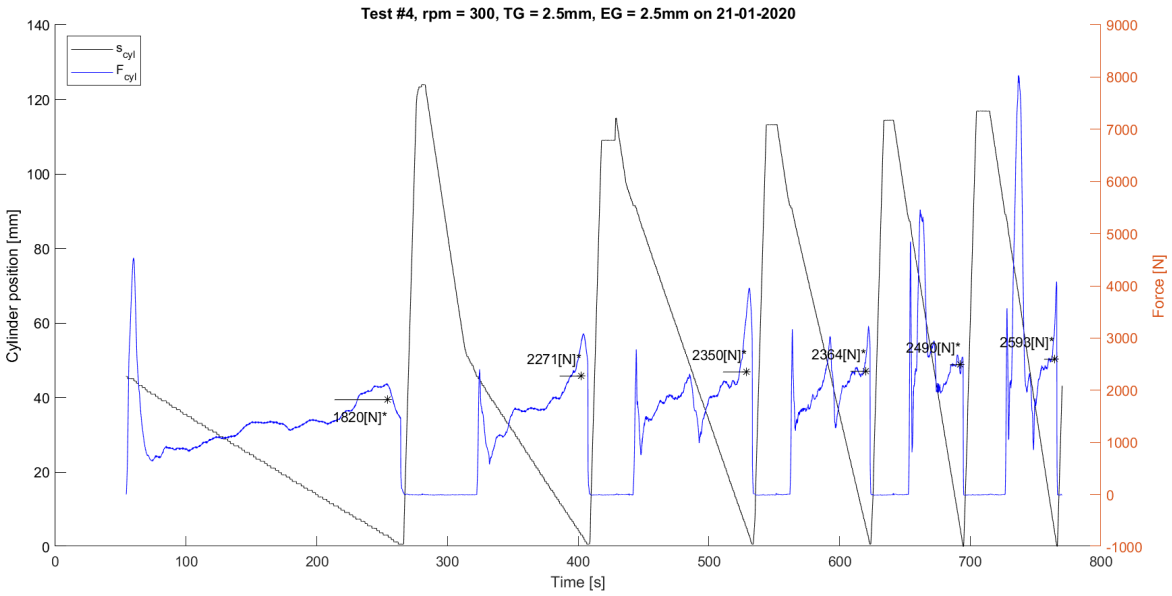




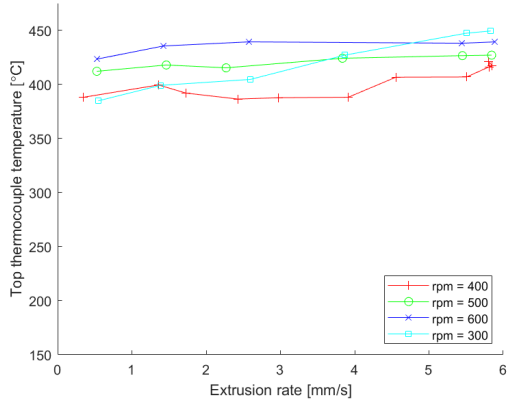




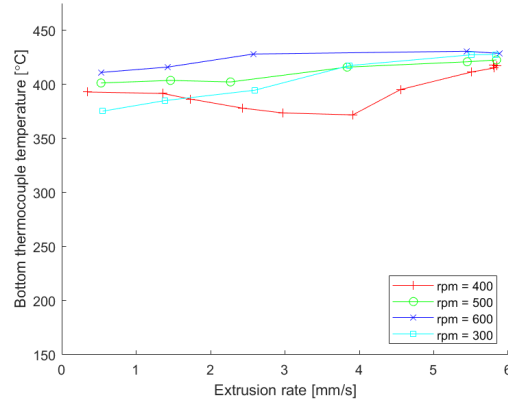




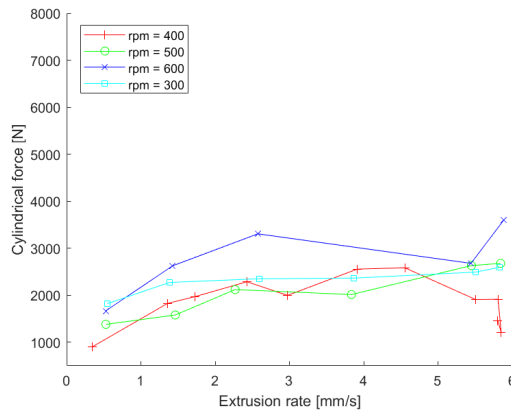
Comparing the temperatures while varying the rotational rate to experiment FSE-2 it seem that the overall setup has heated up more. Another explanation of the increasing behavior of the temperature of a rotational rate of $300rpm$ might be due to heating up the coolant resulting in a less efficient cooling systems since the coolant circulates through a tank. Comparing the extrusion force to experiments FSE-2 the effect of feeding the rods to the conical part seem to significantly reduce the extrusion force for higher rotational rates.



(a) Top nozzle temperature against extrusion rate.



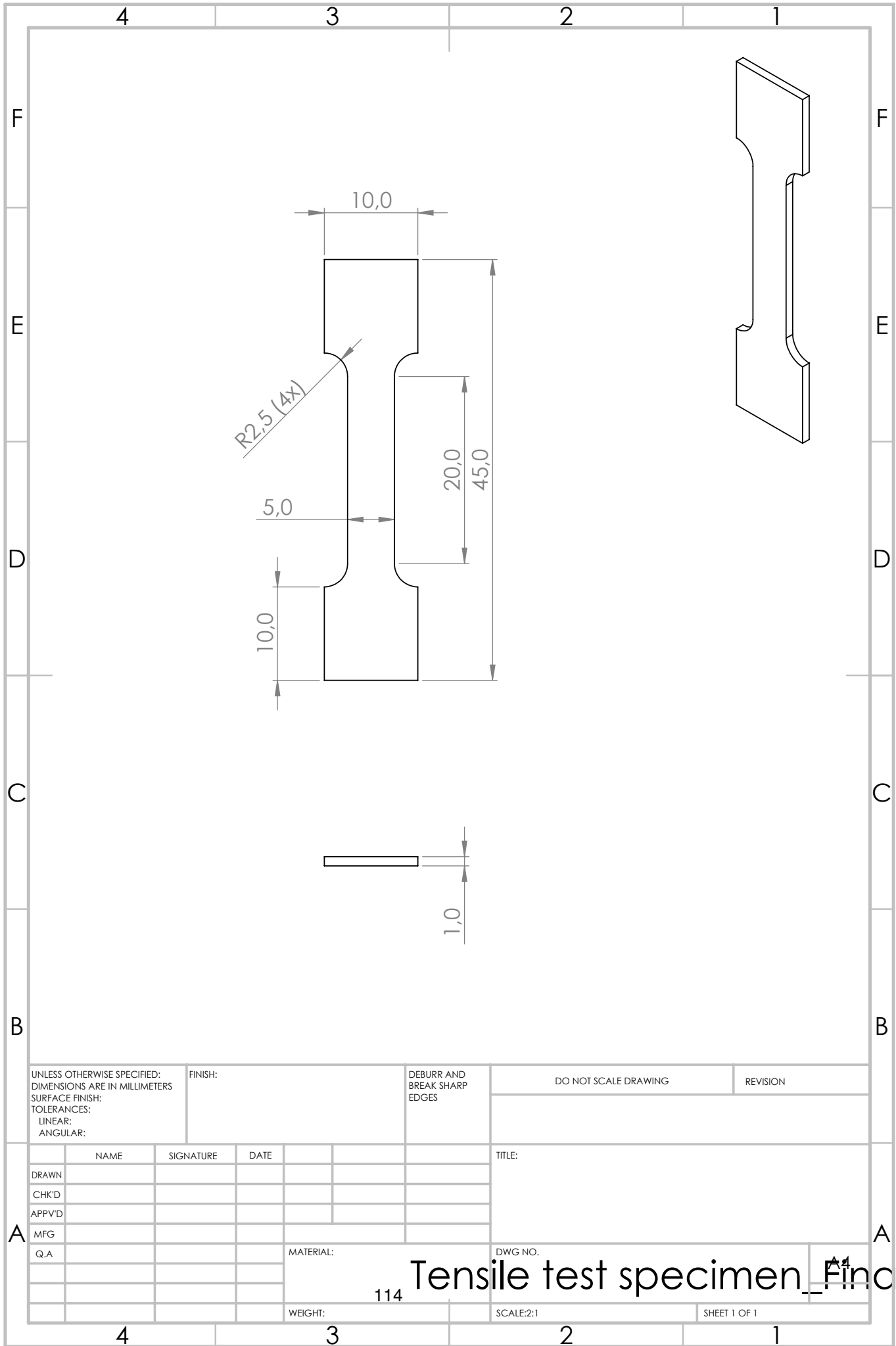
(b) Bottom nozzle temperature against extrusion rate.



(c) Cylindrical force against extrusion rate

Figure B.6: Average temperature and forces plotted against the extrusion rate of experiment FSE-3.

Tensile test dimensions



UNLESS OTHERWISE SPECIFIED:
 DIMENSIONS ARE IN MILLIMETERS
 SURFACE FINISH:
 TOLERANCES:
 LINEAR:
 ANGULAR:

FINISH:

DEBURR AND
 BREAK SHARP
 EDGES

DO NOT SCALE DRAWING

REVISION

	NAME	SIGNATURE	DATE		
DRAWN					
CHK'D					
APPVD					
MFG					
Q.A					
				MATERIAL:	
				WEIGHT:	114

TITLE:	
DWG NO.	
SCALE:2:1	SHEET 1 OF 1

Tensile test specimen_Fincl

A4

Data of FSEAM experiments

The experiments were performed in a slightly different order than mentioned in the main report with different experimental names. These names were also written on the samples and therefore a conversion table is used to keep the data organized and can be found in table D.1. The experiments will be called by their appendix names from now on.

Table D.1: Conversion of experiment name

Report name	Appendix name
AM-1	FSEAM-1
AM-2	FSEAM-3
AM-3	FSEAM-2
AM-4	FSEAM-4
AM-5	FSEAM-6
AM-6	FSEAM-7
AM-7	FSEAM-5

Shown in section 3.3 a transition was made from the extrusion force and nozzle temperature as a function of time to a function of position. As a result, contour graphs were made as a function of the x - and z -coordinate and can easily be related to the deposited aluminium layers. An example of how the contour graphs are related to the layers can be seen in figure D.1. Analysis mentioned in section 3.2.4 are marked in the graphs to relate the samples with the corresponding force and temperature. A legend of what each color means in the contour graph can be found in figure D.2

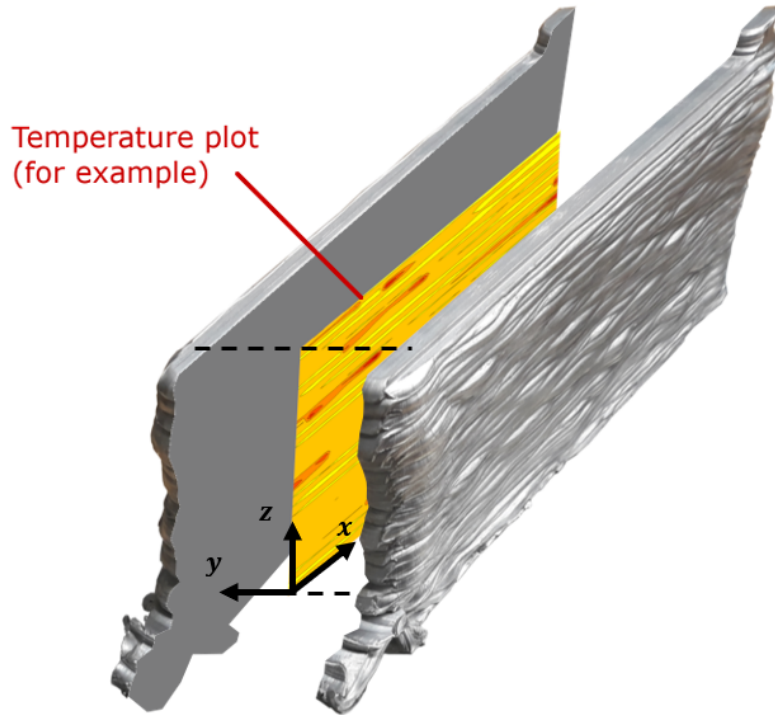


Figure D.1: The implementation of the nozzle temperature and pressure plots relative to the AM product.

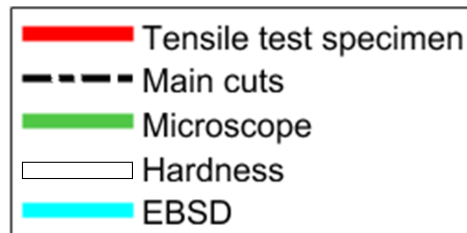


Figure D.2: Legend indicating analysis locations for the contour graph.

D.1 Reference material

The aluminium, AA-6060 T6, that has been used as feed material has been examined using the microscope and hardness tester. These results can be used as reference.

Microscopic images

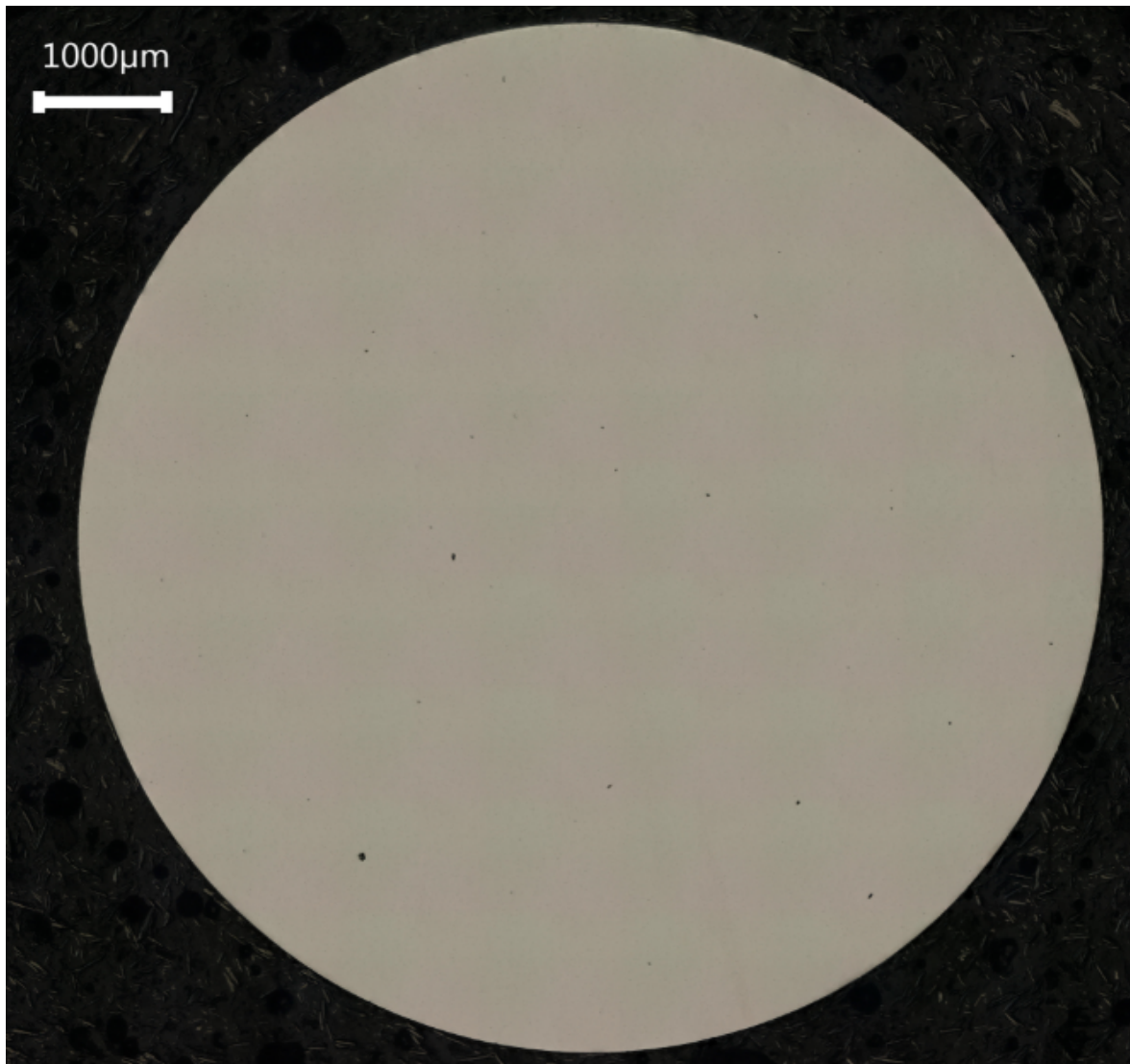


Figure D.3: Transverse cross-section of the feed material.

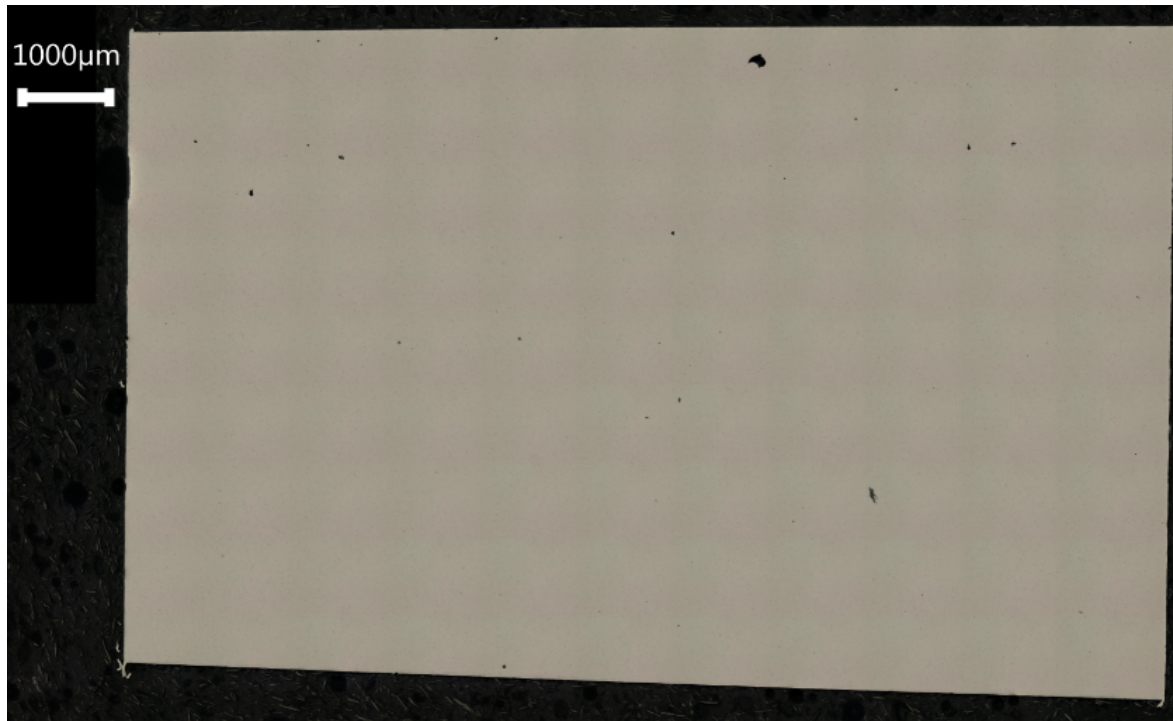
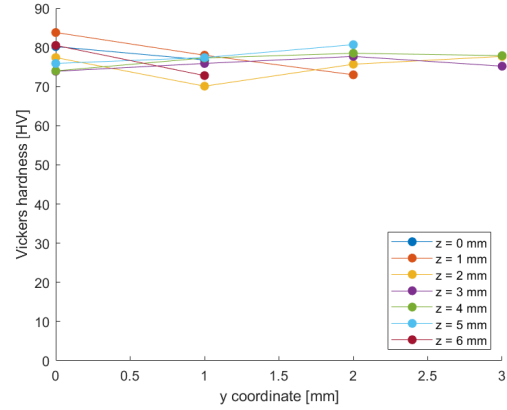
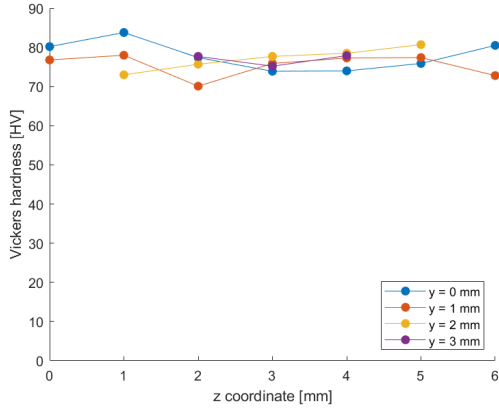


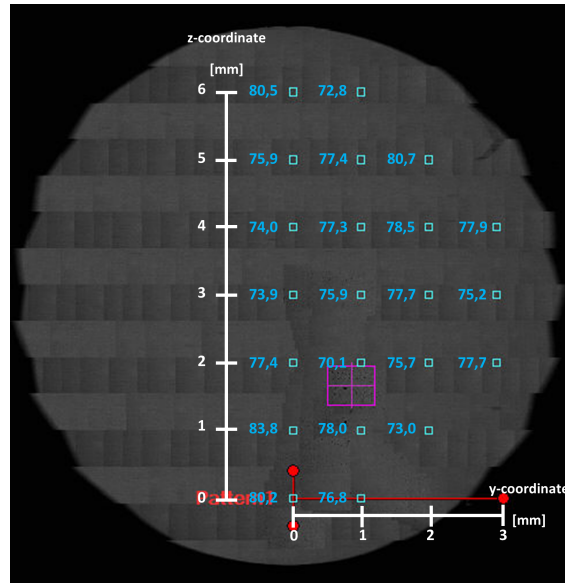
Figure D.4: Longitudinal cross-section of the feed material.

Hardness test



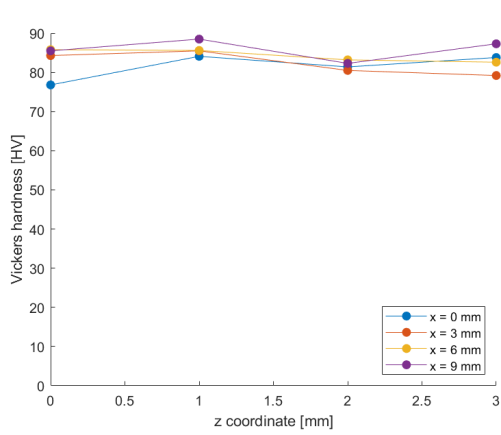
(a) Hardness throughout the height of the reference material in transverse direction.

(b) Hardness throughout the width of the reference material in transverse direction.

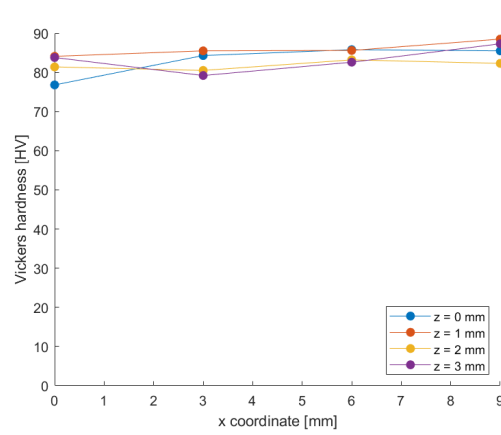


(c) Hardness throughout the transverse cross-section of the reference material

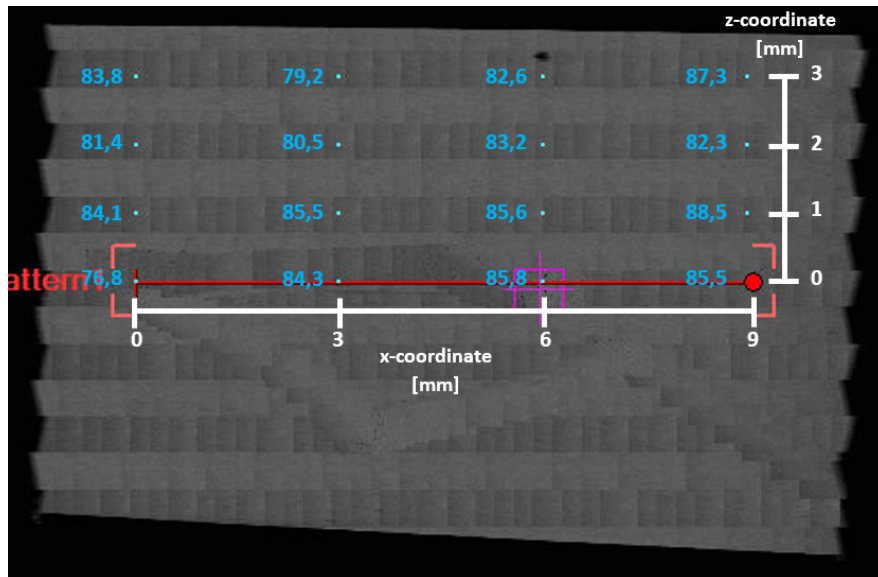
Figure D.5: Overview of the hardness of the reference material in transverse direction.



(a) Hardness throughout the height of the reference material in longitudinal direction.



(b) Hardness throughout the width of the reference material in longitudinal direction.



(c) Hardness throughout the longitudinal cross-section of the reference material

Figure D.6: Overview of the hardness of the reference material in longitudinal direction.

D.2 FSEAM-1

Figure D.7 shows the position of where the microscopic images are taken from, indicated by a letter and a yellow arrow that indicates what side was examined.

Microscopic images

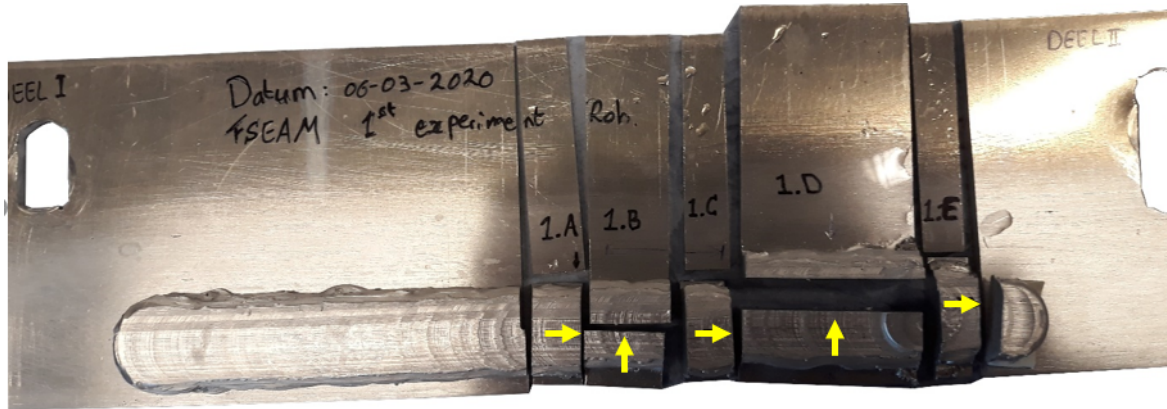


Figure D.7: The yellow arrows indicate the side where the microscopic image is taken from.

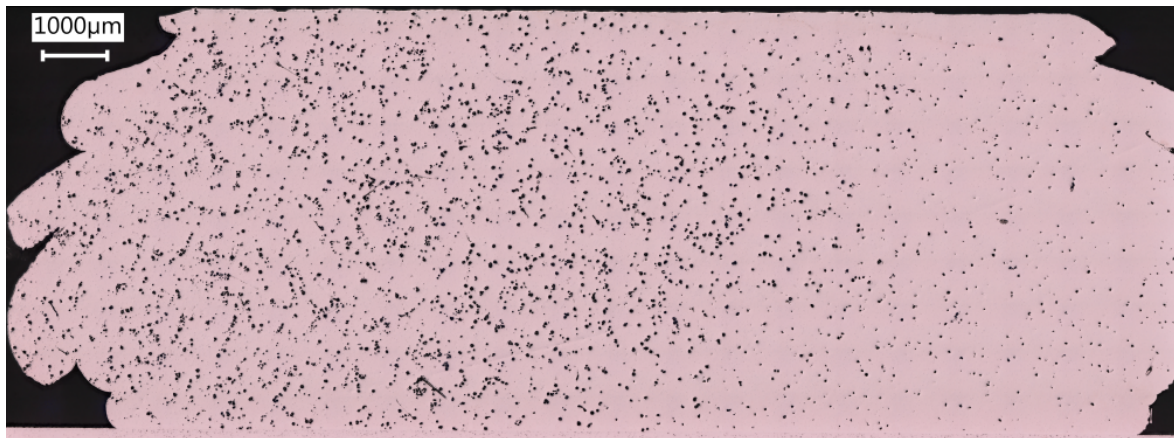


Figure D.8: Section 1.A with scale bar.

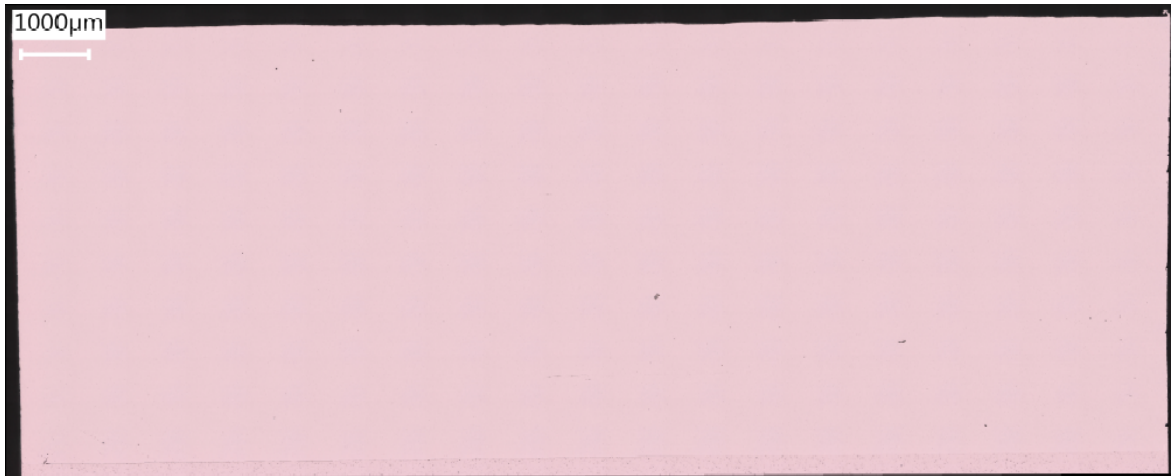


Figure D.9: Section 1.B with scale bar.



Figure D.10: Section 1.C with scale bar.

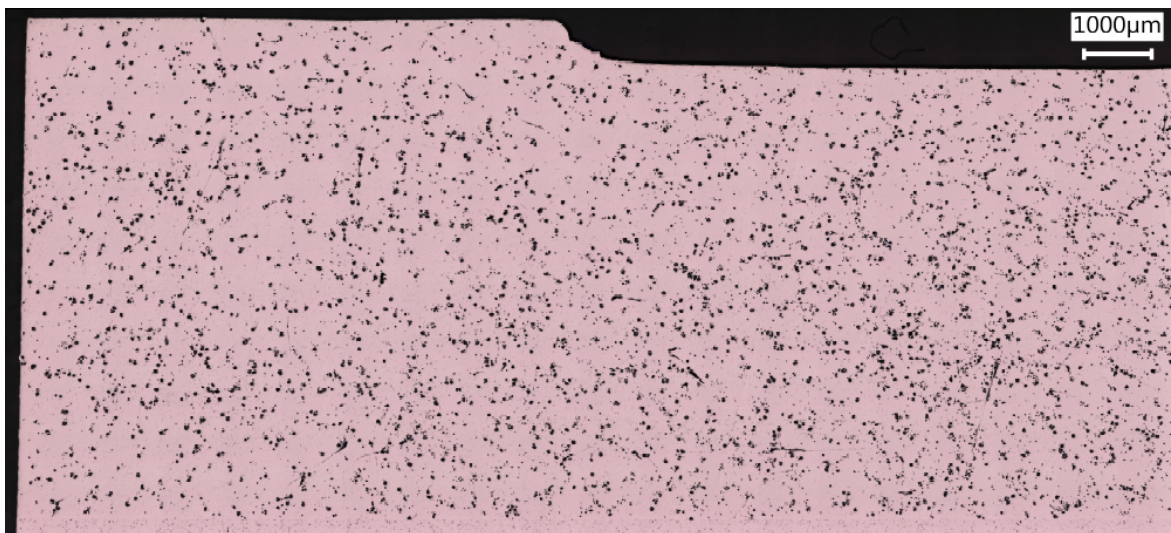


Figure D.11: Section 1.D with scale bar (left side).

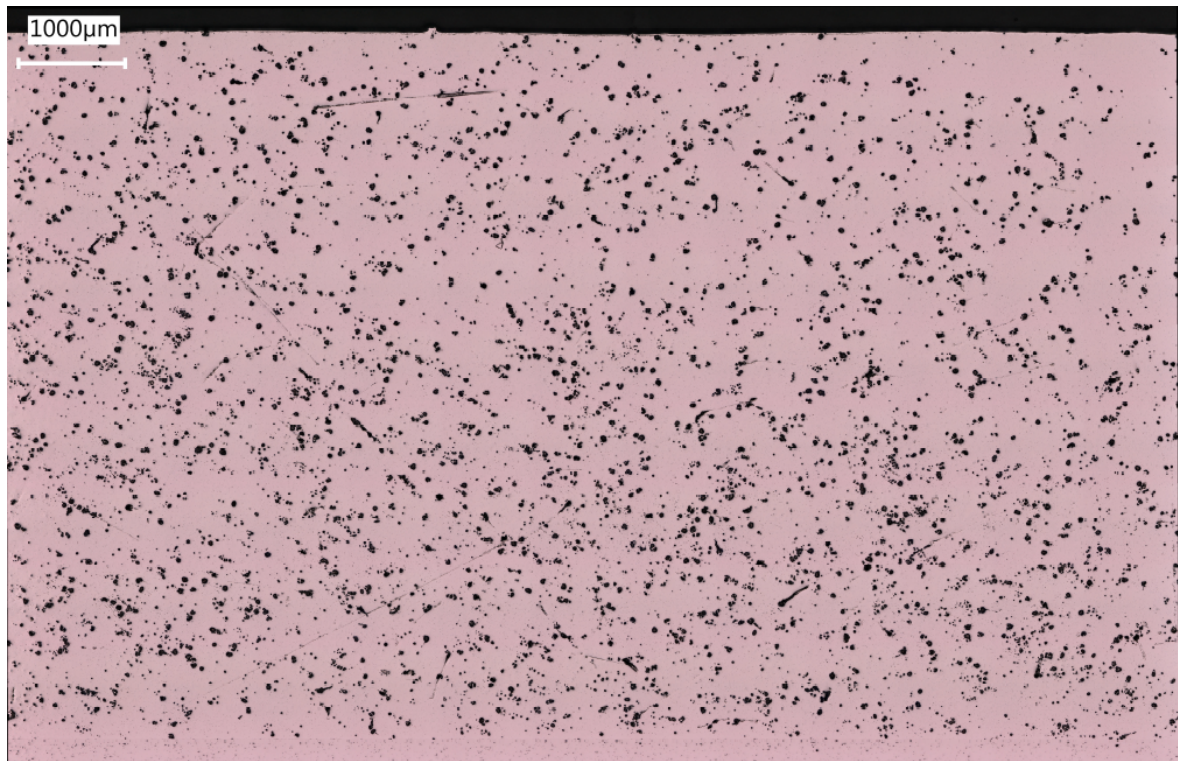


Figure D.12: Section 1.D with scale bar (middle side).

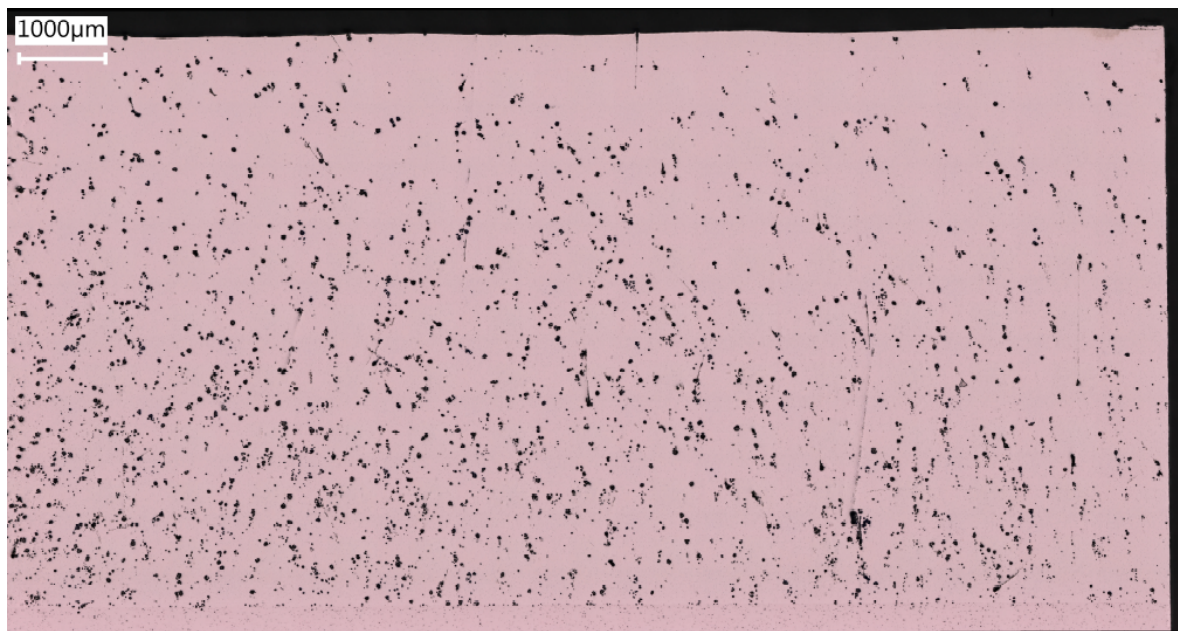


Figure D.13: Section 1.D with scale bar (right side).



Figure D.14: Section 1.E with scale bar (left side).



Figure D.15: Section 1.E with scale bar (right side).

EDX images

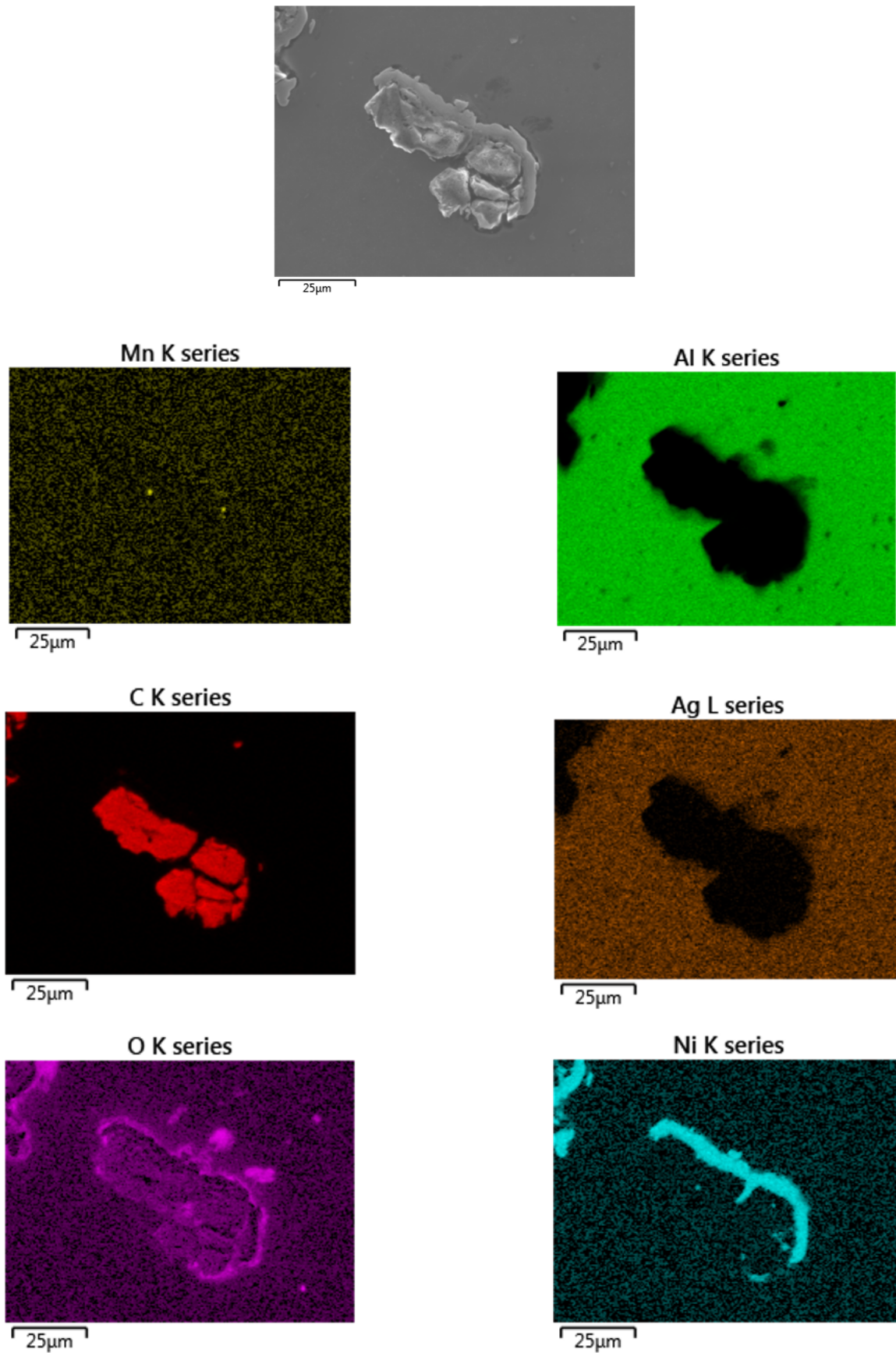


Figure D.16: Overview of which particles are present in the aluminium alloy, position 1.

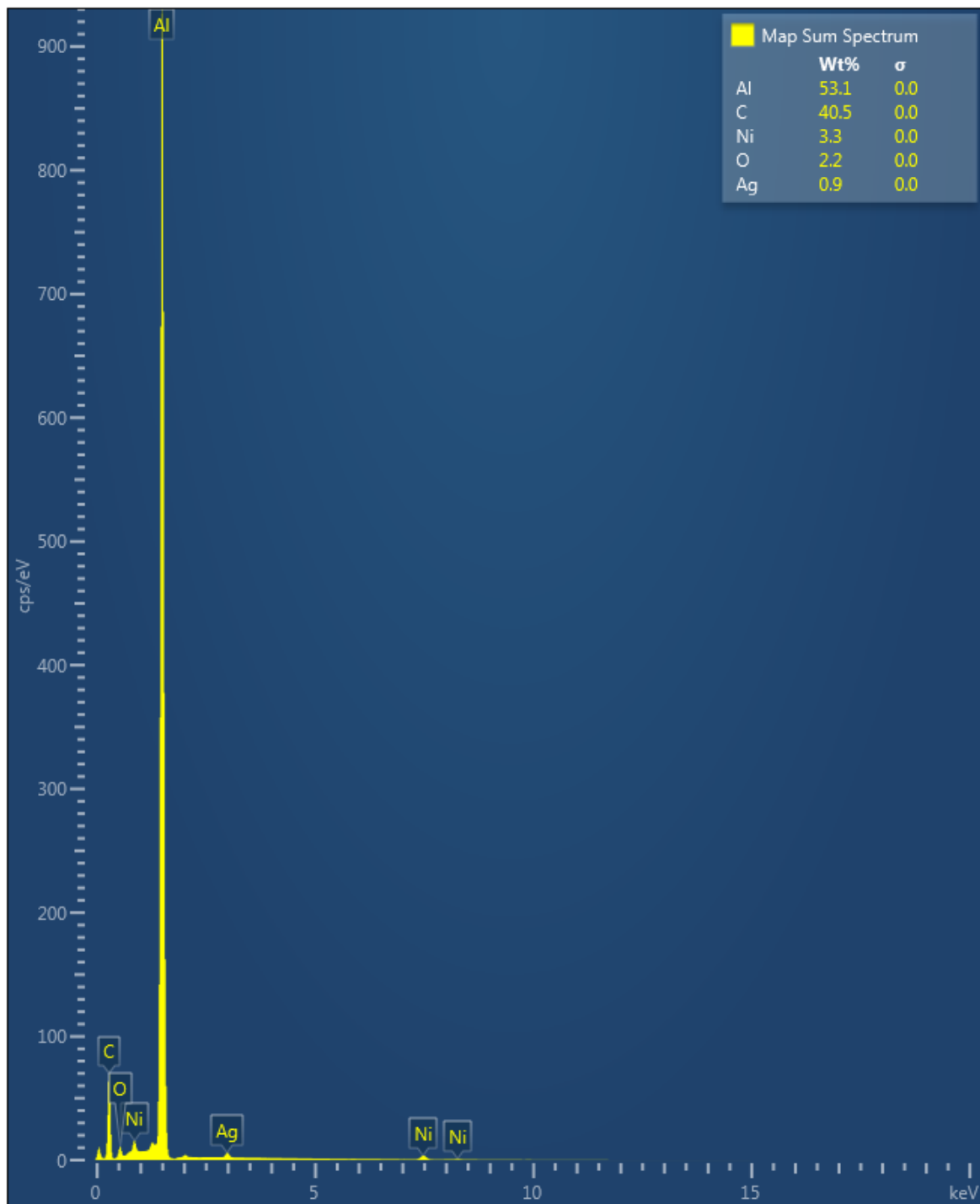


Figure D.17: Content of the EDX analysed area of position 1.

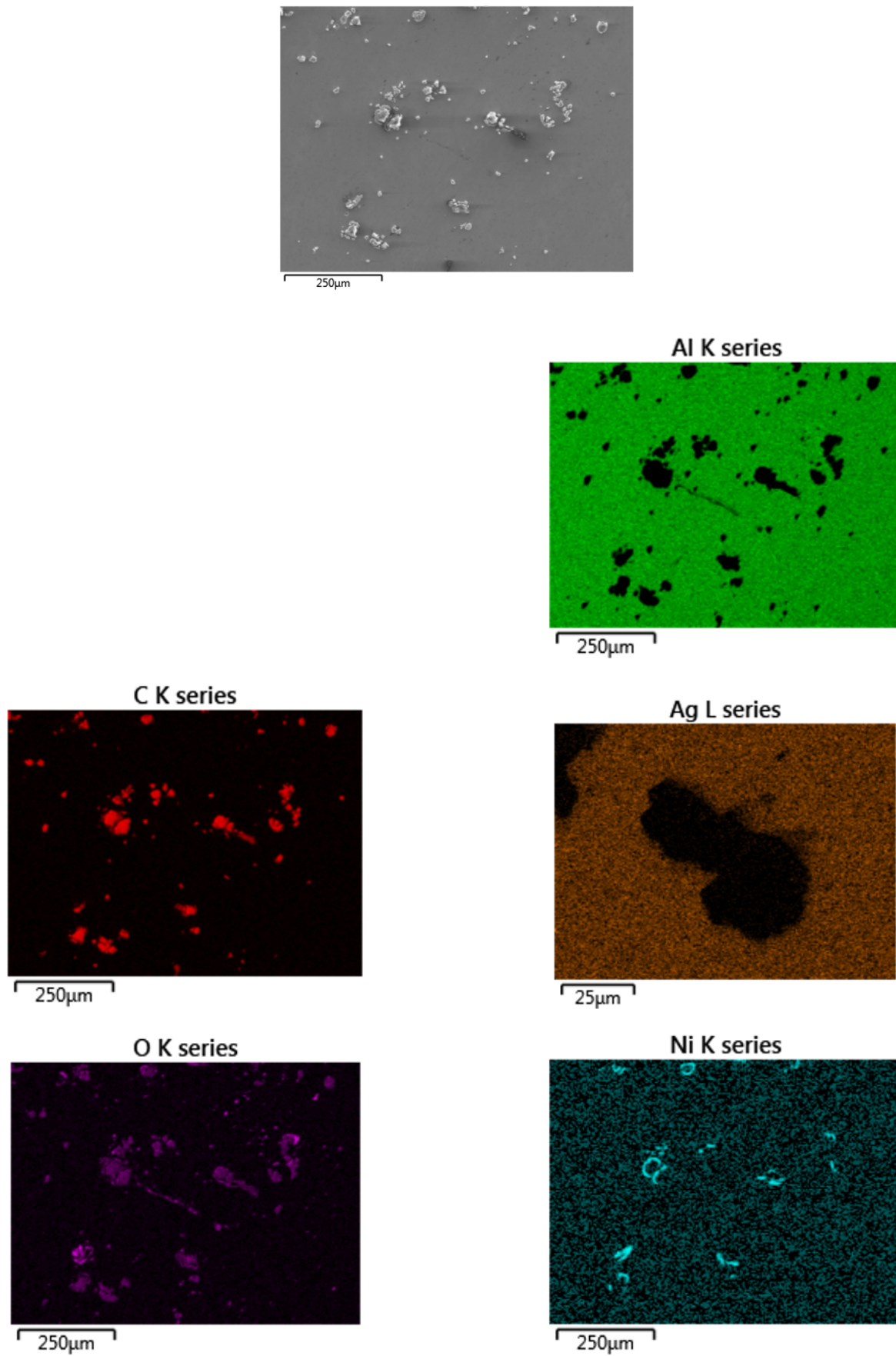


Figure D.18: Overview of which particles are present in the aluminium alloy, position 2.

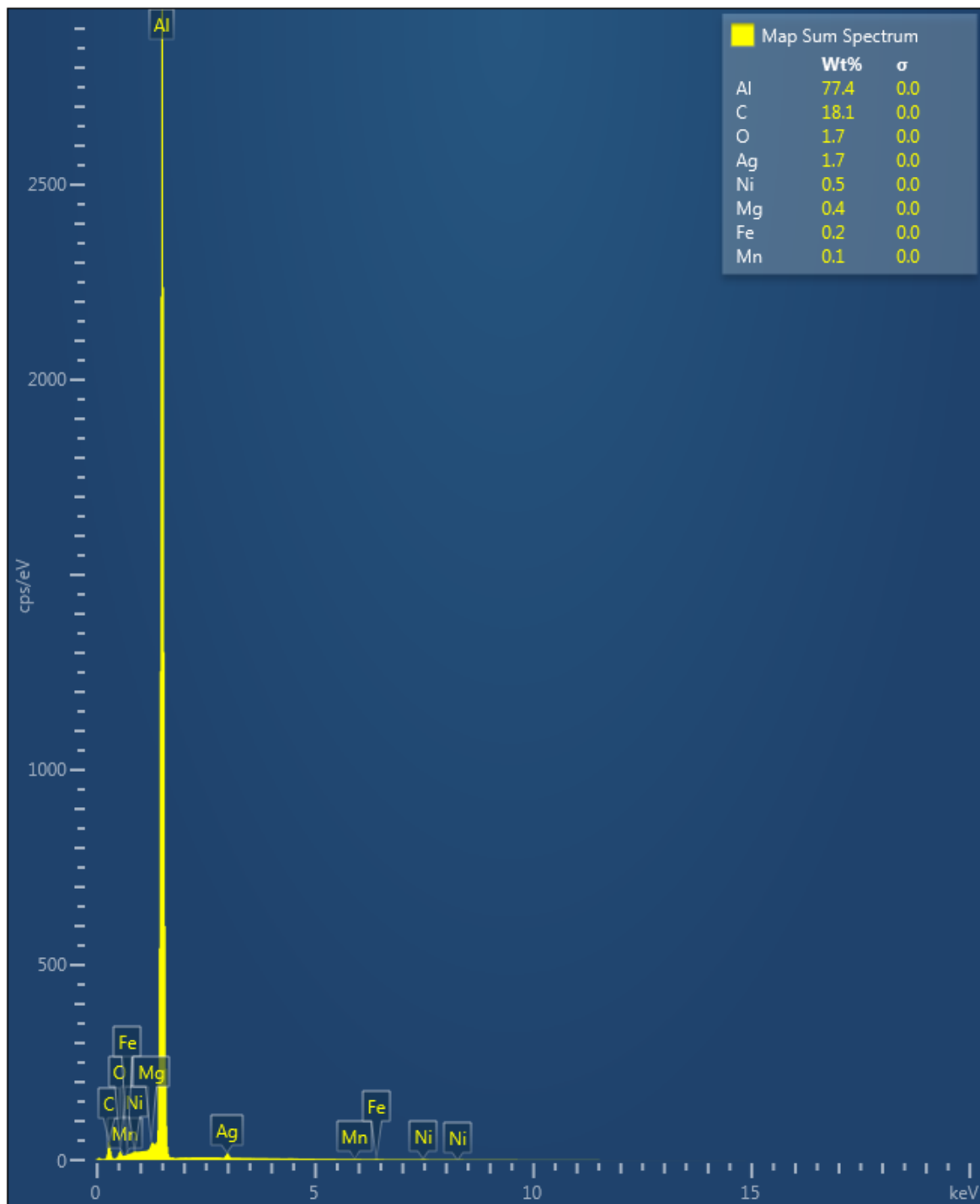
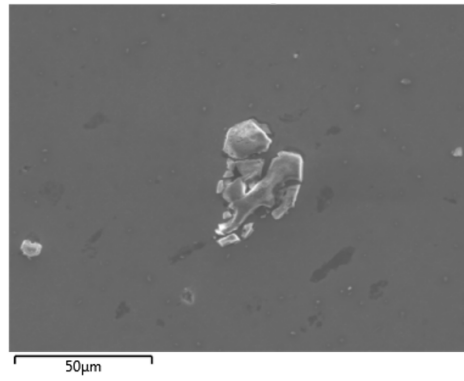
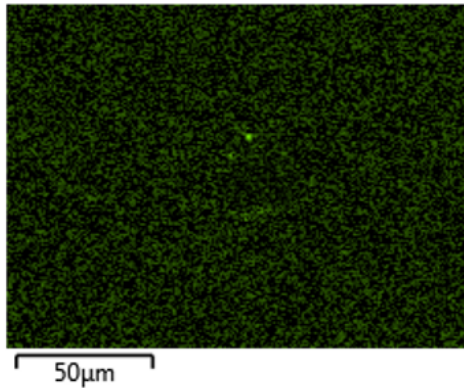


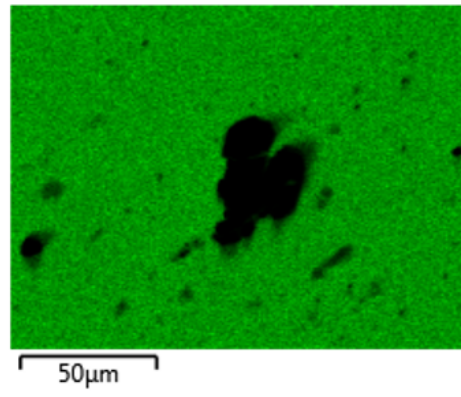
Figure D.19: Content of the EDX analysed area of position 2.



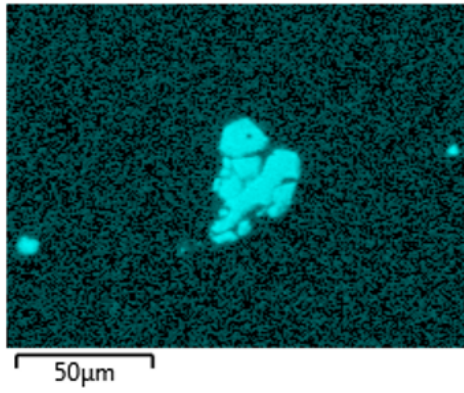
Mn K series



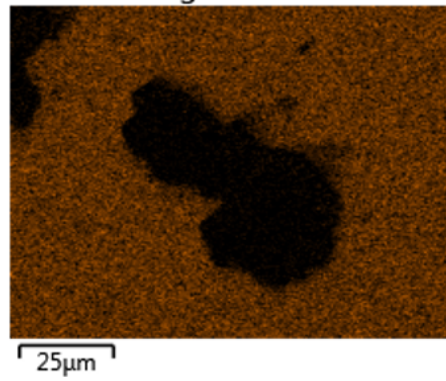
Al K series



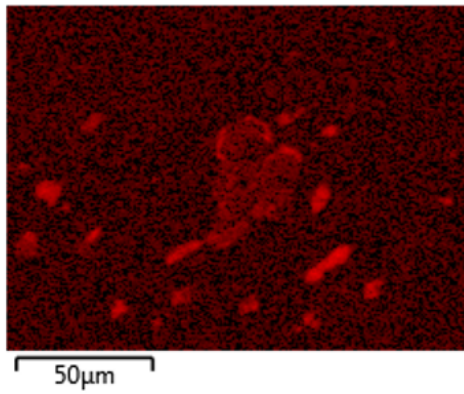
C K series



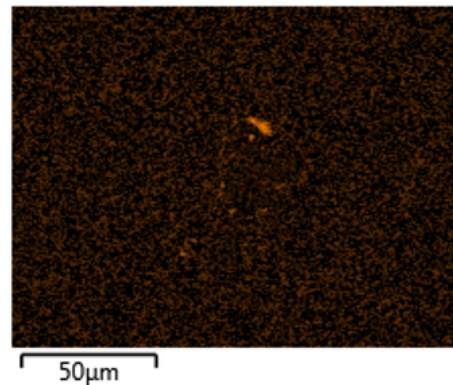
Ag L series



O K series



Ni K series



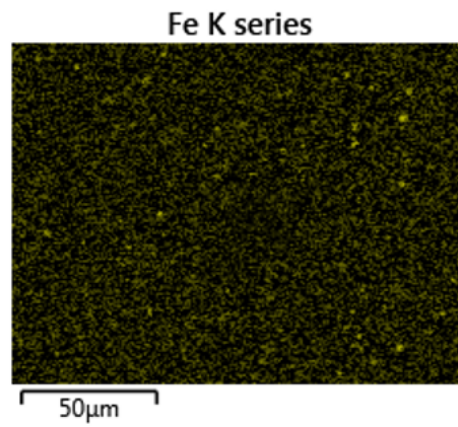


Figure D.20: Overview of which particles are present in the aluminium alloy, position 3.

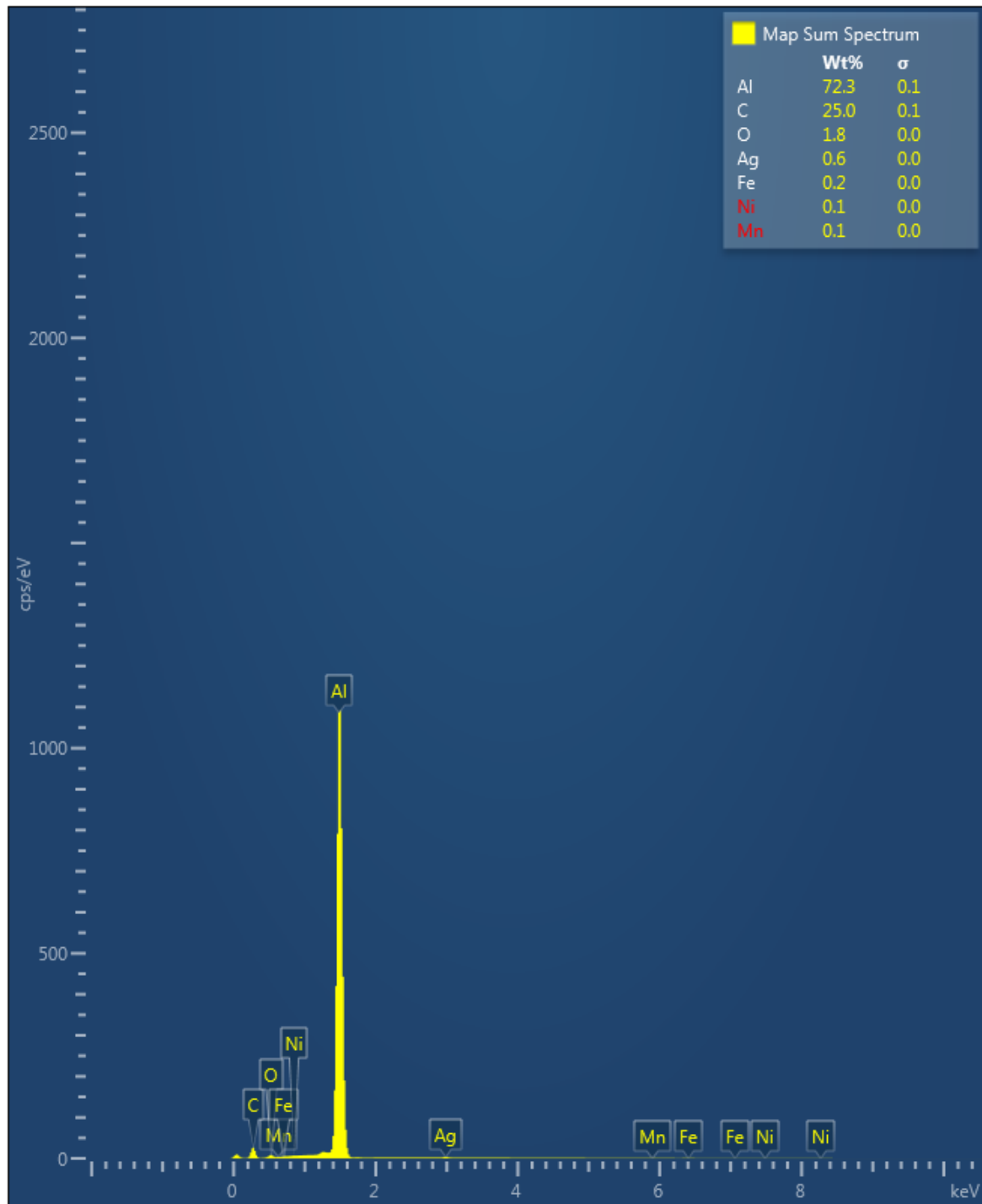


Figure D.21: Content of the EDX analysed area of position 3.

D.3 FSEAM-2

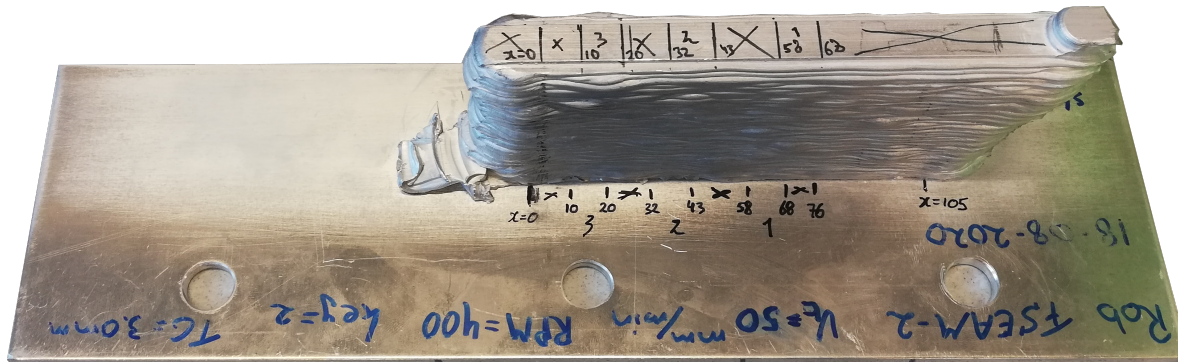


Figure D.22: Indication of the starting position $x = 0$ corresponding to the contour graph of the deposited layers.

Nozzle temperature and extrusion force contour graphs

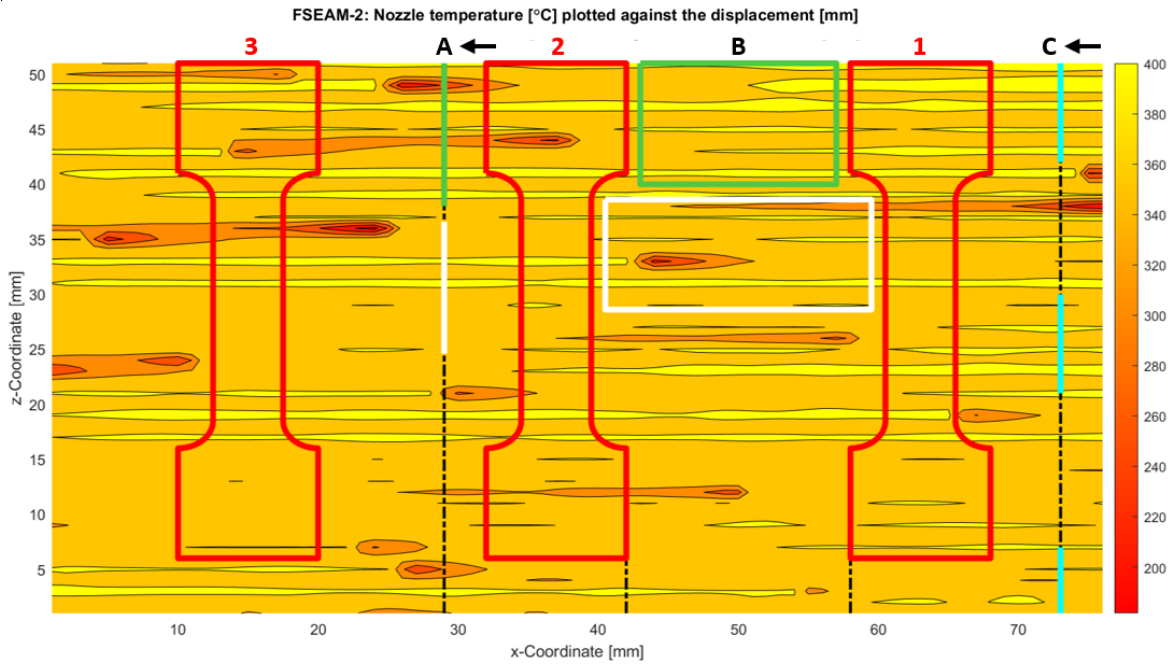


Figure D.23: Nozzle temperature of the second experiment corresponding to the x- and z-coordinate of the AM wall including the locations of the tensile test, microscopy, hardness test, and EBSD.

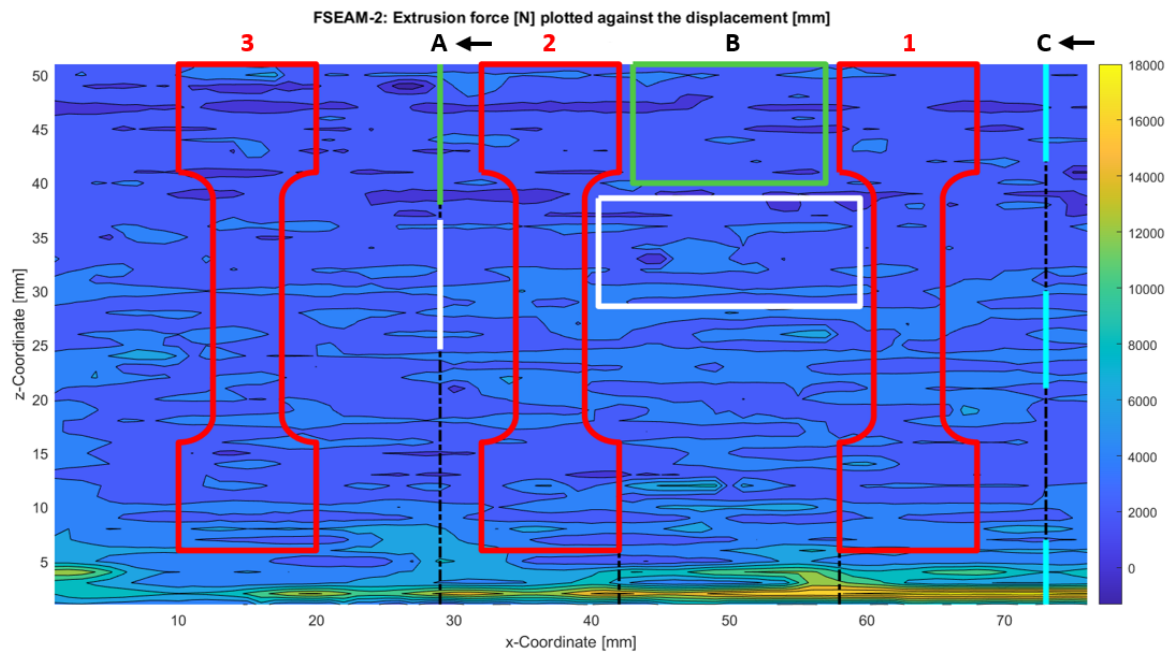


Figure D.24: Extrusion force of the second experiment corresponding to the x- and z-coordinate of the AM wall including the locations of the tensile test, microscopy, hardness test, and EBSD.

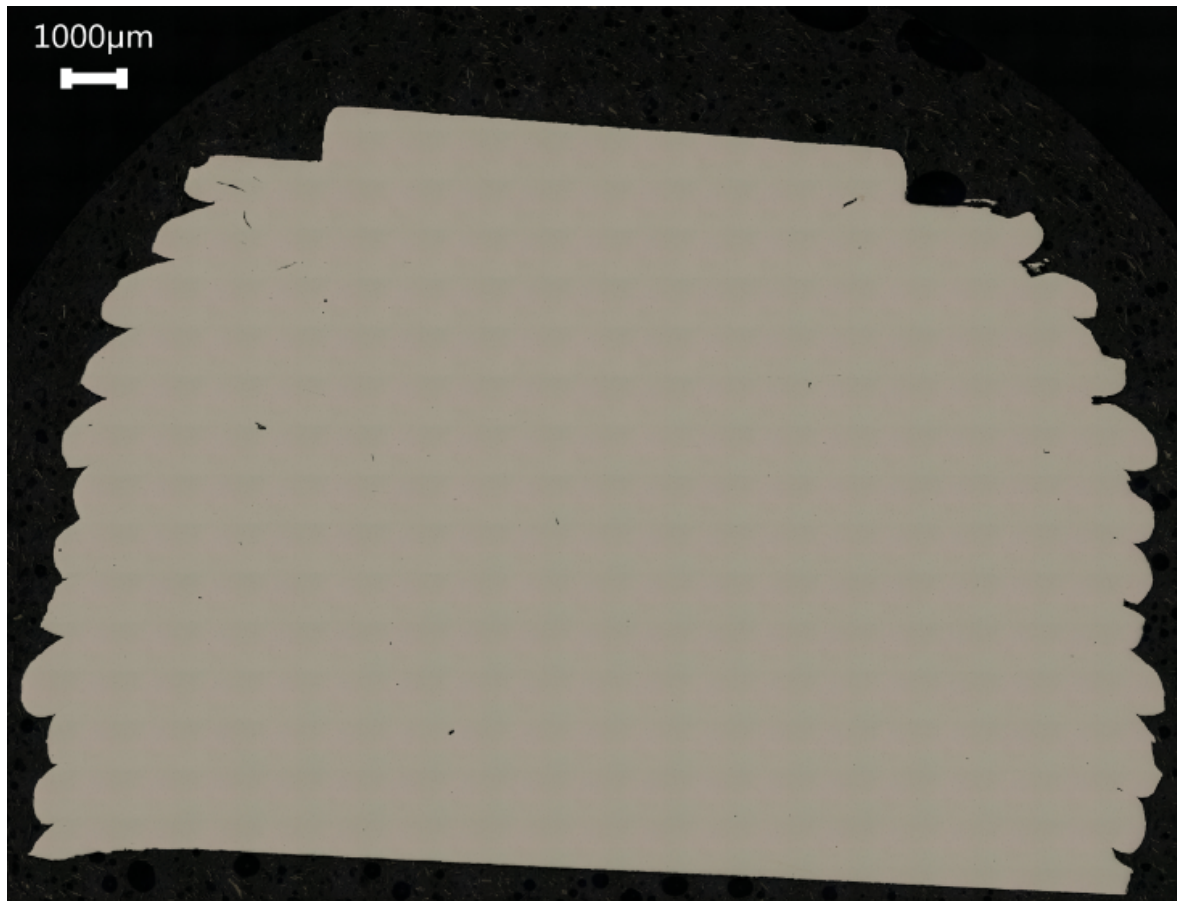
Microscopic images

Figure D.25: Transverse cross-section of FSEAM-2A.

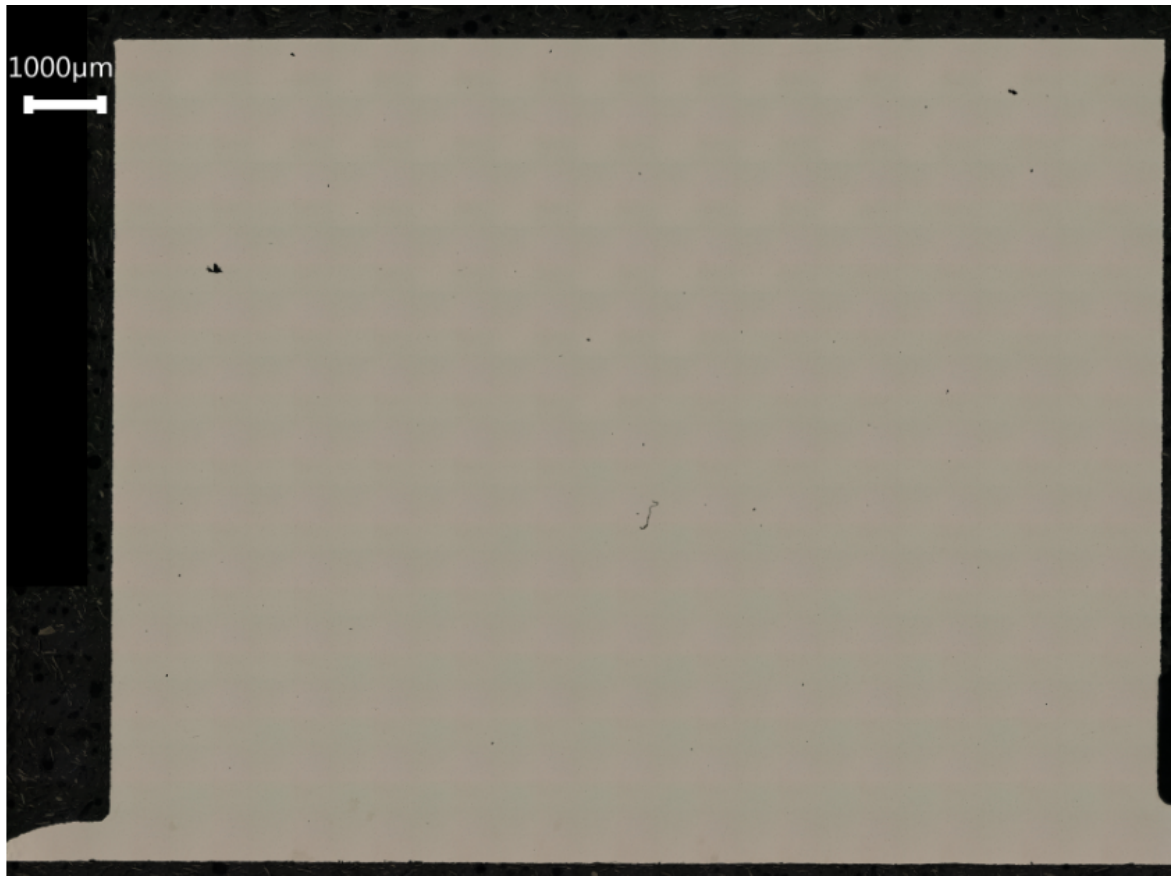
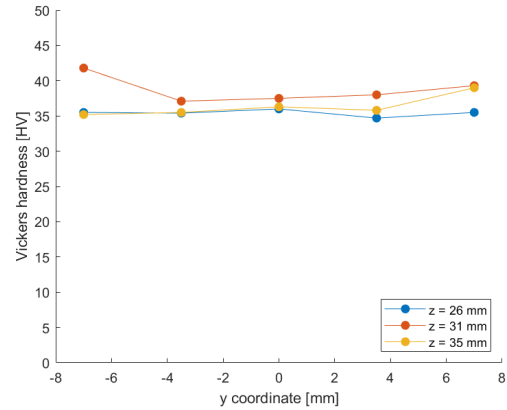
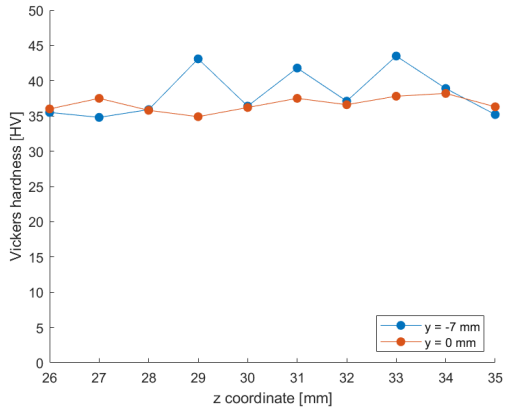


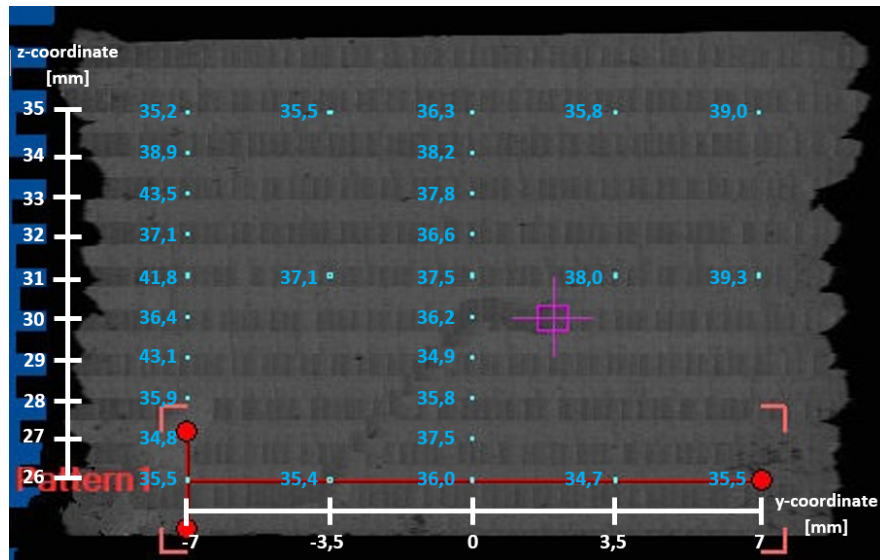
Figure D.26: Longitudinal cross-section of FSEAM-2B.

Hardness test



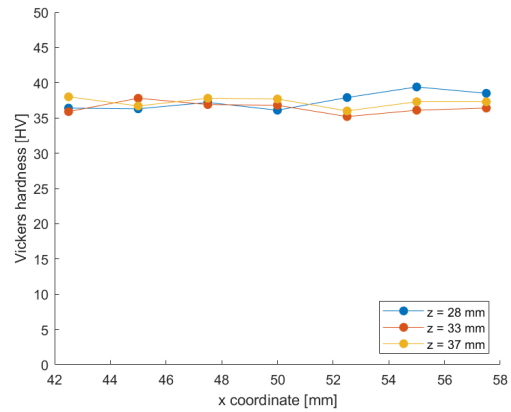
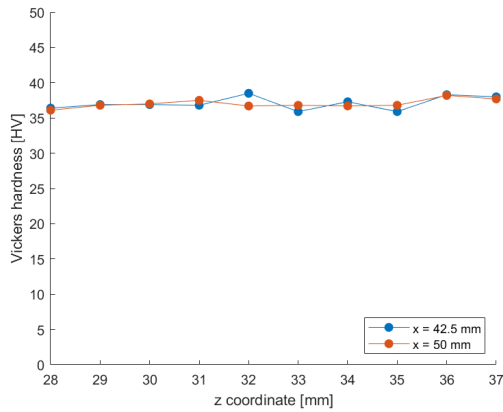
(a) Hardness throughout the height of FSEAM-2A in transverse direction.

(b) Hardness throughout the width of FSEAM-2A in transverse direction.

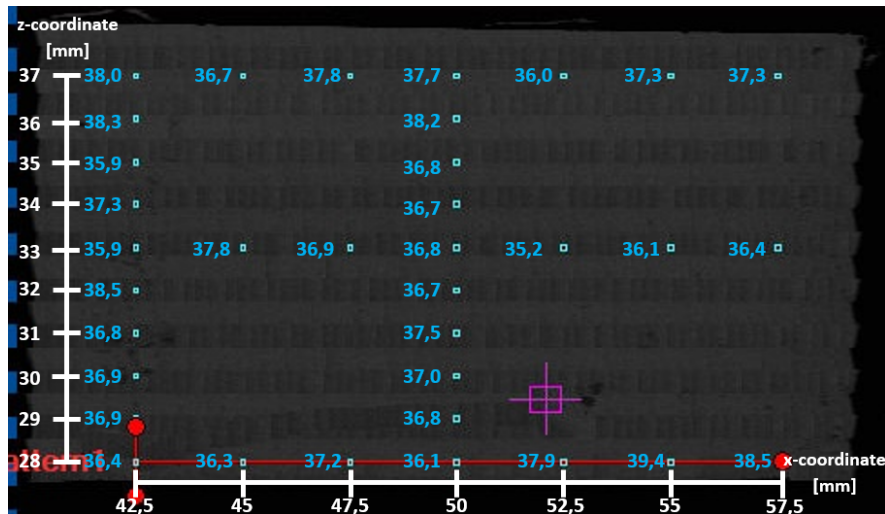


(c) Hardness throughout the transverse cross-section of FSEAM-2A.

Figure D.27: Overview of the hardness of FSEAM-2A in transverse direction.



(a) Hardness throughout the height of FSEAM-2B in longitudinal direction. (b) Hardness throughout the width of FSEAM-2B in longitudinal direction.



(c) Hardness throughout the longitudinal cross-section of FSEAM-2B.

Figure D.28: Overview of the hardness of FSEAM-2B in longitudinal direction.

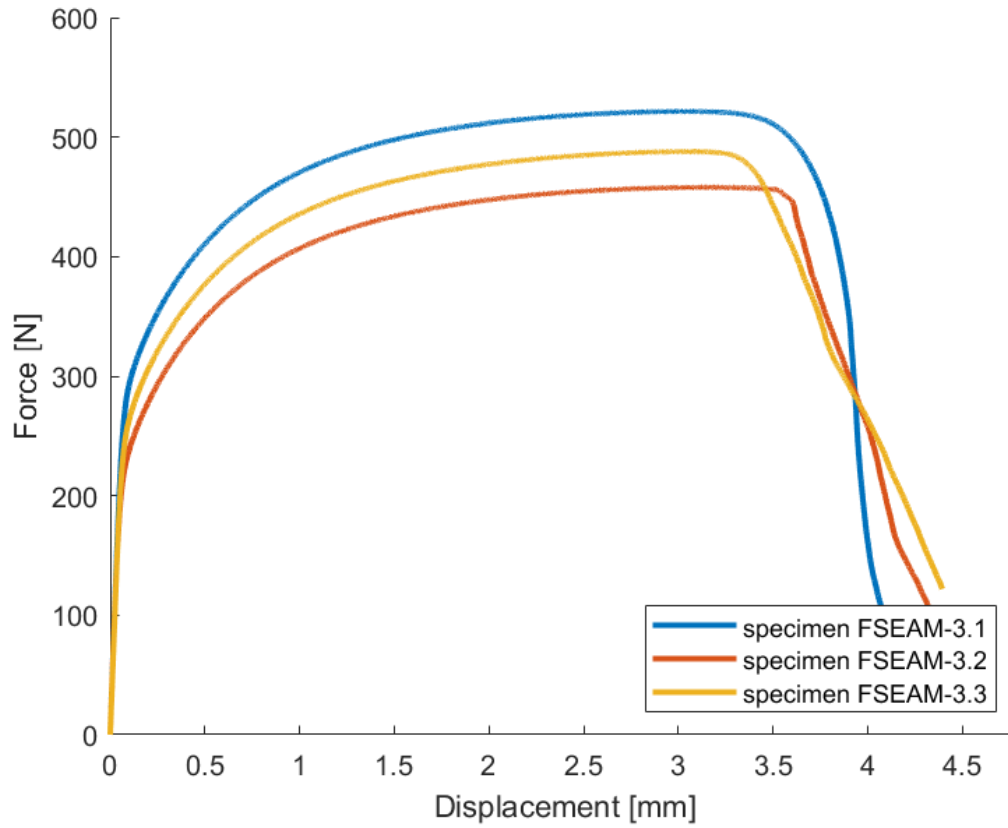
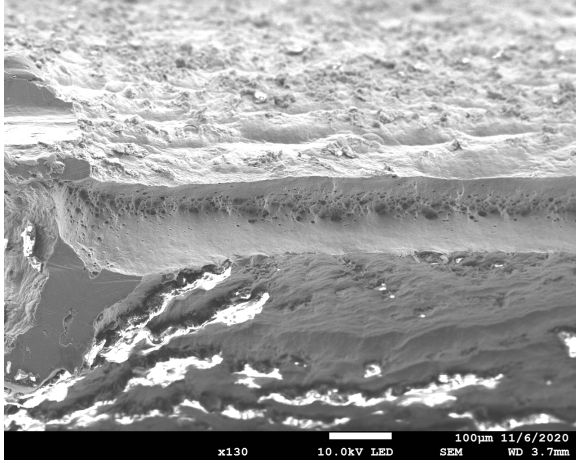
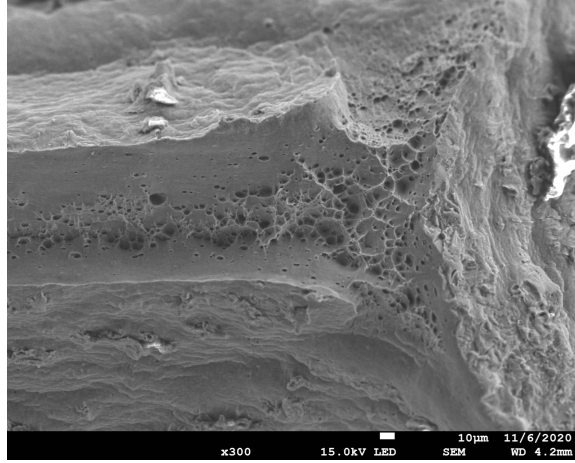
Tensile test

Figure D.29: Force-displacement curves of the tensile test samples of FSEAM-2.

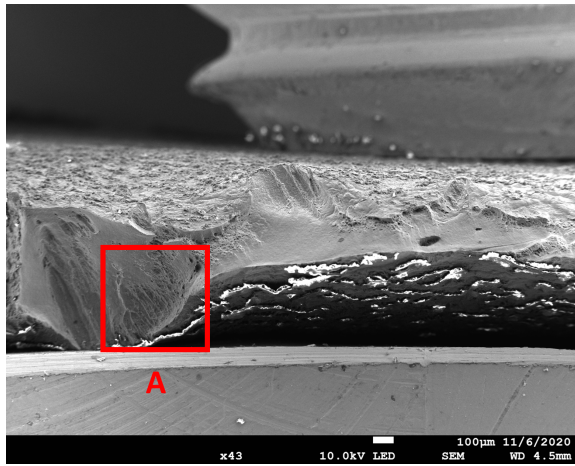
SEM images

(a) SEM of fracture surface of tensile test 2.1 part 1.

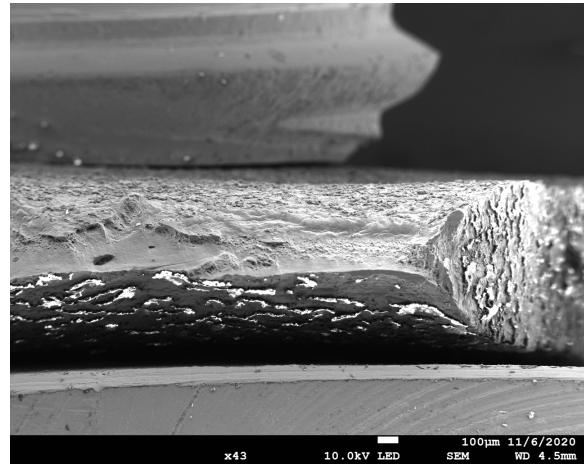


(b) SEM of fracture surface of tensile test 2.1 part 2.

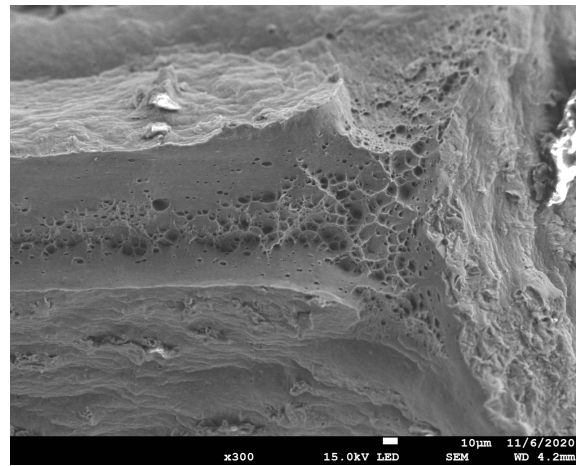
Figure D.30: Fracture surface of tensile test 2.1.



(a) SEM of fracture surface of tensile test 2.3 part 1.



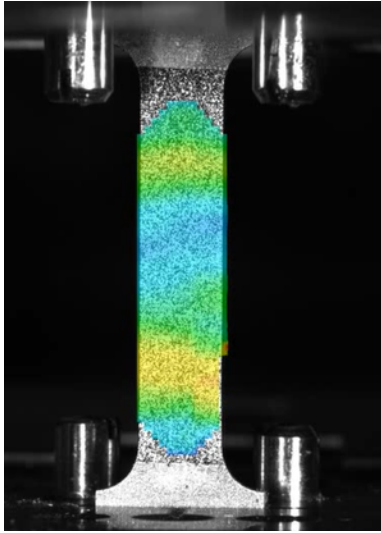
(b) SEM of fracture surface of tensile test 2.3 part 2.



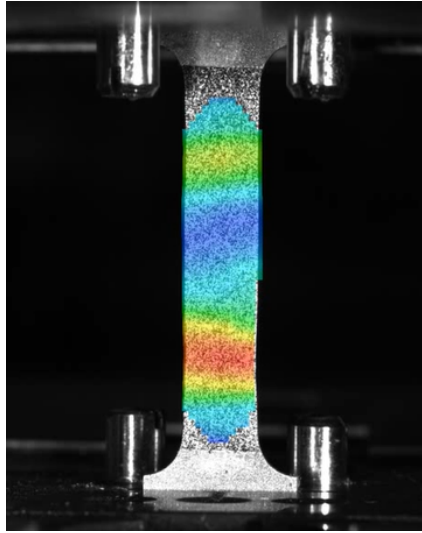
(c) Zoomed in image of section A.

Figure D.31: Fracture surface of tensile test 2.3.

Aramis system

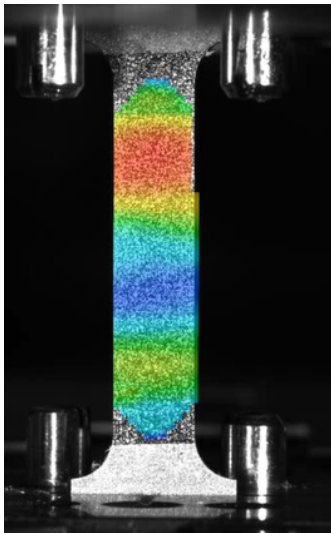


(a) Major strain of tensile test sample 2.1 halfway until it starts to neck.



(b) Major strain of tensile test sample 2.1 before it starts to neck.

Figure D.32: Major strain behaviour of tensile test 2.1.

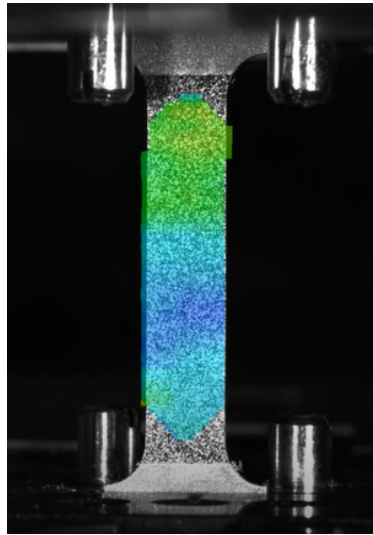


(a) Major strain of tensile test sample 2.2 halfway until it starts to neck.

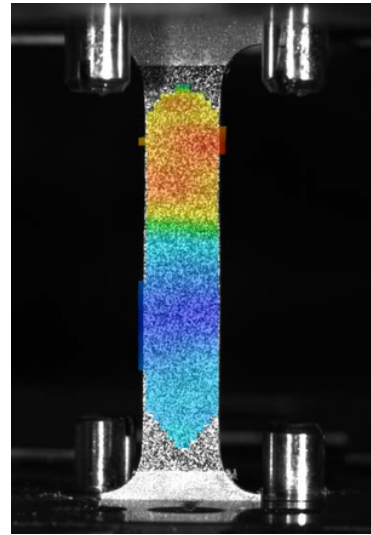


(b) Major strain of tensile test sample 2.2 before it starts to neck.

Figure D.33: Major strain behaviour of tensile test 2.2.



(a) Major strain of tensile test sample 2.3 halfway until it starts to neck.

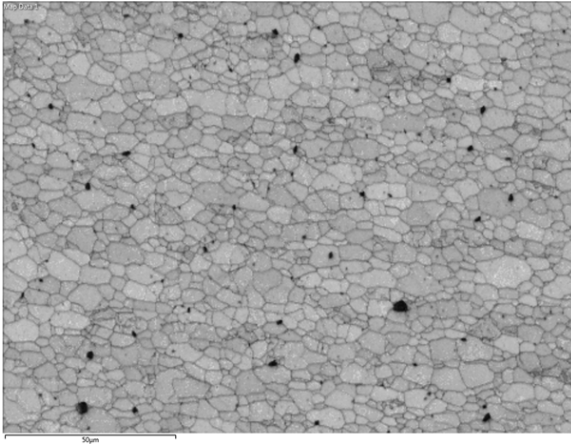


(b) Major strain of tensile test sample 2.3 before it starts to neck.

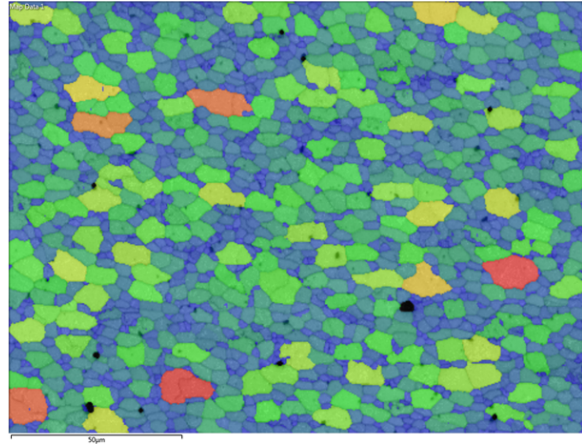
Figure D.34: Major strain behaviour of tensile test 2.3.

EBSD images

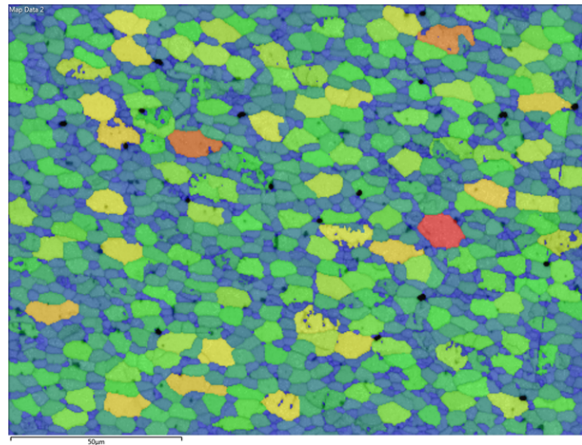
The measurements are taken from the bottom side of the substrate (measurement 1) up to the top of the deposited layers (measurement 6).



(a) Grain boundaries at the bottom part of FSEAM-2 measurement 1.

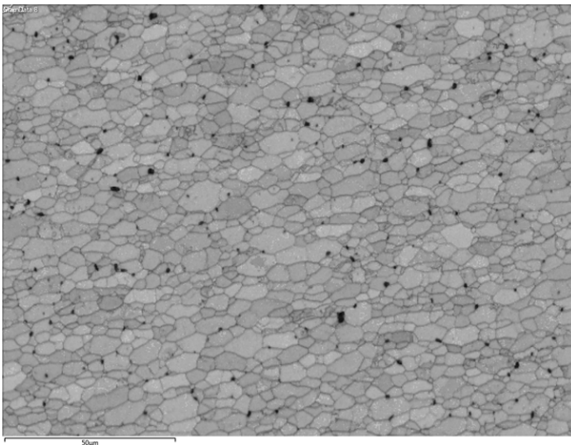


(b) Grain size measurement at the bottom part of FSEAM-2 measurement 1.

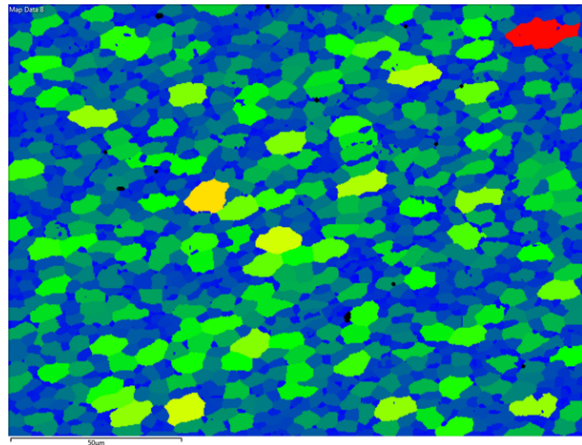


(c) No grain boundaries at the bottom part of FSEAM-2 measurement 2 made.

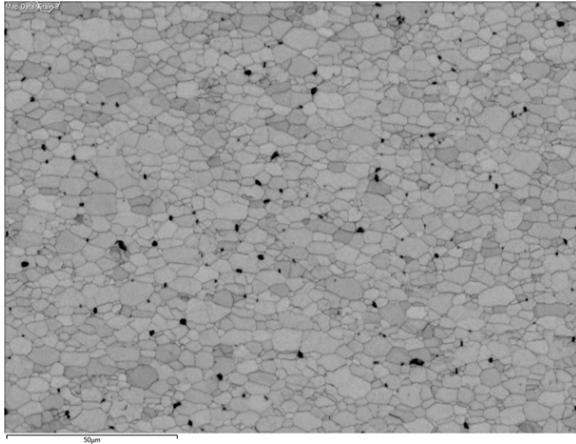
(d) Grain size measurement at the bottom part of FSEAM-2 measurement 2.



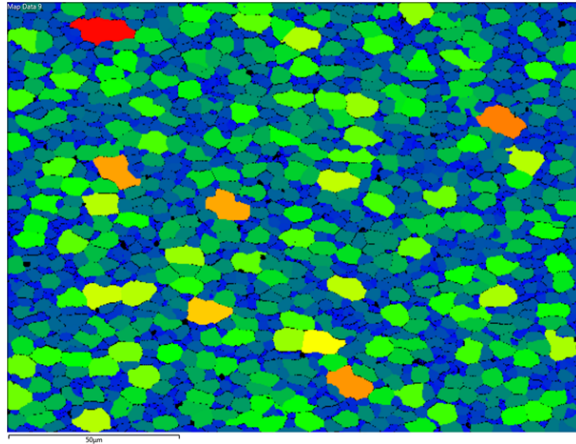
(e) Grain boundaries at the middle part of FSEAM-2 measurement 3.



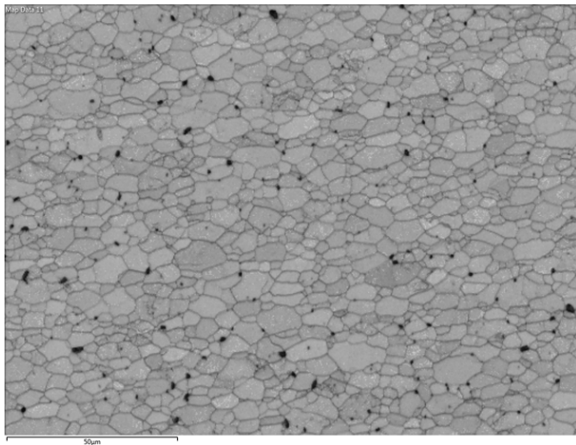
(f) Grain size measurement at the middle part of FSEAM-2 measurement 3.



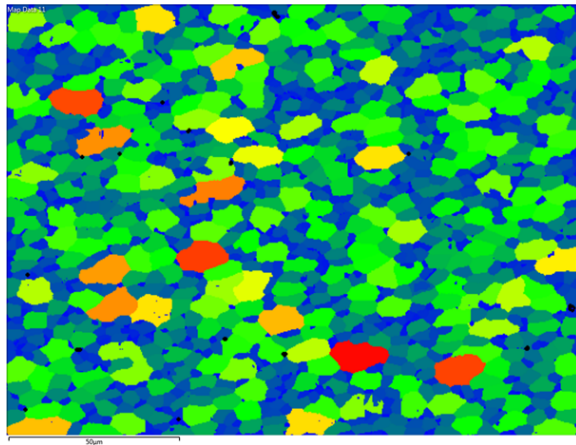
(g) Grain boundaries at the middle part of FSEAM-2 measurement 4.



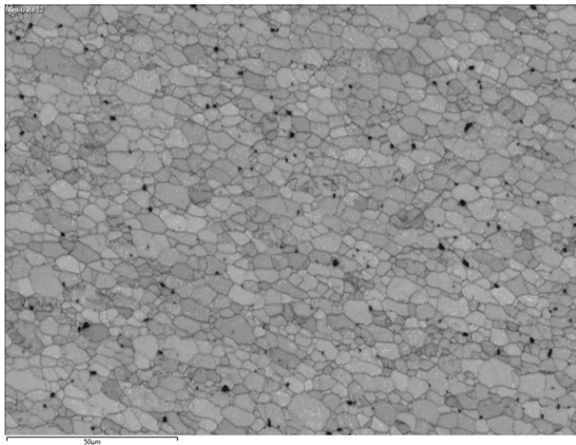
(h) Grain size measurement at the middle part of FSEAM-2 measurement 4.



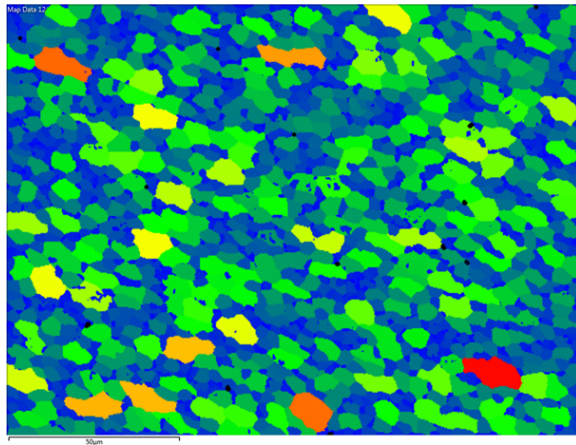
(i) Grain boundaries at the top part of FSEAM-2 measurement 5.



(j) Grain size measurement at the top part of FSEAM-2 measurement 5.



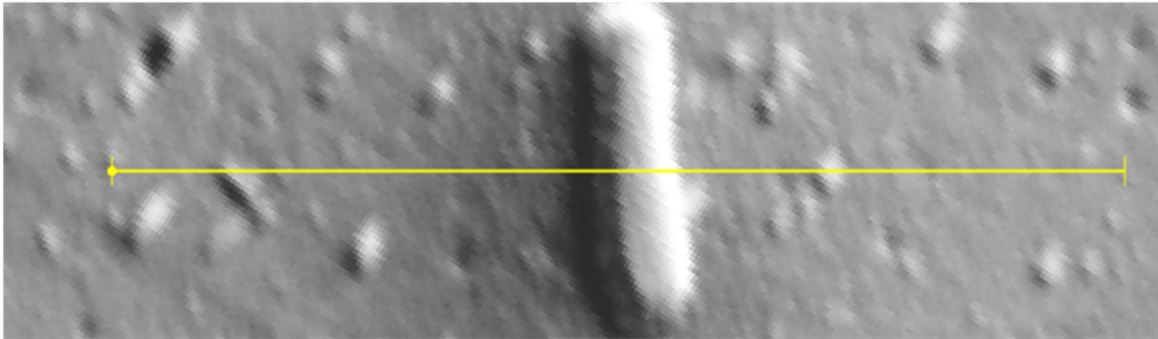
(k) Grain boundaries at the top part of FSEAM-2 measurement 6.



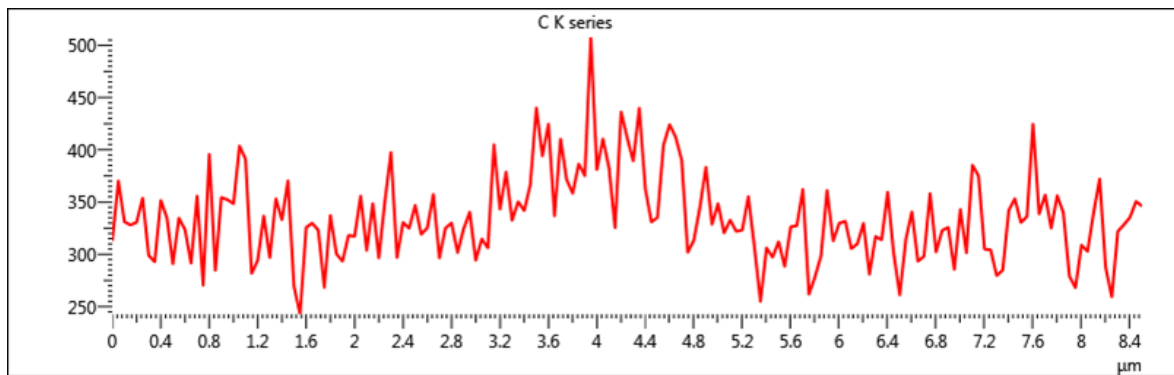
(l) Grain size measurement at the top part of FSEAM-2 measurement 6.

Figure D.35: Grain boundary and size measurement from the substrate side to the top side of the deposited layers, respectively from measurement 1 to 6.

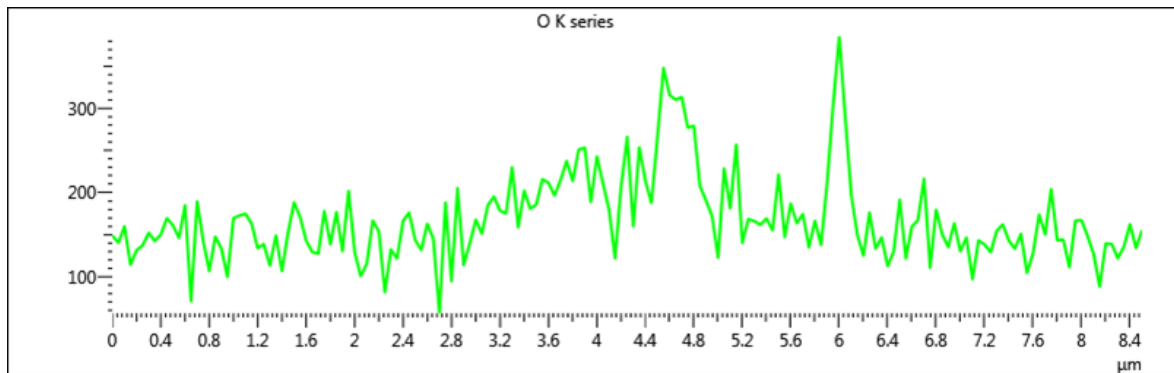
EDX of black particle



(a) Black particle as depicted in the grain boundary images shown in figure D.35.

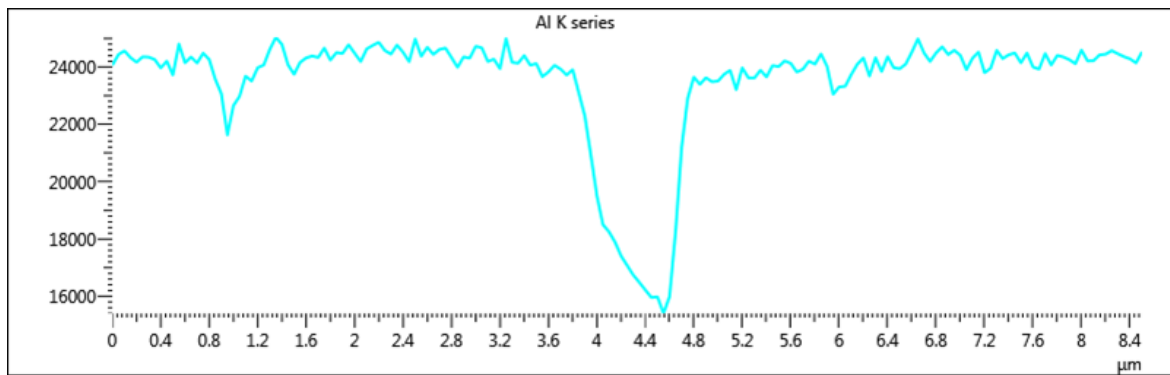


(b) Carbon content across the yellow line in figure D.36a

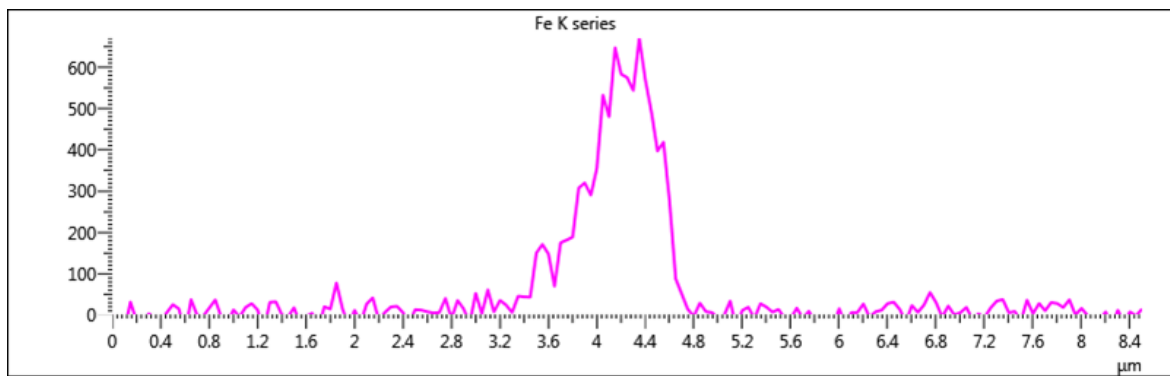


(c) Oxide content across the yellow line in figure D.36a

Figure D.36: Content of a 'black particle' as depicted in the grain boundary images shown in figure D.35.



(a) Aluminium content accross the yellow line in figure D.36a



(b) Iron content accross the yellow line in figure D.36a

Figure D.37: Content of a 'black particle' as depicted in the grain boundary images shown in figure D.35 (continued).

D.4 FSEAM-3

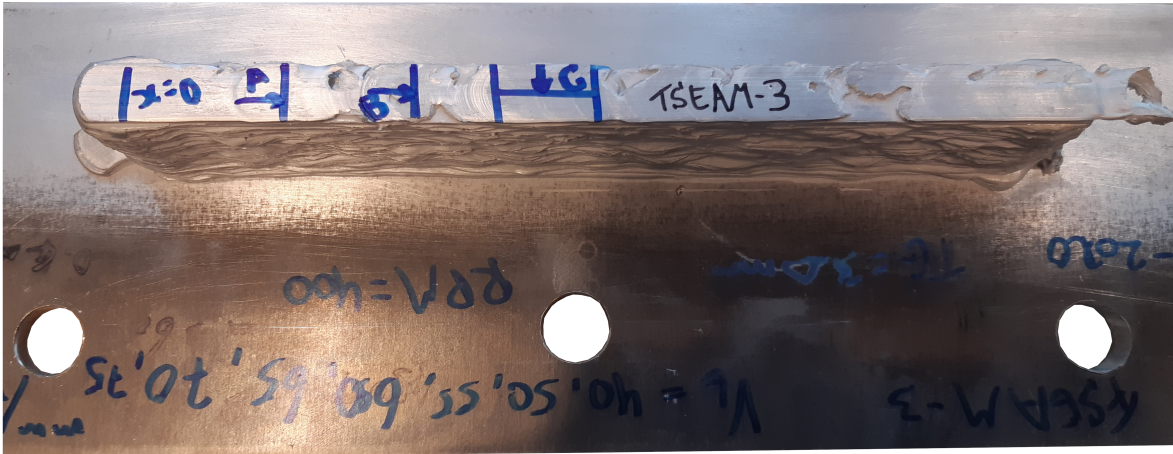


Figure D.38: Indication of the starting position $x = 0$ corresponding to the contour graph of the deposited layers.

Nozzle temperature and extrusion force contour graphs

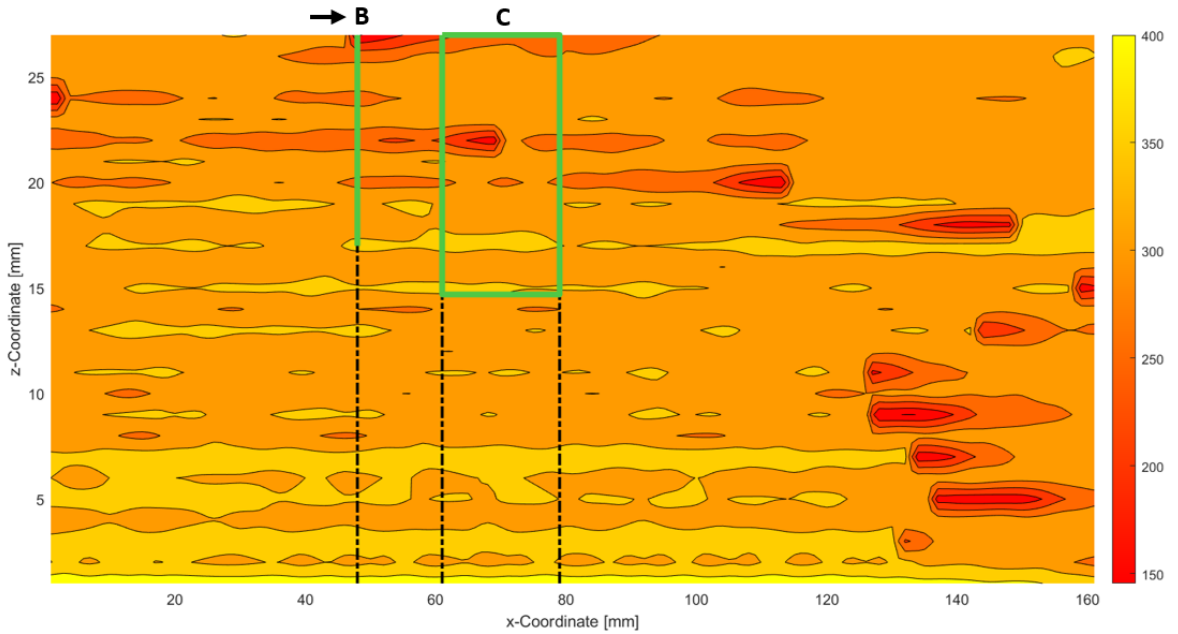


Figure D.39: Nozzle temperature of the third experiment corresponding to the x- and z-coordinate of the AM wall including the locations of the microscopy.

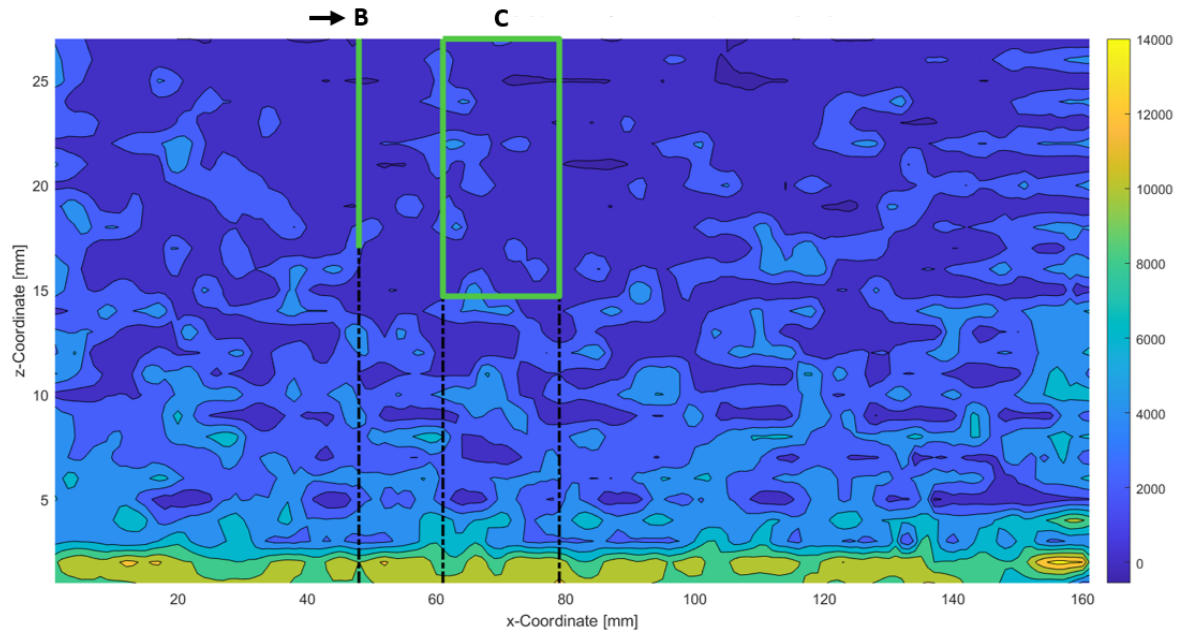


Figure D.40: Extrusion force of the third experiment corresponding to the x- and z-coordinate of the AM wall including the locations of the microscopy.

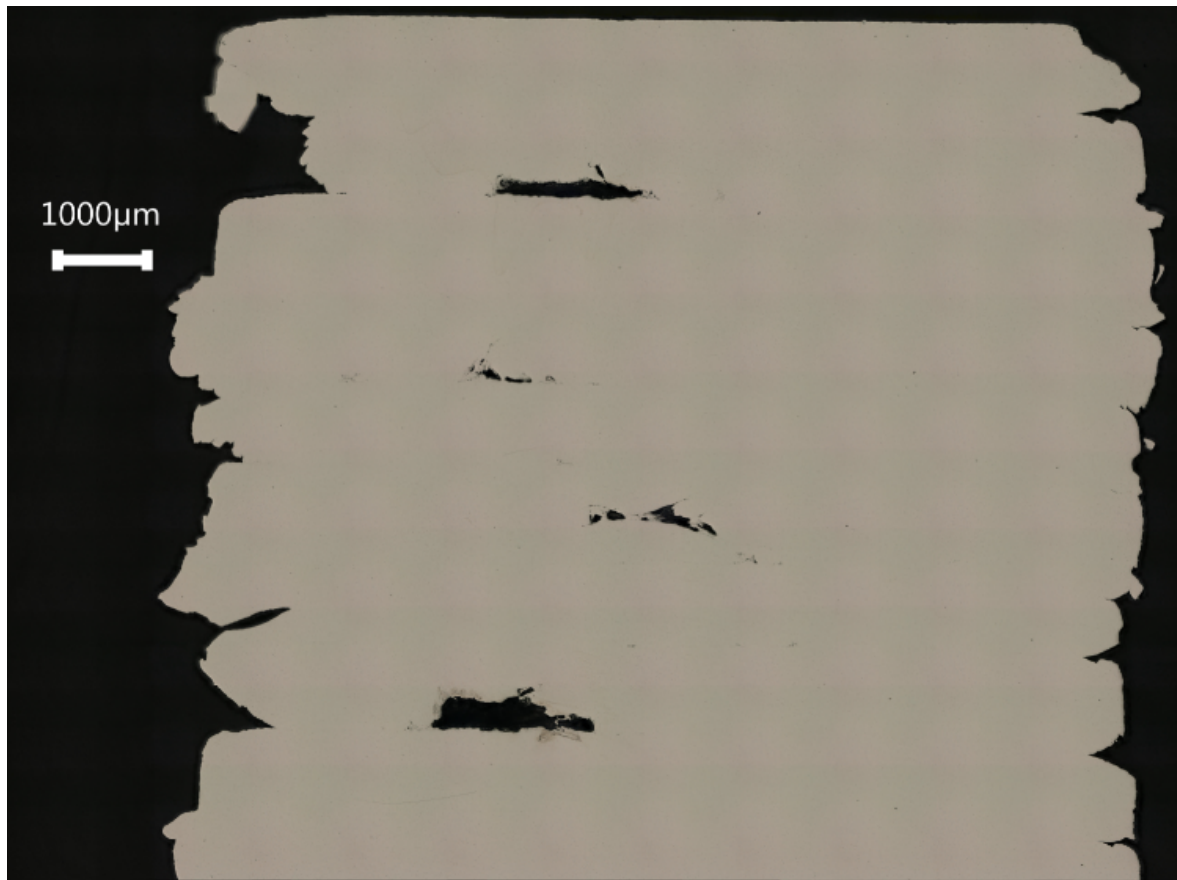
Microscopic images

Figure D.41: Transverse cross-section of FSEAM-3B.

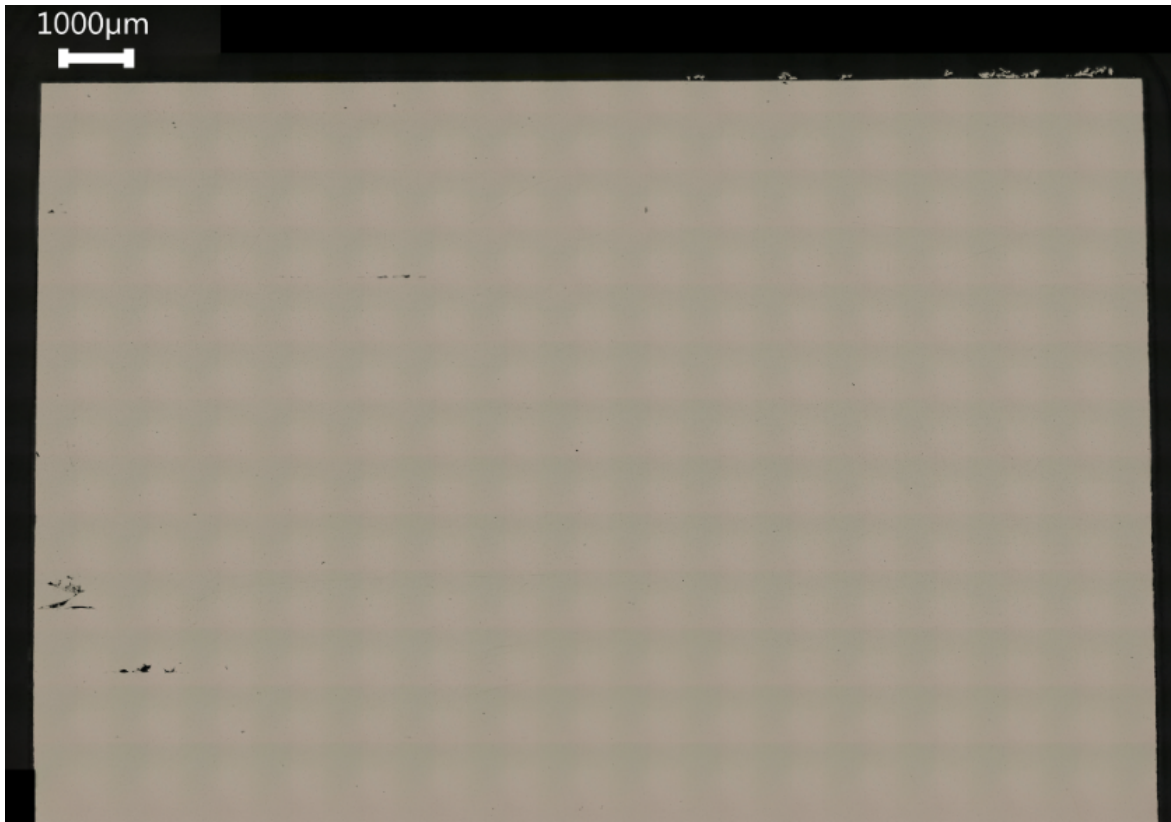


Figure D.42: Longitudinal cross-section of FSEAM-3C.

D.5 FSEAM-4

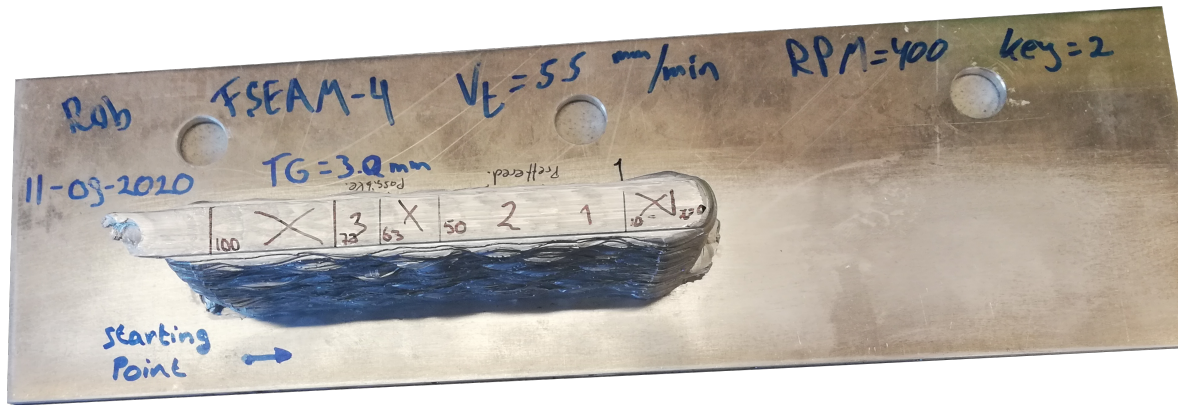


Figure D.43: Indication of the starting position $x = 0$ corresponding to the contour graph of the deposited layers.

Nozzle temperature and extrusion force contour graphs

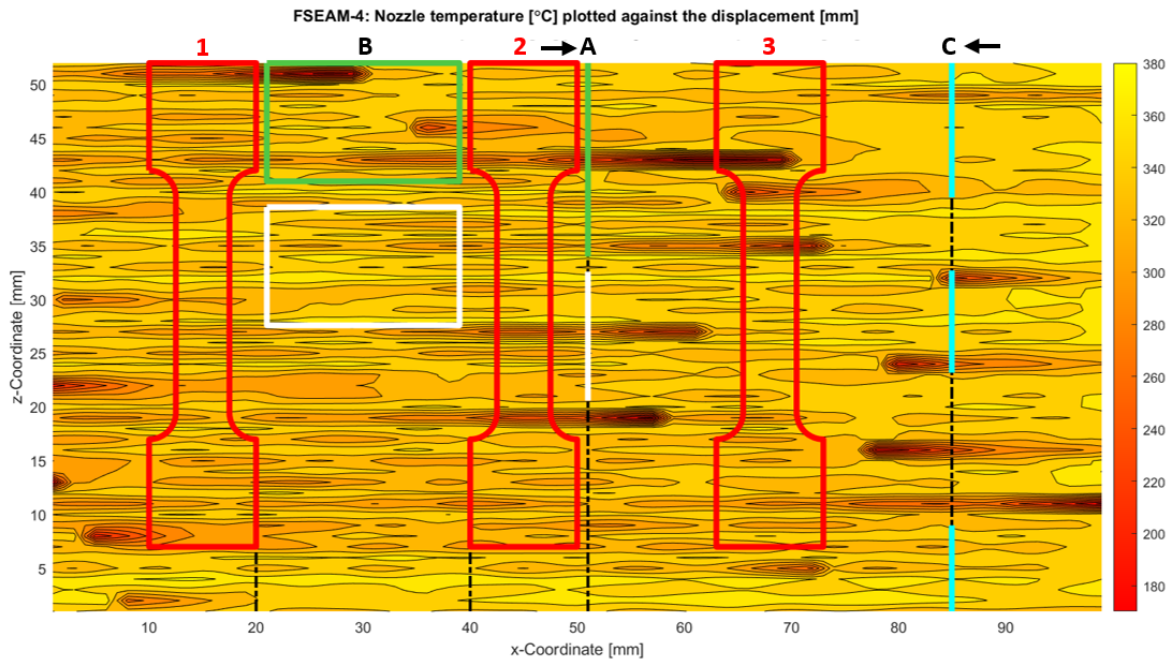


Figure D.44: Nozzle temperature of the fourth experiment corresponding to the x- and z-coordinate of the AM wall including the locations of the tensile test, microscopy, hardness test, and EBSD.

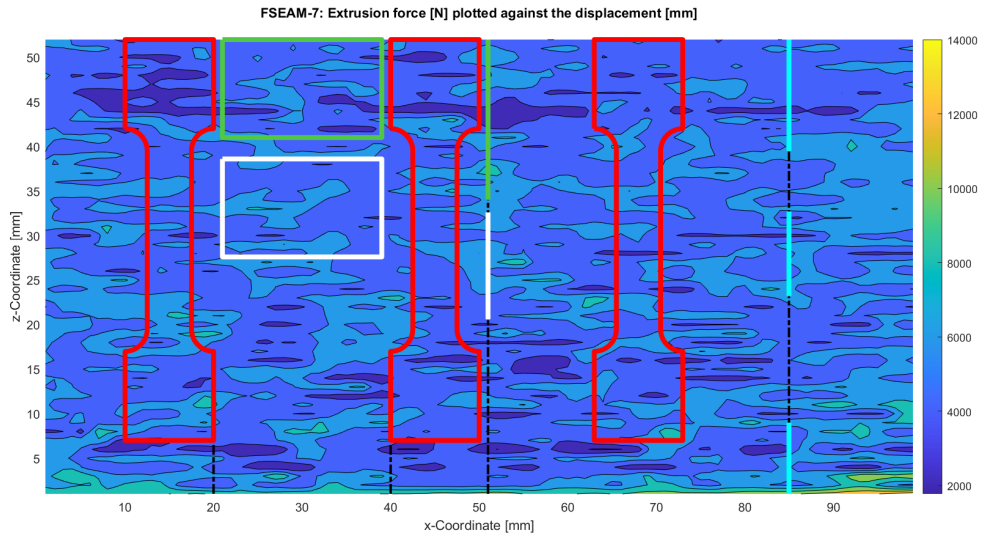


Figure D.45: Extrusion force of the fourth experiment corresponding to the x- and z-coordinate of the AM wall including the locations of the tensile test, microscopy, hardness test, and EBSD.

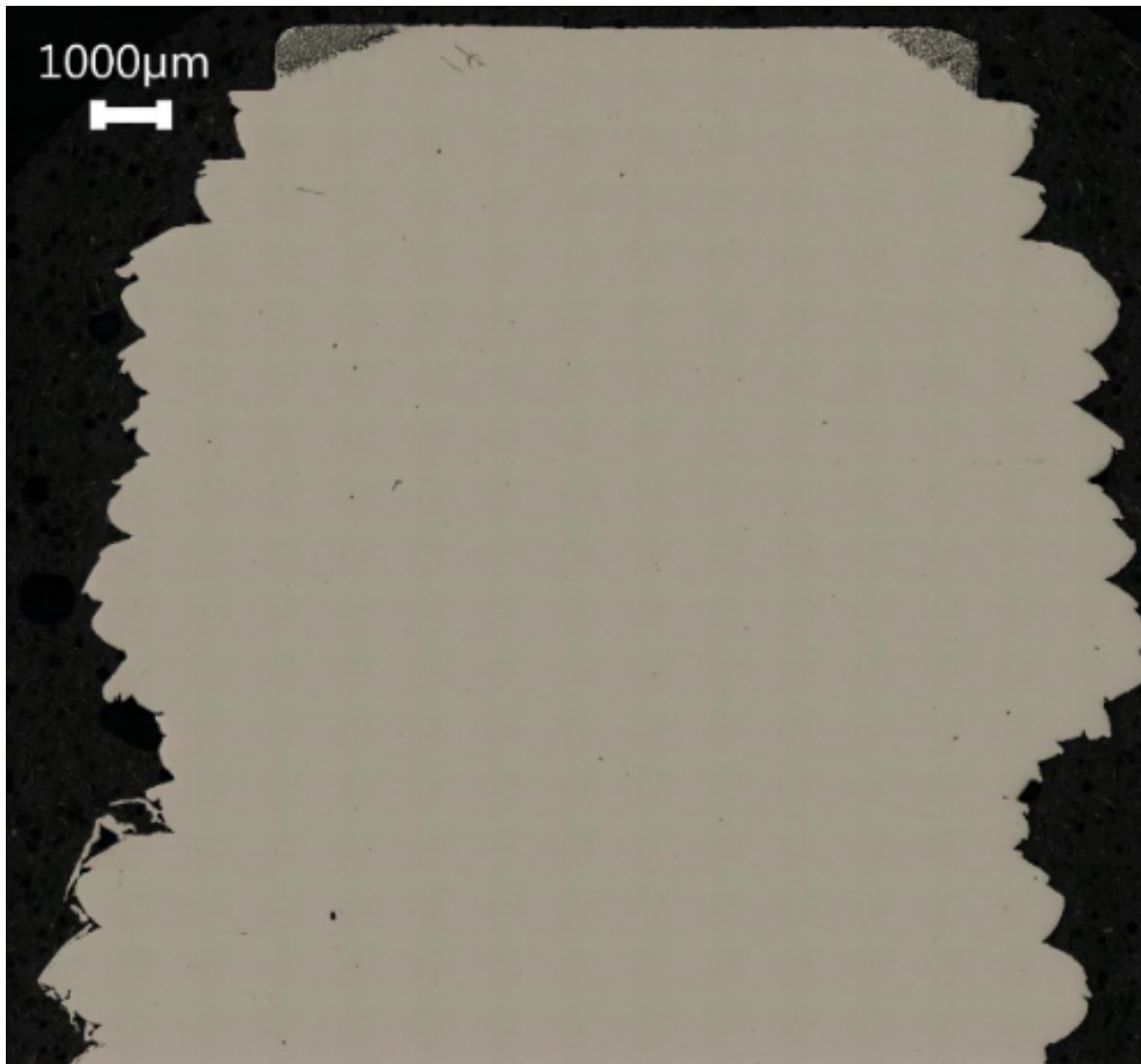
Microscopic images

Figure D.46: Transverse cross-section of FSEAM-4A.

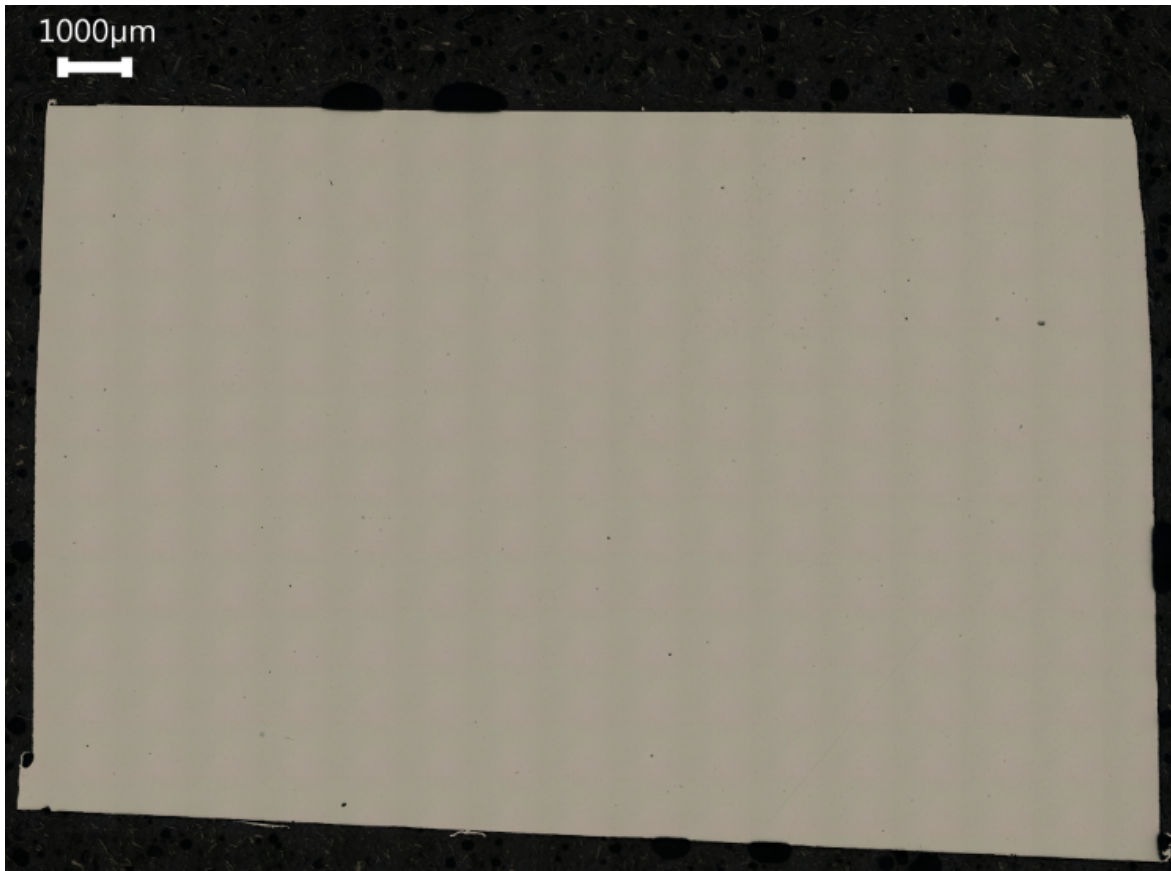
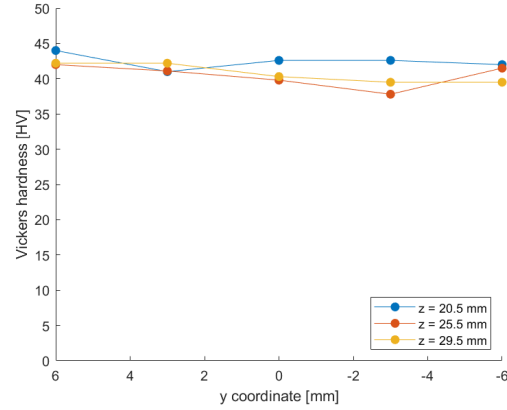
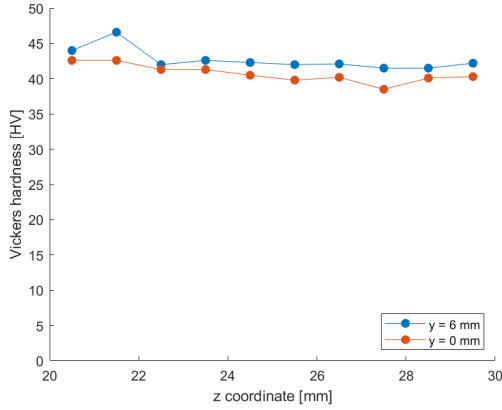
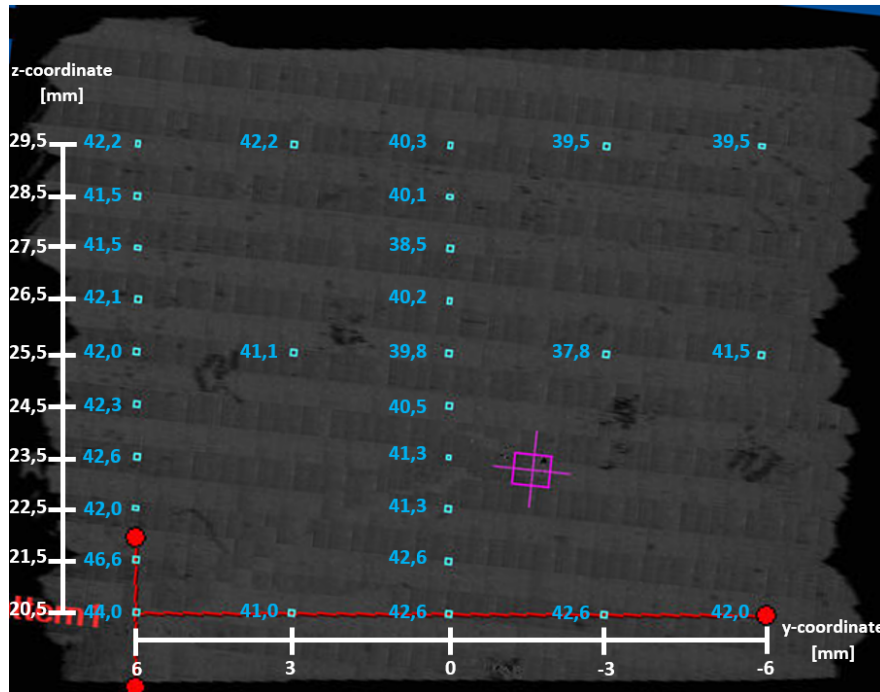


Figure D.47: Longitudinal cross-section of FSEAM-4B.

Hardness test

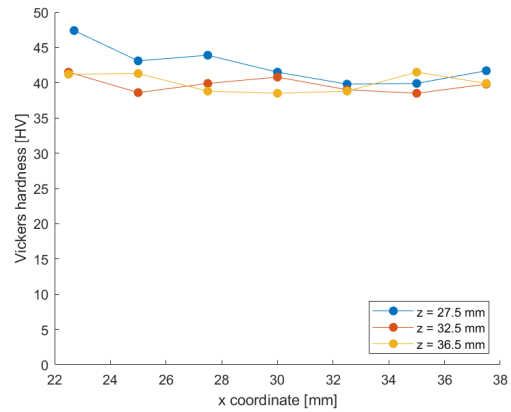
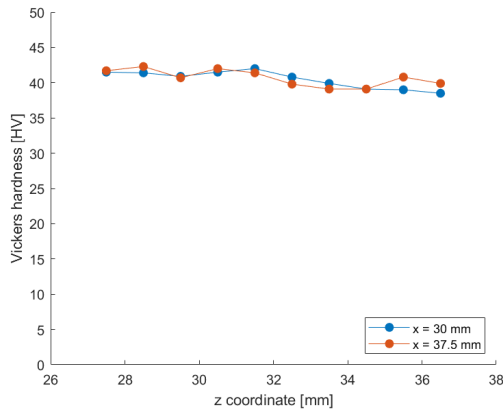


(a) Hardness throughout the height of FSEAM-4A in transverse direction. (b) Hardness throughout the width of FSEAM-4A in transverse direction.

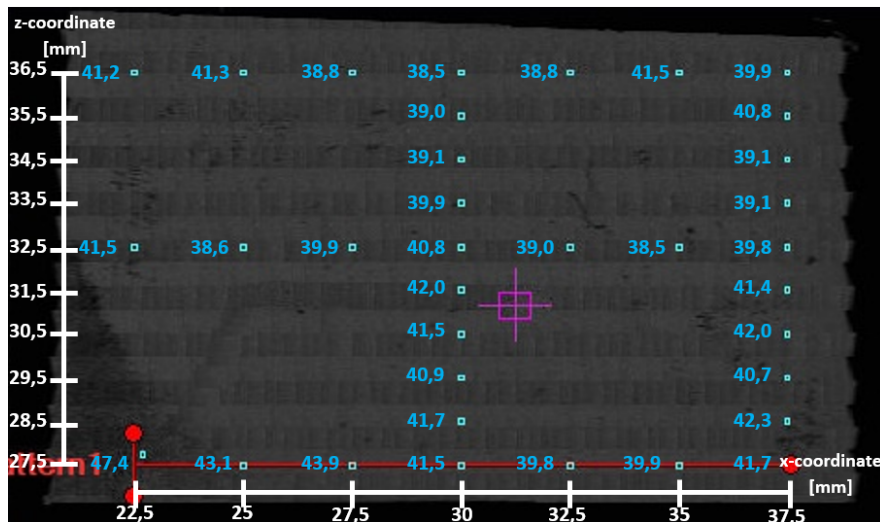


(c) Hardness throughout the transverse cross-section of FSEAM-2A.

Figure D.48: Overview of the hardness of FSEAM-4A in transverse direction.



(a) Hardness throughout the height of FSEAM-4B in longitudinal direction. (b) Hardness throughout the width of FSEAM-4B in longitudinal direction.



(c) Hardness throughout the longitudinal cross-section of FSEAM-2B.

Figure D.49: Overview of the hardness of FSEAM-4B in longitudinal direction.

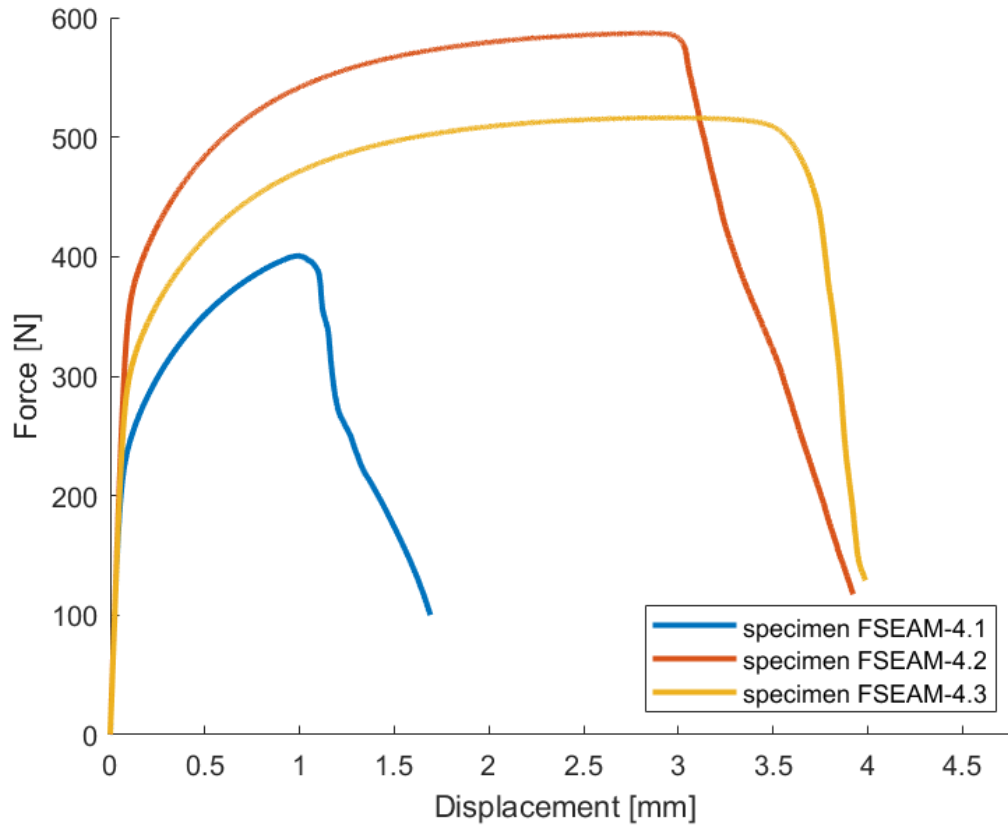
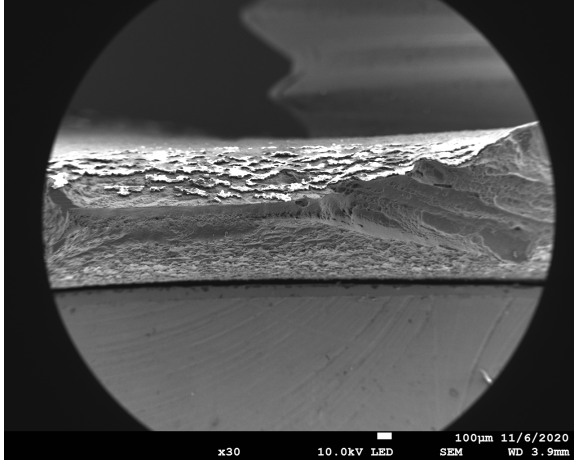
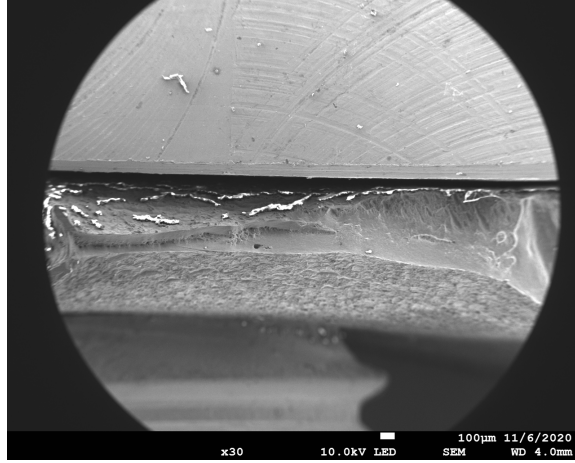
Tensile test

Figure D.50: Force-displacement curves of the tensile test samples of FSEAM-4.

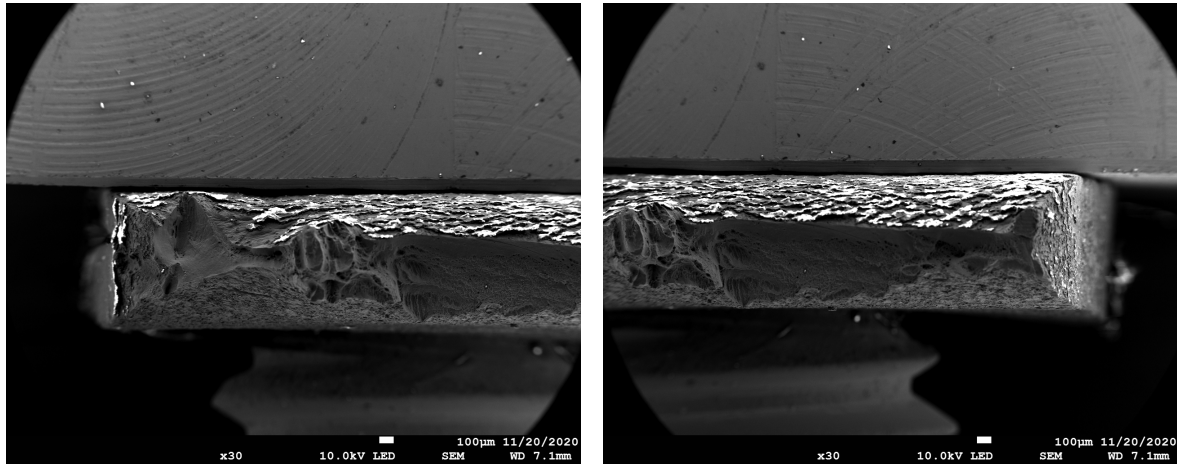
SEM images

(a) SEM of fracture surface of tensile test 4.1.



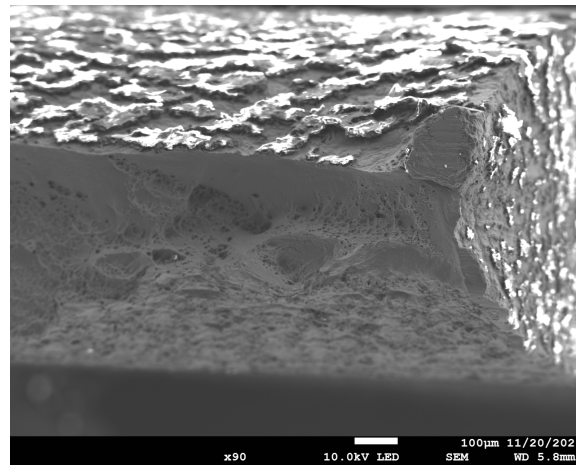
(b) SEM of fracture surface of tensile test 4.2.

Figure D.51: Fracture surface overviews of tensile test 4.1 and 4.2.



(a) SEM of fracture surface of tensile test 4.3 part 1.

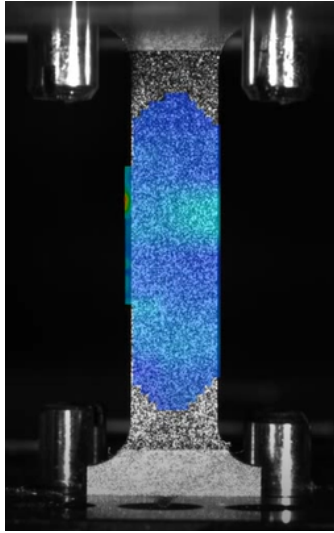
(b) SEM of fracture surface of tensile test 4.3 part 2.



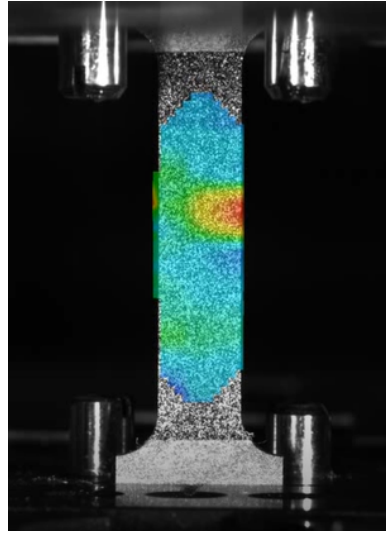
(c) SEM of fracture surface of zoomed of the right part.

Figure D.52: Fracture surface of tensile test 4.3.

Aramis system

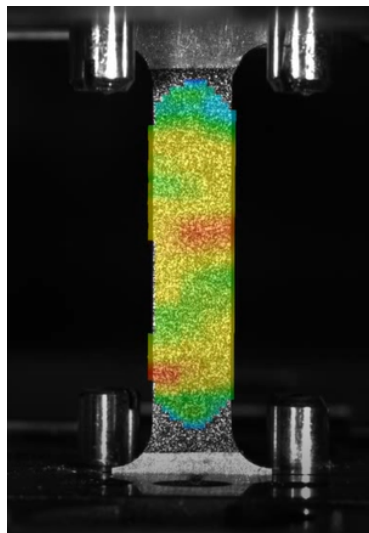


(a) Major strain of tensile test sample 4.1 halfway until it starts to neck.

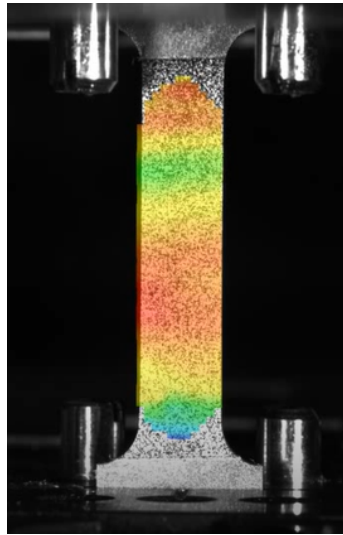


(b) Major strain of tensile test sample 4.1 before it starts to neck.

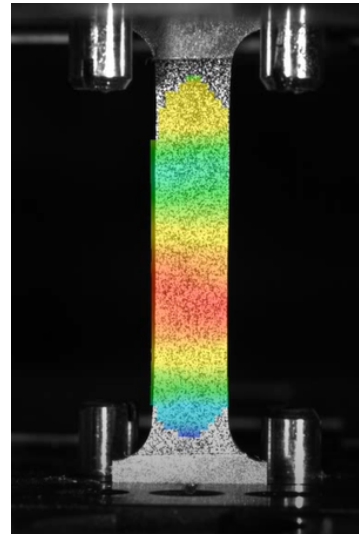
Figure D.53: Major strain behaviour of tensile test 4.1.



(a) Major strain of tensile test sample 4.2 halfway until it starts to neck.



(b) Major strain of tensile test sample 4.3 halfway until it starts to neck.



(c) Major strain of tensile test sample 4.3 before it starts to neck.

Figure D.54: Major strain behaviour of tensile test 4.3.

D.6 FSEAM-5

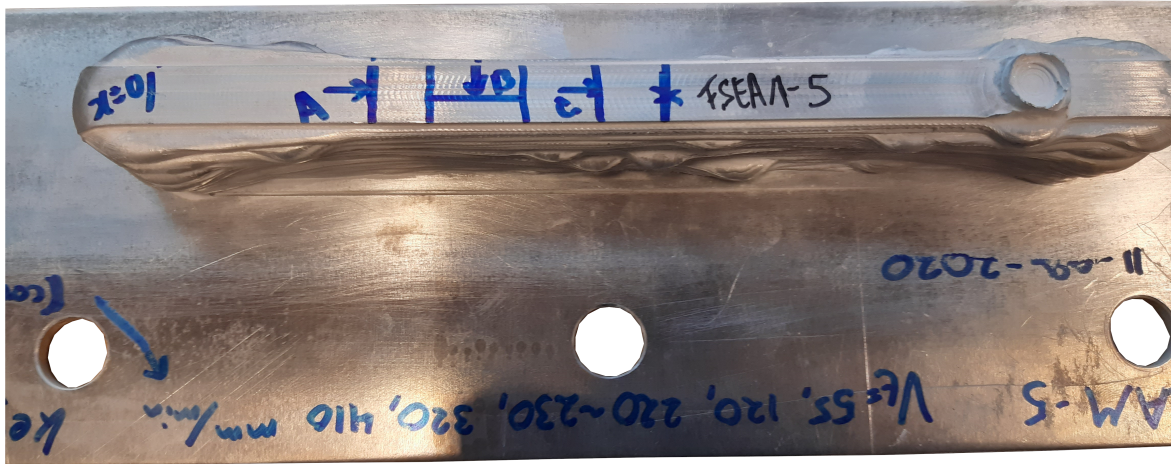


Figure D.55: Indication of the starting position $x = 0$ corresponding to the contour graph of the deposited layers.

Nozzle temperature and extrusion force contour graphs

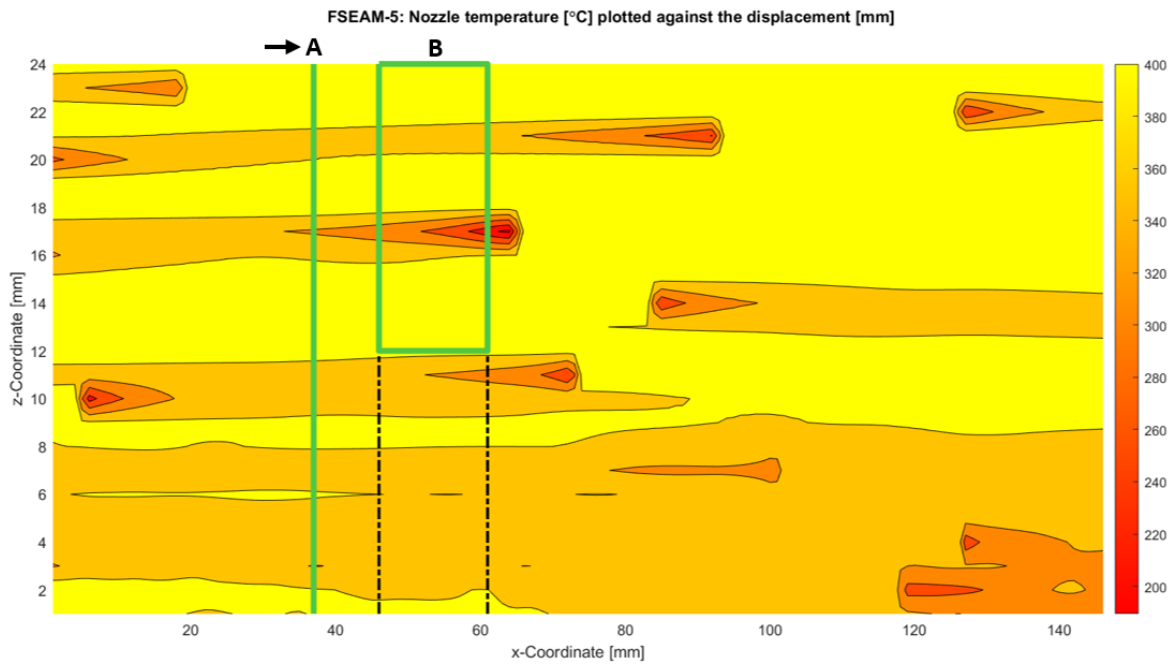


Figure D.56: Nozzle temperature of the fifth experiment corresponding to the x- and z-coordinate of the AM wall including the locations of the microscopy.

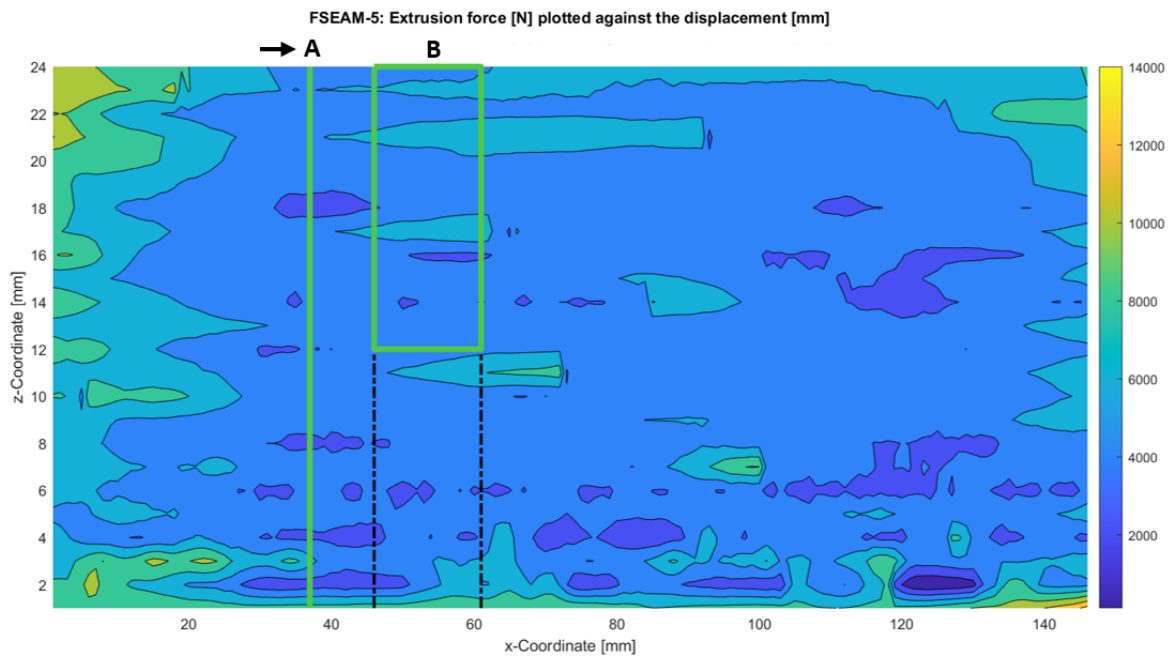


Figure D.57: Extrusion force of the fifth experiment corresponding to the x- and z-coordinate of the AM wall including the locations of the microscopy.

Microscopic images

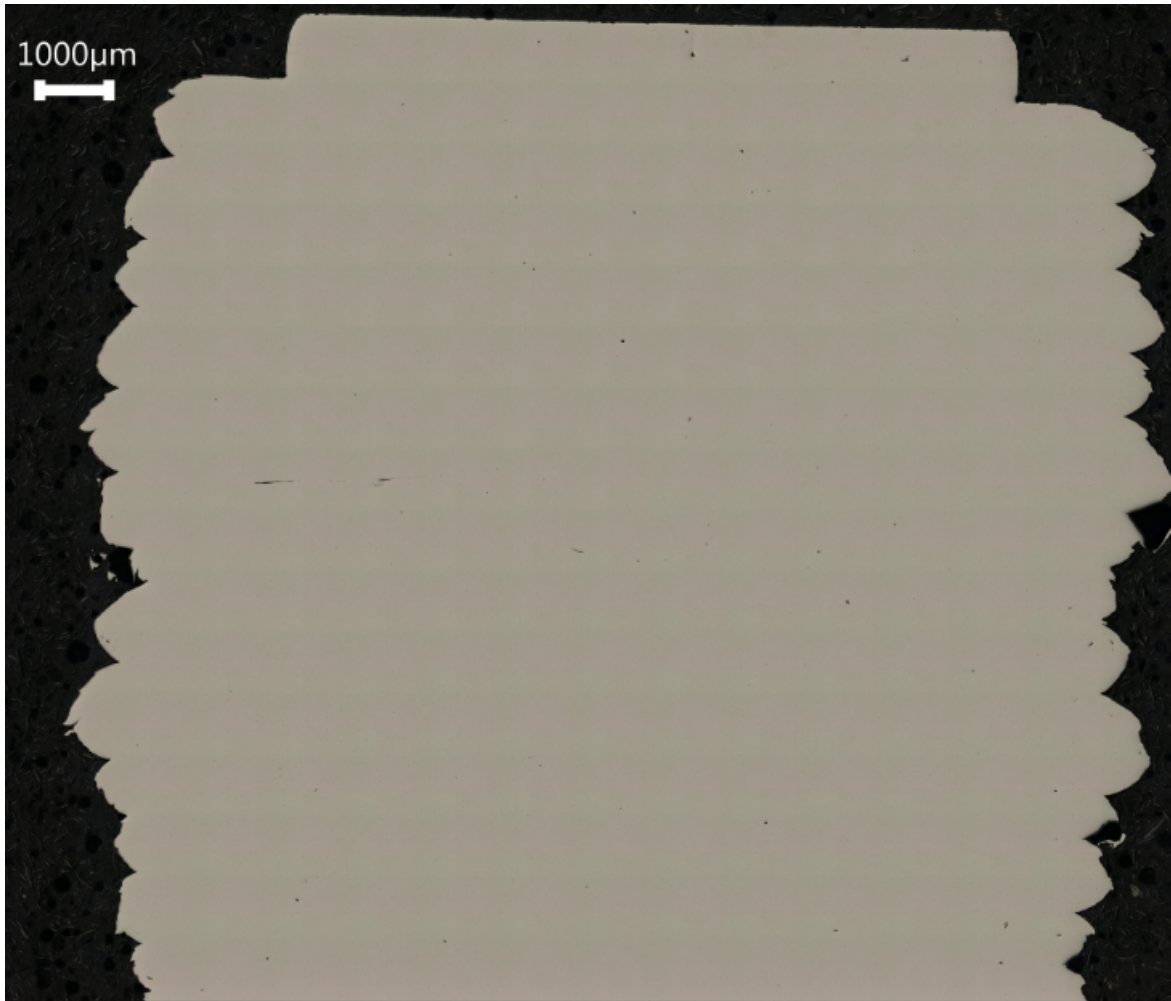


Figure D.58: Transverse cross-section of FSEAM-5A top side.

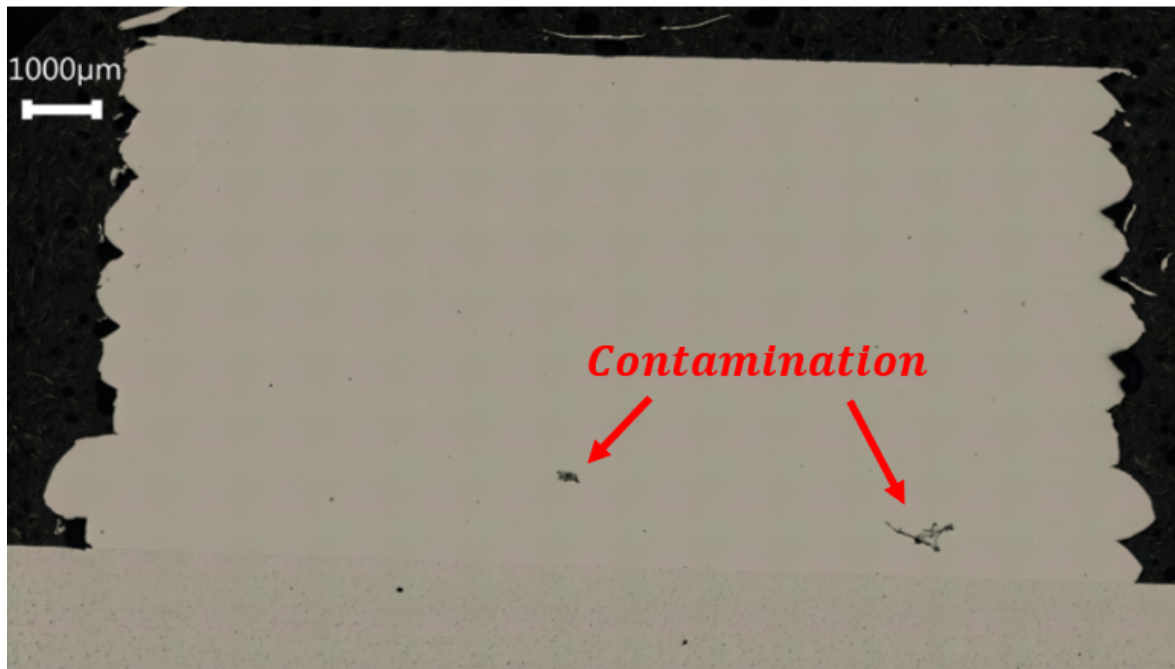


Figure D.59: Transverse cross-section of FSEAM-5A bottom side.

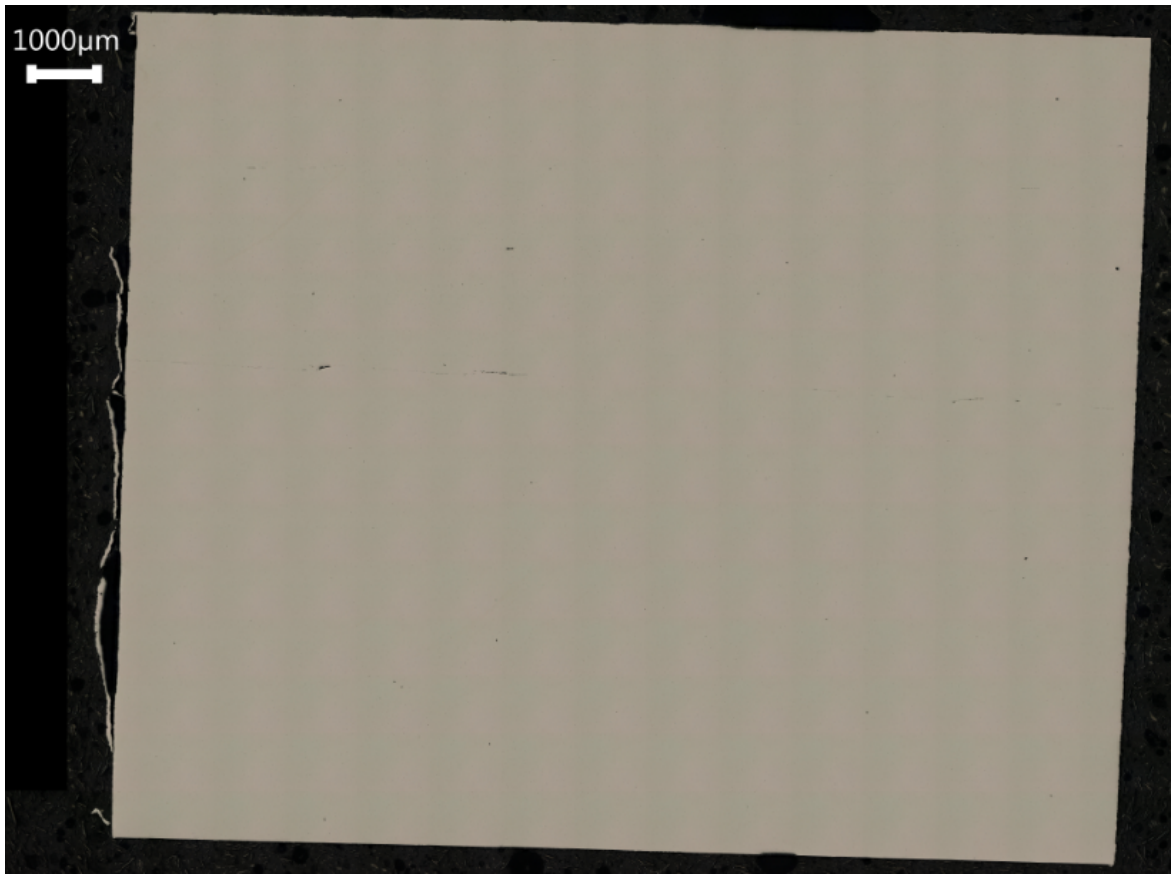


Figure D.60: Longitudinal cross-section of FSEAM-5B.

D.7 FSEAM-6

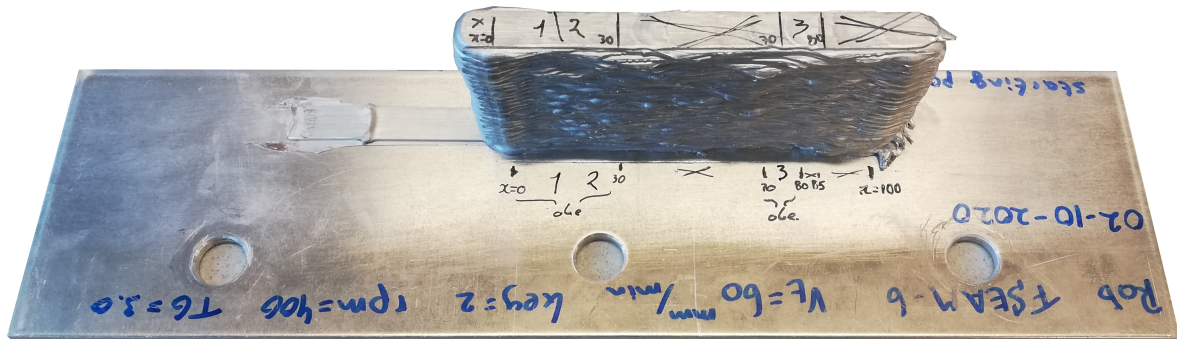


Figure D.61: Indication of the starting position $x = 0$ corresponding to the contour graph of the deposited layers.

Nozzle temperature and extrusion force contour graphs

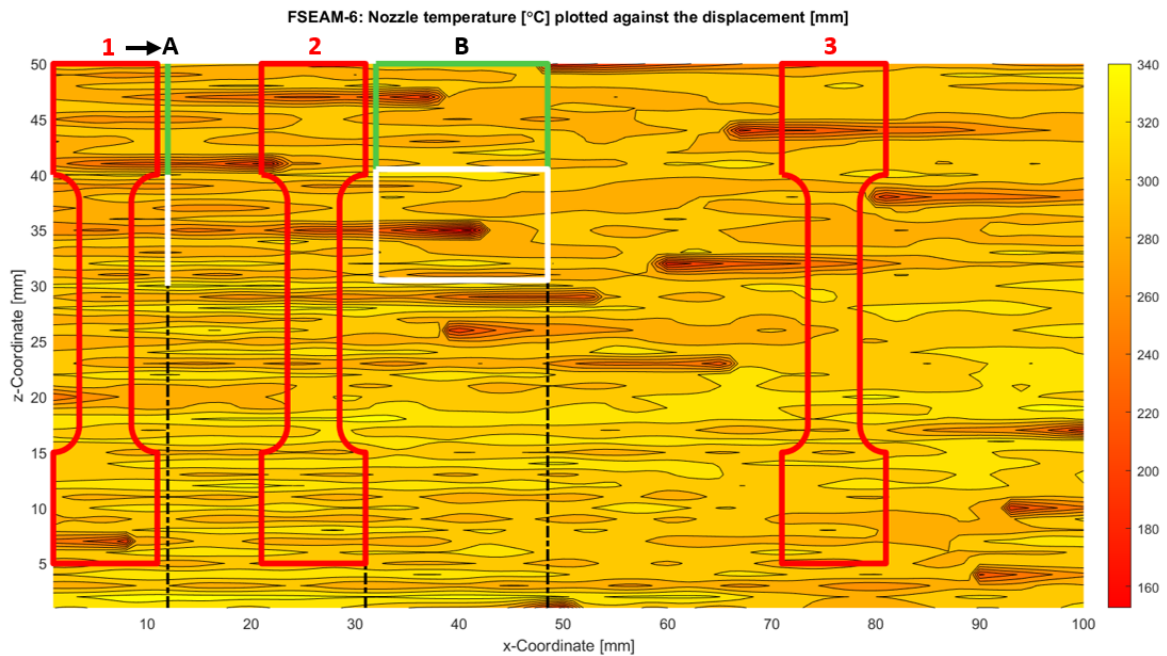


Figure D.62: Nozzle temperature of the sixth experiment corresponding to the x- and z-coordinate of the AM wall including the locations of the tensile test, microscopy, hardness test, and EBSD.

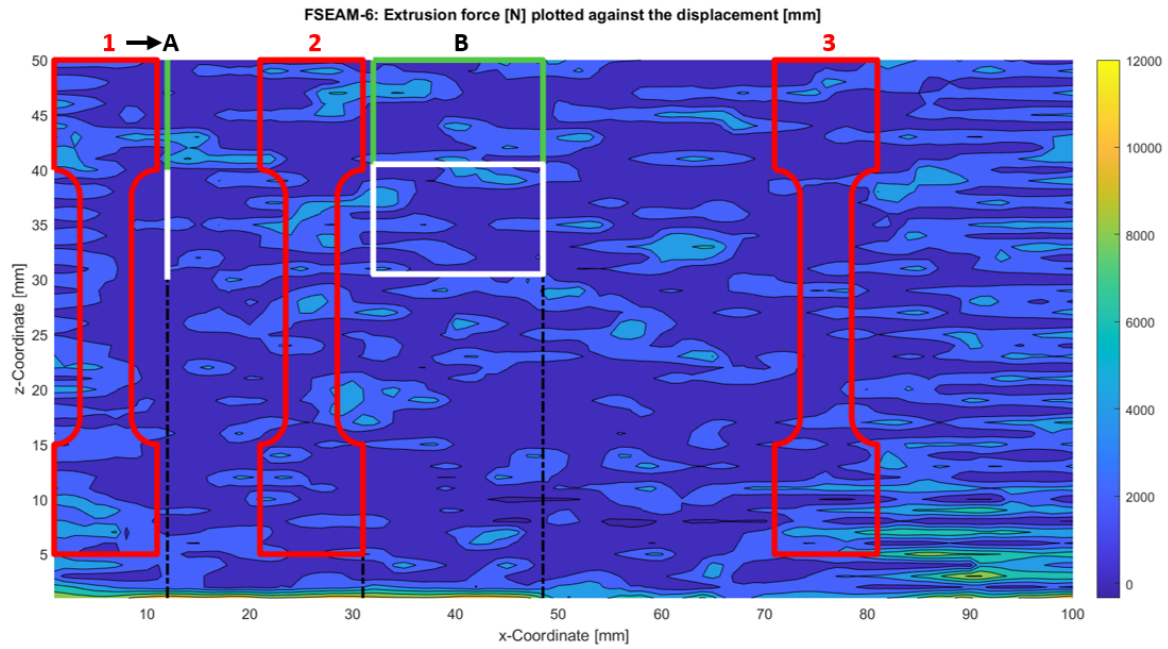


Figure D.63: Extrusion force of the sixth experiment corresponding to the x- and z-coordinate of the AM wall including the locations of the tensile test, microscopy, hardness test, and EBSD.

Microscopic images

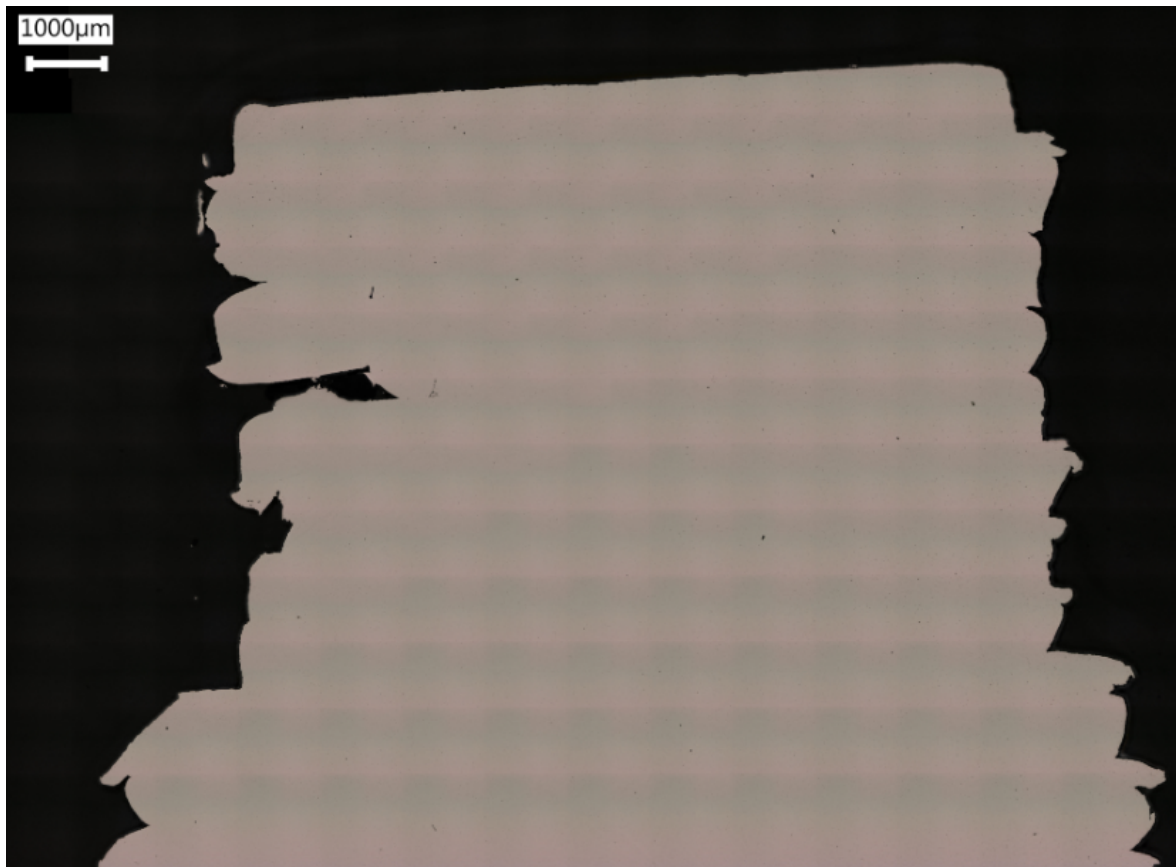


Figure D.64: Transverse cross-section of FSEAM-6A.

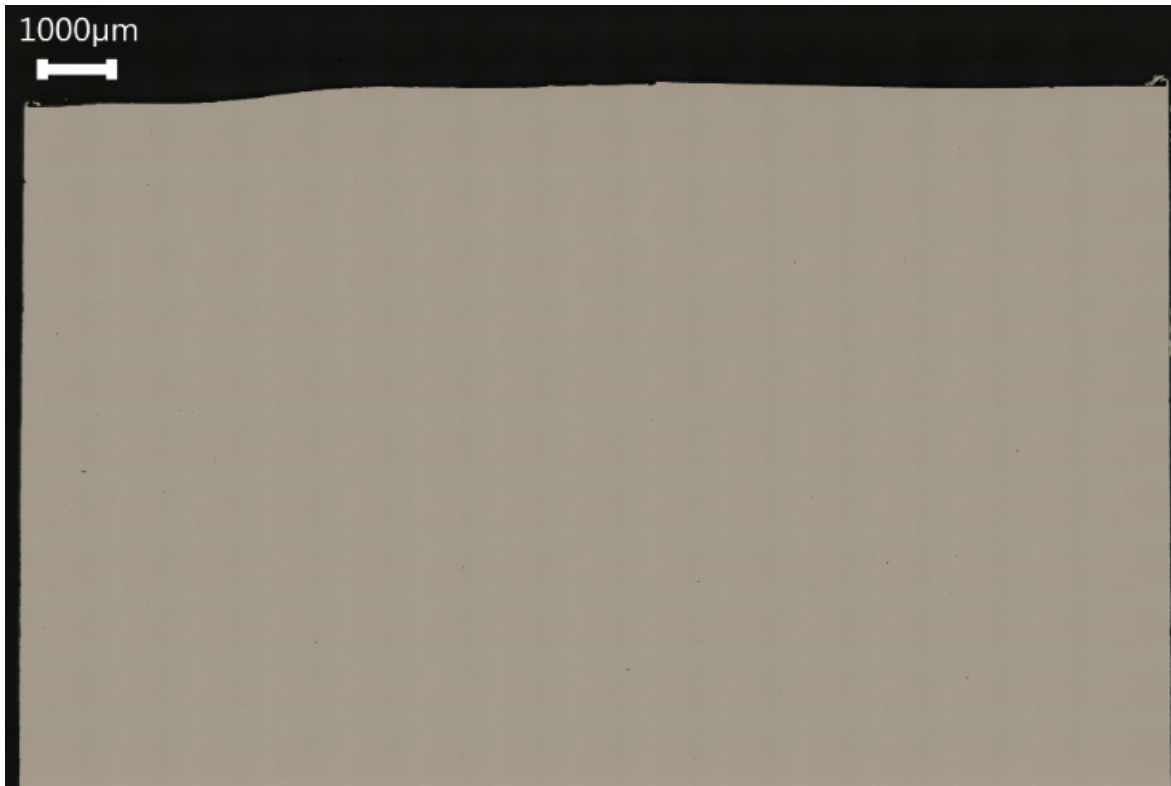
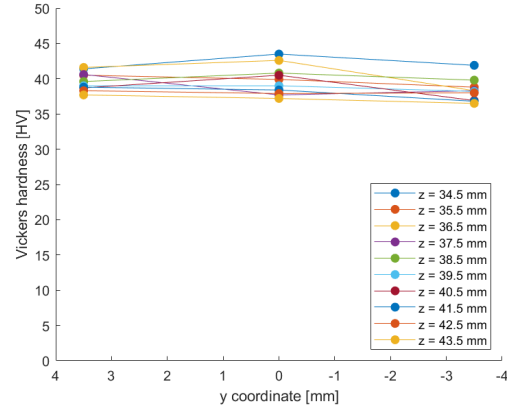
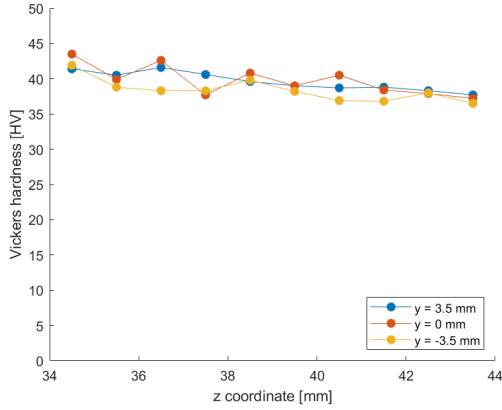
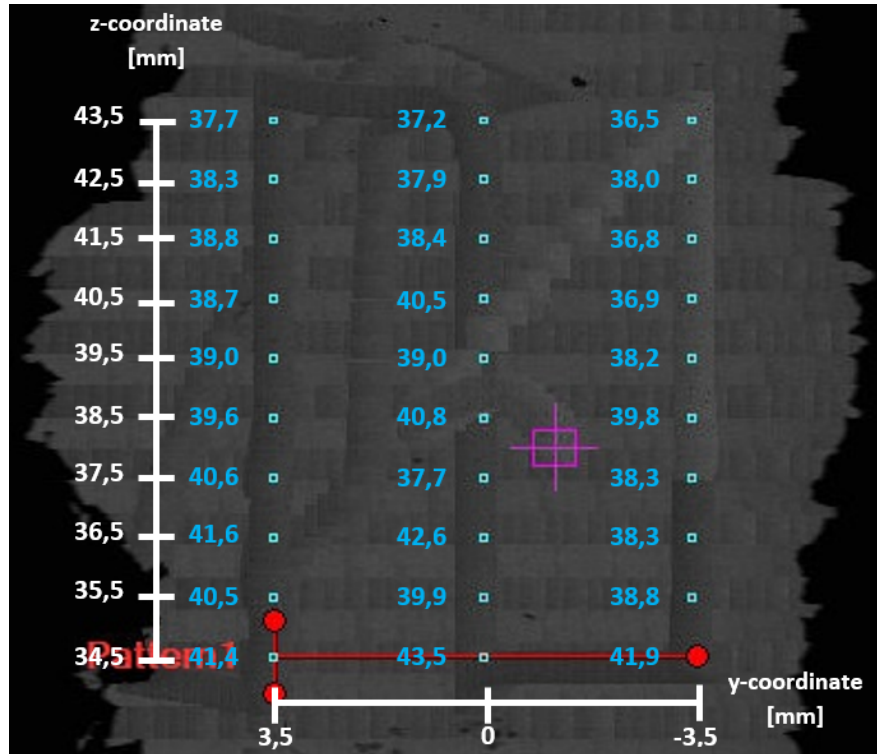


Figure D.65: Longitudinal cross-section of FSEAM-6B.

Hardness test

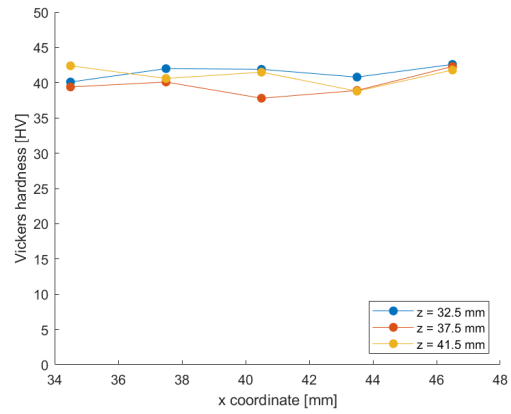
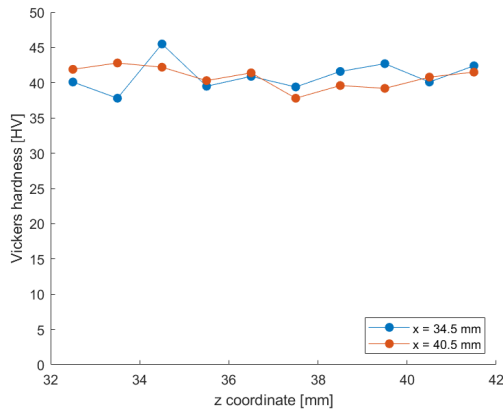


(a) Hardness throughout the height of FSEAM-6A in transverse direction. (b) Hardness throughout the width of FSEAM-6A in transverse direction.

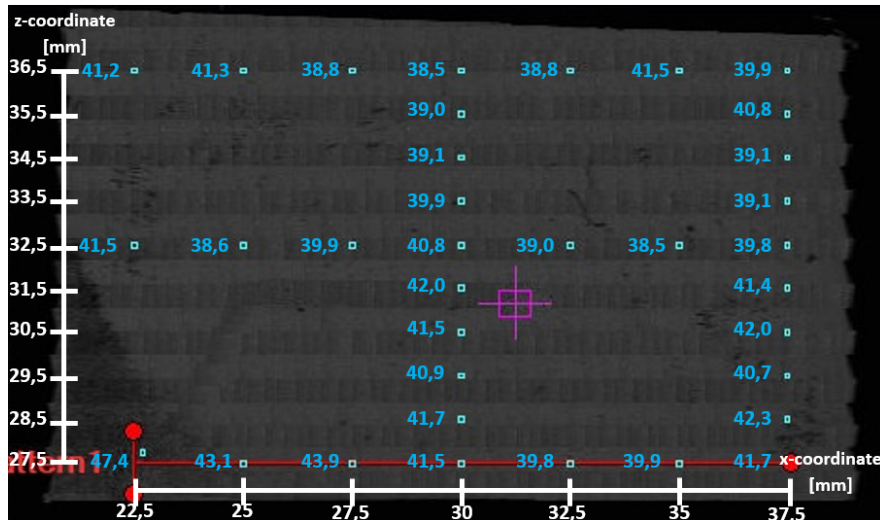


(c) Hardness throughout the transverse cross-section of FSEAM-6A.

Figure D.66: Overview of the hardness of FSEAM-6A in transverse direction.



(a) Hardness throughout the height of FSEAM-6B in longitudinal direction. (b) Hardness throughout the width of FSEAM-6B in longitudinal direction.



(c) Hardness throughout the longitudinal cross-section of FSEAM-6B.

Figure D.67: Overview of the hardness of FSEAM-6B in longitudinal direction.

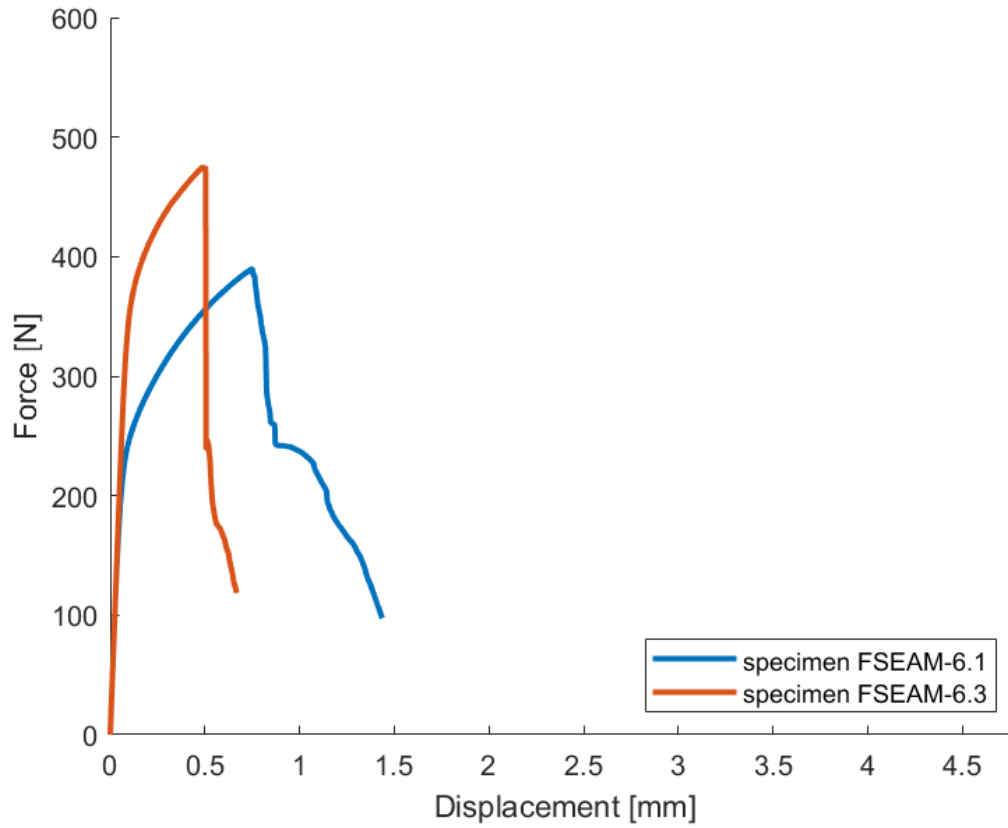
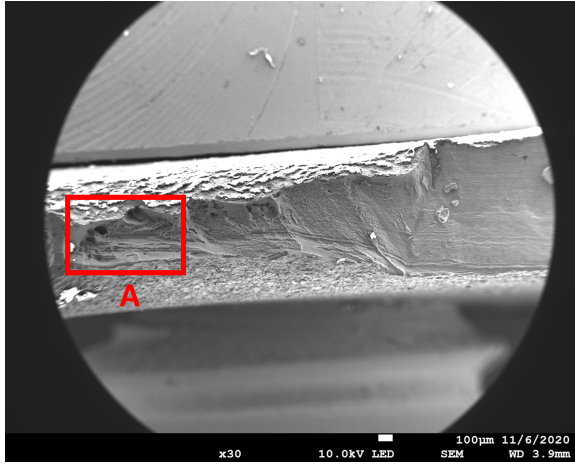
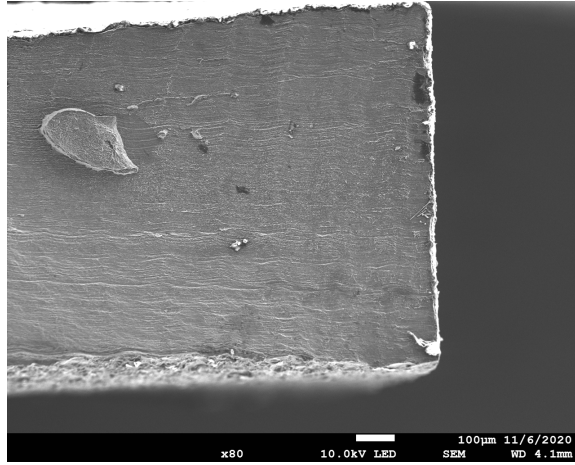
Tensile test

Figure D.68: Force-displacement curves of the tensile test samples of FSEAM-6.

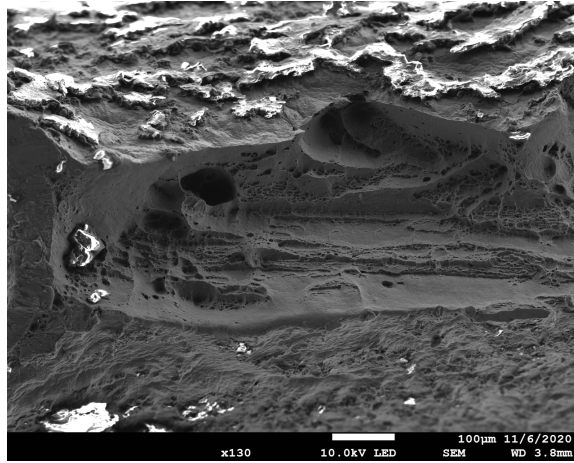
SEM images



(a) SEM of fracture surface of tensile test 6.1 part 1.

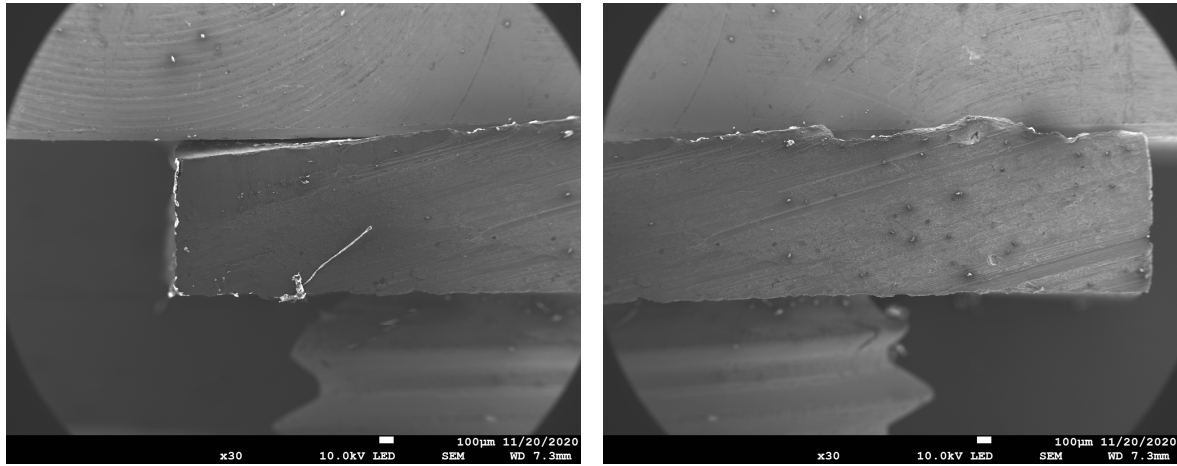


(b) SEM of fracture surface of tensile test 6.1 part 2.



(c) SEM of fracture surface of tensile test 6.1 zoomed in section.

Figure D.69: Fracture surface overviews of tensile test 6.1.



(a) SEM of fracture surface of tensile test 6.3 part 1.

(b) SEM of fracture surface of tensile test 6.3 part 2.

Figure D.70: Fracture surface overviews of tensile test 6.3.

Aramis system

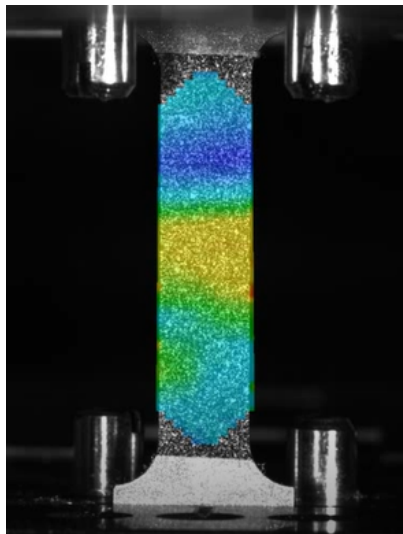


(a) Major strain of tensile test sample 6.1 halfway until it starts to neck.

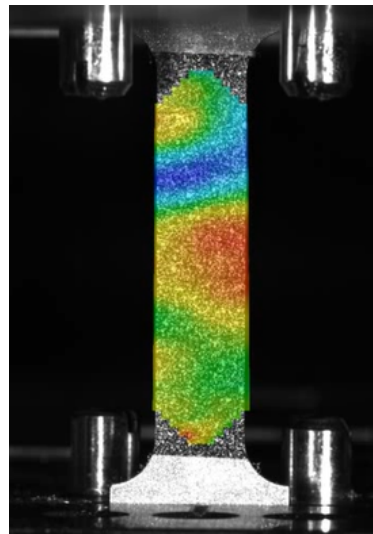


(b) Major strain of tensile test sample 6.1 before it starts to neck.

Figure D.71: Major strain behaviour of tensile test 6.1.



(a) Major strain of tensile test sample 6.3 halfway until it starts to neck.



(b) Major strain of tensile test sample 6.3 before it starts to neck.

Figure D.72: Major strain behaviour of tensile test 6.3.

D.8 FSEAM-7

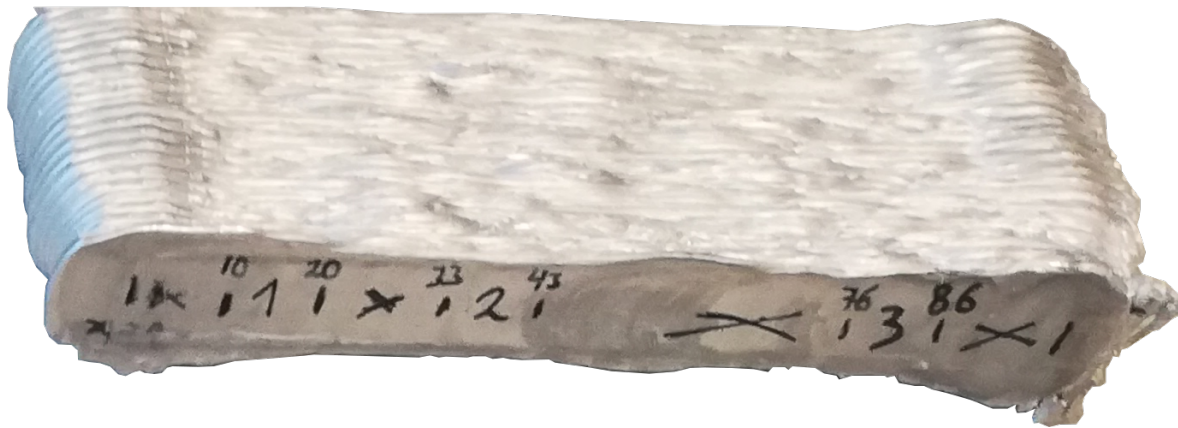


Figure D.73: Indication of the starting position $x = 0$ corresponding to the contour graph of the deposited layers.

Nozzle temperature and extrusion force contour graphs

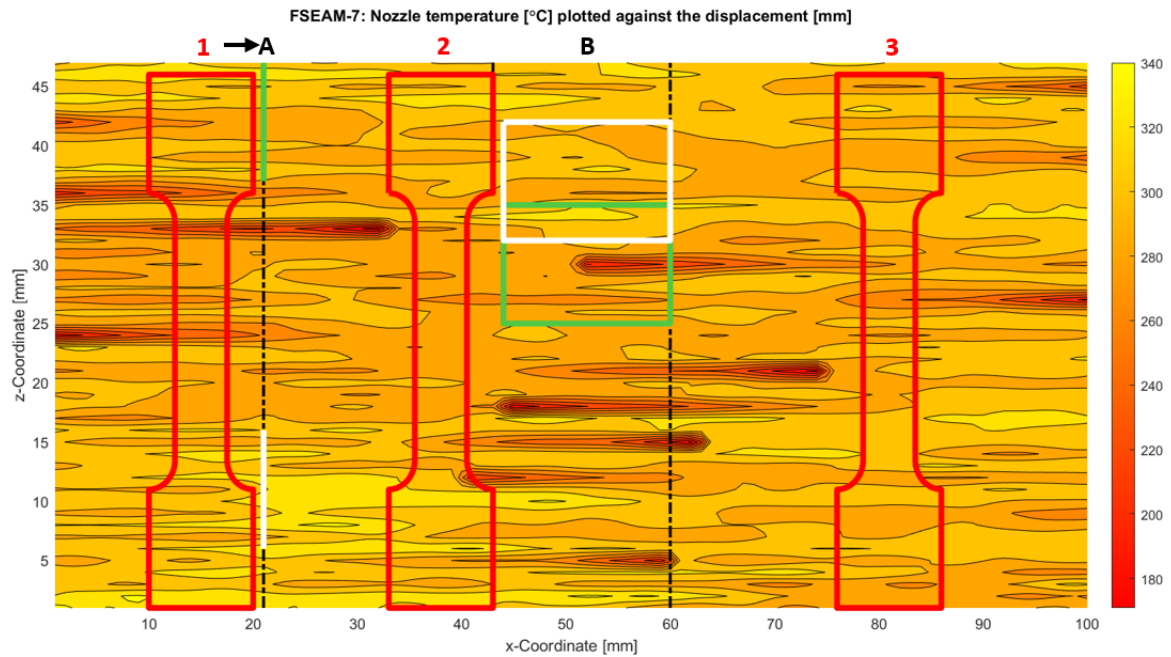


Figure D.74: Nozzle temperature of the seventh experiment corresponding to the x- and z-coordinate of the AM wall including the locations of the tensile test, microscopy, hardness test, and EBSD.

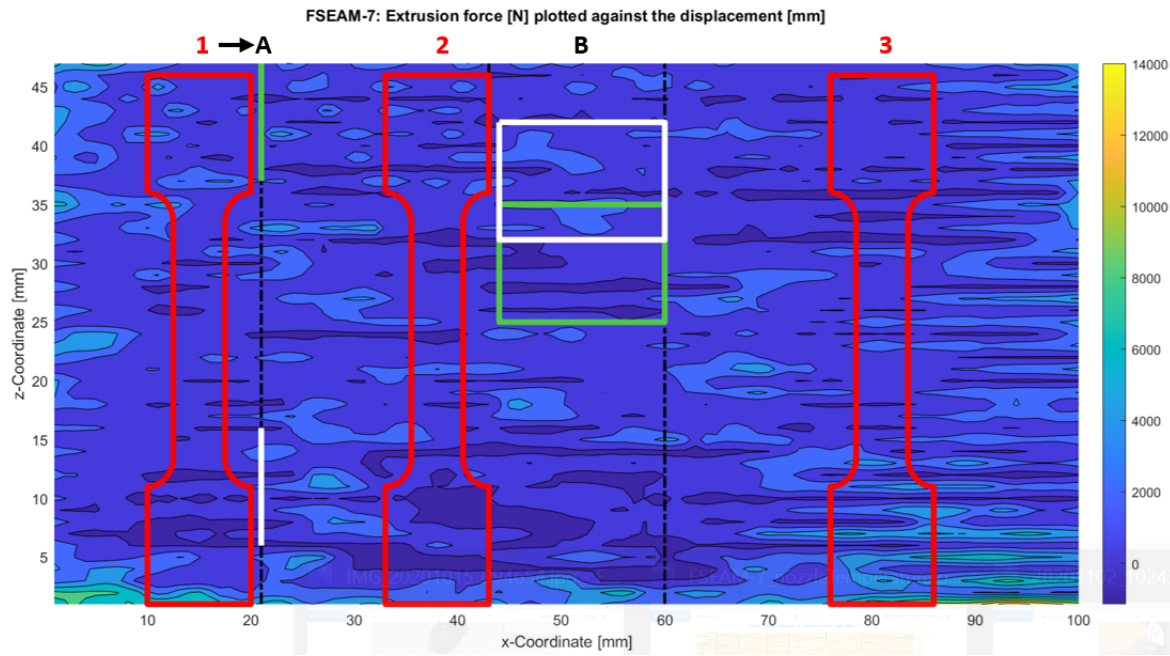


Figure D.75: Extrusion force of the seventh experiment corresponding to the x- and z-coordinate of the AM wall including the locations of the tensile test, microscopy, hardness test, and EBSD.

Microscopic images

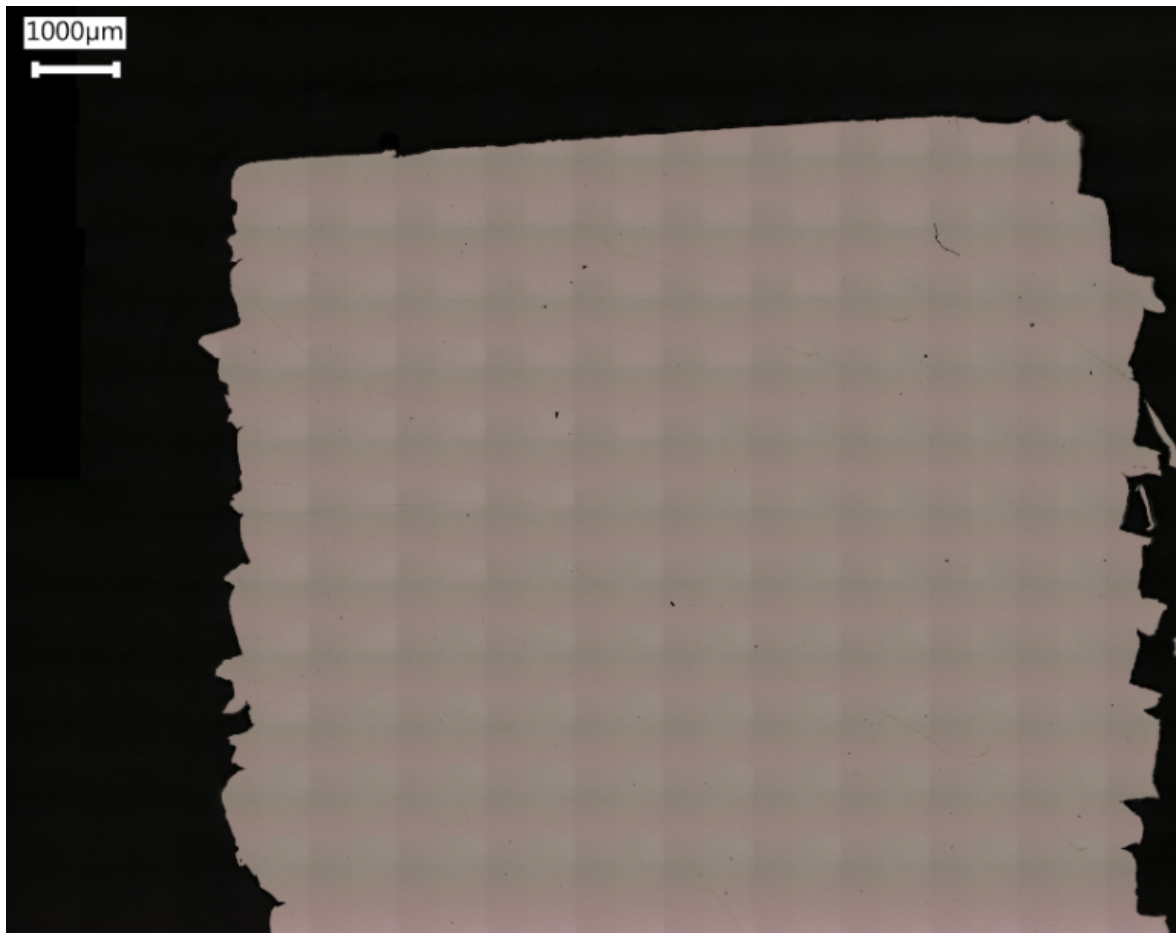


Figure D.76: Transverse cross-section of FSEAM-7A.

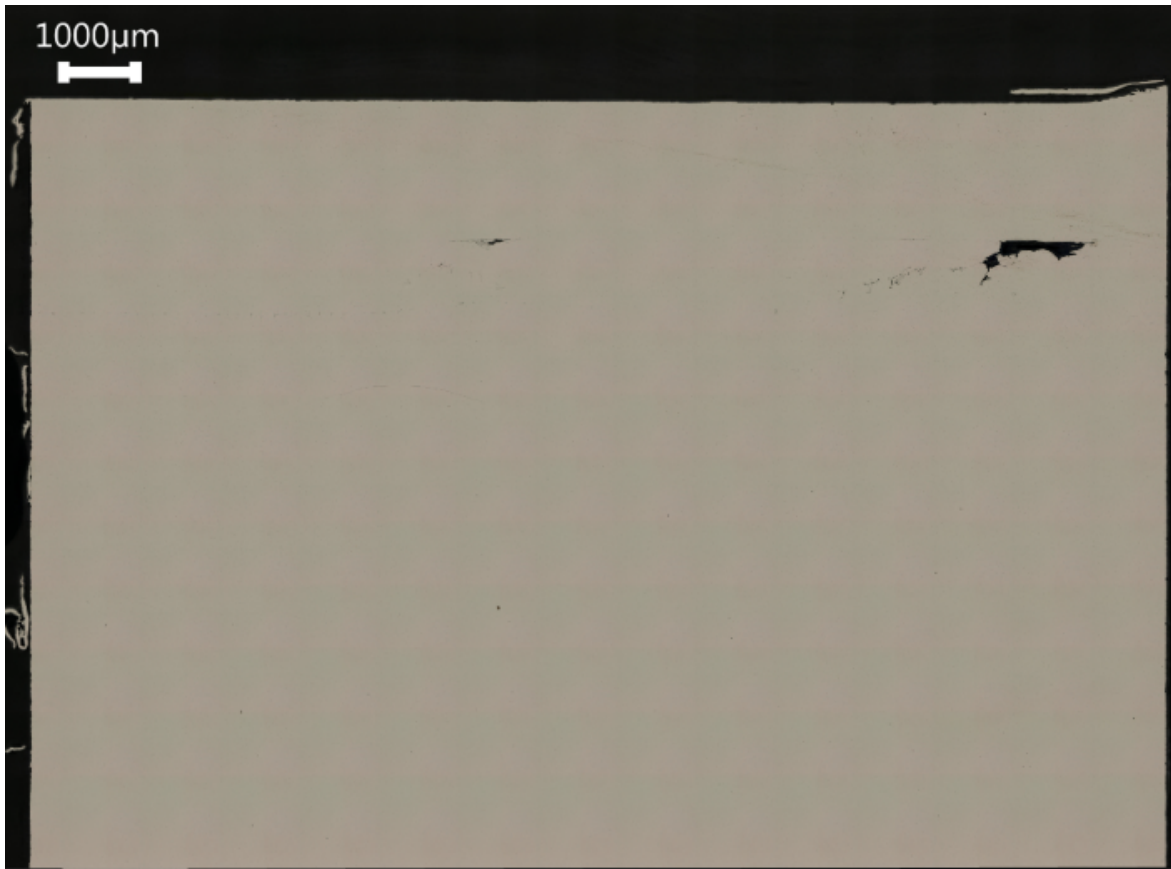
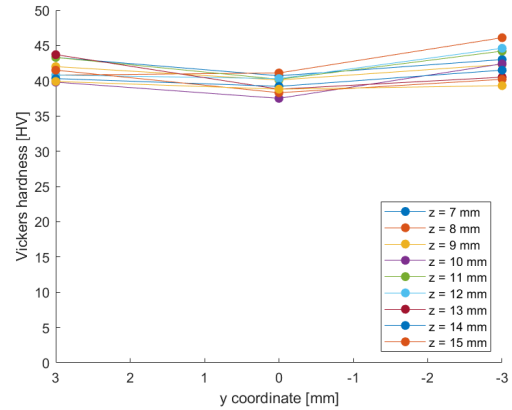
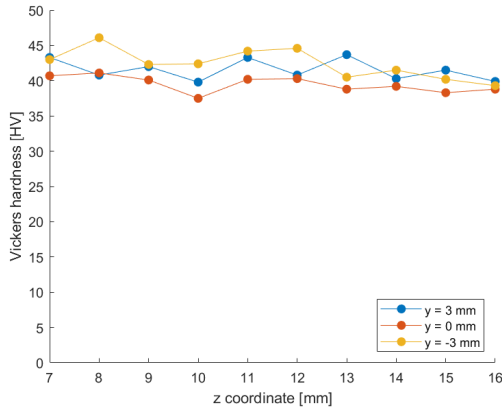
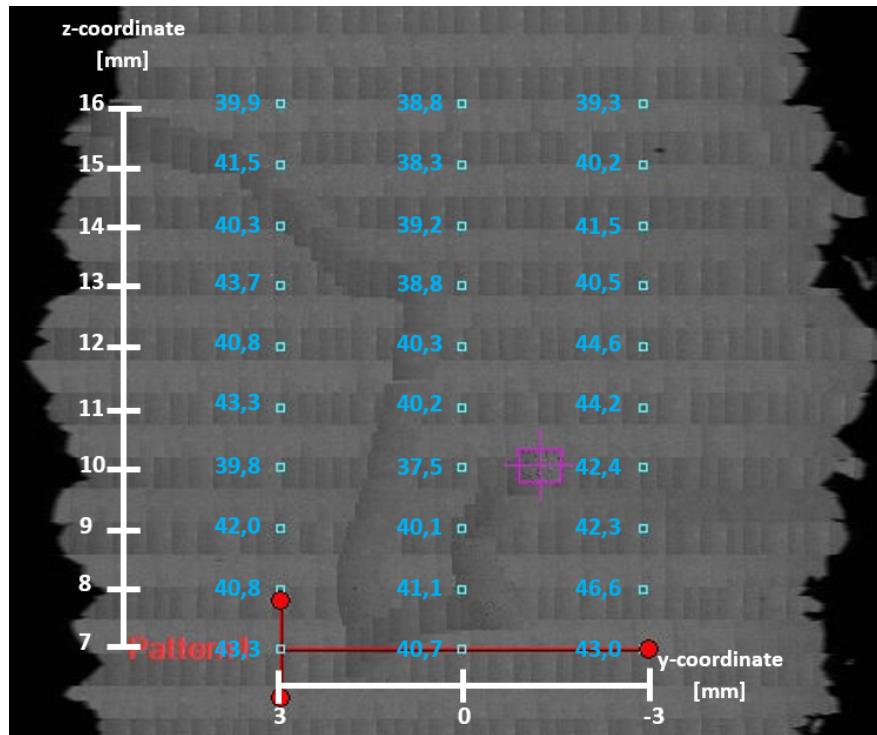


Figure D.77: Longitudinal cross-section of FSEAM-7B.

Hardness test

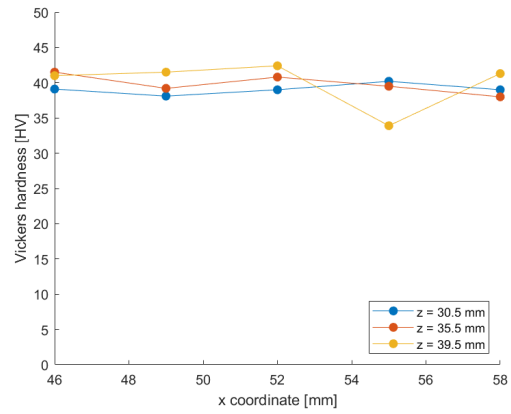
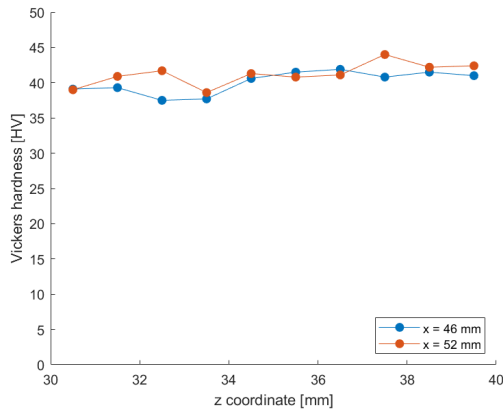


(a) Hardness throughout the height of FSEAM-7A in transverse direction. (b) Hardness throughout the width of FSEAM-7A in transverse direction.



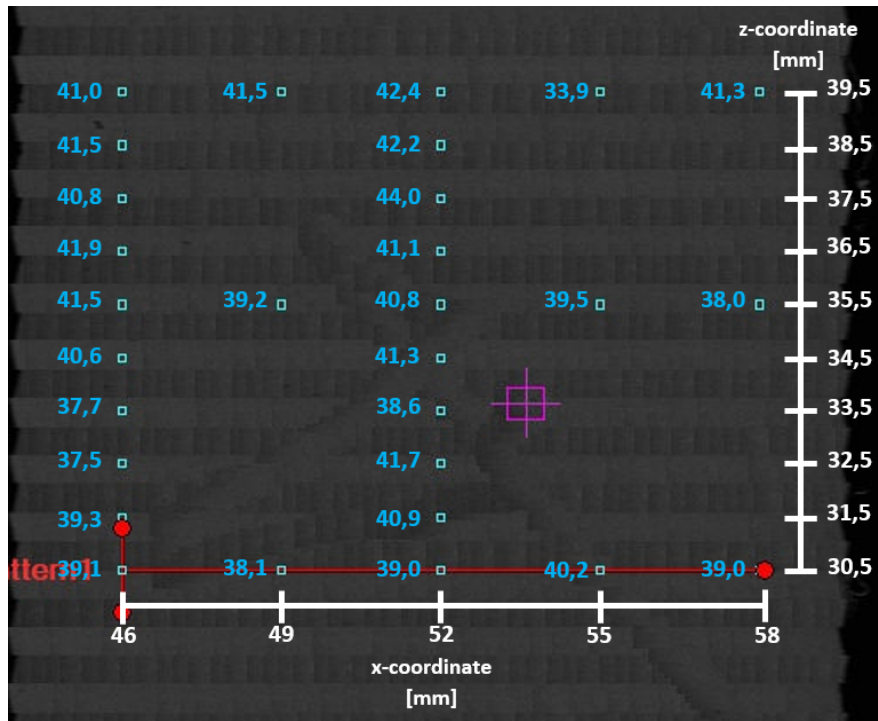
(c) Hardness throughout the transverse cross-section of FSEAM-7A.

Figure D.78: Overview of the hardness of FSEAM-7A in transverse direction.



(a) Hardness throughout the height of FSEAM-7B in longitudinal direction.

(b) Hardness throughout the width of FSEAM-7B in longitudinal direction.



(c) Hardness throughout the longitudinal cross-section of FSEAM-7B.

Figure D.79: Overview of the hardness of FSEAM-7B in longitudinal direction.

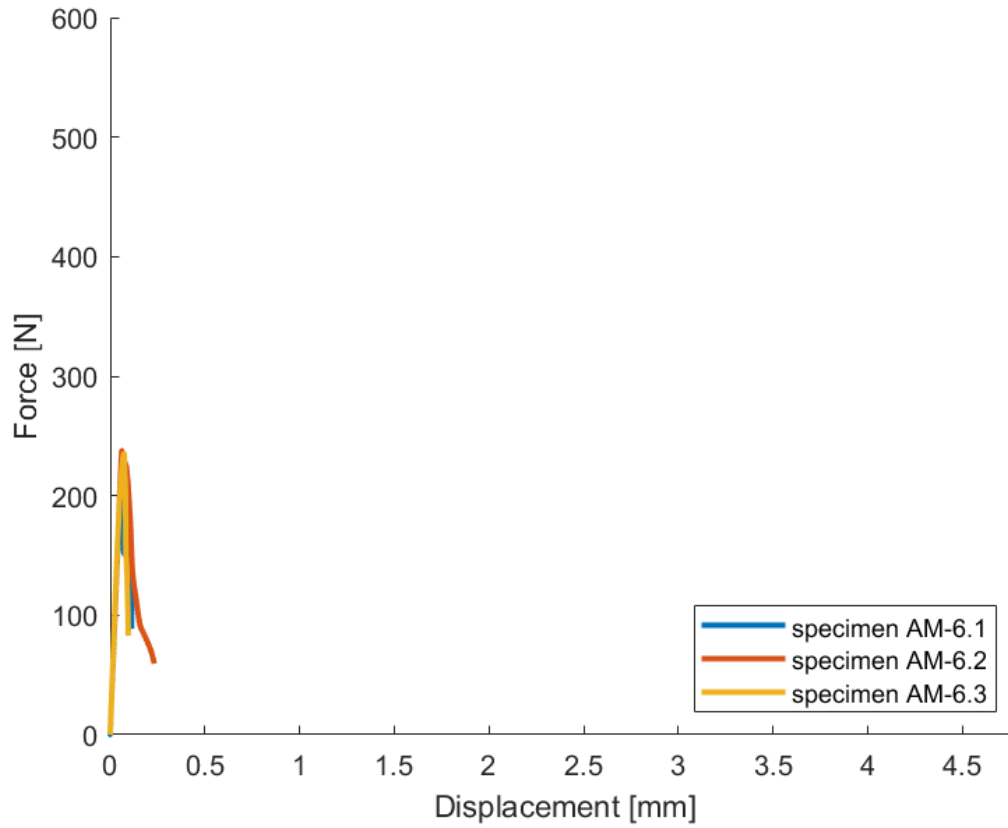
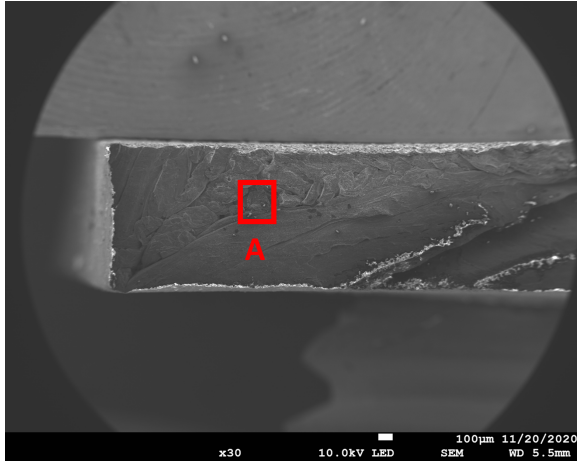
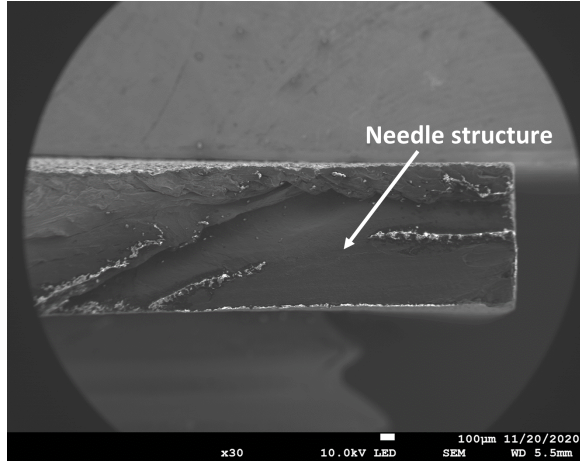
Tensile test

Figure D.80: Force-displacement curves of the tensile test samples of FSEAM-7.

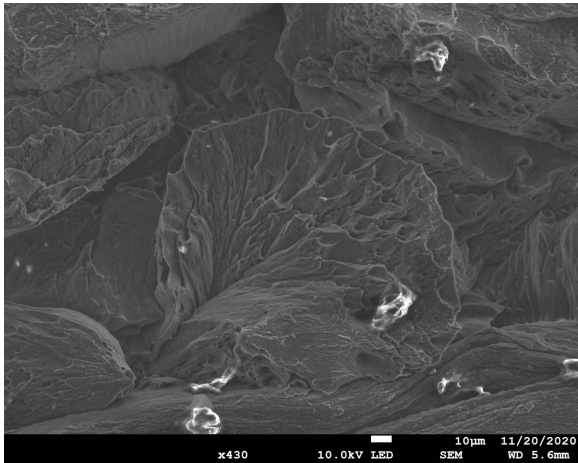
SEM images



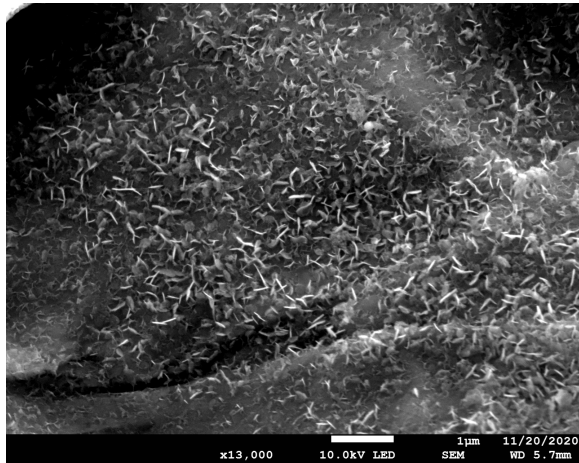
(a) SEM of fracture surface of tensile test 7.1 part 1.



(b) SEM of fracture surface of tensile test 7.1 part 2.

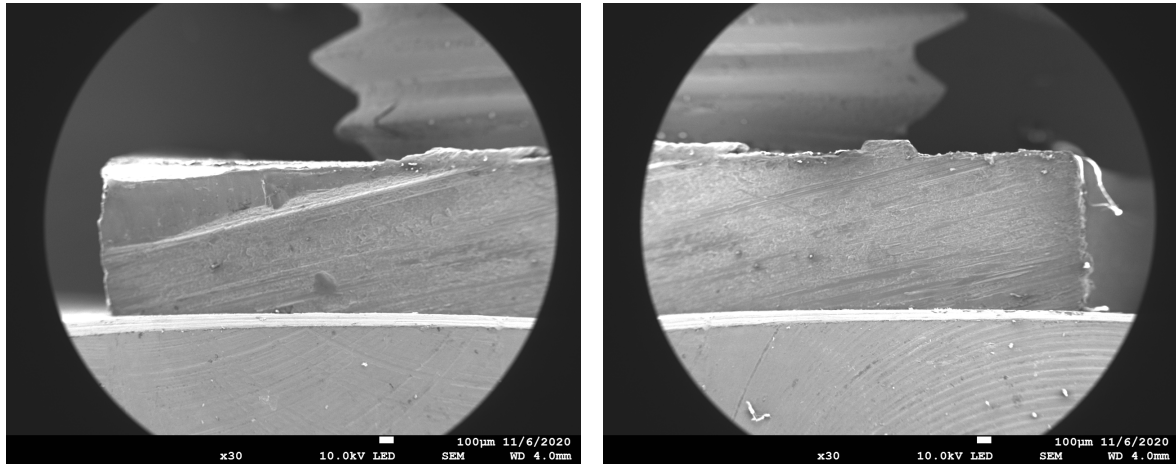


(c) SEM of fracture surface of tensile test 7.1 section A.



(d) SEM of fracture surface of tensile test 7.1 needle structure.

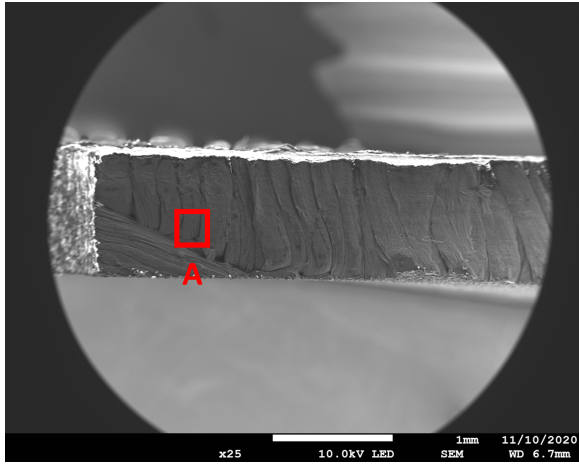
Figure D.81: Fracture surface overviews of tensile test 7.1.



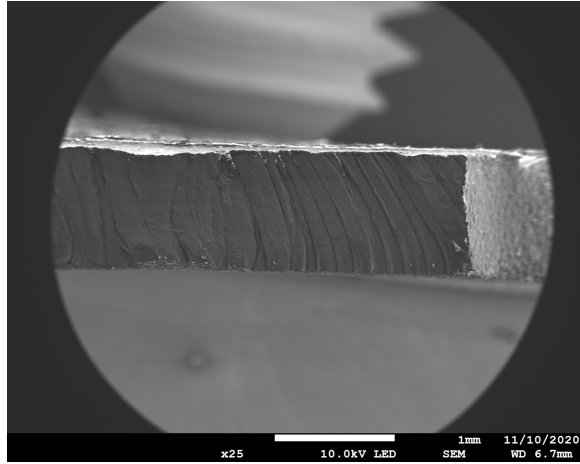
(a) SEM of fracture surface of tensile test 7.2 part 1.

(b) SEM of fracture surface of tensile test 7.2 part 2.

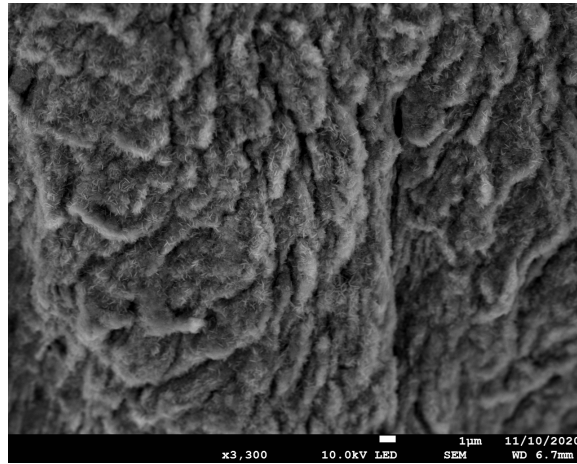
Figure D.82: Fracture surface overviews of tensile test 7.2.



(a) SEM of fracture surface of tensile test 7.3 part 1.



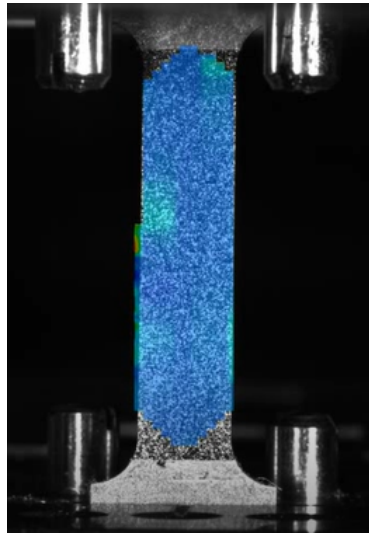
(b) SEM of fracture surface of tensile test 7.3 part 2.



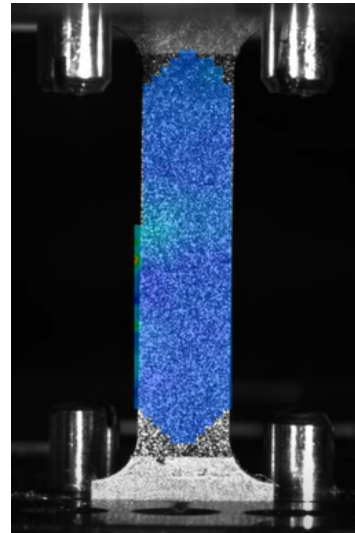
(c) SEM of fracture surface of tensile test 7.3 section A.

Figure D.83: Fracture surface overviews of tensile test 7.3.

Aramis system



(a) Major strain of tensile test sample 7.1 halfway until it starts to neck.

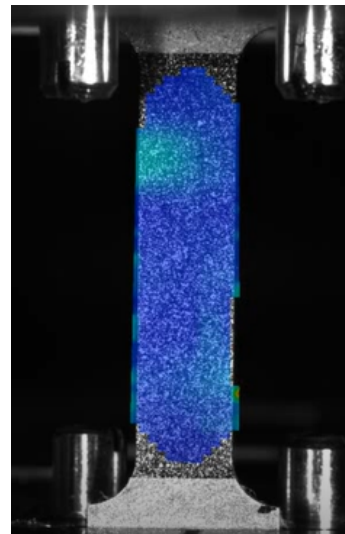


(b) Major strain of tensile test sample 7.1 before it starts to neck.

Figure D.84: Major strain behaviour of tensile test 7.1.

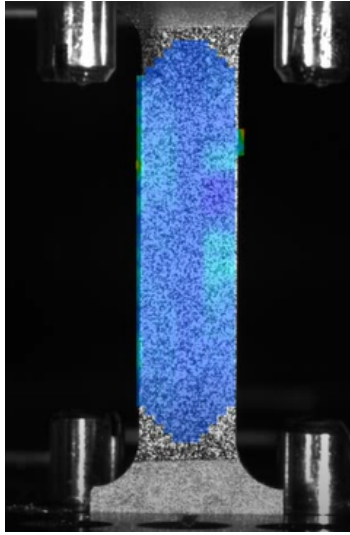


(a) Major strain of tensile test sample 7.2 halfway until it starts to neck.

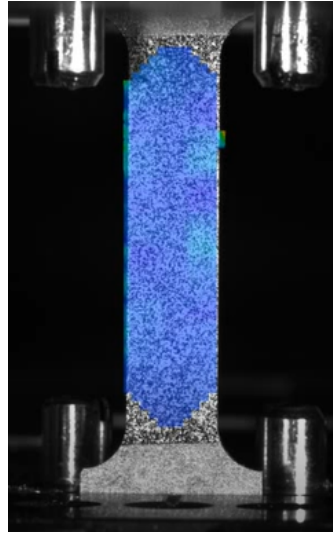


(b) Major strain of tensile test sample 7.2 before it starts to neck.

Figure D.85: Major strain behaviour of tensile test 7.2.



(a) Major strain of tensile test sample 7.3 halfway until it starts to neck.



(b) Major strain of tensile test sample 7.3 before it starts to neck.

Figure D.86: Major strain behaviour of tensile test 7.3.

Angular velocity derivation using the NS equations

The reduced NS equation for the θ -component can be found in equation E.1. The angular velocity as a function of the radius (r) will be derived in this chapter.

$$\frac{\partial}{\partial r} \left(mr^2 \left| \frac{\partial v_\theta}{\partial r} - \frac{v_\theta}{r} \right|^{n-1} \left(\frac{\partial v_\theta}{\partial r} - \frac{v_\theta}{r} \right) \right) = 0 \quad (\text{E.1})$$

Rewriting equation E.1 using $\frac{\partial v_\theta}{\partial r} - \frac{v_\theta}{r} = r \frac{\partial}{\partial r} \left(\frac{v_\theta}{r} \right)$ and integrating equation E.1 with respect to r , results in the following equation.

$$mr^2 \left| r \frac{\partial}{\partial r} \left(\frac{v_\theta}{r} \right) \right|^{n-1} \left(r \frac{\partial}{\partial r} \left(\frac{v_\theta}{r} \right) \right) = C_1 \quad (\text{E.2})$$

The square root term cancels the power in the square root. In addition, both expressions are divided by mr^2 .

$$\left(r \frac{\partial}{\partial r} \left(\frac{v_\theta}{r} \right) \right)^{n-1} \left(r \frac{\partial}{\partial r} \left(\frac{v_\theta}{r} \right) \right) = \frac{1}{mr^2} C_1 \quad (\text{E.3})$$

The terms on the left hand side are similar variables and therefore the power terms can be added, resulting in a term to the power n . Then, multiplying both expression to the power $\frac{1}{n}$.

$$r \frac{\partial}{\partial r} \left(\frac{v_\theta}{r} \right) = \left(\frac{1}{mr^2} C_1 \right)^{\frac{1}{n}} \quad (\text{E.4})$$

Next, both expressions are divided by r and rearranging the equation in terms of

r results in the following expression.

$$\frac{\partial}{\partial r} \left(\frac{v_\theta}{r} \right) = \left(\frac{1}{m} C_1 \right)^{\frac{1}{n}} r^{-\frac{n-2}{n}} \quad (\text{E.5})$$

Integrate equation E.5 with respect to r , multiply it with r , and rewrite the equation leads to the following expression for the angular velocity as a function of the radius.

$$v_\theta(r) = -\frac{n}{m^{1/n}} C_1^{1/n} r^{\frac{n-2}{n}} + C_2 r \quad (\text{E.6})$$

where C_1 and C_2 are unknown constants that can be solved using boundary conditions.